

Studying the electron-electron correlation by pair emission from surfaces

Habilitationsschrift

zur Erlangung des akademischen Grades

Dr. rer. net. habil.

vorgelegt der

Mathematisch-Naturwissenschaftlich-Technischen Fakultät
der Martin-Luther-Universität Halle-Wittenberg

von

Herrn Dr. Frank O. Schumann

geb. am: 7.5.1964 in Dortmund

1. Gutachter : Prof. Dr. J. Kirschner
2. Gutachter : Prof. Dr. W. Widdra
3. Gutachter : Prof. Dr. C. Back

Halle(Saale), verteidigt am 30.01.2012, Probevorlesung am 12.03.2012

Contents

1	Introduction	5
2	The He-atom revisited	7
3	The exchange-correlation hole and its relevance for modern solid theory	9
3.1	The concept of the exchange correlation hole	9
3.2	Exchange hole	10
3.3	Coulomb “hole” and model of screening	13
3.4	The exchange-hole for a nonuniform charge distribution	15
3.4.1	One-dimensional two-electron model	15
3.4.2	Exchange-hole near a surface	19
4	Electron spectroscopy beyond the effective single particle picture	27
4.1	General aspects of electron coincidence spectroscopy	27
4.2	Double photoemission	31
4.3	A fundamental issue of coincidence experiments	33
5	Case studies	39
5.1	Manifestation of the xc-hole in pair emission	39
5.2	Full angular distribution of electron pairs	42
5.3	Spin-resolved (e,2e)	45
5.4	Correlated positron-electron pair emission	47
5.5	Double photoemission illuminates the Auger process	52
6	Summary and Outlook	55
7	References	57
8	Original literature	61
9	Acknowledgement	127

1. Introduction

An integral part of modern technology is microelectronics in which electronic transport plays an important part. First attempts to describe the phenomenon of electrical conductivity in metals can be traced back to the work of Drude and Lorentz [1, 2]. The physical picture was based on the assumption that the electrons do not interact in the metal and that only elastic collisions occur at the positions of the atoms. In an applied electrical field these collisions ensure that the velocity of the electrons converges to a constant value. This rather crude theory gave a satisfactory explanation of the finite resistivity and the observed Ohm's law. However, the application of the classical kinetic gas theory failed completely to describe the behavior of the specific heat.

The experimentally observed linear temperature dependence of the electronic specific heat at low temperatures could be accounted for in the so-called Sommerfeld theory [3]. Again electrons were treated as independent and non-interacting particles, but the rules of quantum mechanics were used, most important was the inclusion of the Fermi-Dirac statistics. The prediction of the correct temperature dependence of the specific heat was an important breakthrough for the emerging quantum theory. Electrons in a solid, however, do not move independently of each other, they experience a mutual force mediated by the Coulomb interaction. Hence one would expect the independent electron picture not to be an inadequate description of electrons in a solid. Solids exhibit features completely missing in atoms. Those are termed many-body effects, which are the manifestation of the electron-electron interaction. Ferromagnetism and superconductivity may suffice as examples. In a ferromagnet the spins at different lattice sites (within a magnetic domain) align parallel to each other, which is due to the exchange interaction between the electrons. This is essentially the Coulomb interaction modified by the Pauli principle. Likewise, electrons forming a Cooper pair interact (within the BCS theory) via electron-phonon coupling [4, 5]. Clearly an independent electron picture is unable to explain this phenomenon. A concept which describes the relation between two electrons is the exchange-correlation hole [6, 7]. The possibility to access this concept via pair emission was theoretically predicted and motivated this work [8, 9]. The presentation has the following structure:

- Chapter 2 explains the meaning of an effective independent electron picture. For this we recall some facts of the He atom.
- Chapter 3 will discuss essential aspects of the exchange-correlation hole. We start with the non-interacting free electron gas [4, 5, 10]. Although the global charge distribution is uniform within this model it turns out that the charge distribution around each electron is not uniform. As a matter of fact, each electron is surrounded by a reduced electronic charge which is called the exchange-hole, the inclusion of the Coulomb interaction leads to the exchange correlation (xc) hole [6, 7]. We will present simplified scenarios containing the exchange-hole alone which will provide

insights in the general behavior of the xc-hole which plays an important role within the Density Functional Theory (DFT).

- Chapter 4 will discuss that the xc-hole is accessible via pair emission from surfaces. More precisely, it is predicted by theory that the manifestation of the xc-hole can be observed in angular distributions via a zone of reduced intensity [8,9]. A simplified discussion of Double Photoemission will be given which explains the emergence of this zone. Before the experimental results are shown, a few general statements regarding coincidence experiments will be made which highlight the challenges faced.
- Chapter 5 summarizes the key findings of this work by presenting case studies. In section 5.1 we show that the predicted zone of reduced intensity (“depletion zone”) exists for electron or photon excitation from insulator surfaces [11,12]. In section 5.2 it is demonstrated that the full angular extension of the “depletion zone” can be observed including metal surfaces [13–15]. In sections 5.3 and 5.4 two approaches are discussed which allow to disentangle the contribution of the Pauli principle from the Coulomb contribution in pair emission. In section 5.3 one uses a spin-polarized primary beam exciting a ferromagnetic sample. Suitable conditions can be found where the spin of the primary electron and the collision partner are parallel or antiparallel. It is observed that the “depletion zones” differ in size [15]. In section 5.4 pair emission upon positron excitation is presented. In this case, the scattering is described by the Coulomb interaction alone. It is proven that the process of correlated positron-electron emission exists [16]. Therefore it is possible to measure angular distributions of positron-electron pairs once a suitable positron is available. In section 5.5 a well-known effect is discussed, namely Auger electron emission. Within a coincidence experiment it turns out that the available energy is shared continuously between the two emitted electrons. This is in contrast to the expectation within a simple two-step model [17]. This observation can be brought into the context of recent theoretical studies on the time evolution of the exchange-correlation hole [18,19].
- Chapter 6 summarizes the experimental observations and provides a perspective for future activities.

2. The He-atom revisited

It is enlightening to discuss the He atom, before moving to solids. It allows to explain what is meant by an effective independent electron picture. The Hamiltonian describing this system can be written as:

$$H = H_1 + H_2 + V_{e-e} \quad (2.1)$$

$$H_{1,2} = \frac{\mathbf{p}_{1,2}^2}{2m} + \frac{Ze \cdot (-e)}{4\pi\epsilon_0 \cdot |\mathbf{r}_{1,2} - \mathbf{R}|} \quad (2.2)$$

$$V_{e-e} = \frac{(-e) \cdot (-e)}{4\pi\epsilon_0 \cdot |\mathbf{r}_1 - \mathbf{r}_2|} \quad (2.3)$$

The terms H_1 and H_2 describe the motion of a single electron with charge $-e$ around a nucleus of charge Ze localized at \mathbf{R} . In the case of a He atom we have $Z=2$. The coordinates of the electrons are given by \mathbf{r}_1 and \mathbf{r}_2 . The solution for H_1 and H_2 can be derived analytically as demonstrated in quantum mechanics classes. We may write for the wave functions $\psi_a(\mathbf{r}_1)$ and $\psi_b(\mathbf{r}_2)$ where the subscripts a and b refer to the appropriate quantum numbers. The mutual Coulomb interaction between the electrons is given by V_{e-e} and the very existence of this term does not allow to write the two-particle wave function as a Slater determinant of the form $\psi(\mathbf{r}_1, \mathbf{r}_2) = \sqrt{\frac{1}{2}}(\psi_a(\mathbf{r}_1)\psi_b(\mathbf{r}_2) - \psi_b(\mathbf{r}_1)\psi_a(\mathbf{r}_2))$. The true wave function is not composed of terms which contain single particle wave functions. In a first step we ignore V_{e-e} completely. Then the binding energy of the ground state can be determined immediately. The experimental counterpart is the double ionization energy of the He atom. We recall that the energy to ionize the H atom is 13.6 eV. This well-known experimental result is matched very well by the analytically obtained result of the Schrödinger equation. This solution can be extended to a nucleus of charge Z surrounded by a single electron. In this case we obtain for the single ionization energy $Z^2 \cdot 13.6 \text{ eV} = 54.4 \text{ eV}$ if we set $Z = 2$. If we completely neglect the electron-electron interaction one obtains for the energy required to double ionize a He atom twice the energy of single ionization which is 108.8 eV. This value is

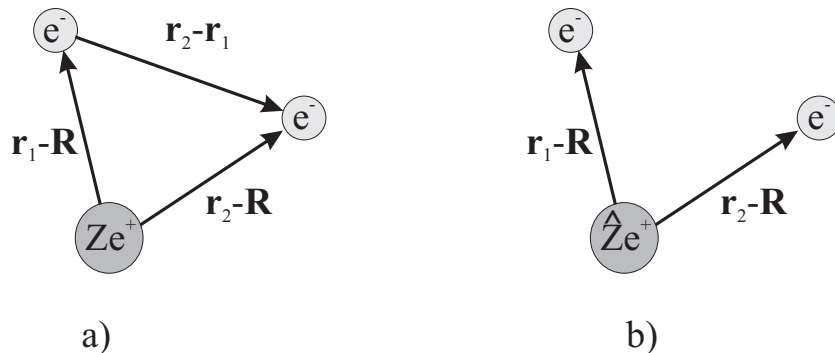


Figure 1. a) In a He atom two electrons experience the attractive Coulomb interaction of the nucleus with charge $Z=2$ and the repulsive electron-electron interaction V_{e-e} among them. b) The approximation of V_{e-e} described in the text results in a formal description of non-interaction electrons in the field of a nuclear charge \hat{Z} .

different by a large margin from the experimental observation [20]. Using photons to double ionize the He atom an energy in excess of 79 eV is required. Clearly, ignoring the electron-electron interaction is too coarse an approximation. Another very serious pitfall of setting $V_{e-e}=0$ is the fact that one can not explain how a single photon can lead to the emission of an electron pair. Simply put, one can not answer the question how the electrons “know” about each other. As we will show below, a finite electron-electron interaction is required to eject an electron pair from an electronic system. Therefore, in order to improve on the ground state energy and to explain double ionization one has to include V_{e-e} at least in an approximate way. With this in mind we rewrite V_{e-e} which is still exact:

$$V_{e-e} = \frac{e^2}{4\pi\epsilon_0 \cdot |\mathbf{r}_1 - \mathbf{r}_2|} = \frac{\frac{1}{2}e^2}{4\pi\epsilon_0 \cdot |\mathbf{r}_1 - \mathbf{R}|} + \frac{\frac{1}{2}e^2}{4\pi\epsilon_0 \cdot |\mathbf{r}_2 - \mathbf{r}_1|} \quad (2.4)$$

The next step consists in making the approximations $|\mathbf{r}_1 - \mathbf{r}_2| \approx |\mathbf{r}_1 - \mathbf{R}|$ and $|\mathbf{r}_2 - \mathbf{r}_1| \approx |\mathbf{r}_2 - \mathbf{R}|$. We are guided to do this because the 1s electron of the hydrogen atom is localized near the nucleus. As far as electron 1 is concerned electron 2 appears to be at the nucleus and vice versa. The net effect is that each electron screens to some extent the potential due to the nucleus. With this approximation we rewrite V_{e-e} as:

$$V_{e-e} = \frac{\frac{1}{2}e^2}{4\pi\epsilon_0 \cdot |\mathbf{r}_1 - \mathbf{R}|} + \frac{\frac{1}{2}e^2}{4\pi\epsilon_0 \cdot |\mathbf{r}_2 - \mathbf{R}|} \quad (2.5)$$

The key point is to recognize that the two terms of V_{e-e} have the same dependence on the coordinates as the nucleus-electron interaction. Therefore our Hamiltonian can be written as a sum of single particle Hamiltonians:

$$H \approx \widehat{H}_1 + \widehat{H}_2 \quad (2.6)$$

$$\widehat{H}_{1,2} = \frac{\mathbf{p}_{1,2}^2}{2m} + \frac{1}{4\pi\epsilon_0} \frac{-(Z - \frac{1}{2})e^2}{|\mathbf{r}_{1,2} - \mathbf{R}|} \quad (2.7)$$

Formally we have an electronic system in which the two electrons experience the Coulomb interaction of a nucleus with charge $\widehat{Z}e = (Z - \frac{1}{2})e$, but do not interact with each other. This situation is depicted in Fig.1 b). In this sense we have an independent electron picture, but the electron-electron interaction V_{e-e} is incorporated, although only in an approximation. This model can be refined by setting $\widehat{Z} = Z - S$ where S plays the role of a screening parameter which we allow to vary. Best agreement with experiment is adopted for $S=0.656$. In this case the double ionization energy is 78.8 eV which is very close to the experimental value of 79.004 eV [20]. The single ionization energy is predicted to be 24.42 eV, in good agreement with the experimental value of 24.588 eV [20]. We learn an important fact, namely that despite a finite electron-electron interaction an effective single electron picture can be an appropriate description. At this point it is useful to make connection to an important theoretical description in particular for solids. This is the so-called Density Functional Theory (DFT), within this framework Kohn-Sham equations are contained [21–24]. Formally they have the structure of a Schrödinger equation for independent electrons although the aspect of exchange and correlation is included via a potential energy term also known as the exchange-correlation functional.

3. The exchange-correlation hole and its relevance for modern solid theory

3.1. The concept of the exchange correlation hole

The concept of the exchange-correlation hole was put forward by Wigner & Seitz and Slater more than 75 years ago [6,7]. They posed essentially the question what is the joint probability to find one electron at one location while the second electron has a distance r from the first one. As we will see, one has to distinguish between parallel and antiparallel spin orientation as sketched in Fig.2. The probability we seek is closely related to the pair correlation function $g_{\uparrow\uparrow}(r)$ and $g_{\uparrow\downarrow}(r)$, where the subscripts denote the relative spin alignment. As shown below, these functions are intimately related to the two-particle wave function. Even without performing any calculation a few statements can be made regarding the behavior of the pair correlation function. A fundamental aspect of quantum mechanics, namely the requirement of the wave function to be antisymmetric upon particle exchange, will tell us that the joint probability to find two electrons with parallel spins at the same location has to be zero, see Fig.3 a). Such a strict law does not exist if the two electrons have antiparallel spins. However, the repulsive Coulomb interaction between the electrons will make it less favorable for two electrons to be close to each other. This interaction will of course also tend to keep parallel spins apart from each other. From these fundamental facts we can conclude that electrons tend to avoid each other irrespective of the relative spin alignment. The qualitative behavior of $g_{\uparrow\uparrow}(r)$ and $g_{\uparrow\downarrow}(r)$ is shown in Fig.3 a) which constitutes a slightly modified presentation of the original figure given by Slater in his landmark paper [7]. It is useful to compute the average $\frac{1}{2}(g_{\uparrow\uparrow}(r) + g_{\uparrow\downarrow}(r))$ pair correlation function, which is plotted in Fig.3 b). The net effect is the emergence of a zone of reduced electronic charge around each electron for which the gray area is a measure. This is the exchange-correlation (xc)-hole. Furthermore, the amount of charge expelled in the vicinity of an electron is exactly one elementary charge. The length scale over which the exchange-correlation

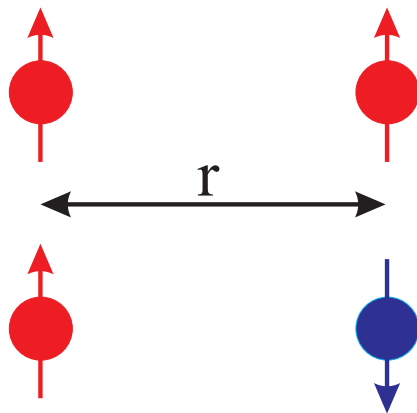


Figure 2. In an arbitrary electronic system one can ask the question about the joint probability to find two electrons which are separated by a distance r . We distinguish between parallel and antiparallel spins.

function changes is of the order a few Å. It is generally believed that the rearrangement of the charge due to the Pauli principle takes place over a larger length scale than due to Coulomb correlation. Simply put, the exchange hole is larger than the Coulomb hole as schematically shown in Fig.3 a). In order to elaborate on these points it is worthwhile to consider two specific examples which can be solved analytically. These are based on the problem of an electron in a rectangular potential well with infinitely high barrier. The solution is a standard exercise in quantum mechanical classes. Extending the solution to a three dimensional potential well is straightforward. Likewise it is easy to include “many” electrons as long as their mutual Coulomb interaction is ignored. At this point we have the model of the so-called free electron gas. The highest occupied state is characterized by the Fermi momentum k_F and Fermi energy E_F . First, we discuss the exchange-hole within the free electron gas model. Second, we explore the charge distribution near a potential step which serves as a model for a surface. This example may serve to illuminate the contribution of the Coulomb correlation. Although this work will focus on solid surfaces, it is important to state that the emergence of an exchange-correlation hole is not limited to solids, but also exists in atoms and molecules. This we will demonstrate by a simple one-dimensional model for an atom.

3.2. Exchange hole

The simplest many-electron system we can think of is the non-interacting free electron gas. Furthermore, the attractive and localized Coulomb potentials due to the ion-cores are replaced by a constant potential also referred to as jellium. The global electronic charge density is constant and labelled with ρ_0 . Within this electronic system we want to determine the joint probability to find one electron at location \mathbf{r}_i , while the other is at \mathbf{r}_j and how does it vary with the difference vector $\mathbf{r}_i - \mathbf{r}_j$. The way to calculate will become immediately clear if we consider at the beginning a two-particle wave function $\psi_{i,j}(\mathbf{r}_i - \mathbf{r}_j)$, where i and j label the occupied states including the spin. The term $|\psi_{i,j}(\mathbf{r}_i - \mathbf{r}_j)|^2 d\mathbf{r}_i d\mathbf{r}_j$ describes the joint probability of finding an electron at location \mathbf{r}_i within a volume $d\mathbf{r}_i$, while the other electron is located at \mathbf{r}_j within a volume $d\mathbf{r}_j$. We write for the joint probability $\rho(\mathbf{r}_i, \mathbf{r}_j)$. For parallel spins we know already from the Pauli principle that two electrons with the same spin cannot be at the same location. For very large distances we expect to find with certainty another electron, after all there are electrons in this model, which are described by plane waves. Consequently what is left to do is to determine the length scale over which the probability rises from 0 to 1. The calculation of $g_{\uparrow\uparrow}(r)$ is straightforward and was first reported by Wigner and Seitz [6], it can be found in solid state physics textbooks, e.g. [10, 25, 26]. Let us sketch the important steps which lead to the final result. The single particle wave functions to be used are plane waves $e^{i\mathbf{k}\mathbf{r}}$. We recall that the total wave function has to be antisymmetric upon particle exchange. Due to the fact that the spin part for parallel spins is symmetric, the antisymmetry is contained within the spatial part of the wave

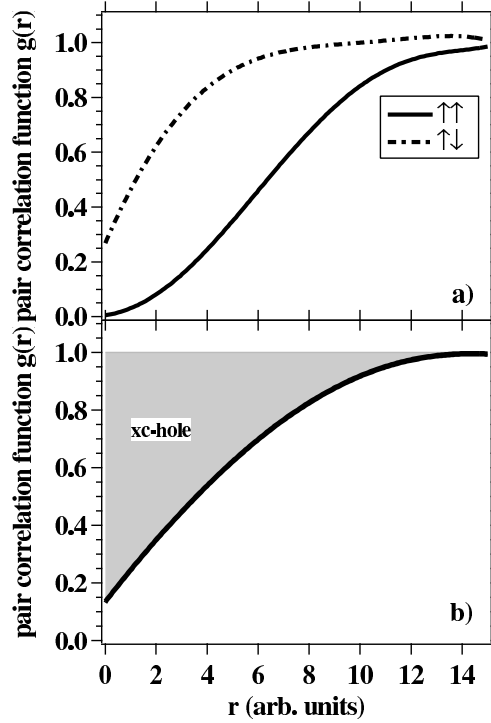


Figure 3. In panel a) we plot the schematic behavior of the pair correlation functions $g_{\uparrow\uparrow}(r)$ (solid curve) and $g_{\uparrow\downarrow}(r)$ (dashed curve) for an interacting electronic system following the idea of Slater [7]. In panel b) we show the average of the two functions. The shaded area is a measure of the charge missing around the vicinity of an electron. This amount equals exactly one elementary charge and is called the exchange-correlation hole.

function for which we write:

$$\psi_{i,j}(\mathbf{r}_i, \mathbf{r}_j) = \frac{1}{\sqrt{2}V} (e^{i\mathbf{k}_i\mathbf{r}_i} e^{i\mathbf{k}_j\mathbf{r}_j} - e^{i\mathbf{k}_j\mathbf{r}_i} e^{i\mathbf{k}_i\mathbf{r}_j}) \quad (3.1)$$

This term can be inserted into the expression for the joint probability $|\psi_{i,j}(\mathbf{r}_i, \mathbf{r}_j)|^2 d\mathbf{r}_i d\mathbf{r}_j$ which can be easily simplified to yield:

$$|\psi_{i,j}(\mathbf{r}_i, \mathbf{r}_j)|^2 d\mathbf{r}_i d\mathbf{r}_j = \frac{1}{V^2} (1 - \cos\{(\mathbf{k}_i - \mathbf{k}_j)(\mathbf{r}_i - \mathbf{r}_j)\}) d\mathbf{r}_i d\mathbf{r}_j \quad (3.2)$$

The most important point becomes clear if one sets $\mathbf{r}_i = \mathbf{r}_j$. In this case the cosine term becomes 1 and joint probability is therefore zero independent of the actual values of the momenta \mathbf{k}_i and \mathbf{k}_j . In the free electron gas, momenta up to the Fermi momentum k_F are occupied and what is left to do is to average over all occupied combinations. Due to the fact that the free electron gas is isotropic, only the length of the distance vector $r = |\mathbf{r}_i - \mathbf{r}_j|$ is of relevance. The integrals which are encountered can be solved analytically and are tabulated. It turns out that the natural variable is the term $k_F \cdot r$ and the result for $g_{\uparrow\uparrow}$ is:

$$g_{\uparrow\uparrow}(k_F r) = 1 - 9 \cdot \frac{(\sin(k_F r) - (k_F r) \cdot \cos(k_F r))^2}{(k_F r)^6} \quad (3.3)$$

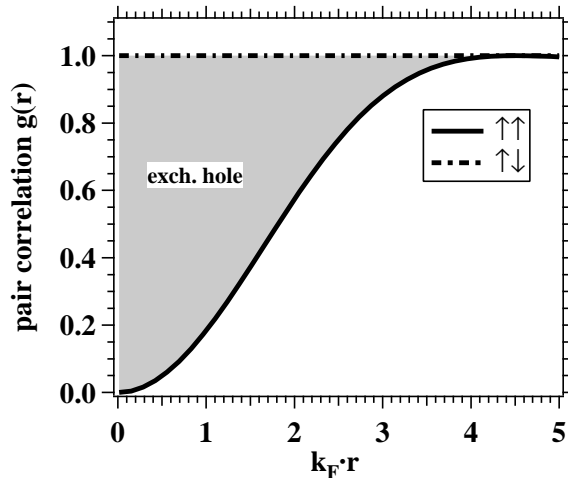


Figure 4. Pair correlation functions $g_{\uparrow\uparrow}(k_F r)$ and $g_{\uparrow\downarrow}(k_F r)$ for the free (non-interacting) electron gas. The solid line shows the dependence for parallel spins, while the dashed line is for antiparallel aligned spins. The shaded area is a measure of the charge missing around the vicinity of an electron. This amount equals exactly one elementary charge and is called the exchange-hole.

We have plotted this result in Fig.4 as the solid line. As expected, $g_{\uparrow\uparrow}$ is zero for two electrons being at the same location. We notice that $g_{\uparrow\uparrow}$ rapidly increases and at about $k_F r = 4$ has essentially approached one. The meaning of this value is that the two electrons are uncorrelated at this distance. We recall that for metals typical values for k_F are of the order $1-2 \text{ \AA}^{-1}$ [4]. This means that, over a length scale of a few nearest neighbors $g_{\uparrow\uparrow}(r)$, approaches a value indicative of uncorrelated electrons. For antiparallel spins, the result for $g_{\uparrow\downarrow}(r)$ is particularly simple since it has a constant value of 1, which is drawn as dashed line in Fig.4. This can be easily understood because the Pauli principle does not prohibit two electrons to be at the same location if their spins are antiparallel. At this point we have exactly determined expressions for the pair correlation functions for our model system. The next step would be to determine from the pair correlation functions the charge surrounding each electron. In the present example the global charge density is constant therefore the integration reduces to the integration of the pair correlation function. More interesting is to ask for the charge missing around the electron of interest. This missing charge is called exchange or Fermi hole and is labelled with q_x . In our isotropic system the volume integration can be reduced to a radial integration:

$$q_x = \rho_0 \int_0^\infty dr r^2 (1 - g_{\uparrow\uparrow}(k_F r)) \quad (3.4)$$

The analytical result is $q_x = -e$, this means that exactly one electron is removed from the vicinity of the electron of interest. This result does hold also for the general case of a finite Coulomb interaction. The more general case of a non-uniform charge distribution will be discussed below.

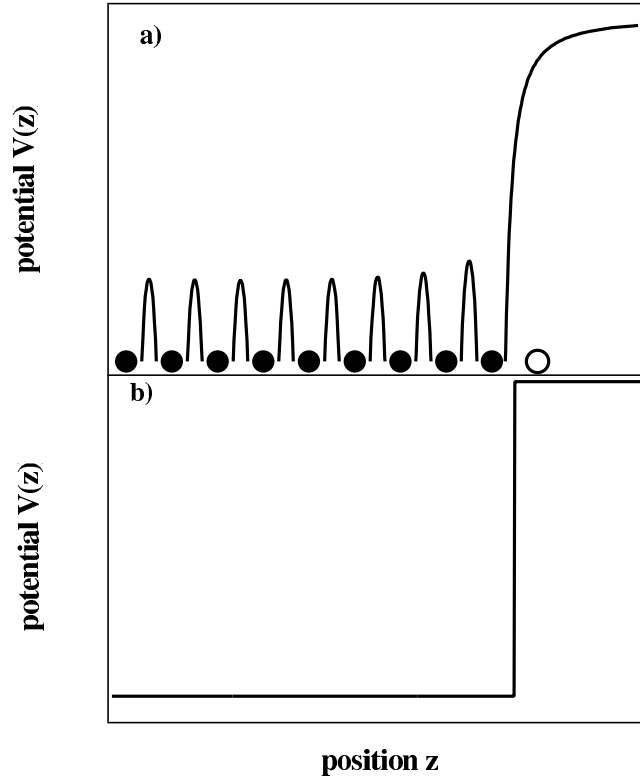


Figure 5. Schematic view of the of the potential energy near a 1D potential step. In panel a) we plot the superposition of the Coulomb potentials of the ionic cores which are marked by the solid circles. The open circle identifies the position of the first missing ion at the surface. In panel b) we plot an approximation of this potential via an abrupt step of infinite height.

3.3. Coulomb “hole” and model of screening

One of the first problems taught in quantum mechanics is the 1D potential well with potential barriers say at $z=-L$ and $z=0$. It is instructive to recall on which basis such a model is constructed. For this we may zoom into the region near the potential step at $z=0$, see Fig.5. We present in a schematic way the potential experienced by electrons in the vicinity of the barrier at $z=0$. We emphasize that the electron-electron interaction is ignored in the following. The solid circles represent the location of the ion cores which are responsible for an attractive potential. We assume a periodic structure, hence the distance between ions is constant. At the barrier the periodicity is broken and the first missing ion core is marked by an open circle. If we add up all the Coulomb potentials of the ion cores we end up with the solid line. We observe that the presence of a surface creates a potential step for the electrons. From an electro-static point of view one can rephrase this fact by stating that the potential step is created by adding a negative charge, thereby compensating the last ion’s contribution. In order to make the model easier in terms of calculation we replace the coulombic potential by an abrupt potential step of infinite height. Since the charge distribution creating this barrier is not made by electrons we can, in a formal sense, regard the particles responsible for this to be

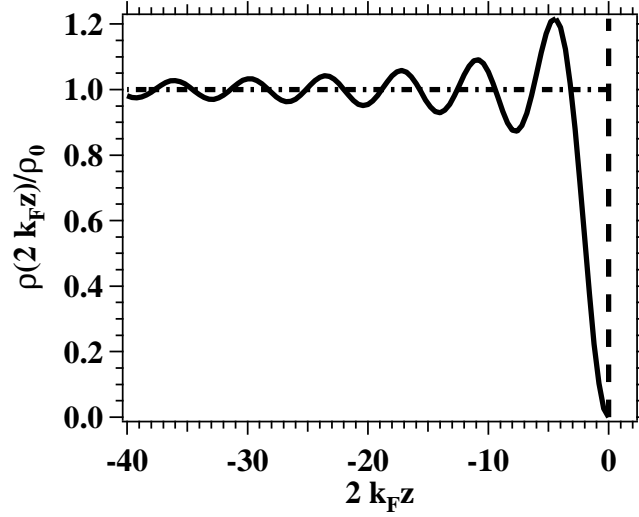


Figure 6. Normalized charge density as function of the position z near an infinitely high potential step. The vertical dashed line marks the position of the step. The horizontal line refers to the constant charge density far away from the step.

distinguishable with electrons inside the material. Furthermore, we assume a constant potential within the system. With this in mind one may ask what is the resulting charge distribution of the electrons in the vicinity of the surface. Under these circumstances the wave functions of the electrons are already known from quantum mechanics classes. They are essentially plane waves along the z -direction with the boundary condition that the wave function has to vanish at the infinitely high steps at $z=-L$ and $z=0$. We find for the wave function $\psi(z) \sim \sin(k_z z)$. From this we determine the charge density $\rho(z)$ normalized to the constant charge ρ_0 density deep inside the system:

$$\rho(z)/\rho_0 = \int_0^{k_F} |\psi_k(z)|^2 dk = 1 - \frac{\sin(2k_F z)}{2k_F z} \quad (3.5)$$

One important feature of this function is its dependence on the term $2k_F \cdot z$. This is very similar to the dependence of $g_{\uparrow\uparrow}(r)$ except for the factor 2. This function is plotted in Fig.6 and we see immediately that this function increases rapidly from zero up to values which are near the global value ρ_0 attained far away from the boundary. We can clearly see that for positive values of z the charge density vanishes because the underlying single particle wave functions have to vanish at this point. This is followed by an oscillatory behavior around the global value. The oscillatory behavior via the $\sin(2k_F z)$ term is also called Friedel oscillation and our case is a specific example of the Lindhard theory of screening [4,27]. In this theory it is shown that an positive (negative) external charge placed within a jellium will attract (repel) electronic charge. This rearrangement is such that the external charge is compensated exactly within a few \AA . Due to the fact that the jellium is electrically neutral the pile-up or repulsion of electrons has to be compensated by the charge density far away from the external charge. In this sense the Coulomb “hole” charge is zero. Formally one can regard an electron within the jellium as an external charge.

The specific examples served to illustrate some general facts of the exchange-correlation hole. We learned that the charge expelled from the vicinity of an electron is exactly one elementary charge. The length scale z over which this takes place is determined by $2k_F \cdot z = 2$. With typical values of k_F in the range 1-2 \AA^{-1} we recognize that this amounts to distances of a few \AA . This means that beyond this length scale the electrons will not “see” each other. A simple explanation was provided as to why the exchange hole is larger than the Coulomb “hole”. In summary, we find that the seemingly unrealistic assumption of a non-interacting electron system can be justified. The next level of sophistication is the use of a screened Coulomb potential of the form $V \sim \frac{1}{r} e^{-\frac{r}{\lambda}}$ rather than the bare Coulomb interaction. In this context the screening length λ is a measure of the lateral dimension of the xc-hole. It is worthwhile to point out that the theoretical description of the pair emission process from surfaces assumes a screened Coulomb interaction.

3.4. The exchange-hole for a nonuniform charge distribution

If the global charge distribution $\rho(\mathbf{r})$ is not uniform, the relation between pair correlation function g and exchange-correlation charge density q_x is not as simple given by eq.(3.4). Therefore it becomes necessary to refine the definitions for the general case. We will show that the exchange-hole charge density is closely related to a conditional probability which is only then proportional to the joint probability in the case of an uniform global charge distribution.

3.4.1. One-dimensional two-electron model Let us discuss this relationship for a two-electron system with parallel spins for which we ignore the mutual Coulomb interaction. In this scenario we can express the two-particle wave function in terms of single particle wave functions. The labels i and j identify the quantum numbers and \mathbf{r}_i and \mathbf{r}_j are the coordinates of the two electrons. The wave functions $\psi_i(\mathbf{r})$ and $\psi_j(\mathbf{r})$ are normalized and orthogonal and we obtain:

$$\psi_{i,j}(\mathbf{r}_i, \mathbf{r}_j) = \frac{1}{\sqrt{2}}(\psi_i(\mathbf{r}_i) \cdot \psi_j(\mathbf{r}_j) - \psi_j(\mathbf{r}_i) \cdot \psi_i(\mathbf{r}_j)) \quad (3.6)$$

With this wave function, the charge density reads as $\rho(\mathbf{r}) = |\psi_i(\mathbf{r})|^2 + |\psi_j(\mathbf{r})|^2$. As discussed above, the joint probability to find one electron at \mathbf{r}_i while the other is at \mathbf{r}_j is given by $\rho(\mathbf{r}_i, \mathbf{r}_j)$ which follows immediately from the two-particle wave function. In statistics one discriminates between the joint and conditional probability.

In order to make this important difference clear we want to visualize this by a simple example, see Fig.7. We consider two independent particles which we associate with the color blue and red, respectively. Within a rectangular target T with area a_T the particles are uniformly distributed. We further define two circular regions A (blue) and B (red), respectively. The circles have an overlap region with area $a(A, B)$. The probability $p(A)$ to find a blue particle within area A is simply given by the ratio of

the areas of the blue circle a_A and the target, hence we write $p(A) = a_A/a_T$. Similarly we obtain for the probability to find a red particle in area B $p(B) = a_B/a_T$. Now we want to calculate the joint probability $p(A, B)$ to find a blue and red particle in the overlap region $a(A, B)$. This is nothing else but the ratio $p(A, B) = a(A, B)/a_T$. Now we proceed and discuss the conditional probability $p(A|B)$. By this is meant that we know already that a red particle is in area B. The probability to find in this instance a blue particle in the overlap region is given by the area $a(A, B)$ divided by the area a_B rather than the area of region T, because we know already that the red particle is in area B. Therefore, we can write for the conditional probability $p(A|B) = a(A, B)/a_B$. Now we can determine the ratio between between conditional and joint probability:

$$\frac{p(A|B)}{p(A, B)} = \frac{a(A, B)}{a_B} \frac{a_T}{a(A, B)} = \frac{a_T}{a_B} = \frac{1}{p(B)} \quad (3.7)$$

We rewrite this result and obtain:

$$p(A|B) = \frac{p(A, B)}{p(B)} \quad (3.8)$$

This expression was derived within a particular scenario, but the formula also holds for the general case, where the probabilities $p(A)$ and $p(B)$ are not constants. In such a case it is important to realize that a small joint probability $p(A, B)$ can still result in a high conditional probability $p(A|B)$ if the value of $p(B)$ is small. Such a scenario we will encounter shortly. Let us adapt the above result to our notation. If we ask for the conditional probability to find an electron at \mathbf{r}_i while another electron is found at \mathbf{r}_j we write $\rho(\mathbf{r}_i|\mathbf{r}_j)$:

$$\rho(\mathbf{r}_i|\mathbf{r}_j) = \frac{\rho(\mathbf{r}_j, \mathbf{r}_i)}{\rho(\mathbf{r}_j)} \quad (3.9)$$

We note that there is an important difference between these two probabilities. If the charge distribution is uniform, as in the case of the free electron gas, both quantities are proportional. As pointed out above, it is more interesting to calculate the charge deficit around the electron of interest which is the exchange charge distribution $\rho_x(\mathbf{r}_i|\mathbf{r}_j)$.

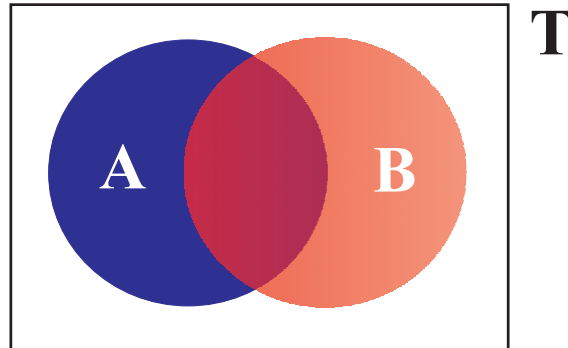


Figure 7. Blue and red particles are uniformly distributed within a rectangular target T. We define two circular regions (A,B) of equal area which have an overlap region.

The charge deficit $\rho_x(\mathbf{r}_i|\mathbf{r}_j)$ is simply the difference of the conditional probability $\rho(\mathbf{r}_i|\mathbf{r}_j)$ from the charge distribution $\rho(\mathbf{r}_i)$:

$$\rho_x(\mathbf{r}_i|\mathbf{r}_j) = \rho(\mathbf{r}_i|\mathbf{r}_j) - \rho(\mathbf{r}_i) \quad (3.10)$$

If we use the wave function of eq.(3.6) and recall that the single particle wave functions are orthogonal and normalized it is straightforward to write down the expression for the joint probability $\rho(\mathbf{r}_i, \mathbf{r}_j)$ which is:

$$\rho(\mathbf{r}_i, \mathbf{r}_j) = \rho(\mathbf{r}_j) \cdot \rho(\mathbf{r}_i) - \left| \sum_a \psi_a^*(\mathbf{r}_i) \cdot \psi_a(\mathbf{r}_j) \right|^2 \quad (3.11)$$

The summation runs over the two occupied states i and j , but it turns out that this expression is also true for an N -electron system if the summation runs over all N occupied states. We would like to explore this result by considering two electrons with parallel

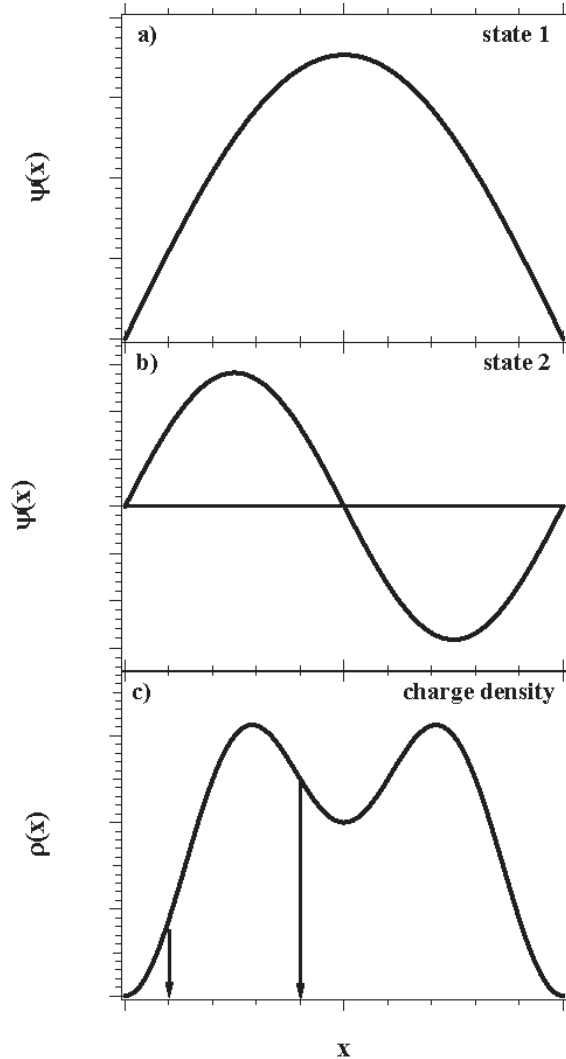


Figure 8. The wave function of the ground state and first excited state for a 1D-potential well with infinite barriers are shown in a) and b), respectively. The resulting charge density $\rho(x)$ is plotted in panel c). The arrows in c) indicate the two positions we considered for the electron of interest.

spins which are localized in a 1D-potential well with infinitely high barriers. As single particle wave functions ψ_i and ψ_j we have chosen the ground state and first excited state plotted in Fig.8 a) and b). The resulting charge density $\rho(x)$ is plotted in Fig.8 c). We have indicated in Fig.8 c) via two arrows the two positions of the electron of interest used for further evaluation. The left arrow is relatively close to the boundary of the potential well therefore the charge density is lower than for locations near the center of the well as indicated by the second arrow. Let us compute the joint probability following eq.(3.11) the result of which is shown in Fig.9 a) and c). As expected from the Pauli principle, we can not find two electrons at the same location $x_j = x_i$. A different picture emerges if we compute the exchange charge density $\rho_x(\mathbf{x}_i|\mathbf{x}_j)$ if the electron of interest is at the locations marked by the arrow. Panels b) and d) clearly reveal that the minimum of $\rho_x(\mathbf{x}_i|\mathbf{x}_j)$ does not coincide with the arrow position but it is shifted. This shift is larger in panel b) compared to d). This may appear at first sight counter-intuitive but can be readily understood if we recall eq.(3.9). As stated above we need to consider the conditional probability $\rho_x(\mathbf{x}_i|\mathbf{x}_j)$ rather than the joint probability $\rho_x(\mathbf{x}_i, \mathbf{x}_j)$. From eq.(3.9) we learn that a small joint probability does not lead to a small conditional probability if the charge density adopts a small value. Therefore the

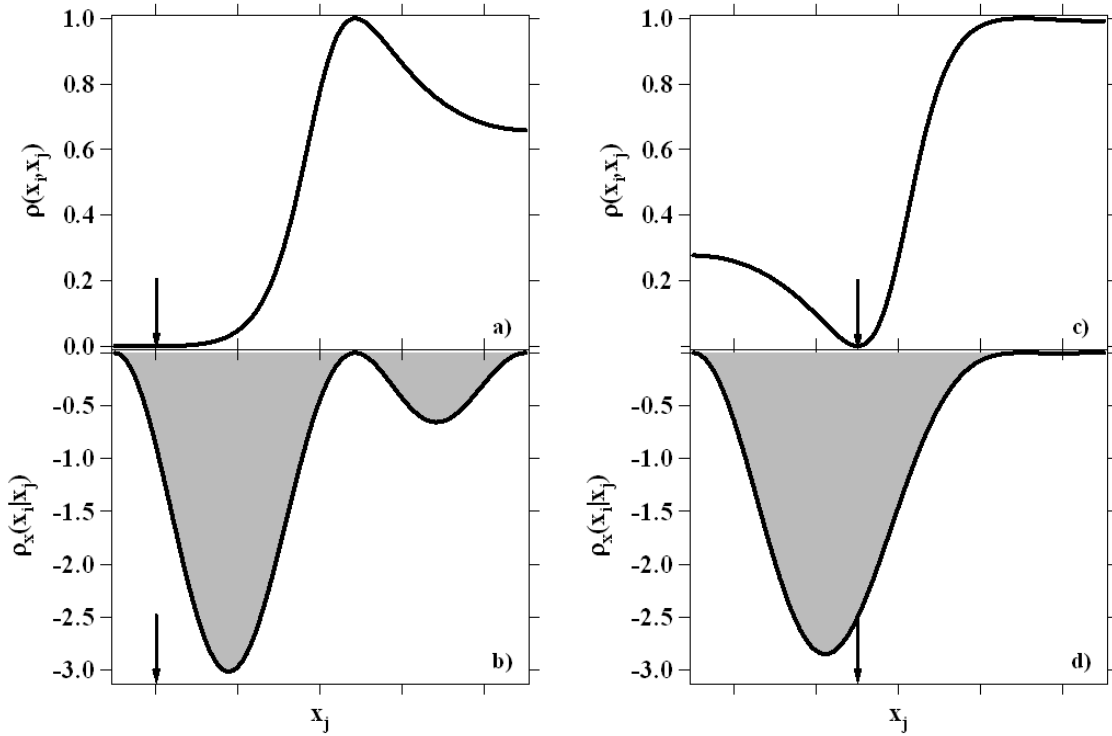


Figure 9. In panels a) and c) the joint density $\rho_x(x_i, x_j)$ as a function of x_j is plotted. The electron of interest is located at x_i which is marked by the positions of the arrows. The resulting exchange charge density $\rho_x(x_i|x_j)$ is presented in panels b) and d). The total integrated exchange charge is given by the grey area which amounts to exactly one electronic charge.

exchange charge density according to eq.(3.10) will not adopt a large negative value. Another way of looking at this is to realize that the sum rule states that the integrated exchange charge amounts to exactly one elementary charge. If the electron of interest is localized in a region of space where the global charge density is low, not enough charge can be “pushed” aside. The deficit has to be made up at other regions where it is not strictly forbidden to find another electron. This simple two-electron system may serve also as a very rudimentary model for a He atom if the two electrons occupy different states, only then are parallel spins possible. From this we learn that the formation of an exchange-hole is not confined to a many-body system, but exist also in a system which contains only few electrons like atoms and molecules [28–31]. The size of the exchange hole is of the order of the atom’s size because in this region is appreciable charge density. We recall that the missing charge has to accumulate to exactly one [32].

After the discussion of a two-electron system we want to go back to a situation involving a solid where we encounter also a varying charge density.

3.4.2. Exchange-hole near a surface In the previous discussion of the exchange-hole we used as an example the free electron gas which has a constant global charge distribution ρ_0 . As far as the Coulomb “hole” was concerned we employed the infinitely potential step which has a rapidly changing charge distribution $\rho(z)$ near the potential step, see Fig.5. Due to the fact that any real electronic system has a non-uniform charge distribution it is appealing to ask for the behavior of the xc-hole in this context. For simplicity we

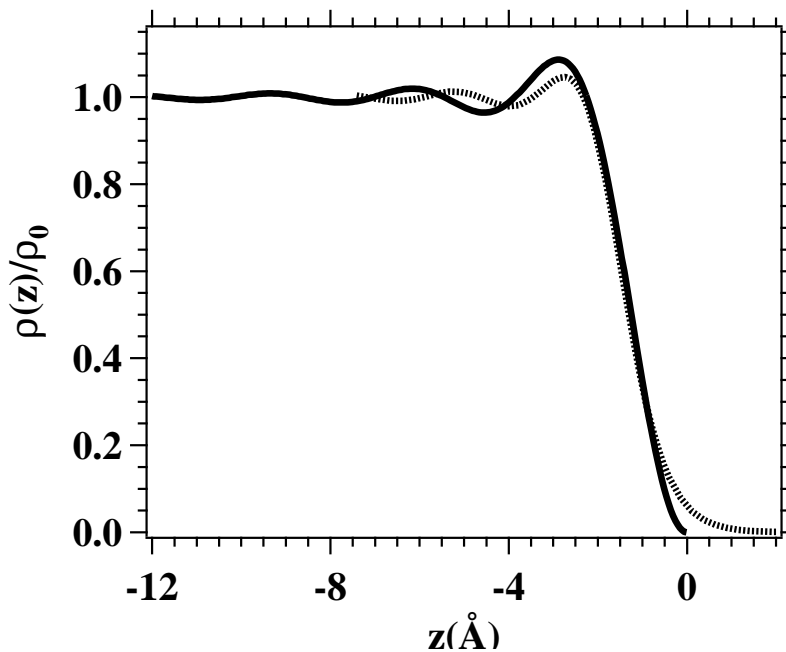


Figure 10. Charge distribution of a jellium/free electron gas system bounded by a potential step at $z=0$. The solid line is for an infinitely high step, while the dashed curve describes a finite step [35, 36]. The chosen electron density amounts to $k_F=1 \text{ \AA}^{-1}$.

will focus on the exchange hole in the following [33,34]. As an example for an electronic system with non-uniform charge distribution we revisit the free electron gas in three dimensions which is bounded by a potential step parallel to the x and y-direction. The abrupt step is localized at $z=0$, which divides the system into a vacuum region for $z>0$ and an interior region for $z<0$. For an infinitely high step the charge density $\rho(z)$ can be calculated analytically and can be found in Sahni [35]. The result is given by:

$$\rho(z)/\rho_0 = \int_0^{k_F} |\psi_k(z)|^2 dk = 1 - \frac{3(\sin(2k_F z) - 2k_F z \cdot \cos(2k_F z))}{(2k_F z)^3} \quad (3.12)$$

Again we discover that the natural variable describing the charge density is the term $2k_F z$. In order to simplify the expressions we continue and set $k_F=1 \text{ \AA}^{-1}$ which is the free electron value for Cu. A finite barrier requires a numerical approach which is reported by Lang & Kohn [36]. In preparation for further discussions we display in Fig.10 the charge distribution $\rho(z)$ for both scenarios. We observe a rapid increase of $\rho(z)$ upon moving from the barrier towards the interior of the system. At approximately $z=-3 \text{ \AA}$ the charge density $\rho(z)$ has already adopted the bulk value ρ_0 . Compared to this the finite barrier shows weaker oscillations, because the underlying wave functions do not vanish at the potential step but decay exponentially. The behavior in the vacuum region is very different but in the interior the systems display qualitatively the same behavior. For ease in the computation we focus for the discussion of the interior region on the infinite barrier, because analytical expressions have been derived [35]. We proceed and show, similar to the 1D two-electron model, the joint density $\rho(z_i, z_j)$ for different positions z_i of the reference electron indicated by arrows in Fig.11 while $x_i = x_j = 0$ and $y_i = y_j = 0$. The Pauli principle demands that $\rho(z_i, z_i)=0$. For $z_i=-10 \text{ \AA}$ the electron of interest is furthest away from the surface. In

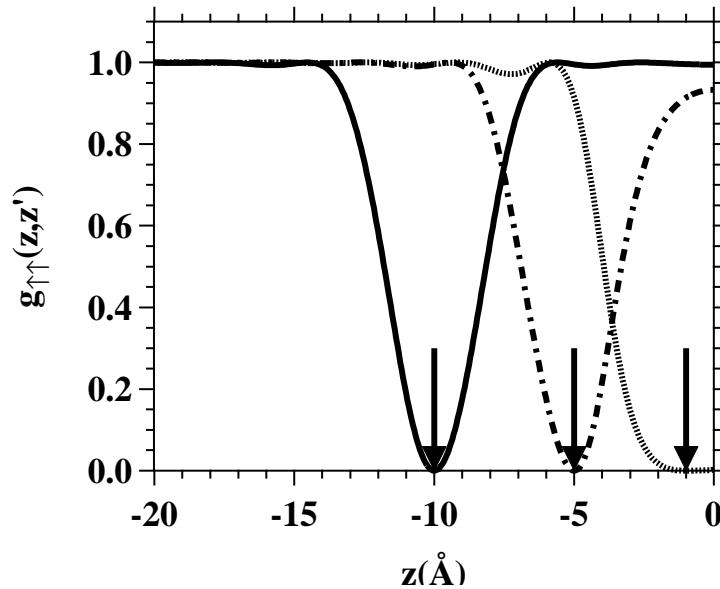


Figure 11. Conditional density $\rho(z_i, z_j)$ for a free electron system bounded by an infinitely high barrier at $z=0$ [35].

this case we notice that within approximately 3 Å a rapid increase of $\rho(z_i, z_j)$ takes place. This is in agreement with Fig.4 and tells us that a distance of 10 Å from the surface is already “infinite”. For $z_i=-5$ Å the situation is rather similar the main difference being that near the boundary $\rho(z_i, z_j)$ does not adopt the same maximum value compared to locations deeper in the interior. Simply put we can say that the reference electron starts to “see” the surface. If the electron of interest is at $z_i=-1$ Å $\rho(z_i, z_j)$ can only take appreciable values towards the interior. This can be understood easily because in order to have a large value one has to be about 3 Å away from the electron of interest. However in the vacuum region there is with certainty not another electron due to the fact that the barrier is assumed to be infinitely high as can be easily read from the charge density $\rho(z)$ shown in Fig.10. Having determined the joint charge density $\rho(z_i, z_j)$ and the charge density $\rho(z)$ we can proceed in presenting the conditional charge density $\rho(z_i|z_j)$ by use of eq.(3.7). The result is displayed in a 2D-plot for which we set $x_i = x_j = 0$, see Fig.12. The electron of interest is marked by a red dot and in Fig.10 a) we show the distribution for $z_i = -10$ Å. The contour lines connect levels of constant density values and the color coding is such that white stands for no displacement of charge while black indicates maximum displacement. We clearly observe that $\rho(z_i|z_j)$ is spherical in this case and centered at the reference electron. The situation starts to change when we select $z_i = -5$ Å, now closer to the barrier, and we can clearly see a distortion from the spherical distribution, see Fig.12 b). Furthermore, we note that the smallest value of $\rho(z_i|z_j)$ is not at the location of the electron of interest but slightly displaced towards the interior. An even more pronounced change from the spherical symmetry occurs for $z_i=-1$ Å in panel c). Now the contour lines are clearly more elliptical and the center of the $\rho(z_i|z_j)$ is significantly separated from the electron of interest. This distribution is practically unaltered if we set the reference electron at $z_i=-0.01$ Å as indicated by the red triangle in Fig.12 c). In this case the reference electron is clearly outside the region where charge displacement occurs, such a situation arises if the electron of interest resides in a region of low charge density.

So far we have discussed the behavior of the exchange hole in the vicinity of the potential barrier upon approaching the barrier from the interior. Due to the fact that the potential step is infinitely high, the charge density in the vacuum region is exactly zero. Therefore the electronic system is bound by the barrier position. A more realistic model would assume a finite potential barrier. A typical barrier height of a few eV will not change the previous results dramatically as we approach the barrier from the interior. Upon crossing the barrier the charge density will not be zero, but will decrease exponentially. This means that in the vacuum region we will find electrons which are part of the many-body system. The immediate consequence is that an electron in the vacuum region must be surrounded by an exchange-hole. Let us assume an electron to be at $z_i=5$ Å away from the barrier. The charge density will adopt appreciable values only for coordinates which are in the interior. This means that only starting at this distance charge can be expelled from the “vicinity” of the electron of interest. These general points are confirmed by a calculation the result of which is plotted in Fig.13.

Analogous to Fig.12 we mark the electron of interest via a red dot. It is apparent that the shape of the exchange hole is very different from the spherical form deep inside a jellium and the more elliptical shape close to the barrier, see Fig.12. We also note that the exchange-hole shows oscillations and becomes more and more delocalized or nonlocal as the electron of interest is localized further away from the barrier. Also the exchange hole becomes detached from the electron of interest. We stress that the inclusion of the Coulomb correlation leading to the xc-hole yields qualitative similar results. In the near surface region the xc-hole becomes detached from the electron of interest [37–39]. It is stated that the xc-hole becomes the image charge once the electron of interest is in the

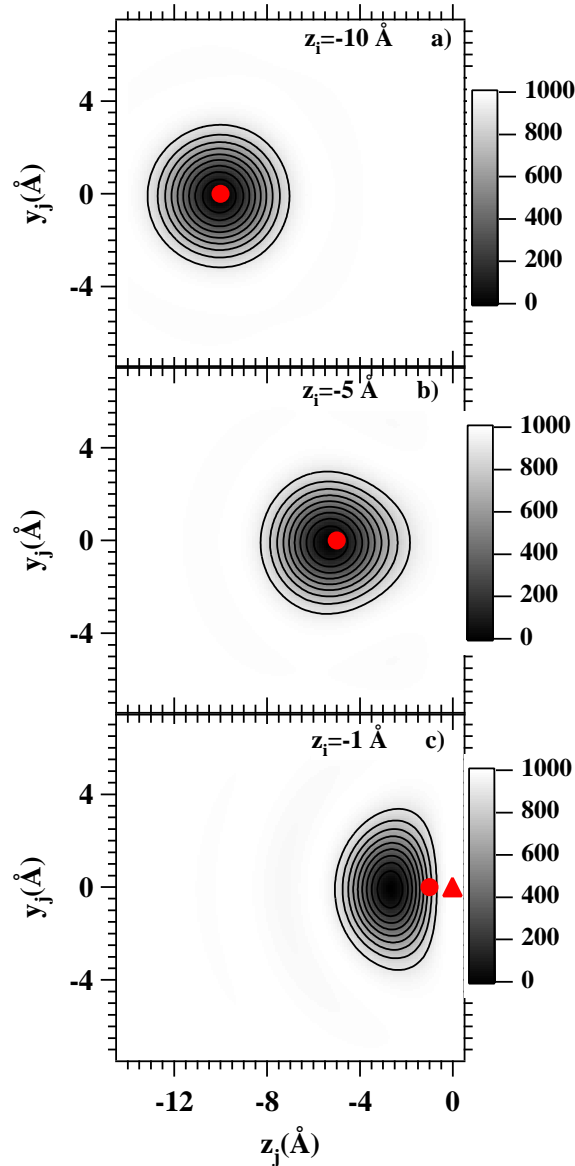


Figure 12. Conditional charge density $\rho(z_i|z_j)$ for different locations z_j of the electron of interest which is marked by the red dot. The red triangle in panel c) indicates the position of the reference electron at $z_i = -0.01$ Å. The color coding for no displacement of charge is white whereas it is black for maximum displacement.

vacuum region [37,38]. A non-spherical xc-hole evolves in bulk Si due to the anisotropy of the crystal which leads to a non-uniform global charge density. The positions of the electron of interest and the center of the xc-hole are separated [40]. The three distances selected for z_i in Fig.13 represent also length scales where so-called image potential states exist. These are electronic states which are energetically localized between the Fermi level and vacuum level of a metal e.g. a Cu(001) surface. The wave functions of these states have the maximum in the vacuum region. In other words they are localized in front of the surface. In the case of a Cu(001) surface the 1st and 2nd image potential state have the maximum of the wave function at 5 and 15 Å. This would represent the distance depicted in panel a) and c) of Fig.13. Inspection of Fig.13 shows that this

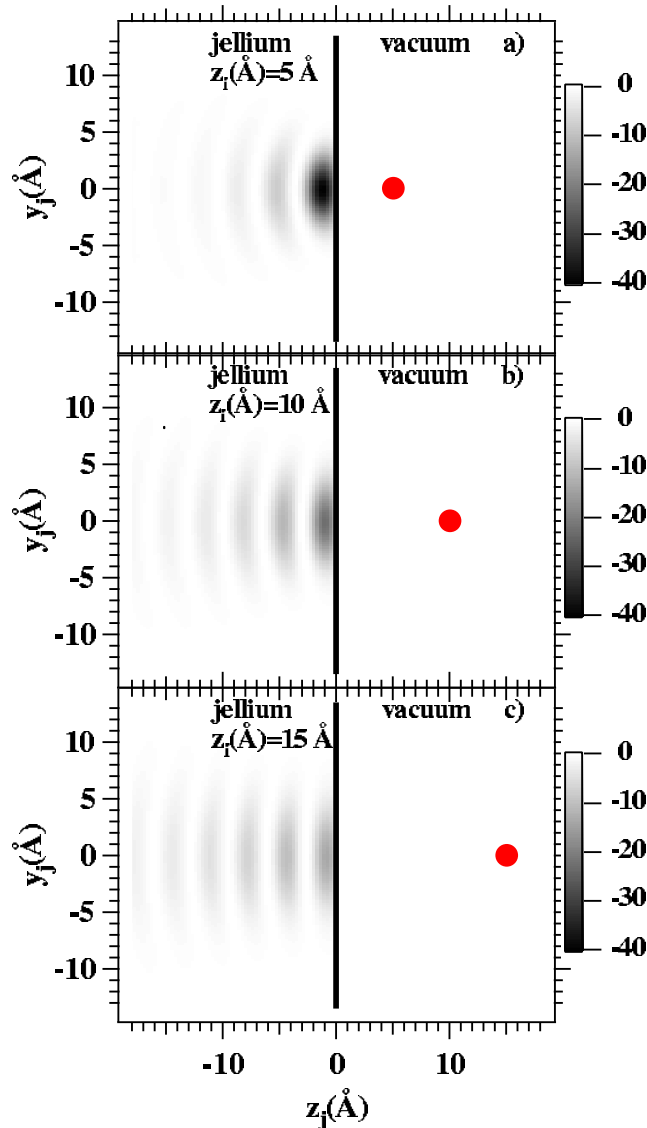


Figure 13. The reference electron is located at different positions of the coordinate z_i outside the jellium which is bounded by a finite barrier at $z=0$. The position of the barrier is given by the black line. The variation of $\rho(z_i|z_j)$ is shown for a color coding such that no (maximum) displacement of charge occurs in the white (black) areas.

should not be a good approximation and is confirmed by a very recent theoretical work on the exchange-correlation hole of a Cu(001) surface [39].

Up to now we have largely ignored the Coulomb interaction among electrons. Realistic calculations of material properties must include this interaction. The determination of the ground state wave function of interacting electrons in a macroscopic sample is a hopeless task. A major breakthrough in the description of the ground state properties of condensed matter was therefore development of the Density Functional Theory (DFT) [21–23]. It was shown that the ground state energy is a functional of the electron density $n(\mathbf{r})$, likewise are all other ground state properties exactly described by functionals of $n(\mathbf{r})$. This concept can be put into a computational scheme by the Local Density Approximation (LDA) leading to the Kohn-Sham equation which formally looks like a Schrödinger equation of single particle moving in an effective potential v_{eff} [21–23]:

$$\left\{-\frac{\hbar^2}{2m}\nabla^2 + v_{eff}(\mathbf{r})\right\}\psi_i(\mathbf{r}) = \varepsilon_i\psi_i(\mathbf{r}) \quad (3.13)$$

The effective potential $v_{eff}(\mathbf{r})$ includes a term $v_{xc}(\mathbf{r})=\delta E_{xc}/\delta n(\mathbf{r})$, where the functional E_{xc} contains all features of the interacting electronic system. The key approximation

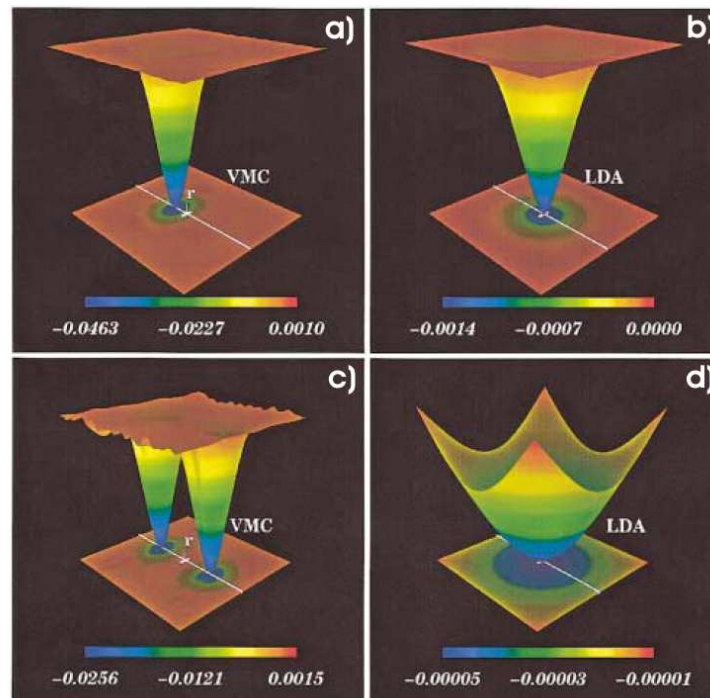


Figure 14. Exchange-correlation hole for different locations of the electron of interest [41]. In panels a) and b) the reference electron is at a location where the charge density begins to drop while in panels c) and d) it is at the density minimum. Two different schemes have been employed which are called VMC (variational quantum Monte Carlo) and LDA. The nonlocal behavior of the xc-hole is clearly visible in c) which is completely missing in the LDA approximation. Reprinted Fig.1 with permission from: M. Nekovee, W.M.C. Foulkes, and R.J. Needs, Phys. Rev. Lett. **87**, 036401 (2001). Copyright (2001) by the American Physical Society

of the LDA is the use of the known functional of the homogenous electron gas for E_{xc} locally. This finally leads to a local potential in the Kohn-Sham equation which aids tremendously in the computations. It is now well-established that the LDA predicts properties of condensed matter systems very well, which is somehow surprising given the rather crude approximation. Let us recall that within the discussion of the uniform free electron system the exchange-hole is spherical and its size is roughly $\frac{3}{k_F}$. This means a decrease in the global charge density increases the exchange-hole size but maintains the shape. On the other hand we also discussed the behavior near a surface where the charge density changes rapidly. This resulted in a non-spherical hole and non-local behavior. This is not captured by the LDA approximation, nevertheless state-of-the art calculations approach an energy accuracy of $\sim 0.1-0.2$ eV (“chemical accuracy”). There is a need to go consistently beyond this limit if, for example, chemical reactions at surfaces are concerned. This requires improved functionals for E_{xc} . Key quantities for E_{xc} are the pair correlation function $g(\mathbf{r}, \mathbf{r}')$ and the exchange correlation hole. Different approaches have been put forward to improve the LDA calculations [41–44]. It was recently demonstrated that the inhomogeneity of the electron gas has a profound effect on the xc-hole which culminates in a nonlocal behavior completely missing in the LDA [41–43]. As an example of the intense efforts we show the xc-hole for an electronic system where the charge density depends only on one coordinate [41], see Fig.14. In this figure, the contrasting behavior within the VMC (variational quantum Monte Carlo) scheme and the LDA is discussed. In panels a) and c) the local charge density has the same value but is larger than for panels b) and d). Within the LDA calculation the xc-hole is spherical and hence the shape does not change in Fig.14 b) and d). The only difference is an increase of the xc-hole which scales with $\frac{1}{k_F}$ as discussed above. The xc-hole is also centered around the electron of interest. Compared to the LDA calculation the VMC scheme shows a strongly changing shape. Whereas in panel a) it resembles a spherical shape (although smaller compared to the LDA hole) it displays two separate regions of reduced charge density. This can be easily understood by recalling our discussion of Fig.12 and Fig.13 where the exchange-hole was not centered at the position of the electron of interest. Clearly the VMC scheme incorporates non-local effects missing in the LDA. A judgement as to whether an improvement in the calculation has been obtained is the comparison of lattice constants, energy bands etc. with experimental data. However, a good agreement with theory and experiment could also be due to a fortuitous cancellation of errors [42].

In this chapter we have learned that the xc-hole is an entity which is a part of any electronic system. Each reference electron is surrounded by a reduced electronic charge which amounts to exactly one elementary charge. Within an uniform global charge density the xc-hole is centered around the electron of interest, but this does not hold anymore for non-uniform charge distributions. The xc-hole plays an important part in modern theory and the incorporation of non-local aspects is intensely pursued. The preceding presentation of the exchange-hole within a jellium model is made within a stationary theory. One may consider the plots shown in Figs.12, 13 as a snapshot of an

electron leaving a solid sample. As the electron goes through the barrier it will become detached from the xc-hole. This electron may reach a detector which constitutes also an electronic system. Within this system the previously emitted electron is surrounded again by an xc-hole. A key question would be how the detachment and subsequent attachment of a new xc-hole occurs which would require a time-dependent description. The time period by which the xc-hole is being filled once an electron has left a system is of the order 100 atto sec according to a recent calculation [18].

4. Electron spectroscopy beyond the effective single particle picture

4.1. General aspects of electron coincidence spectroscopy

We have discussed in the previous chapters the xc-hole and its general relevance. The question comes to mind whether it is possible to “see” the xc-hole in order to aid further theoretical development. For this it is necessary to detect two correlated electrons (the technical term is *in coincidence*). Highly desirable would be a direct real space imaging, this is at present not possible. A viable route, according to theory, is the measurement of the angular (or momentum) distributions of electron pairs from a surface excited by electrons or photons. The prediction is the emergence of a zone of reduced coincidence intensity [8, 9, 45, 46], which is beyond the capabilities of single electron spectroscopy. Before we discuss aspects of the experiment, it is instructive to display this theoretical prediction which motivated the experimental work. As an example we show the double photoemission result from a Cu(100) surface from Fominykh et al. in Fig.15 [9]. In this 2D-momentum distribution the emission direction of one electron fixed as indicated by a white dot in both plots. If the energy and emission direction of an electron is known the in-plane momentum is determined. Both outgoing electrons have a kinetic energy of 16 eV, while the photon energy was set to 42.4 eV. Near the white dots the intensity adopts a small value. At some intermediate distances, a rim of increased intensity evolves which is followed by a fall-off to low intensity values. The absorption of one photon and emission of an electron pair is only possible if the electrons interact to be discussed in some detail below. Another route to study the pair emission is to perform a scattering experiment in the spirit of Rutherford. From the angular deflections of

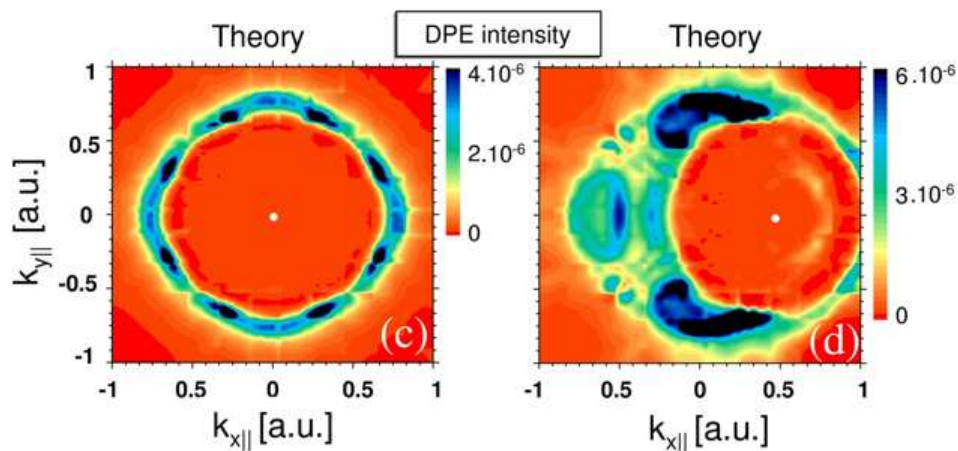


Figure 15. Fig.1 c) and d) from Fominykh et al. is reproduced [9] where the 2D-momentum distribution of correlated pairs is plotted. A Cu(100) surface is excited with 42.4 eV photons while the outgoing electrons have a energy of 16 eV. The emission direction of one electron is fixed as indicated by the white dot located at (0 a.u.,0 a.u.) and (0.5 a.u.,0 a.u.) in panels c) and d), respectively. Reprinted Fig.1 with permission from:N. Fominykh, J. Berakdar, J. Henk, and P. Bruno, Phys. Rev. Lett. **89**, 086402 (2002). Copyright (2002) by the American Physical Society.

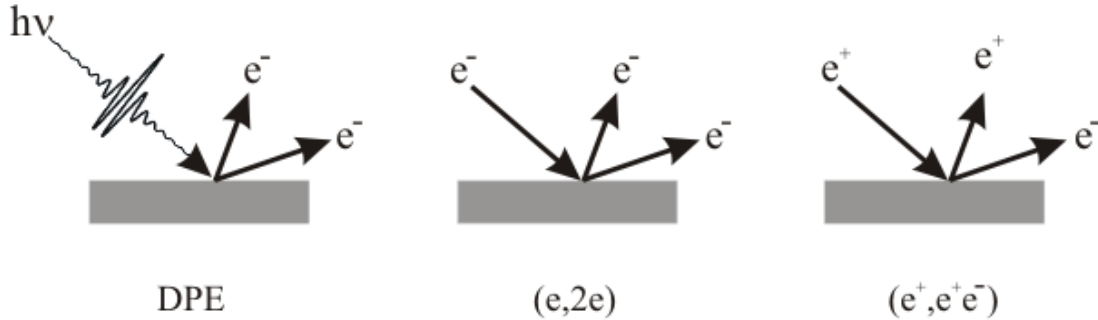


Figure 16. Schematic view of the back reflection geometry. A primary particle hits a surface which reacts by emission of a correlated pair. If the excitation is due to a photon we term it double photoemission (DPE). In the case of a primary electron we call the experiment $(e,2e)$. The emission of a positron-electron pair upon positron impact is named (e^+,e^+e^-) .

the scattered α particles it was possible to make statements of the spatial extension of the nucleus [47]. Applied to our situation, we need to study the collision between two electrons due to primary electron impact. We may term such an experiment as an $(e,2e)$ process. Clearly a finite $(e,2e)$ intensity requires an interaction between electrons and it is predicted that a zone of reduced intensity similar to Fig.15 is formed [8].

The detection of electron pairs is a straightforward, although experimentally demanding, extension of single electron spectroscopy. The following approaches are conceivable. A transmission experiment would require a large kinetic energy of the primary electron, of the order of 20-100 kV, to pass through a thin foil. Such experiments have been indeed performed and have given useful insights into the spectral momentum density [48–50]. The equivalent experiment in a reflection geometry is also possible, where the primary electron has a kinetic energy of 300 eV [51]. Both approaches choose the kinematics such that the scattered primary electron loses a small fraction of its kinetic energy, hence the second electron has a much smaller kinetic energy than the scattered primary. Further, the momentum transfer of the primary electron is very small. This constitutes the optical-limit, where the primary electrons acts like a photon [52]. In this sense an experiment similar to photoemission is possible. Starting almost two decades ago it has been demonstrated that experiments in a reflection geometry are possible with primary energies of 20-30 eV, which were not confined to the optical limit [53–63]. In parallel to the experimental development the theoretical description of pair emission has advanced significantly [8, 57, 64–69]. The low kinetic energy reflection geometry adapts better to our aims than the high kinetic energy transmission geometry. We compare the energy introduced by the primary electron with the energies relevant for electron-electron correlation. Within the Hubbard model, the strength of the electron correlation is described by the parameter U , which is of the order of a few eV. Clearly, the energetics of a transmission experiment is too high to be sensitive to the electron-electron interaction in contrast to a low kinetic energy experiment.

For electrons to leave the sample, they have to overcome the vacuum barrier. Let

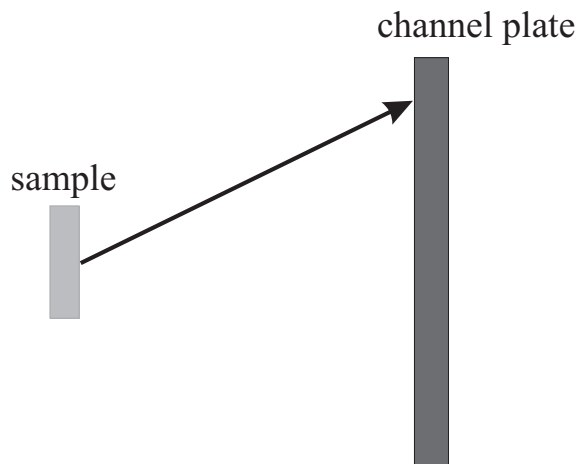


Figure 17. A schematic view of a time-of-flight (TOF) apparatus for single electron detection. After the impact of a primary particle, the sample may emit an electron. The region between the sample and the channel plate detector is field free. Therefore the impact position on the detector determines the flight path taken and the kinetic energy can be computed from the flight time.

us regard an outgoing electron as a classical particle. If it approaches the barrier with an angle of 45° with respect to the normal it needs twice the barrier height in order to leave the sample. For smaller kinetic energies electrons will experience total reflection. Typical values for the work function of metals are in the range of 4-5 eV. From this simple argument we get a lower bound the primary energy should have in order cause the emission of an electron pair, we may quote a value of around 20 eV. Single electron spectroscopy is a well-developed technique [70, 71]. Hence, it appears straightforward to add a second electron analyzer together with a coincidence circuit to an existing apparatus. Coincidence electronics, a readily available technology, ensures that only those electrons are counted which have a counterpart in the other detector. Therefore pair emission studies are in principle possible. Unfortunately an important aspect has been ignored in this line of thinking. A purely statistical analysis to be presented below reveals that the uncorrelated pairs quickly overwhelm in intensity the correlated pairs. The origin of these uncorrelated pairs is related to the simultaneous impact of two primary particles leading to the emission of two independent single electrons. These pairs also fulfill the electronic coincidence condition and are detected. This fact puts severe limitations on the primary flux hitting the sample and one may quote a typical value of the order 10^{-15} A. Standard surface science experiments like low energy electron diffraction (LEED) or Auger electron spectroscopy operate at currents of the order 10^{-6} A. This comparison makes it clear that electron coincidence experiments will be extremely challenging due to the low count rates imposed by the low primary flux. This explains that dedicated instrumentation needs to be devised which detect the emitted electron pairs as efficiently as possible. In the course of the presented work, different approaches were used. One key aspect

is to ensure that the angular acceptance is as large as possible. The detection probability of a single spectrometer will scale with the probed solid angle Ω of the spectrometer. A coincidence experiment is a measurement of the joint probability hence the coincidence intensity will scale by Ω^2 if two identical spectrometers are used. Further, it would be highly desirable to be able to detect electrons over a wide range of kinetic energies. An experiment with high detection efficiency for a large energy window and a large angular acceptance is required. At the same time a good energy resolution is desirable. Both requirements can not be fulfilled at the same time. This work followed two routes. In the first scheme a time-of-flight (TOF) set-up with pulsed excitation source is used. The second scheme explores a pair of hemispherical analyzers. Within the TOF scheme used, emitted electrons traverse a field free region before they are detected. The impact position on a channel plate detector determines the trajectory the electron took, hence the flight path and emission angle with respect to the surface are known. The flight time allows to calculate the kinetic energy. A sketch for a single electron detection is presented in Fig.17 and the conflicting requirements for the coincidence experiment can be seen. The angular acceptance increases if the detector is positioned closer to the sample. The drawback is that the flight path and hence the flight time becomes shorter. The time error remains the same which leads to a poorer energy resolution. In Fig.18 we display the energy resolution dE as function of the kinetic energy E_{kin} of the emitted electrons. Assumed is a flight distance of 100 mm and a time resolution of 0.5 ns. These are not arbitrary values but reflect operational parameters. The general trend is an increase in the energy uncertainty which reaches 2 eV for 50 eV electrons. Acceptable resolution is adopted for electron energies of say 20 eV and below. This suggests to use excitation values below twice this value. A previous estimate gave as lower bound for the primary energy a value of 20 eV. This means a time-of-flight scheme is an appropriate approach for electron coincidence spectroscopy if the primary

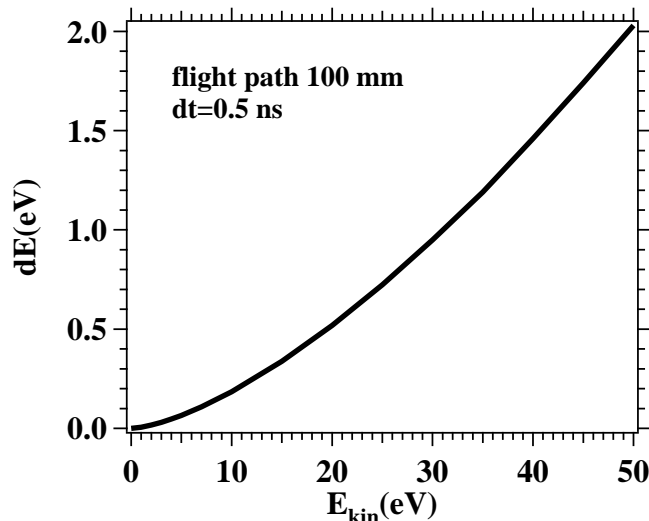


Figure 18. Variation of the energy resolution dE as a function of the kinetic energy for a TOF instrument, with a flight path of 100 mm and a time resolution of 0.5 ns.

energy is in the range 20-40 eV. For higher primary energies an electro-static design is necessary which allows to select the energy resolution independent of the energies of the emitted electrons. This approach was used in an early Auger-photoelectron coincidence experiment [72]. Only recently hemispherical analyzers became available which offer a large enough angular acceptance and the ability to measure a large energy window in parallel required for the intended studies [73].

4.2. Double photoemission

Photoemission concerns the emission of a single electron from a target (e.g. solid surface) upon absorption of a photon. This effect was discovered separately by Hertz and Hallwachs [74, 75] and first explained by Einstein [76]. It has become a widely used tool to study the electronic properties of matter. In his landmark paper Einstein already anticipates that the photon energy is not transferred to one electron alone. We term a process as double photoemission (DPE) if one photon is absorbed and two electrons are emitted. The cartoon shown in Fig.19 depicts the different scenarios if a photon is absorbed. Suppose that a photon is absorbed by an electron. In the absence of an electron-electron interaction other electrons are not affected by this and no DPE intensity can be observed. However, if a finite electron-electron interaction exists other electrons are influenced. This results in a finite DPE intensity as observed in experiments on surfaces, atoms and molecules [55, 72, 77–83]. It is this fact that makes DPE a tool which is particular sensitive to the electron-electron interaction. This hand waving argument can be put on a firm theoretical background [64]. Furthermore, the power to study superconductors and “highly correlated” materials via DPE is demonstrated [84, 85]. In the latter case it is predicted that the DPE intensity scales with U^2 with U being the Hubbard parameter [85]. Let us extend the derivation of the transition probabilities for single photoemission to DPE. We recall the basics for a single electron system with the following Hamiltonian:

$$H = \frac{1}{2m}(\mathbf{p} - \mathbf{A})^2 + V(\mathbf{r}) \quad (4.1)$$

The coupling of the electron to the electro-magnetic wave is mediated via the vector potential \mathbf{A} . Usually one makes two approximations. First, one assumes the photon field to be weak such that \mathbf{A} can be regarded as a perturbation. Second, the wavelength of the light is much larger than the atom dimension or nearest neighbor distance. In this case, also known as the dipole approximation, the transition probability between an initial state $|i\rangle$ and final state $|f\rangle$ is given by the matrix elements $\langle i|D|f\rangle$. The operator describing this transition is $D = -er$, e being the elementary charge. This matrix element is non-zero when the dipole moment changes for a transition leading to selection rules. We extend this description to a two-electron system with vanishing electron-electron interaction. The Hamiltonian reads now as:

$$H = \frac{1}{2m}(\mathbf{p}_1 - \mathbf{A})^2 + V(\mathbf{r}_1) + \frac{1}{2m}(\mathbf{p}_2 - \mathbf{A})^2 + V(\mathbf{r}_2) \quad (4.2)$$

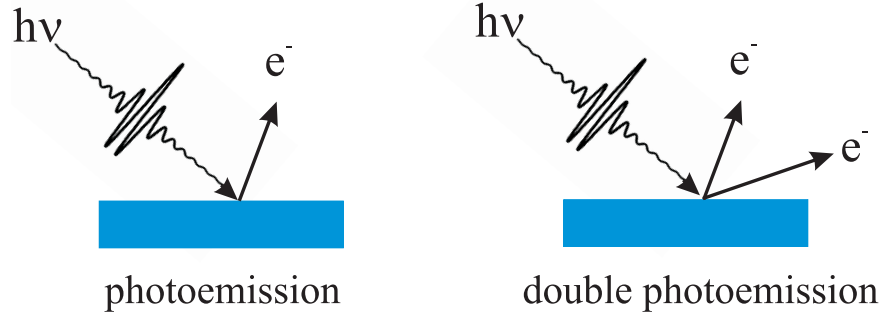


Figure 19. If the absorption of a single photon leads to the emission of electron we speak of (single photoemission). If the system reacts by the emission of an electron pair we talk about double photoemission (DPE).

The indices 1 and 2 refer to the two different electrons. The assumption of non-interacting electrons allows us to write the wave function as Slater determinant containing single particles states. If we write $|i_1, 1\rangle$ it is meant that electron 1 is in a state characterized by the quantum number i_1 . Following this notation we find for the two-particle initial state $|i\rangle$ and final state $|f\rangle$:

$$|i\rangle = |i_1, 1\rangle|i_2, 2\rangle - |i_2, 1\rangle|i_1, 2\rangle \quad (4.3)$$

$$|f\rangle = |f_1, 1\rangle|f_2, 2\rangle - |f_2, 1\rangle|f_1, 2\rangle \quad (4.4)$$

As it will become clear shortly it is sufficient to focus only on one term, e.g $|i\rangle = |i_1, 1\rangle|i_2, 2\rangle$ and $|f\rangle = |f_1, 1\rangle|f_2, 2\rangle$. We write for the transition amplitude from an initial to a final state $\langle i|D|f\rangle$. From the form of the Hamiltonian it is immediately clear that the dipole operator is now a sum of two (single) dipole operators $D = D_1 + D_2 = (-e\mathbf{r}_1) + (-e\mathbf{r}_2)$. These (single) dipole operators act only on one electron. The consequence is apparent if we focus on one term of the matrix element:

$$\begin{aligned} \langle i_1, 1|\langle i_1, 2|D_1|f_1, 1\rangle|f_2, 2\rangle &= \langle i_1, 2|f_2, 2\rangle\langle i_1, 1|D_1|f_1, 1\rangle \\ &= \delta_{i_2, f_2}\langle i_1, 1|D_1|f_1, 1\rangle \end{aligned} \quad (4.5)$$

The operator D_1 does not act on the term $|f_2, 2\rangle$ therefore it can be moved in front of D_1 . There it leads to a Kronecker delta δ_{i_2, f_2} . Therefore the matrix element term is zero if the initial and final state of electron 2 are different. It is straightforward to evaluate all terms of the matrix element $\langle i|D|f\rangle$. It turns out that in each case a non-zero contribution means that one electron does not change its state if one photon is absorbed. This can be rephrased by saying that the absorption of a photon by a non-interacting two-electron system leads only to single photoemission. This fact suggests that a finite electron-electron interaction is required in order to observe a finite DPE intensity. A more thorough theoretical account on this issue confirms this picture [64]. A good starting point is to describe the electron-electron interaction via a screened Coulomb potential $V \propto \frac{1}{r} e^{-\frac{r}{\lambda}}$ where the distance between electrons is given by r . The screening length is labeled with λ . For crystalline solids the Bloch theorem

holds, leading to a description of the electronic properties in momentum space. This is essentially a Fourier transformation. Therefore the screened Coulomb interaction takes the form $V \propto \frac{1}{k^2 + \lambda^2}$, where $k = |\mathbf{k}_1 - \mathbf{k}_2|$ is determined by the momenta of the individual electrons labeled \mathbf{k}_1 and \mathbf{k}_2 , respectively. From this formula one can derive the following picture. If electrons are well-separated in momentum space, e.g. $|\mathbf{k}_1| = 0$ and \mathbf{k}_2 large compared to the the inverse of the screening length, the interaction is weak and one may consider electrons to be independent. This leads to a vanishing DPE intensity. If both momenta have the same value the interaction is very strong, but the probability to find two electrons in such a state is strongly reduced as a consequence of the xc-hole. This leads to a small DPE intensity. In between these two extremes the DPE intensity should have a maximum, since it is more likely to find electrons with slightly different momenta, while the electron-electron interaction is still strong [9].

We expect the DPE intensity as a function of the difference momentum \mathbf{k} to show a minimum for $\mathbf{k} = 0$ which is followed by a maximum for intermediate values of \mathbf{k} . Finally at large k values the DPE intensity vanishes. A dedicated theoretical study of the DPE intensity from a Cu(100) surface reveals exactly this picture as shown in Fig.15 [9]. Extending this argument to (e,2e) experiments one expects a similar behavior, which again is also confirmed by a thorough theoretical description [8, 46]. Experimentally we find that the emission direction of the fixed electron is surrounded by a reduced intensity of the other electron [11–15, 86]. These findings will be presented in chapter 5 in the context of case studies.

4.3. A fundamental issue of coincidence experiments

Coincidence experiments played an important role in the development of modern physics. The first report on a coincidence experiment was given by Bothe and Geiger in 1925 [87] honored by the Noble prize for Bothe in 1954. The scientific question they pursued was related to the Compton effect. Compton discovered in 1923 that the spectrum of x-rays scattered from a graphite target displayed a wavelength shift compared to the original spectrum [88]. The explanation invoked the model of a binary collision between a photon and a loosely bound electron. The recoil electrons were identified by Wilson, both observations were honored by the Noble prize in 1927 jointly awarded to Compton and Wilson. Important is that the detection of the x-rays and recoil electrons were done independently. In other words there was no direct proof that the binary collision model was valid for each collision. This aspect is of relevance because Bohr, Slater and Kramers suggested that Compton's law was correct statistically but not for the individual collision [89]. An experimental test was highly desirable, hence Bothe and Geiger realized an experiment where the photon and electron is detected by two Geiger-Müller counters.

The voltage peaks due to particle impact could be observed by a pair of electrometers. The mechanical deflections of those were projected onto a moving film.

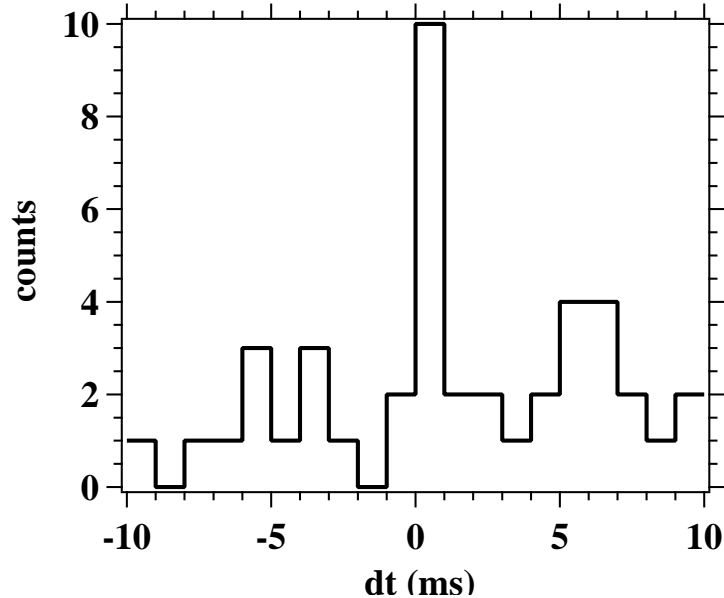


Figure 20. Reproduction of data shown in the original paper by Bothe and Geiger [87]. Plotted is the time difference dt between the detection of the photon signal and electron signal. For $dt = 0$ a peak in the distribution can be noticed which is direct proof that a binary collision between γ -quant and an electron occurs. The experimental data have been obtained over a time period of 126 min which required the exposure of app. 1000 m film and a subsequent visual inspection to determine the time difference dt .

In a post-experiment inspection of the developed film the time difference dt between the deflections of the γ - and electron electrometer was determined with a time resolution of 1 ms. The resulting histogram of events as a function of the time difference dt is reproduced in Fig.20. If the detected γ -quant and electron are the result of a binary collision they should be registered at the same time or $dt = 0$ for which there is clear evidence. This proves the existence of correlated pairs of scattered photon and recoil-electrons. Bothe and Geiger exposed a moving film (app. 1000 m long) for an acquisition time of 126 min. Longer experimental runs were not possible. Via a visual inspection they identified whether two deflections occur at the same time (in *coincidence*). More plainly put the coincidence “electronics” consisted in the human eye! Since then the coincidence electronics has developed significantly and a time resolution of 1 ns or better is a standard technology. Essentially, the electronic signals originating from the impact of the correlated particles have to be in close temporal proximity. If this is the case then a logic “true” signal is generated which serves as a trigger to record relevant experimental parameters.

A general problem of coincidence experiments is the fact that besides the events one is interested in (termed *true* coincidences) also unwanted events (called *random* coincidences) are detected. This aspect was already thoroughly discussed by Bothe and Geiger [87]. The very existence of these *random* coincidences will impose an upper limit on the primary flux. The microscopic origin of the two different contributions are

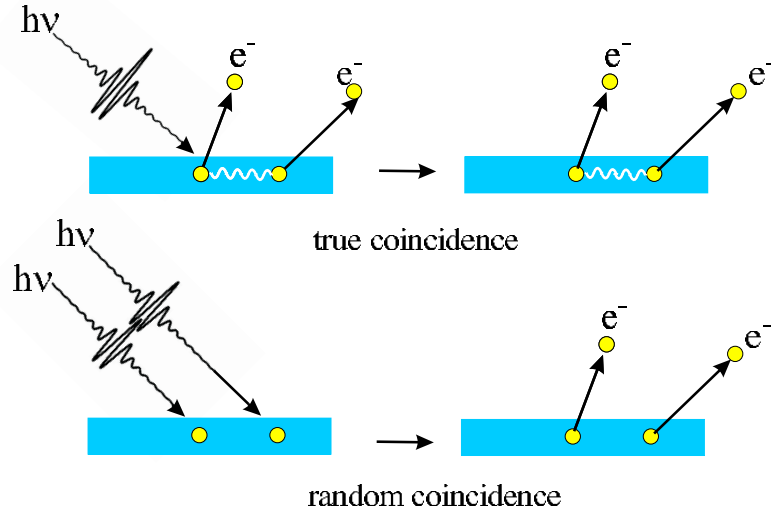


Figure 21. The process of interest concerns the emission of an electron pair due to the absorption of a single photon and is called *true coincidence*. If two photons impact on the surface each may lead to the emission of electron. This uncorrelated pair will also be detected via a coincidence circuit and is called *random coincidence*.

sketched in Fig.21. The process of interest concerns the emission of an electron pair upon impact of a single photon. If two photons hit the sample it can react via the emission of two uncorrelated electrons. These very different scenarios can not be separated by the coincidence circuit. If the *true* and *random* coincidence rates are labeled by t and r , we obtain for the total coincidence rate c :

$$c = r + t \quad (4.6)$$

Taking into account that the probability of pair emission is much smaller than for single electron emission (roughly by a factor of 10^3) a careful statistical discussion is required to identify useful operation conditions. We assume a pulsed photon source operated at a repetition rate f . For present day standard photon sources it is not possible that each photon pulse contains exactly one photon. The distribution of the number of photons in each pulse is of statistical nature and is described by the Poisson statistics. The only adjustment possible is to fix the average number λ of photons in the pulses. This means that the incoming flux F is determined by the product $f \cdot \lambda$. The probability to find n photons in a given pulse is determined by the Poisson statistics $P_\lambda(n)$:

$$P_\lambda(n) = e^{-\lambda} \frac{\lambda^n}{n!} \quad P_\lambda(1) = e^{-\lambda} \lambda \quad P_\lambda(2) = e^{-\lambda} \frac{\lambda^2}{2} \quad (4.7)$$

From eq. (4.7) it follows immediately that the ratio of the probabilities to find one photon versus two photons is given by $2/\lambda$. Therefore the incoming flux allows to us to vary this ratio. Suppose that we adjusted the flux such that the average number of electrons per pulse is $\lambda = 1$. We find for the percentage of pulses containing 0,1 or 2 electrons the values 36.8%, 36.8% and 18.4%, respectively. The pulse can contain also

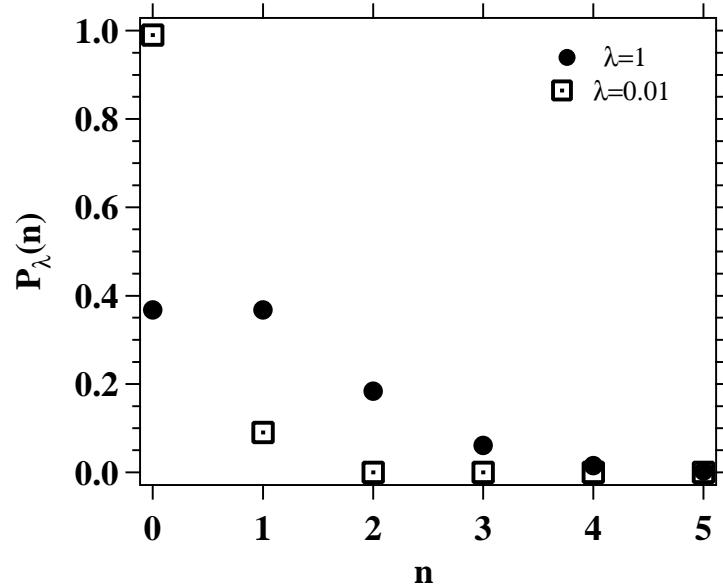


Figure 22. The probability of finding n photons in a pulsed photon beam is determined by the Poisson statistics $P_\lambda(n)$. The average number of photons in the beam is given by λ . As examples we selected $\lambda=0.01$ and 1 , respectively.

more than 2 photons, see Fig.22. Even for an average value of one photon per pulse the probability to find two photons per pulse is only a factor of 2 smaller than to find one photon per pulse. Clearly the contribution of *random* coincidences will overwhelm the *true* coincidences. The obvious escape route is to lower the primary flux and as an example we may select $\lambda=0.01$, see also Fig.22. In this case we have for the percentage of pulses which contain 0,1 and 2 photons values of 99%, 0.99% and 0.00005%. We have achieved a more favorable situation in which the *true* coincidences are more important than the *random* coincidences. However, we realize that 99% of the pulses are empty and for this instances no coincidence experiment is performed! This is not a deficiency of the experimental set-up but dictated by the Poisson statistics.

We simplify the discussion and make some assumption which will not affect the conclusion for the general case. Suppose we operate an experiment with two identical TOF detectors, which are symmetrically aligned such that the count rate on each detector is the same and is given by s , which is proportional to the primary flux F according to:

$$s = \sigma_1 \cdot F = \sigma_1 \cdot f \cdot \lambda \quad (4.8)$$

The constant σ_1 defines the probability for photoemission within the angular acceptance irrespectively of the kinetic energy. Competing with this process is the emission of electron pairs and the count rate of these *true* coincidences is given by t for which we write:

$$t = \sigma_2 \cdot F = \sigma_2 \cdot f \cdot \lambda = \frac{\sigma_2}{\sigma_1} \cdot s \quad (4.9)$$

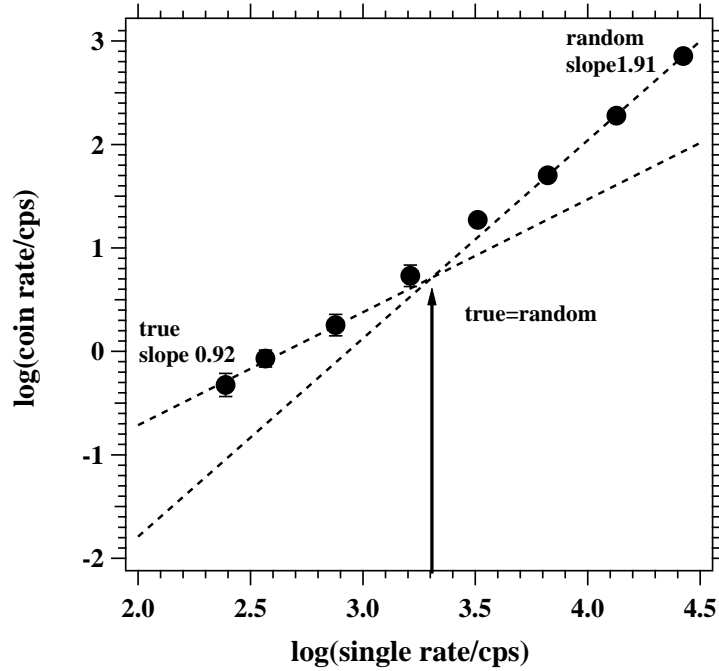


Figure 23. Experimental variation of the coincidence intensity as a function of the singles count rate plotted in a double-logarithmic fashion. The dashed lines are linear curves fitted to the data in the limit of “low” and “high” flux. The resulting slopes are indicated. The intercept of these two lines occurs for $t/r = 1$.

The constant σ_2 describes the probability that one electron is emitted within the acceptance of detector 1, while the other electron is registered by detector 2 irrespectively of the kinetic energies. The ratio of the *true* rate and the single rate s is σ_2/σ_1 , a typical value is of the order 10^{-3} . Therefore $\lambda \ll 1$ and we expand $P_\lambda(n)$ in powers of λ and keep only the leading term:

$$P_\lambda(0) = 1 \quad P_\lambda(1) = \lambda \quad P_\lambda(2) = \frac{1}{2}\lambda^2 \quad (4.10)$$

The probability of finding two photons in a pulse is given by the term $P_\lambda(2)$, the rate by which this occurs is given by the repetition rate f . The probability after photon impact of one electron to be emitted within the angular acceptance is σ_1 , therefore we have the combined probability σ_1^2 . We finally arrive at the expression for the *random* coincidence rate:

$$r = P_\lambda(2) \cdot \sigma_1^2 \cdot f = \frac{1}{2}\lambda^2 \cdot \sigma_1^2 \cdot f = \frac{1}{2} \cdot \sigma_1^2 \cdot \frac{F^2}{f} = \frac{1}{2f} \cdot s^2 \quad (4.11)$$

The important result is that the *random* rate r goes quadratically with the primary flux F in contrast to the *true* rate which goes linear. This means that at a high enough flux the *random* coincidences determine the coincidence spectrum.

The best choice of the flux F would ensure a high ratio of t/r while maintaining a high *true* rate t . For these conflicting requirements no optimum can be found but a rough operational compromise would be to set $t/r = 1$. Due to the fact that the singles

count rate s is strictly proportional to the flux and it is useful to rewrite eq.(4.6) in the following form:

$$c = a \cdot s + b \cdot s^2 \tag{4.12}$$

This functional dependence of the coincidence rate c is of relevance, because it becomes possible to identify the very existence of *true* coincidences and to identify the useful operational conditions of the flux. For this it is necessary to measure for different singles rate s the coincidence intensity c . If one plots $\log(c)$ as a function of $\log(s)$ the contribution of *true* coincidences is described by a linear curve with slope 1 while the *random* coincidences show up as a curve with slope 2. An example of such an analysis is displayed in Fig.23 and confirms the very existence of *true* coincidences. The two dashed lines approximate the behavior for “low” and “high” singles rate, the respective slopes are 0.92 and 1.91. The intercept of these lines occurs for $t/r = 1$ and would suggest a reasonable singles rate.

5. Case studies

From the previous discussion it becomes clear that the experimental challenge asked for dedicated instrumentation. Consequently, the presented work was performed with different generations of instruments. These will be described in due course by discussing key results, more details can be found in the original publications. The focus of these studies was to investigate angular distributions which showed the existence of a “depletion zone” which is a manifestation of the xc-hole. The very existence of a correlated positron-electron pair emission was proven. This observation has the potential to allow access to the Coulomb part of the xc-hole. The well-known Auger electron emission was studied and it was demonstrated that the picture of a two-step process is at odds with the experimental observation. The evidence points clearly towards a single-step process.

5.1. Manifestation of the xc-hole in pair emission

According to theory, access to the xc-hole is possible if the angular distributions of electron pairs are measured [8,9,45,46]. More precisely, if the emission direction of one electron is fixed the intensity distribution for the other electron needs to be determined. The experimental set-up first envisioned for this task is depicted in Fig.24 which employed the TOF technique [11,12]. Upon excitation of the surface with electrons (or photons), an electron pair may leave the sample. The electrons traverse a field free region where the hemispherical grids serve to shield the electric field coming from the multichannel plate. An impact on the channelplate can be either registered on the collector or on a resistive anode. Detection on the collector is only possible if electron

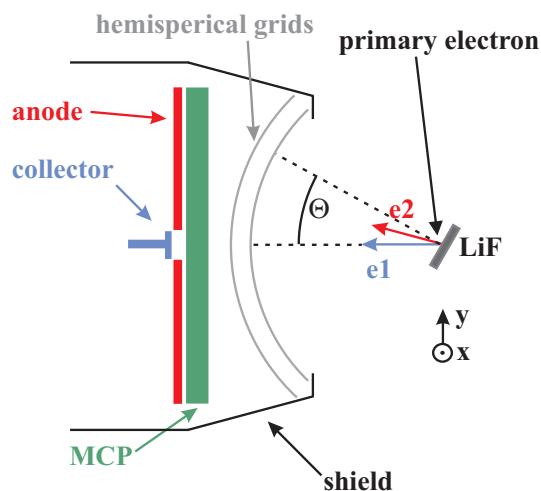


Figure 24. A primary electron excites a LiF sample under grazing incidence. The emitted electrons are detected in coincidence if e_1 hits a small collector while e_2 is registered on a resistive anode. The kinetic energies E_1 and E_2 and in-plane momenta can be determined by the flight time and flight path taken (from ref. [12]). Copyright (2006) by the American Physical Society.

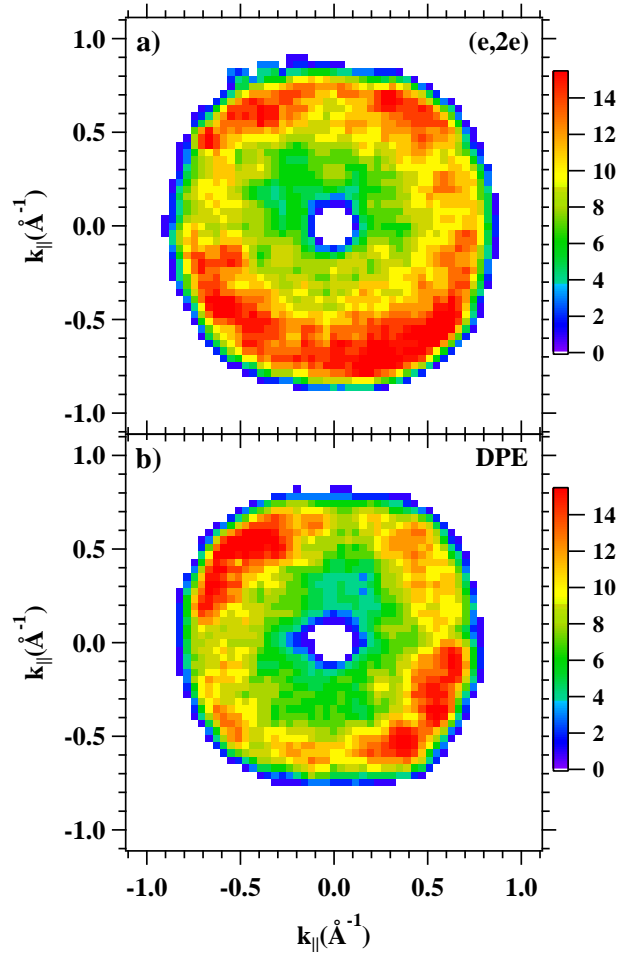


Figure 25. In panel a) we display the momentum distribution of electron e_2 for an (e,2e) experiment on LiF(100) with $E_1 = 7.5$ eV and $E_2 = 9.5$ eV. The primary energy was 30.7 eV [11]. In panel b) we present the momentum distribution of electron e_2 from a DPE experiment on a NaCl(100) surface. The photon energy was $h\nu = 34$ eV. The energies of the outgoing electrons are $E_1 = 5.5$ eV and $E_2 = 9.5$ eV (from ref. [12]). Copyright (2006) by the American Physical Society.

e_1 is emitted within a narrow cone of 0.02 sr, we call this electron “fixed”. The resistive anode covers an solid angle of 1 sr and it is important to note that the impact position of electron e_2 can be determined which in turn allows to determine the emission direction. Geometrical constraints require that the excitation occurs under grazing incidence which is 12° for a polar angle $\theta = 0$. From the flight times and the geometry it is straightforward to determine the energies E_1 , E_2 and the in-plane momenta. As suggested by theory we select the energies of the pairs and plot the intensity as a function of the in-plane momentum of electron e_2 around the fixed emission direction of the “fixed” electron. In Fig.25 a) the result of a (e,2e) experiment of a LiF(100) surface is shown [11]. The energy selection has been made such that valence electrons from the highest occupied state are emitted. This plot displays a zero intensity at a position where the collector is positioned. The position and size of this blind spot depends on the angle θ and momentum of the

“fixed” electron. For $\theta=0$ it is centered at $k_{\parallel}=0$ and has a radius of $\sim 0.1 \text{ \AA}^{-1}$. We clearly observe that the region $k_{\parallel}=0$ (outside the blind spot) is surrounded by a region of diminished intensity which we call “depletion zone”. The intensity increases for larger k_{\parallel} values and reaches a maximum for $k_{\parallel} \sim 0.55 \text{ \AA}^{-1}$ and then falls off rapidly towards the edge of the channelplate. This fall-off is entirely instrumental due to the finite size of the channelplate and does not reflect the true size of the “depletion zone”. Varying the polar angle θ causes this zone to move, but it stays centered around the “fixed” emission direction.

The question arises as to whether such an observation can be made also for DPE. The answer is affirmative as Fig.25 b) shows. The electron energies are selected such that only electrons from the highest occupied state contribute to the intensity. We note again that the emission direction of the fixed electron is surrounded by a region of reduced intensity.

We conclude that there is experimental proof of the emergence of a “depletion zone”. According to theory this zone is a manifestation of the xc-hole. Important is the fact that both experiments (e,2e) and DPE are qualitatively the same. From theory it is predicted that the coincidence intensity should drop off again once the emission angle with respect to the “fixed” emission direction is increased further. The angular range of the instrument depicted in Fig.24 was not sufficient to investigate this point.

5.2. Full angular distribution of electron pairs

Having demonstrated the existence of a “depletion zone” a TOF apparatus with increased angular acceptance was designed, see Fig.26 [13, 14, 86]. Within the drawing plane emission angles within ± 1.57 rad can be detected while a range of ± 0.4 rad is accessible perpendicular to it. Delay line detectors allow to recover the impact positions even if the two electrons forming a pair hit the same detector.

Each coincident event is characterized by six coordinates which are the individual energies and emission angles θ and ϕ . Angular distributions are obtained by the execution of several steps. First, one has to specify the individual energies of the electrons constituting a pair. Second, from this reduced data set one selects only those events in which the emission direction of one electron say e_1 is fixed. From this final data set one presents the coincidence intensity as a function of the emission angle θ and ϕ of electron e_2 . In order to have good enough statistics for the plots the energy intervals are 1.5 eV which are larger than the energy error. Likewise, the emission direction window we allow for electron e_1 is larger than the angular resolution. Using this improved apparatus we performed a DPE study on a Cu(111) surface excited with 50 eV photons hitting the sample under an angle of 32° with respect to the surface normal [13]. In Fig.27 we present typical angular distributions in which the energy of the fixed electron was selected to be 23 eV while the energy of the second electron was 12 eV. This energy selection ensures that the two emitted electron originate from the $3d$ levels. The inspection of the energy spectra showed that in this energy window the coincidence intensity showed a peak. The advantage of this set-up is that it allows to measure spectra for different fixed emission directions in parallel in contrast to the

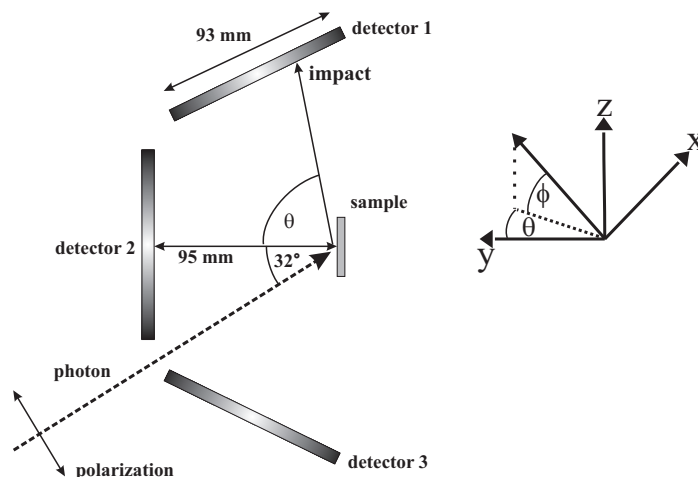


Figure 26. Via photon (or electron) excitation a sample is excited. Emitted electrons can reach one of three detectors. The emission direction is characterized by the angles θ and ϕ (from ref. [13]). Copyright (2007) by the American Physical Society.

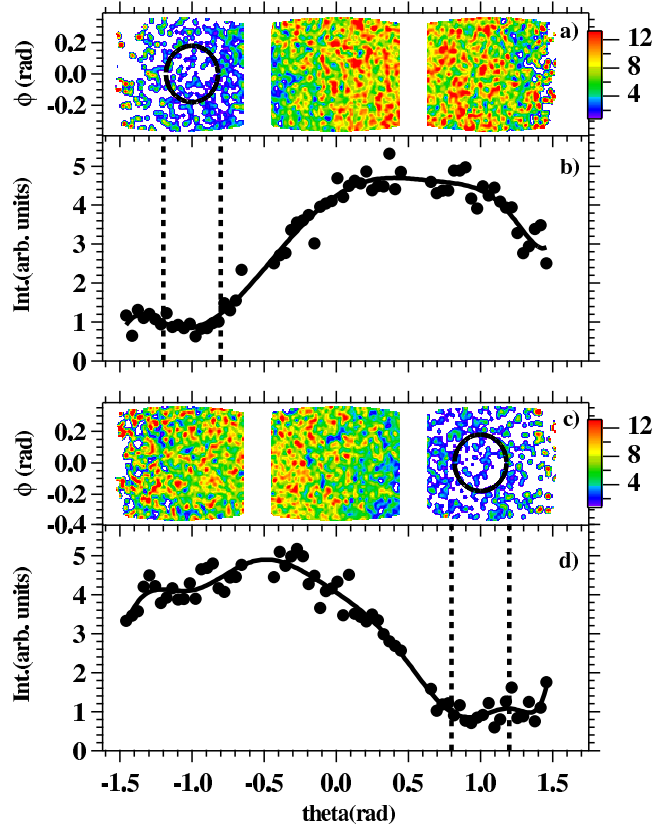


Figure 27. 2D-angular distributions and resulting line scans are shown for electron pairs with $E_1=23$ eV and $E_2=12$ eV. A DPE experiment on a Cu(111) surface was performed, the photon energy was set to 50 eV. The direction of the fixed electron with 23 eV is centered either at $\Theta = -1$ rad for panels a) and b) or $\Theta = 1$ rad for panels c) and d). The line scans of the intensity maps in a) and c) are plotted in panels b) and d). The solid lines are guide to eye, whereas the dashed vertical lines mark the boundaries of the fixed emission directions (from ref. [13]). Copyright (2007) by the American Physical Society.

instrument shown in Fig.24 which required a change in the polar angle to achieve this. We choose a fixed emission direction of either $\Theta = -1$ rad or $\Theta = 1$ rad as indicated by the solid circles in panel a) and c) of Fig.27. In the case of Fig.27 a) we observe a low intensity on the left detector. If we move to the center detector the intensity has increased and finally the intensity on the right detector is smaller than on the center detector. The statistics can be improved via an integration along the Φ direction and the result is plotted in Fig.27 b). The vertical dashed lines in Fig.27 b) mark the range of the allowed Θ values for the fixed electron. This intensity profile peaks at $\Theta \approx 0.2$ rad, while the fixed electron is centered at $\Theta \approx -1.0$ rad. This means that the angular size of the “depletion zone” is ≈ 1.2 rad. More importantly, we see that the coincidence intensity drops off again if the angle between the two electrons is beyond ≈ 1.2 rad as predicted from theory [9, 45]. The equivalent behavior is observed in panels c) and d), this time the center of the “depletion zone” is on the right side. A systematic variation of the emission direction from $\Theta \approx -1.0$ rad to $\Theta \approx 1.0$ rad demonstrates that the “depletion

zone” moves with the fixed emission direction and has a size of approximately 1 rad. We found no significant variation of the angular size of the “depletion zone” on the energy of the outgoing electrons. Therefore we adopted an angular rather than a momentum distribution in which the size will scale with the kinetic energy. This experiment also confirms that the “depletion zone” exists for a metal. Using the same apparatus for (e,2e) experiments on LiF and Cu surfaces demonstrates that the “depletion zone” can be fully mapped [14]. This observation was confirmed by Hattass et al. who used a different apparatus [90].

5.3. Spin-resolved (e,2e)

The possibility to perform spin-polarized (e,2e) experiments on ferromagnetic surfaces has been demonstrated in earlier work [58–60,62]. The required theoretical background has been laid down as well [65,69,91]. The sketch shown in Fig.28 a) explains what exactly is meant by a spin-polarized experiment while Fig.28 b) provides a view of the actual geometry used. A spin-polarized primary electron beam hits a ferromagnetic surface and two electrons are emitted. The spectra are recorded for either parallel (data set I^+) or antiparallel (data set I^-) orientation of the primary spin and the sample magnetization M . The generation of spin-polarized electron beams is an established technique [92], likewise the preparation of ferromagnetic surfaces and films is well-understood. In principle a spin-analysis of the emitted electrons is possible. However, electron spin analyzers are inherently inefficient and the implementation would increase the data acquisition time by at least a factor of 10^4 . This renders a spin analysis of the emitted electrons practically impossible.

In his landmark paper, Slater [7] sketched schematically the pair correlation function for parallel and antiparallel spins, see Fig.3. If one wants to address this in a scattering experiment, it is vital to have a spin-polarized primary beam and a target which has a high spin-polarization. In a joint experimental and theoretical effort the Fe(001) surface was studied. Within the theoretical description of the (e,2e) process a layer and spin-resolved band structure calculation has been performed in order to identify valence states with high spin-polarization. The outcome of this work is that at a binding energy $E_v = -0.8$ eV such a state exists for $k_{\parallel}^v = 0$. In order to access this state we have to recall that the crystalline surface imposes the conservation of the momentum in the plane:

$$k_{\parallel}^v + k_{\parallel}^p = k_{\parallel}^l + k_{\parallel}^r = k_{\parallel}^{sum} \quad (5.1)$$

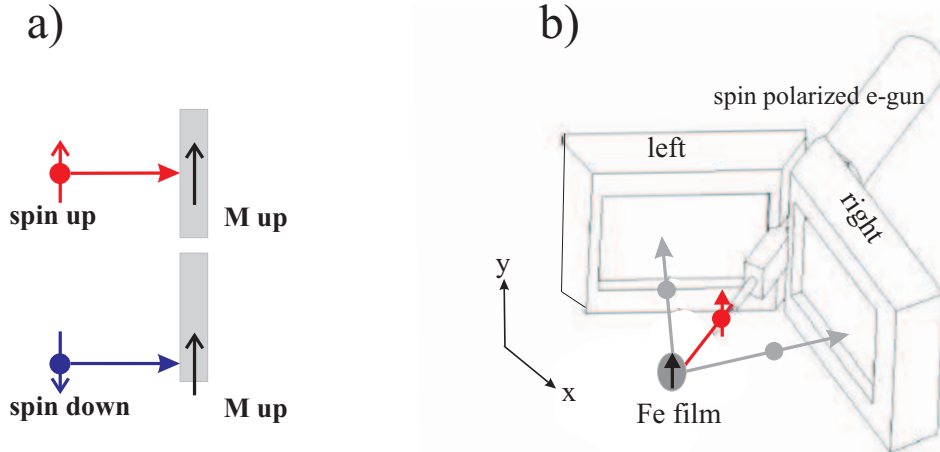


Figure 28. In panel a) we sketch a spin-polarized (e,2e) experiment. In panel b) we show the experimental set-up used to obtain spin-dependent angular distributions (from ref. [15]). Copyright (2010) by the American Physical Society.

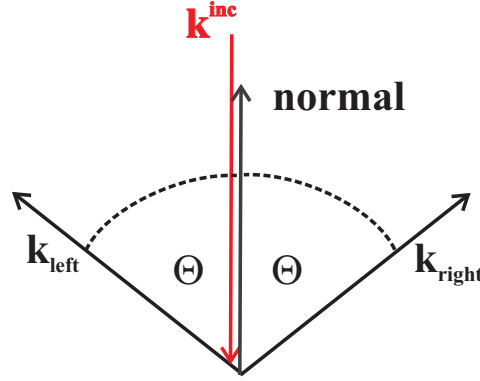


Figure 29. Geometrical view of the constraint $k_{\parallel}^{sum}=0$ and equal energies in normal incidence of the primary beam.

On the left side of the equation we have the contribution of the valence electron k_{\parallel}^v and the primary electron k_{\parallel}^p , while on the right side the contribution of the detected electrons k_{\parallel}^l (“left”) and k_{\parallel}^r (“right”) can be found. The sum of these two terms is called sum momentum k_{\parallel}^{sum} . Since we operate with a normal incidence primary beam, we have $k_{\parallel}^p=0$. We note that k_{\parallel}^{sum} determines the value of the valence electron k_{\parallel}^v . This means if one is interested in $k_{\parallel}^v=0$ one has to set $k_{\parallel}^{sum}=0$. Therefore the two electrons have to leave the surface in opposite directions if the electrons have the same kinetic energy, see Fig.29. Since energy conservation has to hold, the energy of the emitted electrons specifies the binding energy of the valence electron. Therefore the position of the valence electron within the band structure is uniquely defined.

We proceed to display the result for 25 eV excitation which requires the outgoing electrons to have an energy of 9.7 eV, see Fig.30. According to our coordinate system k_x^l is always negative while k_x^r is positive. Therefore, a coincidence event has an entry on the left and right half of the plot. Let us discuss the experimental intensities I^+ and I^- shown in panel a). Starting at $|k_x^{l,r}|=0$ we note that the coincidence intensity is zero which is purely instrumental since there is a gap between the detectors. Outside this blind region, starting at about $|k_x^{l,r}|=0.2 \text{ \AA}^{-1}$, we observe an increase of the coincidence intensity for increasing k values. A maximum is reached at $|k_x^{l,r}|\approx 0.5 \text{ \AA}^{-1}$. This reduced intensity for small $|k_x^{l,r}|$ values is a manifestation of the xc-hole as shown previously in experiment and theory [9, 11, 13, 46].

However, important differences between I^+ and I^- can be noticed. First, the integrated intensity for I^+ is higher than for I^- . Second, the intensity distribution for I^+ is very different from I^- . Intensities of I^- close to the maximum value are confined to $|k_x^{l,r}|$ values near 0.5 \AA^{-1} . For I^+ the intensity levels are close to the maximum value up to $|k_x^{l,r}|$ of 1.1 \AA^{-1} , before a drop can be observed. This is a consequence of

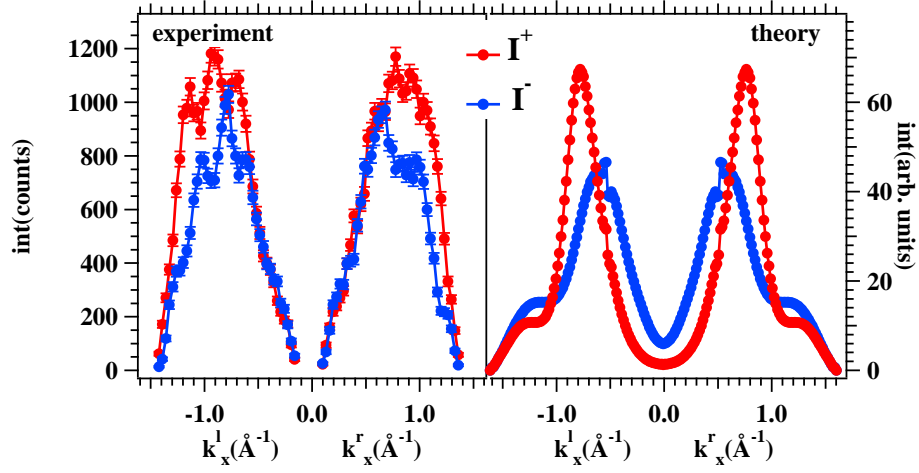


Figure 30. We compare the experimental and theoretical I^+ and I^- spectra. A spin-polarized primary beam hits in normal incidence the Fe(100) surface. Both outgoing electrons have an energy of 9.7 eV and $k_{\parallel}^{sum}=0$ (from ref. [15]). Copyright (2010) by the American Physical Society.

the finite angular acceptance of the instrument. Both experiment and theory clearly show that the maximum intensity for I^+ is larger than the corresponding maximum for I^- . Further agreement consists in the larger extension of the “depletion zone” for I^+ . In contrast to experiment, theory can investigate the spin state of the outgoing electrons. It is found that the intensity distribution I^+ contains predominantly those events where the primary spin and valence electron spin is parallel. Likewise one can show that the intensity I^- is dominated by an antiparallel alignment of primary spin and valence electron spin. This can be traced back to the high spin polarization of the studied valence state. This intrinsic spin resolution has an important consequence, namely, the possibility to separate exchange and correlation effects between the two outgoing electrons. For the parallel spin case $I^{++} \approx I^+$ both exchange and Coulomb correlation determine the size of the “depletion zone”, whereas for the antiparallel spin case $I^{-+} \approx I^-$ only the correlation plays a role. The size of the “depletion zone” for I^+ is larger than for I^- . Therefore one can say that the size of the exchange “depletion zone” has to exceed the size of the “depletion zone” due to Coulomb correlation.

5.4. Correlated positron-electron pair emission

So far we have discussed the emission of electron pairs due to primary electron impact or single photon absorption. In these studies the Pauli principle and Coulomb interaction needs to be considered on an equal footing. As pointed out before, it is highly desirable to disentangle the contribution due to the Pauli principle from the Coulomb correlation. One approach is to perform a spin-polarized (e,2e) experiment which requires a ferromagnetic sample and a valence state with high spin-polarization. In the case of a Fe(001) surface we have demonstrated that this condition can be fulfilled [15]. An alternative way to unravel the two distributions is to study the positron-electron pair

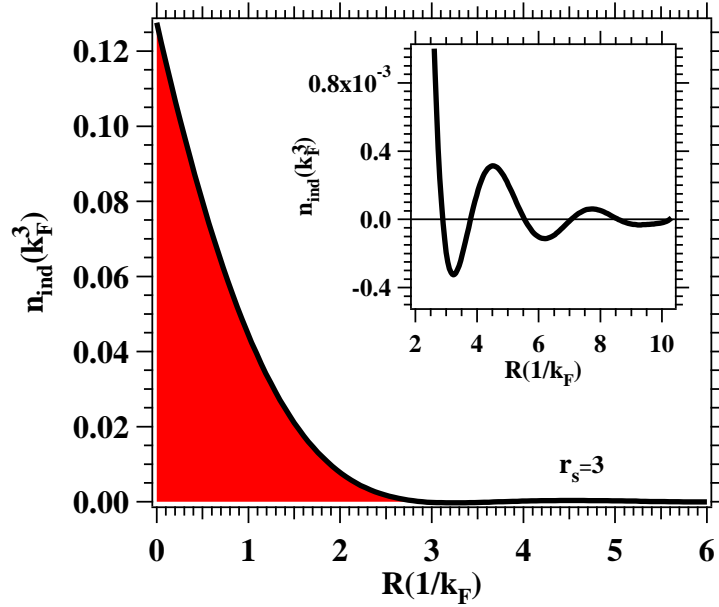


Figure 31. Induced electron charge distribution in the vicinity of a positron immersed into a jellium [93]. The electron density is determined by r_s which is set to 1.5 \AA , which is close to the electron density of Cu. The inset zooms into a region where the induced charge density is approaching zero and Friedel oscillations are visible.

emission upon primary positron impact. Since positron and electron are distinguishable the wave function does not have to fulfill a symmetry rule upon exchanging particles. In other words there is no exchange hole around a positron in an electronic system. Therefore the motion of the positron within the electronic system is entirely governed by the attractive Coulomb interaction between positron and electrons. Let us visualize this within a jellium model in which we place a positive charge. The electrons will rearrange to screen this external charge and the difference to the unperturbed charge density is given by n_{ind} [93]. An example is shown in Fig.31 where the unperturbed charge density is given by $r_s = 1.5 \text{ \AA}$, where r_s is the radius of a sphere in which one electron is found [4]. This choice is the appropriate value for Cu and it leads to $k_F = 1 \text{ \AA}$. We see a pile-up of induced electronic charge at the location of the positron which drops quickly and at $R=3$ it has approached almost 0. We note Friedel oscillations commencing at this distance, which decay quickly. The key point is the emergence of a Coulomb hill within a few \AA of the positron which screens the positron. Comparing the angular distributions of positron-electron pairs with those electron pairs obtained via $(e,2e)$ experiments where the repulsive Coulomb interaction and Pauli is present allows in principle the envisioned separation. Clearly the motivation to perform such a positron experiment is very high. However, upon closer inspection one may wonder whether correlated positron-electron pair emission actually exists. This reservation comes to mind because it is well-known that if matter and antimatter is brought in contact they annihilate and the emission (in most cases) of a pair of γ -quanta takes place. This effect is very interesting and useful in rather diverse contexts. The life

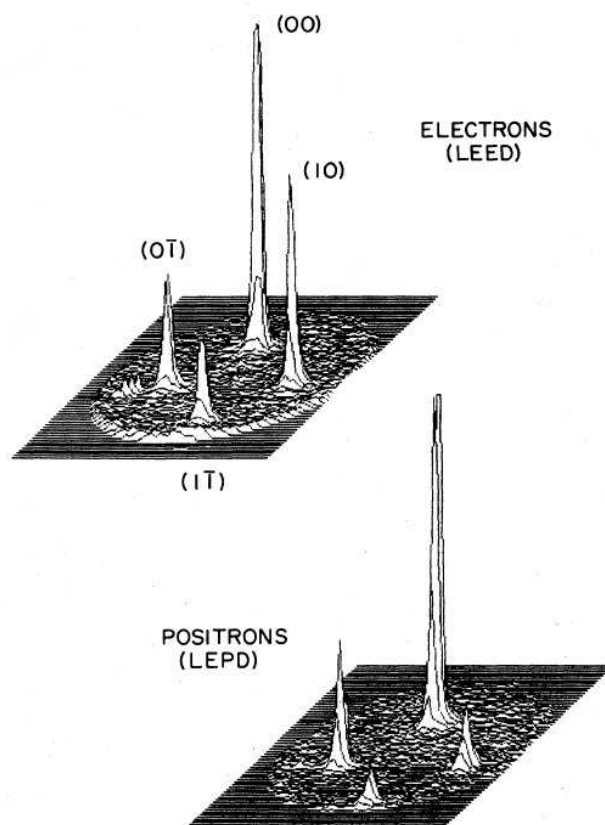


Figure 32. Comparison of low energy electron diffraction (LEED) and low energy positron diffraction (LEPD) from a W(110) surface obtained with a primary energy of 250 eV [95]. Reprinted Fig. 36 with permission from: P.J. Schultz and K.G. Lynn, *Rev. Mod. Phys.* **60**, 701 (1988). Copyright (1988) by the American Physical Society.

time of positrons in matter is on the picosecond time scale and strongly depends on the nature of defects. Therefore positron life-time spectroscopy has developed into a tool to study defects. If one measures the emitted γ -pairs in coincidence one can learn about the Fermi surface of a material [94]. Positron emission tomography (PET) is essentially the same experiment used in medicine. The success of the proposed experiments depends on the life-time of a positron in an electronic system compared to the duration of a scattering event. Before a positron can annihilate it has to lose its kinetic energy which occurs on a time scale of 10^{-12} s. This time is much longer than the duration of a scattering event which occurs over a time period of 10^{-15} s [95].

Some more encouraging facts can be taken out of the available literature. Low kinetic energy positron beams have been used in surface science some 25 years ago [96, 97]. One experimental motivation was to perform low kinetic energy positron diffraction experiments which are called LEPD [98–102]. This experiment is the analog to low kinetic electron energy diffraction (LEED). The advantage of LEPD versus LEED lies in the fact that for a structural analysis via I-V curves no exchange needs to be included. This makes the required computations significantly easier [103, 104]. A

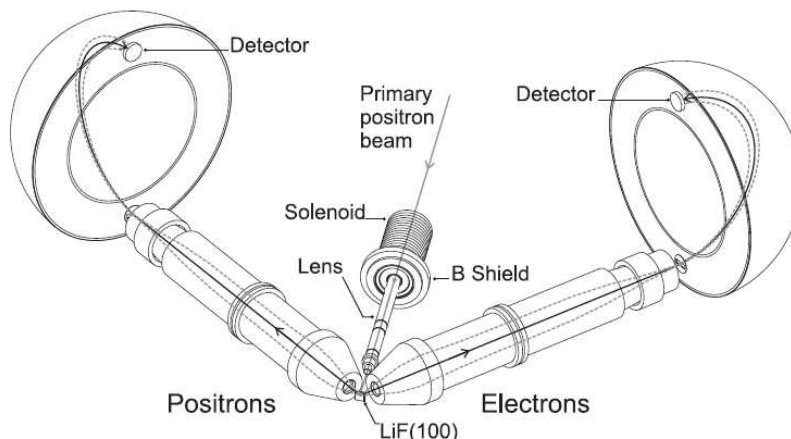


Figure 33. Simplified view of the experiment, which consists of a pair of hemispherical analyzers. The specimen is a LiF(100) surface which is exposed to a primary positron beam impinging along the surface normal. By reversing the polarity of all electron optical elements one analyzer will be sensitive to positrons rather than electrons (from Riessen et. al ref. [16]). Copyright (2008) by the Institute of Physics.

comparison of diffraction images obtained by LEPD and LEED is shown in Fig.32. Schultz et al. studied a W(110) surface with primary positron and electron beam which had a primary energy of $E_p = 250$ eV [95]. Both diffraction patterns reflect the symmetry of the substrate and the different relative intensities compared to the specular beam show that additional information can be extracted from the LEPD experiment. Frieze et al. explicitly mention that the reflectivity of the specular beam in LEPD is a factor of 2 larger than in the case of LEED. It is a rather general observation that the reflectivities of LEPD are of the same order as for LEED. We conclude that positron scattering occurs before annihilation takes place and a high fraction of positrons is reemitted.

Therefore it appears possible that an outgoing positron scatters with a valence electron leading to the emission of a correlated positron-electron pair. This conjecture was tested in a pioneering experiment performed at the high-intensity positron source NEPOMUC at the Research reactor FRM II/Garching [105]. This facility provides a beam of low kinetic energy positrons with a maximum flux of $5 \cdot 10^8$ e^+ per second which is the highest intensity world-wide. If we convert this into a current, we obtain a value of the order 10^{-14} A. This is essentially the upper value before the *random* coincidences become too dominant. Due to the fact that a pulsed positron source fulfilling our special constraints does not exist worldwide, a TOF set-up could not be employed. Therefore we used an electro-static scheme as depicted in Fig.33. The key instrumentation is a pair of hemispherical analyzers which are usually operated to detect electron pairs. Changing the polarity of all voltages applied to the electron-optical components of one analyzer will ensure that positrons are detected. A LiF(100) surface was exposed to a 85 eV primary positron beam. If a correlated positron-electron pair is emitted, both particles will leave the sample at the same time. They will reach the respective detectors at the same instance within the time resolution of the experiment. Experimentally we set the

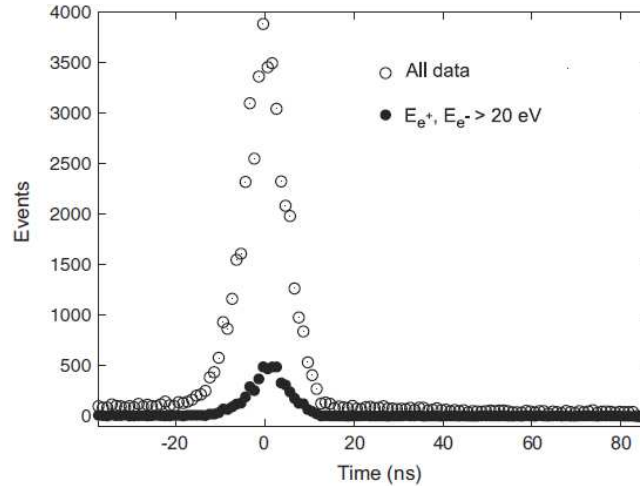


Figure 34. A LiF(100) surface was excited by a 85 eV primary positron beam. The measured coincidences of positron-electron pairs are displayed as a function of the arrival time difference dt . The open symbols refer to all measured pairs whereas the solid symbols include those events where the energy of emitted positron and electron is above 20 eV. The emergence of a peak at $dt = 0$ is experimental proof that correlated positron-electron pair emission exists (from Riessen et. al ref. [16]). Copyright (2008) by the Institute of Physics.

electronics such that if positron detection and electron detection occurs within a time window of 100 ns it is regarded as a coincidence. From the accumulated data set we can compute the arrival time difference dt of the coincidence events and show the result as a histogram, see Fig.34. In this figure we compare the dt histogram for all coincidences (open symbols) with those for which the energy of the positron and electron is larger than 20 eV. We clearly observe peaks in the intensity distribution. The peak position and width is unchanged, but most coincidences belong to positron and electron pairs which have low kinetic energies. The width of the peaks is solely determined by the time resolution of the experiment. The very existence of a peak in the dt histogram proves that a positron impact does lead to the emission of a time-correlated positron-electron pair. It is interesting to note that our proof follows the same route as Bothe and Geiger, see Fig.20. One should emphasize that the total data acquisition time was only 62 h and experimental problems prohibited us to make use of the total available flux. Taking this into account one can state that the positron-electron pair emission intensity is of the order of electron-electron pair emission. Therefore the experimental evidence strongly suggest that the angular distributions of correlated positron-electrons can be obtained. The potential benefit of positron-electron pair emission has been discussed in theory [106]. Moreover, a recent theoretical study on the positron-electron pair emission from a Cu(111) surface was performed. It was shown that the angular distributions display a correlation hill rather than a exchange-correlation hole [107].

5.5. Double photoemission illuminates the Auger process

Auger electron spectroscopy is a standard tool of surface science, because it allows chemical characterization of surfaces [108]. This is achieved by noting that the kinetic energies of Auger electrons are element specific. The Auger effect is usually explained via a two-step process in which first a core-electron is ejected. This may be achieved via the absorption of a photon by a core-electron. After the photoemission event the vacancy in the core-level is filled by an electron from a higher energy level. The gain in energy can be transferred to a third electron which may be consequently emitted. This electron is called the Auger electron [109,110]. The energies of core-levels are specific for each element hence the photoelectron has a well-defined kinetic energy E_{ph} for a given photon energy. Likewise, the kinetic energy of the Auger electron E_{Auger} is characteristic for each element due to the fact that core-levels are involved. From this established picture it follows that the detection of a photoelectron and Auger electron in a double photoemission (DPE) experiment should occur only within well-defined energy regions. Via the choice of the photon energy it is possible to adjust the kinetic energies E_{ph} and E_{Auger} relative to each other. We assume in the following $E_{ph} < E_{Auger}$ and the expected 2D-Energy distribution is schematically depicted in Fig.35. Auger and photoelectron are not emitted with a sharp energy, but display finite peak widths. Therefore one expects coincidence intensity only from the red regions. Experiments detecting an Auger electron in coincidence with a photoelectron have been reported in the literature [72,111–116]. Furthermore, DPE experiments causing the emission of two valence electrons have been

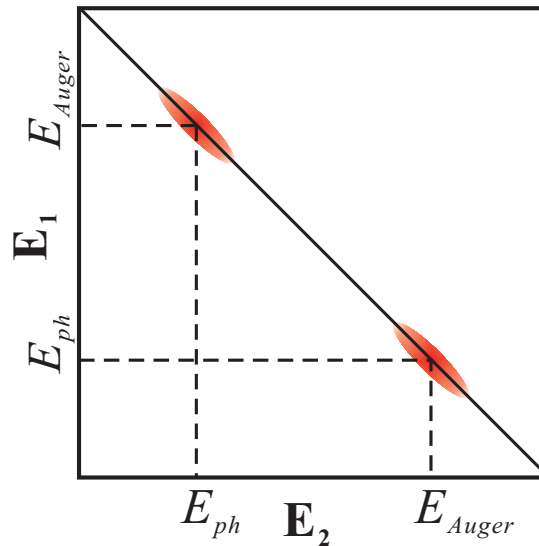


Figure 35. Schematic 2D-Energy distribution if a photo-electron (E_{ph}) and Auger electron (E_{Auger}) are detected in coincidence on the basis of a two-step process. The axis $E_{1,2}$ label the kinetic energy of the detector 1 and 2, respectively. The size of the red regions reflect the line widths of Auger electron and photoelectron. The solid diagonal line goes through the center of the red regions which defines a fixed sum energy $E_{ph} + E_{Auger}$. Coincidence intensity is expected within the red regions only.

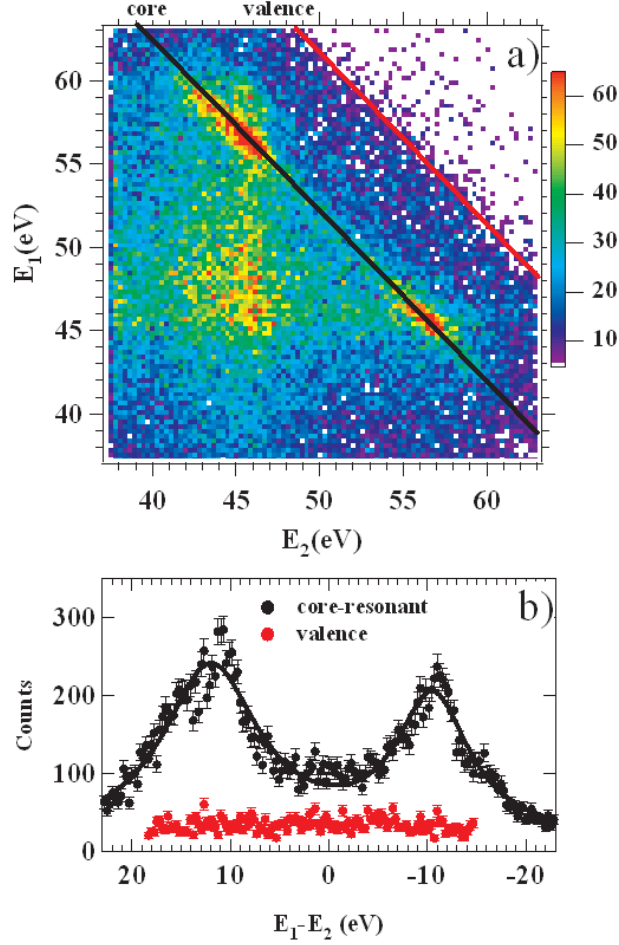


Figure 36. In panel a) we display the experimental 2D-Energy distribution. The red diagonal line marks the onset of pair emission. The black diagonal line goes through high intensity regions which include Auger and photoelectron pairs. In panel b) we present the energy sharing curves along the two diagonal lines of panel a).

studied in the literature and this work [13]. An interesting situation arises if the Auger emission involves besides the core-level also electrons from the valence band. It would be desirable to capture both processes simultaneously. This became possible with the instrument already introduced in Fig.33. For the DPE experiment a Cu(100) surface was excited with a photon energy of 125 eV. The binding energy of the $3p_{1/2}$ and $3p_{3/2}$ level is 75 and 77 eV, respectively. Therefore the photon energy is sufficient to excite the 3p level.

The key results are displayed in Fig.36. In panel a) we present the 2D-Energy distribution of the coincidence events. Two important regions are marked with diagonal lines. Diagonal lines in such an energy distribution refer to coincidence events which have a fixed energy sum $E_{sum}=E_1+E_2$ of the pair. Energy conservation demands that the sum energy has an upper bound given by the photon energy minus twice the work function. The red line marks the onset of DPE from valence states on the basis of this energy consideration. If we plot the intensity along the red line (labeled *valence*)

we obtain a sharing distribution. This is the coincidence intensity as a function of the energy difference $E_1 - E_2$. The red data points in Fig.36 b) refer to the onset of DPE. We note that this curve is continuous and reflects the fact that DPE from valence states proceeds via a single step. The black diagonal (labeled *core*) of Fig.36 a) goes through two narrow regions of high energies. These pockets have the energy coordinates (45 eV, 57 eV) and (57 eV, 45 eV), respectively. These energies can be easily identified as the Auger electron at 57 eV and the 3p photoelectron at 45 eV. From the arguments presented at the beginning we expect coincidence intensity only at these energy positions if the emission process proceeds in two steps. However we can clearly see that there is also intensity connecting these two pockets. If we compute a sharing curve along the solid diagonal line we can get a better view. We note a continuous energy sharing, see black data points in Fig.36 b). A continuous energy sharing is clear evidence that the Auger process does not proceed via two steps but is a single step process.

This surprising result emphasizes the importance of a time dependent description of electron emission. In this respect it is worth noting that there is an emerging field of atto science due to the availability of ultrashort laser sources [117–119]. The connection to this field becomes clear if we translate the width of the sharing curve through the Auger and photoelectron peak into a time via the uncertainty relation. We find a value of roughly 30 atto sec (as), hence the overall process of absorption and decay via emission of an electron pair takes place in such a short time scale that it is not meaningful to identify individual steps. There is a relation to the xc-hole if we recall recent theoretical results [18, 19]. If an electron is suddenly removed from an electronic system it leaves an exchange-correlation hole behind. This hole can be filled and this occurs on times of the order 50 as.

6. Summary and Outlook

In this work it is proven that the important concept of the exchange-correlation hole is experimentally accessible [11–15, 86]. It manifests itself in the emergence of a zone of reduced intensity in angular distributions. This is in line with theoretical predictions [8, 9]. It is found that the excitation with electrons or photons gives qualitatively similar results. The size of this “depletion zone” is insensitive to the value of the primary energy and the energy of the outgoing electrons. For Cu and LiF surfaces the angular size of the “depletion zone” is app. 1 rad.

The microscopic origin of the exchange-correlation holes stems from the Pauli-principle and the Coulomb interaction. One approach to disentangle the different contributions is to use a spin-polarized primary beam on a ferromagnetic target. It is demonstrated for a Fe(001) surface that suitable conditions exist where the spin orientation of primary electron and valence electron is either parallel or antiparallel [15]. This allows the envisioned separation since for anti-parallel orientation only the Coulomb interaction play a role. We find for parallel spins that the size of the “depletion zone” is larger than for antiparallel spins. This means that in angular space the exchange-hole is larger than the Coulomb hole.

In a pioneering experiment it could be proven that correlated positron-electron emission exists [16]. This provides the potential to separate out the contribution of the Coulomb correlation, because positron and electron are distinguishable.

A study of the Auger electron emission from a Cu(001) surface is presented in which the Auger electron is measured in coincidence with the photoelectron. Usually a two-step model is invoked to explain the Auger electron emission, it is found that this model is at odds with the experimental observed energy distributions [17].

It is fair to say that the pair emission spectroscopy from surfaces has experienced a steady development. Studies of this kind will always be demanding due to low count rates, but the prospect for the future appears bright. One may outline a few aspects:

Most of the presented work has been on materials like insulators of the type LiF and transition metal surfaces. These are usually not considered to be “highly” correlated. In contrast to these, oxides of the type NiO and CoO are referred to as “highly” correlated. By this it is meant that a description within an effective independent picture is not sufficient to capture important material properties. Therefore it appears warranted to focus on these materials. As a matter of fact, (e,2e) experiments have already begun and first results are very promising. An important observation is an increase of the coincidence intensity by a factor 5-10 compared to a metallic substrate. This is of course a welcomed message for the experimentalist, but it may also be understood as a sign of a stronger electron correlation. This is corroborated by a recent theoretical work on DPE from “strongly” correlated systems [85].

Superconductivity is a phenomenon clearly beyond an effective single particle description and to detect Cooper pairs via electron pair emission would be of great

interest. The power of DPE in studying superconductors has been demonstrated in theory [84]. The experimental challenges are formidable, but could be overcome.

DPE experiments using a TOF set-up need a suitable pulsed light source. The special requirements of the coincidence experiments make it mandatory to use a synchrotron source like the BESSY II storage ring. However, the special operational mode required is offered only 4 weeks per year in the case of BESSY II. This impairs strongly the possibility to perform systematic studies. An avenue for extending measurement time is to make use of recent advances in laser technology [117–119]. It is possible to produce light pulses which have a duration of a few hundred atto seconds via the generation of higher harmonics. The generation of photon energies in excess of 30 eV is possible. The current challenge lies in tuning the repetition rate to values appropriate for coincidence experiments. Another advantage of this type of excitation lies in the much shorter pulse length compared to the synchrotron pulses which are in the pico seconds range. This allows to address the question how the size of the “depletion zone” depends on the temporal width of the photon pulse. It is expected that changes occur on the time scale 100 atto seconds [18, 19].

Correlated positron-electron pair emission is a reality and this warrants further studies. The available beamtime at user facilities is rather limited. Therefore systematic work requires the development of a lab-based positron source, which is currently underway. The ultimate goal would be the availability of a pulsed positron source to record angular distributions revealing a Coulomb “hill” [107].

7. References

- [1] P. Drude, *Annalen der Physik* **306**, 566 (1900).
- [2] H. A. Lorentz, *The Theory Of Electrons*, B.G. Teubner, Leipzig, 1909.
- [3] A. Sommerfeld, *Naturwissenschaften* **15**, 63 (1927).
- [4] N. W. Ashcroft and N. D. Mermin, *Solid State Physics*, Saunders College, Philadelphia, 1987.
- [5] C. Kittel, *Introduction to Solid State Physics*, John Wiley & Sons, Inc., New York, Chichester, Brisbane, Toronto, Singapore, 1991.
- [6] E. Wigner and F. Seitz, *Phys. Rev.* **43**, 804 (1933).
- [7] J. C. Slater, *Rev. Mod. Phys.* **6**, 209 (1934).
- [8] J. Berakdar, H. Gollisch, and R. Feder, *Solid State Commun.* **112**, 587 (1999).
- [9] N. Fominykh, J. Berakdar, J. Henk, and P. Bruno, *Phys. Rev. Lett.* **89**, 086402 (2002).
- [10] H. Ibach and H. Lüth, *Solid-State Physics*, Springer-Verlag, Berlin, 1991.
- [11] F. Schumann, J. Kirschner, and J. Berakdar, *Phys. Rev. Lett.* **95**, 117601 (2005).
- [12] F. Schumann, C. Winkler, G. Kerherve, and J. Kirschner, *Phys. Rev. B* **73**, 041404(R) (2006).
- [13] F. O. Schumann, C. Winkler, and J. Kirschner, *Phys. Rev. Lett.* **98**, 257604 (2007).
- [14] F. O. Schumann, C. Winkler, and J. Kirschner, *New J. Phys.* **9**, 372 (2007).
- [15] F. O. Schumann, C. Winkler, J. Kirschner, F. Giebels, H. Gollisch, and R. Feder, *Phys. Rev. Lett.* **104**, 087602 (2010).
- [16] G. A. van Riessen, F. O. Schumann, M. Birke, C. Winkler, and J. Kirschner, *J. Phys.: Condens. Matter* **20**, 442001 (2008).
- [17] G. A. van Riessen, Z. Wei, R. S. Dhaka, C. Winkler, F. O. Schumann, and J. Kirschner, *J. Phys.: Condens. Matter* **22**, 092201 (2010).
- [18] J. Breidbach and L. S. Cederbaum, *Phys. Rev. Lett.* **94**, 033901 (2005).
- [19] A. I. Kuleff and L. S. Cederbaum, *Phys. Rev. Lett.* **98**, 083201 (2007).
- [20] H. Lebius, H. R. Koslowski, K. Wiesemann, and B. A. Huber, *Annalen der Physik* **503**, 103 (1991).
- [21] P. Hohenberg and W. Kohn, *Phys. Rev.* **136**, B864 (1964).
- [22] W. Kohn and L. J. Sham, *Phys. Rev.* **140**, A1133 (1965).
- [23] W. Kohn, *Rev. Mod. Phys.* **71**, 1253 (1999).
- [24] K. Capelle, *Brazilian Journal of Physics* **34**, 1318 (2006).
- [25] W. Jones and N. H. March, *Theoretical Solid State Physics*, volume 1, John Wiley & Sons, New York, 1973.
- [26] C. Kittel, *Quantum theory of solids*, John Wiley & Sons, New York, 1987.
- [27] G. Grosso and G. P. Parravicini, *Solid State Physics*, Academic Press, San Diego, 2000.
- [28] V. Maslen, *Proc. Phys. Soc. A* **69**, 734 (1956).
- [29] J. Ugalde and R. Boyd, *Journal of Physics B: Atomic and Molecular Physics* **18**, L701 (1985).
- [30] R. J. Boyd and C. A. Coulson, *Journal of Physics B: Atomic and Molecular Physics* **7**, 1805 (1974).
- [31] M. A. Buijse and E. J. Baerends, *Molecular Physics* **100**, 401 (2002).
- [32] R. McWeeny, *Rev. Mod. Phys.* **32**, 335 (1960).
- [33] H. J. Juretschke, *Phys. Rev.* **92**, 1140 (1953).
- [34] H. J. Juretschke, *Phys. Rev. B* **36**, 6168 (1987).
- [35] V. Sahni and K.-P. Bohnen, *Phys. Rev. B* **31**, 7651 (1985).
- [36] N. D. Lang and W. Kohn, *Phys. Rev. B* **1**, 4555 (1970).
- [37] J. Bardeen, *Surf. Sci.* **2**, 381 (1964).
- [38] J. E. Inglesfield and I. D. Moore, *Solid State Commun.* **26**, 867 (1978).
- [39] D. B. Jochym and S. J. Clark, *Phys. Rev. B* **76**, 075411 (2007).
- [40] P. Krüger, G. Wolfgarten, and J. Pollmann, *Solid State Commun.* **53**, 885 (1985).
- [41] M. Nekovee, W. C. Foulkes, and R. J. Needs, *Phys. Rev. Lett.* **87**, 036401 (2001).
- [42] P. P. Rushton, D. J. Tozer, and S. J. Clark, *Phys. Rev. B* **65**, 235203 (2002).

-
- [43] A. Puzder, M. Y. Chou, and R. Q. Hood, *Phys. Rev. A* **64**, 022501 (2001).
- [44] L. A. Constantin, J. P. Perdew, and J. Tao, *Phys. Rev. B* **73**, 205104 (2006).
- [45] N. Fominykh, J. Henk, J. Berakdar, and P. Bruno, *Surf. Sci.* **507-510**, 229 (2002).
- [46] H. Gollisch, N. v. Schwartzberg, and R. Feder, *Phys. Rev. B* **74**, 075407 (2006).
- [47] E. Rutherford, *Philosophical Magazine* **21**, 669 (1911).
- [48] R. Camilloni, A. G. Guidoni, R. Tiribelli, and G. Stefani, *Phys. Rev. Lett.* **29**, 618 (1972).
- [49] I. McCarthy and E. Weigold, *Rep. Prog. Phys.* **54**, 789 (1991).
- [50] M. Vos and I. McCarthy, *Rev. Mod. Phys.* **67**, 713 (1995).
- [51] S. Iacobucci, L. Marassi, R. Camilloni, S. Nannarone, and G. Stefani, *Phys. Rev. B* **51**, R10252 (1995).
- [52] M. Iinokuti, *Rev. Mod. Phys.* **43**, 297 (1971).
- [53] O. M. Artamonov, S. Samarin, and J. Kirschner, *Phys. Rev. B* **51**, 2491 (1995).
- [54] J. Kirschner, O. M. Artamonov, and S. Samarin, *Phys. Rev. Lett.* **75**, 2424 (1995).
- [55] R. Herrmann, S. Samarin, H. Schwabe, and J. Kirschner, *Phys. Rev. Lett.* **81**, 2148 (1998).
- [56] J. Berakdar, S. Samarin, R. Herrmann, and J. Kirschner, *Phys. Rev. Lett.* **81**, 3535 (1998).
- [57] R. Feder, H. Gollisch, D. Meinert, T. Scheunemann, O. M. Artamonov, S. N. Samarin, and J. Kirschner, *Phys. Rev. B* **58**, 16418 (1998).
- [58] S. Samarin, J. Berakdar, O. M. Artamonov, and J. Kirschner, *Phys. Rev. Lett.* **85**, 1746 (2000).
- [59] S. Samarin, O. M. Artamonov, J. Berakdar, A. Morozov, and J. Kirschner, *Surf. Sci.* **482-485**, 1015 (2001).
- [60] A. Morozov, J. Berakdar, S. N. Samarin, F. U. Hillebrecht, and J. Kirschner, *Phys. Rev. B* **65**, 104425 (2002).
- [61] S. Samarin, O. M. Artamonov, A. D. Sergeant, J. Kirschner, A. Morozov, and J. F. Williams, *Phys. Rev. B* **70**, 073403 (2004).
- [62] S. Samarin, O. M. Artamonov, A. D. Sergeant, and J. F. Williams, *Phys. Rev. B* **72**, 235419 (2005).
- [63] S. Samarin, O. M. Artamonov, A. D. Sergeant, R. Stamps, and J. F. Williams, *Phys. Rev. Lett.* **97**, 096402 (2006).
- [64] J. Berakdar, *Phys. Rev. B* **58**, 9808 (1998).
- [65] H. Gollisch, X. Yi, T. Scheunemann, and R. Feder, *J. Phys.: Condens. Matter* **11**, 9555 (1999).
- [66] N. Fominykh, J. Henk, J. Berakdar, P. Bruno, H. Gollisch, and R. Feder, *Solid State Commun.* **113**, 665 (2000).
- [67] N. Fominykh and J. Berakdar, *J. Electron. Spectrosc. Relat. Phenom.* **161**, 125 (2007).
- [68] H. Gollisch and R. Feder, *J. Phys.: Condens. Matter* **16**, 2207 (2004).
- [69] U. Rücker, H. Gollisch, and R. Feder, *Phys. Rev. B* **72**, 214424 (2005).
- [70] B. Feuerbacher, B. Fitton, and R. F. Willis, *Photoemission and the Electronic Properties of Surfaces*, John Wiley & Sons.
- [71] S. Hüfner, *Photoelectron Spectroscopy*, Springer, 2003.
- [72] H. W. Haak, G. A. Sawatzky, and T. D. Thomas, *Phys. Rev. Lett.* **41**, 1825 (1978).
- [73] N. Mårtensson, P. Baltzer, A. Brambilla, P. A. Brühwiler, J. O. Forsell, A. Nilsson, A. Stenborg, and B. Wannberg, *J. Electron. Spectrosc. Relat. Phenom.* **70**, 117 (1994).
- [74] H. Hertz, *Annalen der Physik und Chemie* **267**, 983 (1887).
- [75] W. Hallwachs, *Annalen der Physik und Chemie* **269**, 301 (1888).
- [76] A. Einstein, *Annalen der Physik* **17**, 132 (1905).
- [77] C. Gazier and J. Prescott, *Phys. Lett. A* **32**, 425 (1970).
- [78] H. Biester, M. Besnard, G. Dujardin, L. Hellner, and E. Koch, *Phys. Rev. Lett.* **59**, 1277 (1987).
- [79] M. Munoz-Navia, C. Winkler, R. Patel, M. Birke, F. O. Schumann, and J. Kirscher, *J. Phys.: Condens. Matter* **21**, 355003 (2009).
- [80] G. Dujardin, M. J. Besnard, L. Hellner, and Y. Malinovitch, *Phys. Rev. A* **35**, 5012 (1987).
- [81] J. Viehhaus et al., *Phys. Rev. Lett.* **77**, 3975 (1996).
- [82] F. U. Hillebrecht, A. Morozov, and J. Kirschner, *Phys. Rev. B* **71**, 125406 (2005).

-
- [83] O. Schwarzkopf, B. Krässig, J. Elmiger, and V. Schmidt, *Phys. Rev. Lett.* **70**, 3008 (1993).
- [84] K. A. Kouzakov and J. Berakdar, *Phys. Rev. Lett.* **91**, 257007 (2003).
- [85] B. D. Napitu and J. Berakdar, *Phys. Rev. B* **81**, 195108 (2010).
- [86] F. O. Schumann, N. Fominykh, C. Winkler, J. Kirschner, and J. Berakdar, *Phys. Rev. B* **77**, 235434 (2008).
- [87] W. Bothe and H. Geiger, *Zeitschrift für Physik A Hadrons and Nuclei* **32**, 639 (1925).
- [88] A. H. Compton, *Phys. Rev.* **21**, 483 (1923).
- [89] N. Bohr, H. A. Kramers, and J. C. Slater, *Zeitschrift für Physik A Hadrons and Nuclei* **24**, 69 (1924).
- [90] M. Hattass et al., *Phys. Rev. B* **77**, 165432 (2008).
- [91] J. Berakdar, *Phys. Rev. Lett.* **83**, 5150 (1999).
- [92] D. T. Pierce and F. Meier, *Phys. Rev. B* **13**, 5484 (1976).
- [93] J. Langer and S. Vosko, *Journal of Physics and Chemistry of Solids* **12**, 196 (1959).
- [94] H. Kondo, T. Kubota, H. Nakashima, T. Kawano, and S. Tanigawa, *J. Phys.: Condens. Matter* **4**, 4595 (1992).
- [95] P. J. Schultz and K. G. Lynn, *Rev. Mod. Phys.* **60**, 701 (1988).
- [96] P. G. Coleman, *Applied Surface Science* **194**, 264 (2002).
- [97] C. Duke, *Surf. Sci.* **299-300**, 24 (1994).
- [98] C. B. Duke, A. Paton, A. Lazarides, D. Vasumathi, and K. F. Canter, *Phys. Rev. B* **55**, 7181 (1997).
- [99] I. J. Rosenberg, A. H. Weiss, and K. F. Canter, *Phys. Rev. Lett.* **44**, 1139 (1980).
- [100] A. H. Weiss, I. J. Rosenberg, K. F. Canter, C. B. Duke, and A. Paton, *Phys. Rev. B* **27**, 867 (1983).
- [101] W. E. Frieze, D. W. Gidley, and K. G. Lynn, *Phys. Rev. B* **31**, 5628 (1985).
- [102] A. P. Mills and W. S. Crane, *Phys. Rev. B* **31**, 3988 (1985).
- [103] R. Feder, *Solid State Commun.* **34**, 541 (1980).
- [104] S. Y. Tong, *Surf. Sci.* **457**, L432 (2000).
- [105] C. Hugenschmidt, T. Brunner, S. Legl, J. Mayer, C. Piochacz, M. Stadlbauer, and K. Schreckenbach, *phys. stat. sol. (c)* **4**, 3947 (2007).
- [106] J. Berakdar, *Nucl. Instrum. Methods Phys. Res. B* **171**, 204 (2000).
- [107] F. Giebels, H. Gollisch, and R. Feder, *J. Phys.: Condens. Matter* **21**, 355002 (2009).
- [108] G. Ertl and J. Küppers, *Low Energy Electrons and Surface Chemistry*, VCH Verlag, 1985.
- [109] P. Auger, *Compt. Rend. (Paris)* **177**, 169 (1923).
- [110] P. Auger, *Surf. Sci.* **48**, 1 (1975).
- [111] E. Jensen, R. A. Bartynski, S. L. Hulbert, E. D. Johnson, and R. Garrett, *Phys. Rev. Lett.* **62**, 71 (1989).
- [112] S. Thurgate, *Surface and Interface Analysis* **20**, 627 (1993).
- [113] A. Liscio, R. Gotter, A. Ruocco, S. Iacobucci, A. G. Danese, R. A. Bartynski, and G. Stefani, *J. Electron. Spectrosc. Relat. Phenom.* **137-140**, 505 (2004).
- [114] T. Kakiuchi, E. Kobayashi, N. Okada, K. Oyamada, M. Okusawa, K. K. Okudaira, and K. Mase, *J. Electron. Spectrosc. Relat. Phenom.* **161**, 164 (2007).
- [115] R. Gotter, F. Da Pieve, A. Ruocco, F. Offi, G. Stefani, and R. A. Bartynski, *Phys. Rev. B* **72**, 235409 (2005).
- [116] W. S. M. Werner, W. Smekal, H. Störi, H. Winter, G. Stefani, A. Ruocco, F. Offi, R. Gotter, A. Morgante, and F. Tommasini, *Phys. Rev. Lett.* **94**, 038302 (2005).
- [117] A. L. Cavalieri, N. Müller, Th. Uphues, V. S. Yakovlev, A. Baltuska, B. Horvath, B. Schmidt, L. Blumel, R. Holzwarth, S. Hendel, M. Drescher, U. Kleineberg, P. M. Echenique, R. Kienberger, F. Krausz, and U. Heinzmann, **449**, 1029 (2007).
- [118] M. Schultze, M. Fiess, N. Karpowicz, J. Gagnon, M. Korbman, M. Hofstetter, S. Neppl, A. L. Cavalieri, Y. Komninos, Th. Mercouris, C. A. Nicolaides, R. Pazourek, S. Nagele, J. Feist, J. Burgdorfer, A. M. Azzeer, R. Ernstorfer, R. Kienberger, U. Kleineberg, E.

- Goulielmakis, F. Krausz, and V. S. Yakovlev, *Science* **328**, 1658 (2010).
- [119] M. Hentschel, R. Kienberger, C. Spielmann, G. A. Reider, N. Milosevic, T. Brabec, P. Corkum, U. Heinzmann, M. Drescher, and F. Krausz, *Nature* **414**, 509 (2001).

8. Original literature

The key results have been presented in the following publications which are attached:

- (i) F.O. Schumann, J. Kirschner, and J. Berakdar, *Mapping Out Electron-Electron Interactions at Surfaces*, Phys. Rev. Lett. **95**, 117601 (2005).
(Copyright (2005) by the American Physical Society.)
- (ii) F.O. Schumann, C. Winkler, G. Kerhervé, and J. Kirschner, *Mapping the electron correlation in two-electron photoemission*, Phys. Rev. B **73**, 041404(R), (2006).
(Copyright (2006) by the American Physical Society.)
- (iii) F.O. Schumann, C. Winkler, and J. Kirschner, *Correlation Effects in Two Electron Photoemission*, Phys. Rev. Lett. **98**, 257604 (2007). (Copyright (2007) by the American Physical Society.)
- (iv) F.O. Schumann, C. Winkler, and J. Kirschner, *Mapping out electron-electron interactions in angular space*, New J. Phys. **9**, 372 (2007).
(Copyright (2007) by the Institute of Physics.)
- (v) F.O. Schumann, N. Fominykh, C. Winkler, J. Kirschner, and J. Berakdar, *Electron pair emission from a Cu(111) surface upon photon absorption*, Phys. Rev. B **77**, 235434 (2008).
(Copyright (2008) by the American Physical Society.)
- (vi) G.A. van Riessen, F.O. Schumann, M. Birke, C. Winkler, and J. Kirschner, *Correlated positron-electron emission from surfaces*, J. Phys.: Condens. Matter **20**, 442001 (2008).
(Copyright (2008) by the Institute of Physics. Journal homepage iopscience.org/jpcm.)
- (vii) A preproduction version of the final manuscript: F.O. Schumann, C. Winkler, and J. Kirschner, *Sensing the electron-electron correlation in solids via double photoemission*, physica status solidi (b) **246**, 1483 (2009).
(Copyright Wiley-VCH Verlag GmbH & Co. KGaA. Reproduced with permission.)
- (viii) G.A. van Riessen, Z. Wei, R.S. Dhaka, C. Winkler, F.O. Schumann, and J. Kirschner, *Direct and core-resonant double photoemission from Cu(001)*, J. Phys.: Condens. Matter **22**, 092201 (2010).
(Copyright (2010) by the Institute of Physics. Journal homepage iopscience.org/jpcm.)
- (ix) F.O. Schumann, C. Winkler, J. Kirschner, F. Giebels, H. Gollisch, and R. Feder, *Spin-Resolved Mapping of Spin Contribution to Exchange-Correlation Holes*, Phys. Rev. Lett. **104**, 087602 (2010).
(Copyright (2010) by the American Physical Society.)

Mapping Out Electron-Electron Interactions at Surfaces

F. O. Schumann, J. Kirschner, and J. Berakdar

Max-Planck Institute of Microstructure Physics, Weinberg 2, 06120 Halle, Germany

(Received 19 January 2005; published 6 September 2005)

Using a high resolution coincidence technique, we measured for the first time the angular and energy correlation of an electron pair emitted from the valence band of a single crystal upon the impact of an electron with a specified momentum. We observe a hole in the measured two-particle correlation function when the two excited electrons have comparable momentum vectors, a fact traced back to exchange and repulsion among the electrons. We find the hole is not isotropic, has a finite extension, and is strongly suppressed when decoherence is operating.

DOI: [10.1103/PhysRevLett.95.117601](https://doi.org/10.1103/PhysRevLett.95.117601)

PACS numbers: 79.20.Kz, 68.49.Jk

A cubic centimeter of condensed matter contains, typically, 10^{23} electrons that repel one another and are attracted by a comparable number of positively charged nuclei. Displacing one electron elicits a disturbance in the whole system. So an adequate microscopic description of all the electrons appears a desperate undertaking. Surprisingly, this system of strongly interacting charged particles can be recast into a simpler one, composed of weakly or even noninteracting quasiparticles [1], while still capturing the basic physics of a variety of materials. In the condensed phase bare electrons are screened or dressed with a cloud of positive charge, and this composite object is called a quasiparticle [1–3]. If the Coulomb interactions among the valence electrons are not sufficiently screened, the quasiparticle concept is not viable and a number of electronic correlation-induced phenomena emerge. Prominent examples are high temperature superconductivity in cuprates [4] and the colossal magnetoresistance materials [5]. Thus, it is of a fundamental importance to develop a technique capable of exploring the details of the electron-electron interaction in a given sample. Present day experiments such as single photoelectron emission [6] and electron energy loss spectroscopy [7] trace the influence of electronic correlation as modifications and subsidiary structures superimposed on the single particle spectrum [8]. As pointed out by Wigner [9], in condensed matter the hallmark of the electron-electron Coulomb repulsion is a “hole” in the pair correlation function (the Coulomb or correlation hole) when the two electrons approach each other. Slater also indicated [10,11] that, due to Pauli’s principle, exchange effects result additionally in a reduced magnitude of the pair correlation function (the exchange or the Fermi hole) when the two electrons possess equal spin projections and equal momenta. This theoretical concept of the pair exchange and correlation is at the heart of past and current developments in quantum theories for describing and predicting reliably the behavior of matter [2,3,12–14]. Over the past 60 years numerous theoretical studies explored various aspects of the exchange-correlation (xc) hole in the condensed phase [15–21], yet an experimental realization remained beyond reach. To access information

on the electron-electron interaction, one focuses ideally on an electron pair in the system and monitors the probability of finding one electron in some region in momentum space while changing in a controlled manner the momentum vector of the second electron; i.e., one determines the momentum-space pair correlation function. An experimental technique capable of addressing these issues is the $(e, 2e)$ spectroscopy in reflection [22–25]. Here we report on a novel time-of-flight coincidence setup to investigate the electron pair correlation. As sketched in Fig. 1(a), a specimen is approached by an electron generated by a pulsed electron gun with an energy, E_0 , and momentum vector, \mathbf{k}_0 , which interacts with another electron residing in the valence band. The detected electron pair energies E_1, E_2 are deduced from their flight times. So the absolute values of $|\mathbf{k}_1|$ and $|\mathbf{k}_2|$ are determined. The impact position on the resistive anode determines the direction of \mathbf{k}_2 within a solid angle of ~ 1 sr except for the center, which is occupied by the central collector. It is exactly this feature that constitutes the major experimental advance. The small collector in turn fixes the direction of \mathbf{k}_1 . In this way we map out the energy and momentum dependence of the electron pair correlation. The experimental energy and momentum resolution are 0.5 eV and 0.1 \AA^{-1} , respectively. As inferred from Fig. 1(b), the energy, ϵ , and the wave vector, k , of the valence electron follow from the energy and wave vector conservations, e.g.,

$$\epsilon = E_0 - (E_1 + E_2) - W, \quad (1)$$

where W is the energy difference between the vacuum level and the highest occupied level with the energy $\hat{\mu}$ [cf. Fig. 1(b)]. We have chosen LiF as a sample for the following reasons. In addition to a higher coincidence rate compared to metals, the sample remains clean if kept at ~ 400 K. For LiF the energy W is ~ 14 eV which ensures a good separation between the elastic peak and electrons ejected from the valence band in the time-of-flight spectrum. In Eq. (1) E_0, E_1, E_2 are controllable experimentally and can be chosen such that only one valence band electron is emitted, as done in this work.

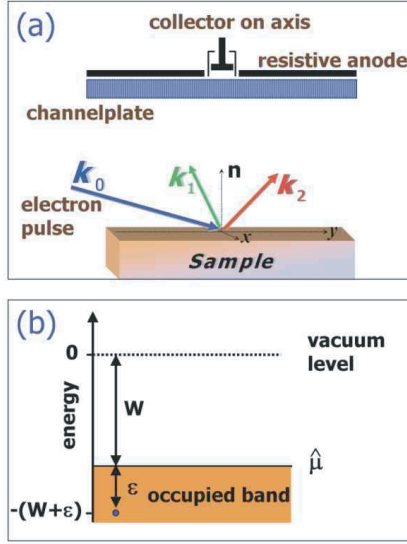


FIG. 1 (color). (a) An electron with momentum \mathbf{k}_0 interacts with another electron residing at the top of the valence band of the sample. Two excited electrons with momenta \mathbf{k}_1 , \mathbf{k}_2 and energies E_1 and E_2 are detected in coincidence by a resistive anode and central collector. (b) Energy position of the ejected valence band electron.

A quantity of key importance for the electronic correlation in an N particle system is the reduced (two-particle) density matrix, which is given in terms of the (exact) wave function Ψ as

$$\gamma_2(x_1, x_2, x'_1, x'_2) = N(N-1) \int \Psi(x_1, x_2, x_3, \dots, x_N) \times \Psi^*(x'_1, x'_2, x_3, \dots, x_N) dx_3 \cdots dx_N. \quad (2)$$

For fermions this equation dictates that $\gamma_2(x_1, x_2, x'_1, x'_2) = -\gamma_2(x_2, x_1, x'_1, x'_2)$. Here x_j , $j = 1, \dots, N$ stand for spin and position coordinates. The two-particle density derives from γ_2 as $\rho_2(x_1, x_2) = \gamma_2(x_1, x_2, x_1, x_2)$. Hence for fermions ρ_2 vanishes for $x_2 = x_1 = x$, i.e., $\rho_2(x, x) = 0$. On the other hand, for completely independent particles $\rho_2(x_1, x_2)$ is related to the single particle density $\rho(x)$ via $\rho_2(x_1, x_2) = \rho(x_1) \frac{N-1}{N} \rho(x_2)$. Thus, even for noninteracting (but overlapping) fermions the antisymmetry of Ψ implies a correlation among the particles that results in the existence of the (Fermi) hole in the two-particle density for $x_1 = x_2$. The Coulomb repulsion between the electrons results in additional contribution to the hole. Usually the hole is quantified by introducing the xc hole [2] $h_{xc}(x_1, x_2) = \frac{\rho_2(x_1, x_2)}{\rho(x_1)} - \rho(x_2)$ [26]. To unravel the relation of ρ_2 to the present experiment we note the following: The probability P_{if} for the transition depicted in Fig. 1 is given by [27] $P_{if} = S_{if} S_{if}^*$ where the S matrix elements are given

by $S_{if} = \langle \Psi_{E_f} | \Psi_{E_i} \rangle$ and Ψ_{E_i} (Ψ_{E_f}) is the normalized wave function describing the system in the initial (final) state with the appropriate boundary conditions. The initial state with energy E_i describes the incident electron interacting with an electron in the valence band in the presence of all other particles in the system. The final state with energy E_f describes the two electrons that escape the sample. Within a frozen-core picture, i.e., if we assume the surrounding medium is not affected while the incident and the valence band electron are interacting and during the emission of the two electrons, we can write $\Psi_{E_i} \approx \psi_{E_i}(x_1, x_2) \chi(x_3, \dots, x_N)$. ψ_{E_i} is the electron pair wave function in the initial state with the energy $E_i = E_0 - (\epsilon + W)$. The surrounding medium is described by χ . The reduced density matrix (2) attains then the form $\gamma_2(x_1, x_2, x'_1, x'_2) \approx 2\psi(x_1, x_2)\psi^*(x'_1, x'_2)$. Furthermore, assuming the emitted electron pair state ψ_{E_f} ($E_f = E_1 + E_2$) to be described by plane waves, we find for the measured, spin (σ_j) unresolved probability $P_{if} \propto \sum_{\sigma_1, \sigma_2, \sigma'_1, \sigma'_2} \tilde{\psi}_{E_i}(\sigma_1 \mathbf{k}_1, \sigma_2 \mathbf{k}_2) \tilde{\psi}_{E_i}^*(\sigma'_1 \mathbf{k}_1, \sigma'_2 \mathbf{k}_2)$, where $\tilde{\psi}_{E_i}$ is the double Fourier transform of ψ_{E_i} . Hence what is measured in our experiment is the spin-averaged diagonal elements of the reduced density matrix in momentum space, i.e., the spin-averaged momentum-space two-particle density ρ_2 . P_{if} possesses all aforementioned properties of ρ_2 ; in particular, P_{if} vanishes for $\mathbf{k}_1 = \mathbf{k}_2$. So we study correlation within the pair consisting of the approaching electron coupled to a valence band electron. The indistinguishability of these two electrons contributes to the xc hole through the exchange part.

We concentrate in the following on analyzing directly the measured (unnormalized) coincident probability $P_{if}(\mathbf{k}_1, \mathbf{k}_2)$, which we refer to by the intensity I . The relation between the initial-state correlation and the measured correlation features (in particular, the xc hole) is illustrated below: the pair correlation diminishes when slightly changing the initial state (by changing ϵ) while keeping the final state (i.e., $\mathbf{k}_1, \mathbf{k}_2$) unaltered. On the other hand, the spectra are hardly affected for the same initial state but different final state energy.

Figure 2 shows the energy correlation in the measured electron pair coincidence intensity, $I(E_1, E_2)$ with the direction of \mathbf{k}_1 fixed. Because of their low energies entailing a short escape depth, only the electrons from the first few atomic layers of the sample are involved [25,28]. Figure 2 reveals which electron energies are favored by the electron-electron interaction at surfaces. We recall that the electron-electron scattering in free space is governed by the form factor of the Coulomb potential that behaves as $|\mathbf{k}_1 - \mathbf{k}_2|^{-2}$. That is, when a swift electron interacts with another electron the most likely outcome is one fast and one slow electron so that $|\mathbf{k}_1 - \mathbf{k}_2|^{-2}$ is maximal. Figure 2 indicates, however, a much more complex energetic dependence of the electron-electron correlation function at surfaces; theory predicts that generally the behavior shown

in Fig. 2 is determined by the surface electronic and structural properties [29]. The pair correlation is mapped out as a function of the momentum of one electron (hitting the resistive anode). The momentum of the other electron is fixed because of the small central collector (marked by the black dot in Fig. 3). The existence of the exchange and correlation-induced hole is evidenced by Figs. 3(a) and 3(b). In free space the electron-pair correlation function is dominated by the factor $2\pi\alpha[\exp(2\pi\alpha) - 1]^{-1}$ [30], where $\alpha = 1/|\mathbf{k}_1 - \mathbf{k}_2|$. In a condensed medium the surrounding charges modify decisively the properties of the electron-electron interaction. While theory cannot provide yet a general expression for $I(E_1, E_2, \mathbf{k}_1, \mathbf{k}_2)$ the experimental findings in Figs. 3(a) and 3(b) reveal hole features that are qualitatively different from those known in the free-space or in atomic species [30]. Crystal symmetry and the direction of electron momenta determine the hole shape [31]. If the momentum vector of one electron lies in a crystal high symmetry plane the hole should possess the discrete crystal symmetry. In Fig. 3(a) we cannot clearly resolve the symmetry of the fourfold sample surface due to insufficient statistics. In Fig. 3(b) we break the alignment of electron momenta with the high symmetry planes upon a 20° rotation of the sample. As evidenced by Fig. 3(a) the hole is shifted so as to surround the fixed electron (black dot), meaning that this hole is, indeed, associated with the fixed electron. A further key issue is the range of the electron-electron interaction in a given sample which is determined by the size of the hole. In free space the bare electron-electron interaction is of an infinite range and hence $\lim_{|\mathbf{k}_1 - \mathbf{k}_2| \rightarrow \infty} I(E_1, E_2, \mathbf{k}_1, \mathbf{k}_2) \rightarrow 1/|\mathbf{k}_1 - \mathbf{k}_2|$. When the electron pair is immersed in an electron gas, the electron-electron interaction is screened and the xc hole shrinks. It is only for a diminishing hole (strong screening) that the material can be viewed convincingly as a collec-

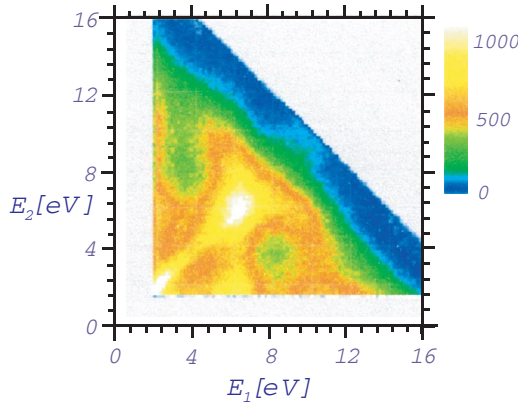


FIG. 2 (color). Energy-correlation intensity $I(E_1, E_2)$ (in arbitrary units) with the direction of \mathbf{k}_1 fixed. The incoming electron has an energy of 30.7 eV and the sample is a LiF(100) surface.

tion of independent quasiparticles [2]. Hence, the present technique may serve as a powerful tool to assess the validity of theory and to trigger new conceptual developments. In this context it is instructive to compare with the [vacuum ultraviolet (VUV)] photoemission spectroscopy (PES) [6] that has been used to study a variety of correlated materials. One can utilize Eq. (1) to study specific occupied energy states in the sample, as in PES. In contrast to VUV photons, electrons can transfer momentum and hence sample's electrons with certain energy, and the wave vector can be selected and, depending on the emitted electron energies our method can be highly surface sensitive. The energy scale at which the correlation between the selected sample electron and the test charge (incident electron) can be studied is set by $E_0 - (\epsilon + W)$, which has to be larger than W . A further key finding of the present experiments is that the electron-electron interaction, as manifested in the

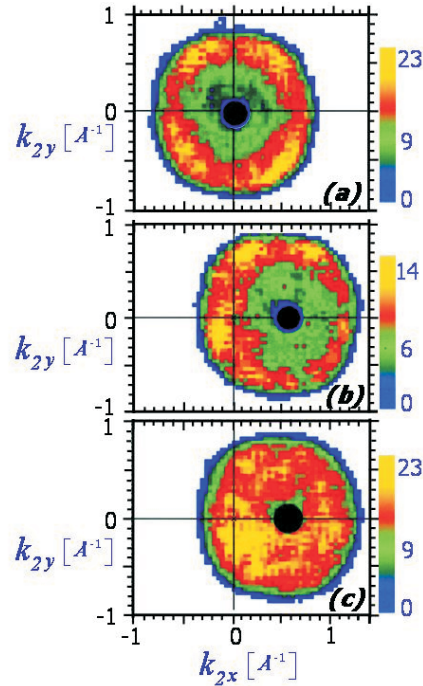


FIG. 3 (color). Intensity of the electron correlation function (in arbitrary units) versus the surface momentum components (k_{2x} and k_{2y}) of the electron with energy E_2 . The energies E_1 and E_2 are 8 and 9 eV, respectively. The black dot marks the regime where the central collector is. (a) The primary energy is 30.7 eV. (b) As in (a) but the sample has been rotated by 20° . (c) As in (b), however, the impact energy is increased to 33.7 eV, i.e., the valence electron stem not from top of the valence band but from an energy band with 3 eV width below. Thus, the electron pair may undergo inelastic scattering processes resulting in decoherence of the electron waves.

xc hole is fragile to decoherence effects. To our knowledge this issue is still largely unexplored theoretically in the present context. Decoherence sets in when the correlated electron pair scatters inelastically from other surrounding electrons. We can switch off and on such mechanisms by tuning appropriately the electron energies: If E_0 , E_1 , and E_2 are such that the valence electron resides at the highest occupied level $\hat{\mu}$, i.e., if $\epsilon = 0$ [cf. Fig. 1(b)] the electron pair does not inelastically scatter from other particles, for such a scattering entails an energy loss of the electron pair and hence a violation of the energy conservation in Eq. (1). Electron wave coherence is not affected by elastic scattering. On the other hand, as inferred from Fig. 1(b), keeping the electron pair energies E_1 and E_2 fixed and increasing E_0 we access, in addition to the state with the energy $\epsilon = E_0 - (E_1 + E_2) - W$, a band of occupied electronic states lying between $\hat{\mu}$ and ϵ . An electron pair originating from this band has in the solid the excess energy $E_1 + E_2 + \delta$. Because of inelastic scattering from the occupied levels above ϵ , the electron pair loses the energy δ and arrives at the detector with the energies E_1 and E_2 . These scattering events, whose amount can be tuned by changing δ , randomize the phase of the electron waves and eventually lead to a loss of correlation within the pair. This situation is illustrated in Fig. 3(c) for which the energies E_1, E_2 are kept fixed to be the same as in Fig. 3(a). When the primary energy E_0 is increased by $\delta = 3$ eV, the decoherence channel opens, and a complete loss of correlation within the pair is observed. Consequently, the xc hole diminishes; i.e., two incoherent electrons approach each other much closer than in situations where decoherence is suppressed and the correlation hole is fully developed [cf. Fig. 3(a)]. This finding is of key importance for the potential use of correlated electron pairs in solids for quantum information processing, as discussed in Ref. [32], for such applications require coherence within the pair. We find in this study that coherent electron pairs are only those that have the energy $E_0 - W$, i.e., where one electron originates from the valence band maximum. A realistic theoretical description of the presented experimental results, especially including the issue of decoherence is currently beyond the capabilities of existing theories. It is, however, evident that the present novel technique can serve as a probe for the nature of the electron-electron interaction in modern materials, in particular, as many of those, such as high temperature superconductors, are strongly influenced by the correlated motion of the electrons. A future implementation of a spin-polarized electron will allow the study of spin correlation of magnetic surfaces. In particular, as the electron pair interaction in metals is screened on the scale of few lattice constants the present technique holds the promise of providing information on the short-range order of the spin projections.

[1] L.D. Landau, Sov. Phys. JETP 3, 920 (1957).

- [2] P. Fulde, *Electron Correlations in Molecules and Solids*, Springer Series in Solid State Sciences Vol. 100 (Springer, Berlin, 1993).
- [3] G.D. Mahan, *Many-Particle Physics* (Plenum, New York, 2000), 3rd ed.
- [4] R.W. Hill, C. Proust, L. Taillefer, P. Fournier, and R.L. Greene, *Nature (London)* **414**, 711 (2001).
- [5] M. Uehara, S. Mori, C.H. Chen, and S.W. Cheong, *Nature (London)* **399**, 560 (1999).
- [6] *Solid-State Photoemission and Related Methods: Theory and Experiment*, edited by W. Schattke and M.A. van Hove (Wiley-VCH, Weinheim, 2003).
- [7] H. Ibach and D.L. Mills, *Electron Energy Loss Spectroscopy and Surface Vibrations* (Academic Press, New York, 1982).
- [8] R. Neudert *et al.*, *Phys. Rev. Lett.* **81**, 657 (1998).
- [9] E. Wigner, *Trans. Faraday Soc.* **34**, 678 (1938).
- [10] J.C. Slater, *Introduction to Chemical Physics* (McGraw-Hill, New York, 1939).
- [11] J.C. Slater, *Phys. Rev.* **81**, 385 (1951).
- [12] R.G. Parr and W. Yang, *Density Functional Theory of Atoms and Molecules* (Oxford University Press, New York, 1989).
- [13] A. Gonis *et al.*, *Phys. Rev. Lett.* **77**, 2981 (1996).
- [14] P. Ziesche, *Int. J. Quantum Chem.* **60**, 1361 (1996); *Phys. Lett. A* **195**, 213 (1994).
- [15] M. Nekovee, W.M.C. Foulkes, and R.J. Needs, *Phys. Rev. Lett.* **87**, 036401 (2001).
- [16] J.P. Perdew, K. Burke, and Y. Wang, *Phys. Rev. B* **54**, 16533 (1996).
- [17] P.H. Acioli and D.M. Ceperley, *Phys. Rev. B* **54**, 17199 (1996).
- [18] W.E. Pickett and J.Q. Broughton, *Phys. Rev. B* **48**, 14859 (1993).
- [19] J.P. Perdew *et al.*, *Phys. Rev. B* **46**, 6671 (1992).
- [20] J.E. Inglesfield and J.D. Moore, *Solid State Commun.* **26**, 867 (1978).
- [21] O. Gunnarsson and B.I. Lundqvist, *Phys. Rev. B* **13**, 4274 (1976).
- [22] J. Kirschner, O.M. Artamonov, and S.N. Samarin, *Phys. Rev. Lett.* **75**, 2424 (1995).
- [23] S. Iacobucci, L. Marassi, R. Camilloni, S. Nannarone, and G. Stefani, *Phys. Rev. B* **51**, R10252 (1995).
- [24] S.N. Samarin *et al.*, *Rev. Sci. Instrum.* **74**, 1274 (2003).
- [25] A. Morozov, J. Berakdar, S.N. Samarin, F.U. Hillebrecht, and J. Kirschner, *Phys. Rev. B* **65**, 104425 (2002).
- [26] The pair correlation function g is defined as $g(x_1, x_2) = h_{xc}(x_1, x_2)/\rho(x_2) + 1 = \rho_2(x_1, x_2)/[\rho(x_1)\rho(x_2)]$.
- [27] J. Berakdar, *Concepts of Highly Excited Electronic Systems* (Wiley-VCH, Weinheim, 2003), p. 189.
- [28] A. Liscio *et al.*, *J. Electron Spectrosc. Relat. Phenom.* **137-40**, 505 (2004).
- [29] J. Berakdar, H. Gollisch, and R. Feder, *Solid State Commun.* **112**, 587 (1999).
- [30] H.A. Bethe and E. Salpeter, *Quantum Mechanics of One- and Two-Electron Atoms* (Plenum, New York, 1977).
- [31] N. Fominykh, J. Berakdar, J. Henk, and P. Bruno, *Phys. Rev. Lett.* **89**, 086402 (2002).
- [32] D.S. Saraga, B.L. Altshuler, D. Loss, and R.M. Westervelt, *Phys. Rev. Lett.* **92**, 246803 (2004).

Mapping the electron correlation in two-electron photoemission

F. O. Schumann, C. Winkler, G. Kerhervé, and J. Kirschner

Max-Planck Institut für Mikrostrukturphysik, Weinberg 2, 06120 Halle, Germany

(Received 2 November 2005; revised manuscript received 23 December 2005; published 26 January 2006)

Electronic correlations are manifested in many-body effects like superconductivity and magnetism. Established theoretical concepts show that the Coulomb and exchange interaction result in a tendency of two electrons to avoid each other, leading to an exchange-correlation (xc) hole. We will report on double photoemission (DPE) experiments using a time-of-flight setup consisting of a small central collector surrounded by a resistive anode. The first allows detection only within a narrow solid angle, therefore fixing the momentum. The resistive anode covers a solid angle of ~ 1 sr, the determination of the impact position results in momentum resolution. As a pulsed light source we used synchrotron radiation and we studied a NaCl(100) surface upon excitation with 34 eV photons. The very existence of coincidences is already a manifestation of the correlation. The onset of pair emission occurs when energy conservation allows the ejection of two electrons from the highest occupied level. We have made two key observations. If E_1 and E_2 are fixed such that a pair emission from the top of the valence band is possible, a zone of reduced intensity with a diameter of $\sim 1.1 \text{ \AA}^{-1}$ is visible. Recent calculations on DPE from a Cu(100) surface display exactly such a feature due to the xc hole. Hence we prove experimentally the very existence of the xc hole in double photoemission. The zone of reduced intensity disappears whenever emission below the top of the valence band becomes possible, indicating the sensitivity of the xc hole to inelastic scattering.

DOI: [10.1103/PhysRevB.73.041404](https://doi.org/10.1103/PhysRevB.73.041404)

PACS number(s): 79.60.Bm

I. INTRODUCTION

Electrons in solids constitute a strongly interacting system and the description via independent particles ought to fail. However, Landau introduced the concept of quasiparticles.¹ It is in essence a transformation of the strongly interacting electron system to weakly interacting particles (quasiparticles) that still carry the spin and charge of an electron, albeit a renormalized mass. This concept may be understood in the context of screening. Intuitively it is clear that two electrons tend to avoid each other. First, the Coulomb interaction makes it energetically unfavorable for electrons to be close to each other. Second, the Pauli principle demands that electrons with parallel spin cannot be at the same location. Averaging over both spin directions still gives a reduced probability of finding two electrons at the same location. A more elaborate theoretical treatment for solids confirms this picture, and a pair correlation $\mathbf{g}(\mathbf{r}, \mathbf{r}')$ function can be introduced.² This function describes the probability to find an electron at coordinates \mathbf{r} when a second is located at \mathbf{r}' . The key result is that \mathbf{g} is essentially constant (usually normalized to 1) except for small distances $|\mathbf{r} - \mathbf{r}'| < \text{a few } \text{\AA}$ where \mathbf{g} adopts smaller values. The spatial extent of this region is called the exchange-correlation (xc) hole and describes the length scale over which the correlation between electrons is relevant. This result can be rephrased by saying that each selected electron is surrounded by a positive charge exactly compensating for the electrons' charge. This feature is reminiscent of the screening of the Coulomb potential in solids. Hence, if the average distance between electrons is larger than the diameter of the xc hole they can be regarded as noninteracting particles and the description using independent-particle theories is appropriate.

Despite the fundamental importance of the concept of the xc hole, not much is known experimentally about the size

and material dependence of the xc hole. A technique capable of studying the correlation between electron pairs is electron coincidence spectroscopy, where the excitation is due to electrons or photons [either termed $(e, 2e)$ or $(\gamma, 2e)$].³⁻⁷ In fact, a recent publication theorized that k mapping of the double photoelectron emission (DPE) intensity opens an avenue of imaging the xc hole.⁸ We will discuss our results obtained by DPE on a NaCl(100) surface that prove the existence of the xc hole and provide experimental determination of its spatial extent.

II. EXPERIMENT

Our experiments were conducted under UHV conditions featuring a time-of-flight spectrometer depicted in Fig. 1. The sample was a NaCl(100) surface that was kept at a temperature of $\sim 100^\circ \text{C}$. This temperature is sufficient to prevent charging up of the sample as evidenced by single electron spectra. The incident light hits the sample with an angle $\sim 80^\circ$ with respect to the surface normal. As a pulsed light source the BESSY II storage ring operating in the single bunch mode was employed, and the photon energy was fixed to 34 eV. In order to detect an electron pair, two detectors are required. A central collector accepts electrons only within a solid angle of ~ 0.02 sr, the detected electron we may term as the "fixed electron." A resistive anode⁹ serves as the second detector which allows for a spatial resolution of the impact position.¹⁰ Electrons within a solid angle of ~ 1 sr are registered, and we term them "free electrons". It is exactly this feature that constitutes the major experimental advance. The time differences between a photonbunch marker signal from the synchrotron and the fast-timing signals from the detectors were determined via time-to-amplitude converters in a coincidence circuit. With knowledge of the flight times

SCHUMANN *et al.*

PHYSICAL REVIEW B 73, 041404(R) (2006)

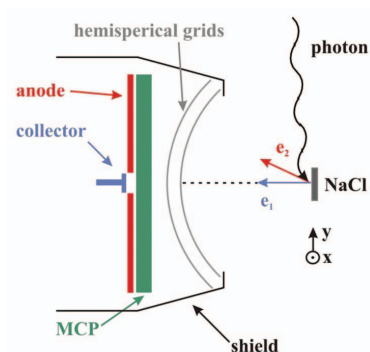


FIG. 1. (Color) Electron pair detection technique. Two electrons with momenta $\mathbf{k}_1, \mathbf{k}_2$ and energies E_1 and E_2 are detected in coincidence by a resistive anode and central collector.

of an electron pair the energies E_1, E_2 can be calculated. The total time resolution achieved in both channels was about 1 ns, while the energy resolution of the detected electrons depends on the particular energy value. For the electron energies discussed here the energy resolution amounts to ~ 0.5 eV. The impact position on the resistive anode determines the direction of \mathbf{k}_1 within a solid angle of ~ 1 sr except for the center, which is occupied by the central collector. The small collector in turn fixes the direction of \mathbf{k}_2 . In this way we map out the energy and momentum dependence of the electron pair correlation. The experimental momentum resolution is 0.1 \AA^{-1} . For all experiments the sample normal was pointing towards the central collector. This means that electrons reaching the central collector have an in-plane momentum of $|k_{\parallel}| < 0.1 \text{ \AA}^{-1}$. The low coincidence count rate required a data acquisition time of 10 days.

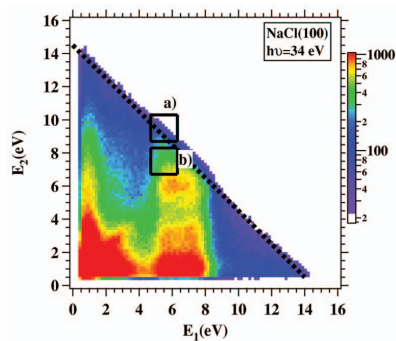


FIG. 2. (Color) The 2D energy distribution of coincidence electron pairs from a NaCl(100) surface is plotted. The photon energy was 34 eV. The energy E_1 (E_2) refers to the fixed electron (free electron). The dashed diagonal line marks the onset of pair emission, which occurs for a sum energy of ~ 14.6 eV. The square boxes labeled (a) and (b) indicate the events used to generate the 2-D momentum plots displayed in Fig. 3.

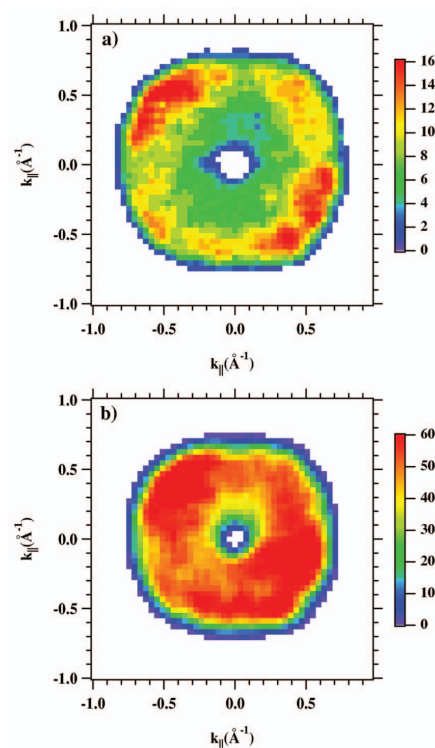


FIG. 3. (Color) The 2D in-plane momentum distribution for two different energy pairs from a NaCl(100) surface. In panel (a) we have selected $E_1=5.5$ eV and $E_2=9.5$ eV, whereas in panel (b) we have chosen $E_1=5.5$ eV and $E_2=7.5$ eV, respectively.

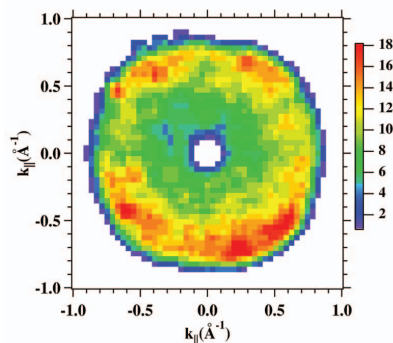


FIG. 4. (Color) The 2D in-plane momentum distribution as in Fig. 3 but for a LiF(100) surface excited with 30.7 eV electrons. The energies are $E_1=7.5$ eV and $E_2=9.5$ eV, respectively.

III. RESULTS

In Fig. 2 we plotted the 2D energy distribution of coincidence of electron pairs upon excitation with 34 eV photons. The energy of the fixed electron is labeled E_1 whereas that of the free electron is labeled E_2 . We observe the onset of DPE when the sum energy $E_1 + E_2$ equals ~ 14.6 eV. This is indicated by the dashed diagonal line in Fig. 2. This can be easily understood when considering the known binding energies of NaCl as determined by photoemission.¹¹ Wertheim *et al.* found that the highest occupied level (Cl 3p band) has a binding energy of $E_B = 9.66$ eV with respect to the vacuum level.¹¹ Since for DPE two electrons leave the solid, this energy needs to be accounted for twice and subtracting this value from the photon energy yields the maximum kinetic sum energy

$$E_1 + E_2 = h\nu - 2E_B. \quad (1)$$

The numerical result is 14.68 eV and is in agreement with our observation. The very existence of a DPE intensity already implies the existence of correlation within the electron pair. This is a key result of a recent calculation by Berakdar.¹² The two-dimensional (2D) energy distribution shows a preferred emission of the fixed electron with energies of 6–8 eV, which is not present for the free electron.

More insight can be obtained if we take advantage of the lateral resolution of the setup. As a first step we select only those coincidences for which the energies E_1 and E_2 are fixed. In other words, we pick a point in the 2D energy distribution shown in Fig. 2. In order to obtain sufficient statistics we actually select an energy window of ± 0.8 eV around the respective energies. This has been indicated by the square boxes in Fig. 2 labeled (a) and (b). We can now proceed and plot the coincidence intensity as a function of the in-plane momentum k_{\parallel} of the free electron. We have selected two different regimes within the 2D energy distribution highlighted in Fig. 2 by the black squares. In case (a) we are right at the onset of pair emission. Case (b) describes the situation if emission below the highest occupied level is possible. In Fig. 3 we display the resulting momentum distributions. We would like to point out that all momentum plots display a zero intensity at a position where the central collector is positioned. The position and size of this blind spot depend on the momentum of the free electron. For the plots shown in Fig. 3 this blind spot is centered at $k_{\parallel} = 0$ and has a radius of $\sim 0.1 \text{ \AA}^{-1}$. In Fig. 3(a) the energies are $E_1 = 5.5$ eV and $E_2 = 9.5$ eV [region (a) in Fig. 2]. We clearly observe that the region $k_{\parallel} = 0$ (outside the blind spot) is surrounded by a region of diminished intensity. The intensity increases for larger k_{\parallel} values and reaches a maximum for $k_{\parallel} \sim 0.55 \text{ \AA}^{-1}$ and then falls off rapidly towards the edge of the channelplate. A dramatically different situation is depicted in Fig. 3(b) where we select $E_1 = 5.5$ eV and $E_2 = 7.5$ eV. Now the ring of enhanced intensity is essentially gone. Energetically the sum energy $E_1 + E_2$ has been reduced from 15 eV to 13 eV. This energy difference allows for emission of a deeper-laying valence band electron or inelastic scattering losses if the electrons originate from the top of the valence band. Our results demonstrate the importance of in-

elastic scattering, which is very effective in destroying the hole shown in Fig. 3(a).

We may summarize our observations as follows: (i) If we select the energies E_1 and E_2 such that the sum energy $E_1 + E_2$ has the largest possible value for pair emissions the 2D momentum plots display a region of reduced intensity that is centered around the fixed electron. (ii) If the sum energy is below the maximum value, a more or less uniform momentum distribution is the result.

IV. DISCUSSION

As we stated in the introduction, we expect each electron to be surrounded by an xc hole. It can be easily shown within the dipole approximation that a product of a single particle wave function yields a zero DPE intensity. However, due to the correlation/interaction such a product of wave functions is not correct and a nonzero DPE intensity results when going beyond the single-particle picture.¹² Therefore we can explain the momentum distribution in Fig. 3(a) as a consequence of the xc hole.

Such a notion is corroborated by the more thorough calculation by Fominykh *et al.* on the double photoemission of Cu(100).⁸ They computed the in-plane momentum distribution (of the free electron) similarly to the plots shown in Fig. 3 for a photon energy of 42 eV and found that it exhibits a reduced intensity until k_{\parallel} adopts a value of $\sim 1.4 \text{ \AA}^{-1}$. At this point the intensity rises sharply by roughly an order of magnitude. Shortly thereafter the intensity quickly returns to a small value. The ring of enhanced intensity has a diameter of 2.8 \AA^{-1} and a width of $\sim 0.2 \text{ \AA}^{-1}$. The important outcome of the theoretical work is that the reduced intensity is a manifestation of the xc hole. Further, it was found that the DPE intensity also displayed the crystallographic symmetry of the surface. For NaCl we find the diameter of the reduced intensity region to be $\sim 1.1 \text{ \AA}^{-1}$ if the energy of the free electron is 9.5 eV, and this diameter is significantly smaller than the theoretical value for Cu. Whether this difference is due to a comparison between different materials (noble metal versus insulator) is not clear. In that case we may take this as a hint of a material dependence. We emphasize that the size of the xc hole has been determined from the diameter of the maximum-intensity ring, which is near the edge of the detector, hence it is possible that the ring is even larger. This view is supported by the observation that the diameter increases with the increasing energy E_2 of the free electron (from 0.9 to 1.3 \AA^{-1} for 7.5 to 13 eV) because the covered momentum space of the detector becomes larger. According to theory the xc hole shrinks if E_2 is increased.⁸ Nevertheless, our key observation of a region of reduced intensity due to the xc hole remains valid and we quote the value for $E_2 = 9.5$ eV. In this context we would like to point out that we have performed a similar series of experiments on a LiF(100) surface, albeit excited by a primary electron gun.¹³ As an example of the resulting momentum distributions we display in Fig. 4 the situation for a primary energy of 30.7 eV. The energies E_1 and E_2 are 7.5 eV and 9.5 eV, respectively. With this selection the sum energy has the highest possible value and only pair emission without any inelastic scattering of the pair

is possible. Further, we have chosen the same value of E_2 as that used in Fig. 3(a) in order to facilitate direct comparison. We immediately notice that there is no qualitative difference between Figs. 3(a) and 4. The study on LiF also showed that inelastic scattering destroys the region of reduced intensity similar to the plot in Fig. 3(b). Although two different materials have been studied (NaCl versus LiF) their electronic properties are very similar. Hence, we conclude that DPE [or $(\gamma, 2e)$] and $(e, 2e)$ experiments give qualitatively similar results despite the fact that the underlying mechanisms bear some significant differences. This point deserves further comment. The calculation of Fominykh *et al.*⁸ did include only those contributions to the intensity where two electrons are ejected simultaneously upon absorption of a single photon. Energetically single photoemission is also possible whereby the excited electron may be regarded as a primary electron of an internal $(e, 2e)$ process. Experimentally we cannot discriminate between these two channels. The question arises what fraction these individual contributions make to the total DPE intensity. A hint is given by another theoretical study of Fominykh *et al.*¹⁴ There they calculated the DPE intensity for Cu(100) and Ni(100) surfaces as a function of E_1-E_2 while keeping the sum energy E_1+E_2 constant at the highest value possible (pair emission from E_F). They showed that for Cu(100) the internal $(e, 2e)$ process is much less efficient compared to that for the Ni(100) surface, due to the higher density of states (DOS) at E_F for Ni.⁸ From this study we learn that the contribution of the internal $(e, 2e)$ process does depend on the system. As far as NaCl and LiF

are concerned, we are not aware of a theoretical study dealing with this aspect and hence we cannot comment on the significance of this contribution to the total DPE intensity. Nevertheless we conclude from our work that we have mapped the xc hole via DPE. In contrast to theory we were not able to resolve the crystallographic symmetry, which may be due to insufficient statistics. An aspect not treated theoretically so far is the sensitivity of the xc hole on inelastic scattering, which is very effective in suppressing the emergence of the xc hole as this study shows.

V. SUMMARY

We have shown that with momentum mapping of the DPE intensity imaging of the xc hole is possible. We have determined the diameter of the xc hole to be $\sim 1.1 \text{ \AA}^{-1}$ (for $E_2 = 9.5 \text{ eV}$) for a NaCl(100) surface. Qualitatively similar results can be achieved if a pulsed electron gun is used. A larger angular acceptance would ultimately allow us to study the material dependence of the xc hole. In order to disentangle the exchange from the Coulomb part, experiments on ferromagnetic surfaces with photons of different helicities appear to be promising.

ACKNOWLEDGMENT

We thank the staff of the BESSY II storage ring for the excellent support.

¹L. D. Landau, *Sov. Phys. JETP* **3**, 920 (1957).

²P. Fulde, *Electron Correlations in Molecules and Solids*, Springer Series in Solid State Sciences Vol. 100 (Springer, Berlin, 1993).

³H. W. Biester, M. J. Besnard, G. Dujardin, L. Hellner, and E. E. Koch, *Phys. Rev. Lett.* **59**, 1277 (1987).

⁴J. Kirschner, O. M. Artamonov, and S. N. Samarin, *Phys. Rev. Lett.* **75**, 2424 (1995).

⁵S. Iacobucci, L. Marassi, R. Camilloni, S. Nannarone, and G. Stefani, *Phys. Rev. B* **51**, R10252 (1995).

⁶A. Morozov, J. Berakdar, S. N. Samarin, F. U. Hillebrecht, and J. Kirschner, *Phys. Rev. B* **65**, 104425 (2002).

⁷R. Herrmann, S. Samarin, H. Schwabe, and J. Kirschner, *Phys. Rev. Lett.* **81**, 2148 (1998).

⁸N. Fominykh, J. Berakdar, J. Henk, and P. Bruno, *Phys. Rev. Lett.*

89, 086402 (2002).

⁹Quantar Technology Incorporated, Model 3300 SERIES MCP.

¹⁰S. N. Samarin, O. M. Artamonov, D. K. Waterhouse, J. Kirschner, A. Morozov, and J. F. Williams, *Rev. Sci. Instrum.* **74**, 1274 (2003).

¹¹G. K. Wertheim, J. E. Rowe, D. N. E. Buchanan, and P. H. Citrin, *Phys. Rev. B* **51**, 13675 (1995).

¹²J. Berakdar, *Phys. Rev. B* **58**, 9808 (1998).

¹³F. O. Schumann, J. Kirschner, and J. Berakdar, *Phys. Rev. Lett.* **95**, 117601 (2005).

¹⁴N. Fominykh, J. Berakdar, J. Henk, S. Samarin, A. Morozov, F. U. Hillebrecht, J. Kirschner, and P. Bruno, *Solid-State Photoemission and Related Methods* (Wiley-VCH, Weinheim, 2003)

Correlation Effects in Two Electron Photoemission

F. O. Schumann, C. Winkler, and J. Kirschner

Max-Planck Institute of Microstructure Physics, Weinberg 2, 06120 Halle, Germany

(Received 26 March 2007; published 22 June 2007)

Many-body effects in solids are ultimately related to the correlation among electrons, which can be probed by double photoelectron emission. We have investigated the electron pair emission from a Cu(111) surface upon photon absorption. We are able to observe for the first time the full extension and shape of a depletion zone around the fixed emission direction of one electron. It has an angular extension of ~ 1.2 rad, which is independent of the electron energy.

DOI: 10.1103/PhysRevLett.98.257604

PACS numbers: 79.60.-i, 73.20.At

Photoemission has become an indispensable tool to study the electronic properties of solids. Peaks in the angle-resolved energy distributions are usually associated with effective single-particle energies, which can be compared with band structure calculations. High-resolution photoemission has been able to discover effects of the electron-electron interaction or coupling to other degrees of freedom (e.g., phonons and spin waves). These show up as so-called kinks in the dispersion $E(k)$ curve [1]. A different and more direct approach to study the electron-electron interaction in solids is possible via double photoemission (DPE), which is the absorption of a single photon followed by the simultaneous emission of an electron pair. Within the dipole approximation, a noninteracting electron system has a vanishing DPE intensity; therefore, a finite DPE intensity requires a finite electron-electron interaction [2]. The mutual influence of the electron motion is the consequence of the Pauli principle and the Coulomb interaction. In fact, electrons tend to stay away from each other, thereby creating a zone of reduced electronic charge around each electron. This constitutes the concept of the exchange-correlation (XC) hole [3,4]. It is important to note that the XC hole also exists in momentum space [5]. The mutual influence among electrons is ultimately responsible for many-body effects such as magnetism, superconductivity, heavy fermions, etc. These “highly correlated” systems are the focus of intense research activities. The possibility to probe the XC hole via DPE exists, as a theoretical treatment for a Cu(100) surface showed [6]. This is beyond the capabilities of single photoemission. The experimental possibility to detect a finite DPE intensity from solids has been demonstrated previously [7–11]. In this Letter, we show for the first time that the technique of DPE has reached a status which allows the complete mapping of the XC hole. This is of fundamental interest for solid state theory; e.g., the XC hole is an integral part of the local density approximation, which is a widely used and a very successful description for solids [12]. We have studied a Cu(111) surface and found that the XC hole can be probed experimentally. It manifests itself as a depletion zone in the angular distribution of the intensity. More precisely, the emission direction of one electron is sur-

rounded by a reduced intensity of the other electron. The size in angular space is ~ 1.2 rad and independent of the kinetic energy of the electrons. We have therefore proven that the concept of the XC hole is an experimental reality.

Our experiment consists of 3 channel plate detectors; see Fig. 1. These ensure a large angular acceptance, which is in the drawing plane ± 1.57 rad; perpendicular to it, ± 0.4 rad is available. Delay line anodes allow the determination of the impact positions of electrons even if two electrons hit the same detector. These events we term as “double hits,” whereas we refer to “single hits” if the electrons are registered on different detectors. A pulsed photon source was provided by the synchrotron radiation facility in Berlin (BESSY II) operating in the single bunch mode; we used beam line TGM 4. The time period between light pulses is 800 ns, while the flight times for 5 and 20 eV electrons are 72 and 36 ns, respectively. The photon energy was set to 50 ± 0.2 eV. The propagation direction of the linear polarized light has an angle of 32° with respect to the surface normal. The polarization plane is in the drawing plane; see Fig. 1. The electron energies are determined via the flight times, where the time reference comes from the BESSY bunch marker. A coincidence circuit ensures that only electron pairs are detected. The ratio between true and

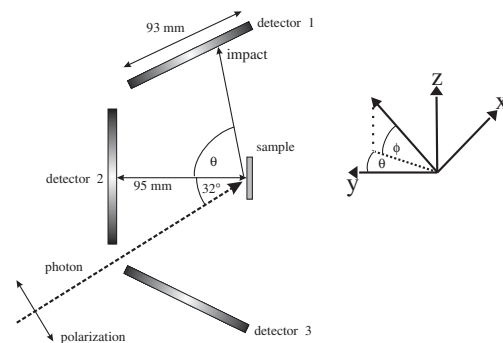


FIG. 1. Sketch of the experimental apparatus.

random coincidences is ≈ 1 . The single count rate is about a factor of 500 higher than the coincidence count rate. The spectrometer is part of an ultrahigh vacuum system equipped with standard surface science tools. The impact positions are characterized by two angles measured with respect to the surface normal. The angle Θ is in the drawing plane of Fig. 1, while Φ is perpendicular to the drawing plane. Each coincident event is then characterized by 6 coordinates, namely, the individual energies and the pair of angles Θ and Φ . The total time resolution is approximately 1.4 ns. This will lead to an energy-dependent energy resolution, which is 1.5 eV for 20 eV electrons. We studied a clean and well-ordered Cu(111) surface, which was prepared via Ar sputtering and annealing up to 800 K. The experiments were performed at room temperature. The crystallographic $[\bar{2}11]$ axis is in the drawing plane of Fig. 1 and was fixed throughout the experiment.

In the case of double hits, a meaningful label is to term one electron “fast” and the other “slow” with the energies E_{fast} and E_{slow} , respectively. This implies that $E_{\text{fast}} > E_{\text{slow}}$; consequently we have to label single hits in the same fashion.

We display the resulting 2D energy distribution containing both contributions in Fig. 2. The bar on the panel defines the color code for the intensity, which is given in counts. Further, we added equidistant contours to the plot [13]. The onset of the DPE intensity occurs for a sum energy $E_{\text{sum}} = E_{\text{fast}} + E_{\text{slow}} \approx 40$ eV, which amounts to the photon energy minus twice the work function (≈ 5 eV). If E_{sum} decreases from the maximum value, we note a steady increase of the intensity. For $E_{\text{fast}} > 20$ eV, most of the coincidence intensity is found for $E_{\text{slow}} < 10$ eV. In other words, there is a preference of one electron being fast while the other is slow in this energy regime.

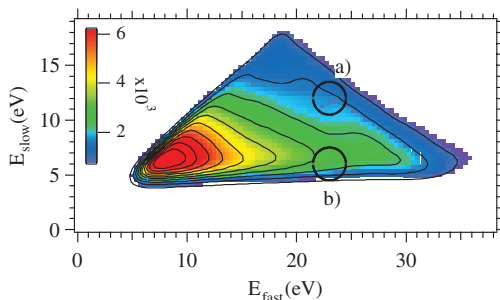


FIG. 2 (color). 2D energy distribution of the DPE intensity from a Cu(111) surface; the photon energy is 50 eV. One electron is termed fast, whereas the other is called slow, with energies $E_{\text{fast}} > E_{\text{slow}}$. The two circles with radius 1.5 eV indicate energy regions centered at $E_{\text{fast}} = 23$ eV ($E_{\text{slow}} = 12$ eV) and $E_{\text{fast}} = 23$ eV ($E_{\text{slow}} = 6$ eV). Coincident events within these windows are used for angular distributions of the coincidence intensity.

Individual 2D energy plots including only either single or double hits reveal that this is due to the contribution of double hits. Since those hits occur on the same detector, we know that the trajectories of these electrons must include smaller angles compared to single hits. This aspect will become important later on. The ratio of single to double hits is ≈ 6 . A 2D angular presentation of our data requires the execution of several steps. First, we select values for E_{fast} and E_{slow} , respectively. In order to select enough coincidence events, we allow an uncertainty in the energy of ± 1.5 eV. This has been indicated by the circles drawn in Fig. 2. Now we can derive the angular distributions of the fast and slow electrons. These are not independent of each other, since electron pairs are detected. We emphasize that every fast electron has a slow counterpart. As an example, we show in Fig. 3 the angular distributions for fast and slow electrons centered at $E_{\text{fast}} = 23$ eV and $E_{\text{slow}} = 12$ eV [region (a) in Fig. 2]. Both distributions display the highest intensity if the electrons leave the sample along the surface normal. The intensity drops for increasing values of $|\Theta|$. The above energy selection for E_{fast} and E_{slow} focuses on the emission from the 3D states. Contributions from the Shockley surface state were too weak to be identified in our

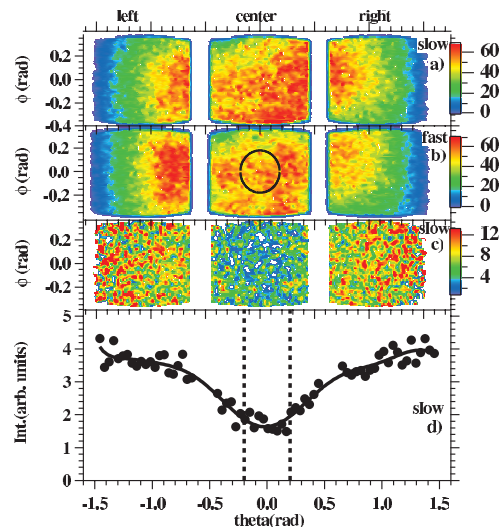


FIG. 3 (color). Angular distributions with $E_{\text{fast}} = 23$ eV and $E_{\text{slow}} = 12$ eV are displayed. (a) shows the 2D angular intensity for the slow electron, whereas in (b) the same for the fast electron is plotted. In (c), we plot the intensity for the slow electron if the fast electron is constrained to be within the area defined by the black circle of the center detector 2 in (b). From (c), a line scan can be computed, which is plotted in (d). The solid line is a guide to the eye, whereas the dashed vertical lines mark the boundary of the fixed direction. The intensity is given in counts, and the color code is on the right-hand side of the plot.

experiments. In the next step, we impose a geometrical constraint. We select only those fast electrons which leave the sample within a narrow angular direction. As an example, we have drawn a black circle in Fig. 3(b) which is centered at $\Theta = \Phi = 0$ rad. The emission direction is a cone with an angle of 0.18 rad, which is the radius of the circle in Fig. 3(b). In other words, we fix the direction of the fast electron and ask for the intensity of the slow electron around this direction. This is displayed in Fig. 3(c) after normalization to the intensity of the slow electron in Fig. 3(a). This procedure is necessary in order to take into account varying detection efficiencies. It is obvious that the intensity on the center detector is lower than on the left and right detectors.

To emphasize the point and to improve the statistics, we integrated the data along the Φ direction and show the resulting line scan along the Θ direction in Fig. 3(d). The vertical dashed lines mark the boundary of the allowed Θ values of the fast electron. The solid line through the data serves as a guide for the eye; the y axis is in arbitrary units as a result of our normalization procedure. We applied the same procedure for all line scans. Hence, direct comparison is possible. As already evident in Fig. 3(c), we observe that the fast electron is surrounded by a reduced slow electron intensity. We find that the intensity reaches a constant value at a radius $\Theta \sim 1.2$ rad, which is well inside the angular range of our experiment. This is the experimental manifestation of the exchange-correlation hole. Such a behavior was theoretically predicted for DPE from a Cu(100) surface [6]. The key observation is that we are able to show the full extension and shape of the depletion zone for the first time. It is, of course, possible to fix the emission direction of the slow electron and determine the intensity map of the fast electron. The result of such a presentation is qualitatively and quantitatively identical as far as the size of the depletion zone is concerned. The depletion zone could be observed for different values of E_{fast} and E_{slow} , where the size was independent of the selected energies. We will discuss below under which circumstances we observe an almost vanished depletion zone.

If we choose the fixed direction to be centered at $\Theta = 0$ rad, the maximum angle of the counterpart cannot exceed 1.57 rad if they are to leave the sample surface. However, it is possible to detect electron pairs whose trajectories include larger angles and to study the angular distribution. The significant advantage of our detection scheme is the ability to select the emission direction of one electron (either slow or fast) anywhere within the angular acceptance. We demonstrate this in Fig. 4. The fixed emission directions are defined by a circle in the 2D angular distribution equivalent to Fig. 3(b), which again has a radius of 0.18 rad. The center is at $\Theta = -1.0$ rad for Figs. 4(a) and 4(b); the case $\Theta = 1.0$ rad is depicted in Figs. 4(c) and 4(d). The vertical dashed lines in Figs. 4(b)

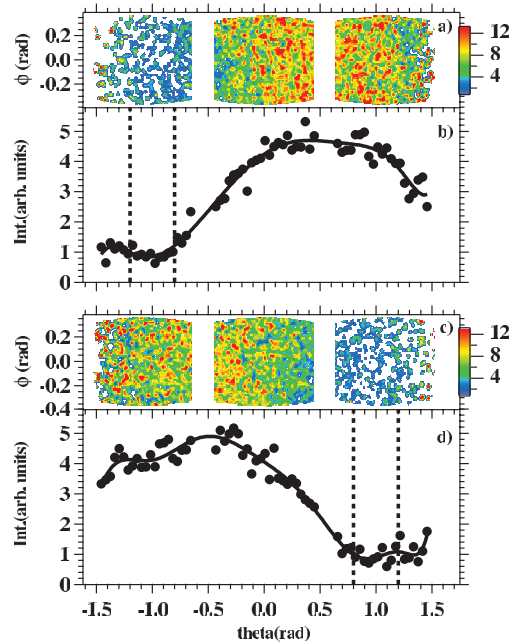


FIG. 4 (color). 2D angular distributions and resulting line scans are shown for electron pairs with $E_{\text{fast}} = 23$ eV and $E_{\text{slow}} = 12$ eV. The direction of the fixed fast electron is centered at either $\Theta = -1$ rad for (a) and (b) or $\Theta = 1$ rad for (c) and (d). The line scans of the intensity maps in (a) and (c) are plotted in (b) and (d), respectively. The solid lines are a guide to the eye, whereas the dashed vertical lines mark the boundaries of the fixed emission directions.

and 4(d) mark the range of the allowed Θ values for the fixed electron. We lose the information of the intensity for Θ values on one side of the selected emission direction, but we gain a larger angular range on the other side. In other words, the maximum angle between the trajectories of the fixed fast and slow electrons is larger in this direction. Using the same procedure as before, we finally derive the 2D angular distribution of the slow electron around the fixed direction of the fast electron. These are plotted in Figs. 4(a) and 4(c). In the case of Fig. 4(a), we observe a low intensity on the left detector, if we move to the center detector the intensity has increased, and finally the intensity on the right detector is smaller than on the center detector. Again, improving the statistics via an integration along the Φ direction is appropriate and gives a more detailed view; the resulting line scan can be seen in Fig. 4(b). Two important observations can be made. First, we see that the intensity peaks at $\Theta \sim 0.2$ rad, while the “fixed” electron is centered at $\Theta \sim -1.0$ rad. This means that the angular size of the depletion zone is ~ 1.2 rad, in line with the result shown in Fig. 3(d). More importantly,

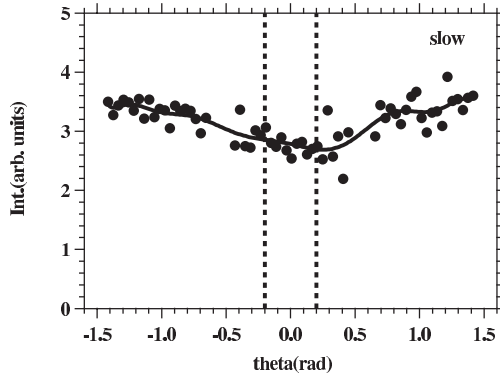


FIG. 5. Coincidence intensity for the slow electron if the direction of the fast electron is fixed at $\Theta = 0$ rad. We selected $E_{\text{fast}} = 23$ eV and $E_{\text{slow}} = 6$ eV. The solid line is a guide to the eye, whereas the dashed vertical lines mark the boundary of the fixed direction.

we see that the coincidence intensity drops off again if the angle between the two electrons is beyond ~ 1.2 rad. An equivalent situation is observed in Fig. 4(d) despite the breaking of symmetry. We have to emphasize that the photon beam hits the sample with an angle of 32° ; see Fig. 1. Therefore, we cannot *a priori* expect to observe a symmetric behavior as we do. We can clearly see that the reduced intensity regime follows the fixed emission direction. The falloff of the coincidence intensity for large angles between the fast and slow electrons is expected, because ultimately two electrons are not correlated if they are well separated (in angular or momentum space).

Because of the size of the depletion zone, it is also justified to allow the fixed direction to be rather large. We have found no significant variation of the angular size of the depletion zone for other values of E_{fast} and E_{slow} . This means that in momentum space the depletion zone size will scale with the square root of the energy. It would be desirable to compare our experimental depletion zone size with theory. This is, however, beyond the capability of current solid state theory. Eventually, the comparison of theory and experiment of the depletion zone may lead to an improved description of the exchange-correlation hole in solids.

We would like to come back to the 2D energy distribution shown in Fig. 2. We have pointed out before that most of the coincidence intensity occurs for $E_{\text{slow}} < 10$ eV. This preference was mainly due to double hits. Detection on the same detector implicitly means that the trajectories of the electrons include small angles; hence, they are “close” to each other. If we select the energies centered at $E_{\text{fast}} = 23$ eV and $E_{\text{slow}} = 6$ eV [region (b) in Fig. 2], we are focusing on such events and ask how the angular distribu-

tions are affected. The result for the slow electron around the fixed direction of the fast electron is plotted in Fig. 5. We observe that the depletion zone has been “filled,” and an almost constant intensity as a function of Θ is observed. This filling of the depletion zone occurs gradually if we vary E_{slow} from 12 to 6 eV. More specifically, the size of the depletion zone stays essentially constant, but the minimum is filled up. A simple picture of the electron-electron scattering, where the interaction between the electrons is mediated by the Coulomb interaction, shows that if the trajectories are forced to be close to each other, one electron is fast while the other is slow. In general, two electrons tend to avoid each other (due to the Pauli principle and Coulomb interaction), leading to the concept of the depletion zone. Our experiments confirm this picture as long as the individual energies E_{fast} and E_{slow} are not too unequal as just shown.

We conclude that we are able to fully map the depletion zone. This statement constitutes the major achievement of our work. We find for the depletion zone from electrons originating from a Cu(111) surface a size of ~ 1.2 rad independent of the energy of the electrons. We also discovered a correlation in energy space proven by an almost disappearing depletion zone if the electron energies are very unequal. The prospect of investigating the material dependence of the depletion zone is promising.

We acknowledge the expert assistance by H. Engelhard and D. Hartung. We thank the staff of the BESSY storage ring for excellent support.

- [1] K. Byczuk, M. Kollar, K. Held, Y.-F. Yang, I. A. Nekrasov, T. Pruschke, and D. Vollhardt, *Nature Phys.* **3**, 168 (2007), and references therein.
- [2] J. Berakdar, *Phys. Rev. B* **58**, 9808 (1998).
- [3] E. Wigner and F. Seitz, *Phys. Rev.* **43**, 804 (1933).
- [4] J. C. Slater, *Rev. Mod. Phys.* **6**, 209 (1934).
- [5] P. Fulde, *Electron Correlations in Molecules and Solids*, Springer Series in Solid State Sciences Vol. 100 (Springer, Berlin, 1993).
- [6] N. Fominykh, J. Berakdar, J. Henk, and P. Bruno, *Phys. Rev. Lett.* **89**, 086402 (2002).
- [7] H. W. Biester, M. J. Besnard, G. Dujardin, L. Hellner, and E. E. Koch, *Phys. Rev. Lett.* **59**, 1277 (1987).
- [8] R. Herrmann, S. Samarin, H. Schwabe, and J. Kirschner, *Phys. Rev. Lett.* **81**, 2148 (1998).
- [9] F. U. Hillebrecht, A. Morozov, and J. Kirschner, *Phys. Rev. B* **71**, 125406 (2005).
- [10] F. O. Schumann, C. Winkler, G. Kerherve, and J. Kirschner, *Phys. Rev. B* **73**, 041404(R) (2006).
- [11] F. O. Schumann, J. Kirschner, and J. Berakdar, *Phys. Rev. Lett.* **95**, 117601 (2005).
- [12] W. Kohn, *Rev. Mod. Phys.* **71**, 1253 (1999).
- [13] In order to smooth the contour lines, we employed a Gaussian filter.

New Journal of Physics

The open-access journal for physics

Mapping out electron–electron interactions in angular space

F O Schumann¹, C Winkler and J Kirschner

Max-Planck Institute of Microstructure Physics, Weinberg 2,
06120 Halle, Germany

E-mail: schumann@mpi-halle.de

New Journal of Physics **9** (2007) 372

Received 27 June 2007

Published 12 October 2007

Online at <http://www.njp.org/>

doi:10.1088/1367-2630/9/10/372

Abstract. Many-body effects in solids are related to the correlation among electrons. This mutual interaction between the electrons can be probed by electron pair emission spectroscopy. We have investigated the electron pair emission from a LiF(100) surface upon excitation with low kinetic energy electrons. Our angular distributions clearly show that the emission direction of one electron is surrounded by a reduced intensity of the other electron. This depletion zone of electronic intensity is a manifestation of the exchange and correlation hole. We show that we are able to observe the full extension and shape of the depletion zone. It has an angular extension of ≈ 1.2 rad and is independent of the electron energy. Additionally, we discovered that the angle between the trajectories of the electrons has a profound effect on the two-dimensional energy distribution.

Contents

1. Introduction	2
2. Experiment	3
3. Normal incidence excitation	6
4. Non-normal incidence excitation	8
5. Discussion	13
6. Summary	13
Acknowledgments	14
References	14

¹ Author to whom any correspondence should be addressed.

1. Introduction

Electronic transport is an integral part of modern technology, if we recall microelectronics for example. First attempts to describe the phenomenon of electrical conductivity in metals can be traced back to the work of Drude [1] and Lorentz [2]. The physical picture they devised was based on the assumption that the electrons do not interact in the metal and that only elastic collisions occur at the positions of the atoms. In an applied electrical field, these collisions ensure that the velocity of the electrons converges to a constant value. This rather crude theory gave a satisfactory explanation of the finite resistivity and the observed Ohm's law. However, the application of the classical kinetic gas theory failed completely to describe the behavior of the specific heat. The linear temperature dependence of the electronic specific heat at low temperatures could be accounted for in the so-called Sommerfeld theory [3]. Again electrons were treated as independent and non-interacting particles, but the rules of quantum mechanics were used, most important was the inclusion of the Fermi–Dirac statistics. Electrons in a solid, however, do not move independently of each other, they experience a mutual force mediated by the Coulomb interaction. Hence one would expect the independent electron picture to be an inadequate description of electrons in a solid. This apparent contradiction could be resolved by the fundamental work of Wigner and Seitz [4] and Slater [5], introduced more than 70 years ago. This can be understood by recalling that the Pauli principle demands that two electrons cannot be at the same location if they have parallel spins. The Coulomb interaction makes it energetically more favorable for electrons to be separated. The net effect is that each electron is surrounded by a missing electronic charge, this electronic depletion zone has been termed as the exchange-correlation (xc)-hole. The xc-hole has a spatial extension of the order of a few ångström and amounts to exactly the charge of an electron. This means that over distances larger than the size of the xc-hole each electron is screened from the other electrons. Another description would be to regard the electron and the xc-hole as a ‘quasi-particle’ with no charge. The work of Wigner and Seitz and Slater explains why the approximation of Lorentz, Drude and Sommerfeld, namely a non-interacting electron gas, can give reasonable results. However, it is clear that many-body phenomena like magnetism, superconductivity and heavy fermions to name a few are beyond the independent electron picture. The determination of the ground state wavefunction of interacting electrons in a macroscopic sample is a hopeless task. A major breakthrough in the description of the ground state properties of condensed matter was therefore the development of the density functional theory (DFT) [6]–[8]. It was shown that the ground state energy is a functional of the electron density $n(\mathbf{r})$, likewise all other ground state properties are exactly described by the functionals of $n(\mathbf{r})$. This concept can be put into a computational scheme by the local density approximation (LDA) leading to the Kohn–Sham equation, which formally looks like a Schrödinger equation of a single particle moving in an effective potential [6]–[8]. An important contribution to this potential comes from $\delta E_{xc}/\delta n(\mathbf{r})$, where the functional E_{xc} contains all features of the interacting electronic system. Key quantities for E_{xc} are the pair correlation function $\mathbf{g}(\mathbf{r}, \mathbf{r}')$ and the xc-hole (function) $\mathbf{n}_{xc}(\mathbf{r}, \mathbf{r}')$. The first quantity is the probability to find an electron at coordinates \mathbf{r} , when a second is located at \mathbf{r}' [4, 5, 9]. As discussed before, \mathbf{g} is essentially constant (normalized to 1) except for small distances $|\mathbf{r} - \mathbf{r}'|$ of the order of a few ångström, where \mathbf{g} adopts smaller values. The term xc-hole is linked to the pair correlation function via $\mathbf{n}_{xc}(\mathbf{r}, \mathbf{r}') = \mathbf{n}(\mathbf{r}')[\mathbf{g}(\mathbf{r}, \mathbf{r}') - 1]$. Simply put, the LDA, a very successful description for condensed matter, incorporates the xc hole. Different approaches have been put forward to improve the LDA calculations via

different choices for $\mathbf{n}_{xc}(\mathbf{r}, \mathbf{r}')$ [10]–[15]. It would be therefore desirable to access the key function $\mathbf{n}_{xc}(\mathbf{r}, \mathbf{r}')$ via experiment. This is not yet directly possible, but we are able to measure the angular distribution. Due to the electron–electron interaction, electrons will scatter from each other while moving in the solid. Scattering is also the key to studying the electron–electron interaction, and scattering experiments have a long tradition in physics. The angular distributions of the projectile have been used to study the interaction between projectile and target. We recall the landmark experiments by Rutherford and co-workers, their angular distribution of the scattered α particles led to the discovery that most of the mass of an atom is confined in a small region of space. Clearly, studying the electron–electron interaction via a scattering experiment is most appropriate [16]. Our experimental approach reflects this argument and we excite the solid surface via a primary electron beam and measure the angular distribution of the emitted electron pairs. Recent advances on the experimental side have made it possible to address the aforementioned concept of the xc-hole [17, 18]. In this paper, we show that it is experimentally possible to measure the full angular distribution of the electron pairs ejected from a solid surface. Our studies highlight the fact that the xc-hole is an experimental reality.

2. Experiment

Before we discuss our experiment in detail, a few general statements about our experimental approach are in order. Our goal is to study the electron–electron interaction in solids and the size of the exclusion zone or xc-hole. The most obvious experiment is to perform a scattering experiment in the spirit of Rutherford. Applied to our situation, we need to study the collision between two electrons after a primary electron hits the sample. We may term such an experiment as an (e, 2e) process. The detection of electron pairs is a straightforward, although experimentally demanding, extension of single electron spectroscopy. The following approaches are conceivable, a transmission experiment would require a large kinetic energy of the primary electron, of the order of 20–100 kV, to pass through a thin foil. Such experiments have been indeed performed and have given useful insights into the spectral momentum density [19, 20]. The equivalent experiment in a reflection geometry is also possible, where the primary electron has an kinetic energy of 300 eV [21]. Both approaches choose the kinematics such that the scattered primary electron loses a small fraction of its kinetic energy, hence the second electron has a much smaller kinetic energy than the scattered primary. Further the momentum transfer of the primary electron is very small. This constitutes the so-called optical-limit, where the primary electron acts like a photon [22]. This allowed comparison with photoemission results. Over the past decade it has been demonstrated that experiments in a reflection geometry employing primaries with energies of 30 eV are possible, which were not confined to the optical limit [23]–[25]. In parallel to the experimental advances the theoretical description of the (e, 2e) process made significant progress, too [24], [26]–[29]. The low kinetic energy reflection geometry adapts better to our aims than the high kinetic energy transmission geometry. The energy introduced to the system by the primary electron needs to be compared with the energies relevant for electron–electron correlation. Within the Hubbard model, the strength of the electron correlation is described by the parameter U , which is of the order of a few electron volts. Clearly, the energetics of a transmission experiment is too high to be sensitive to the electron–electron interaction in contrast to a low kinetic energy experiment. The key for a successful reflection experiment is a high probability of reflection, which is

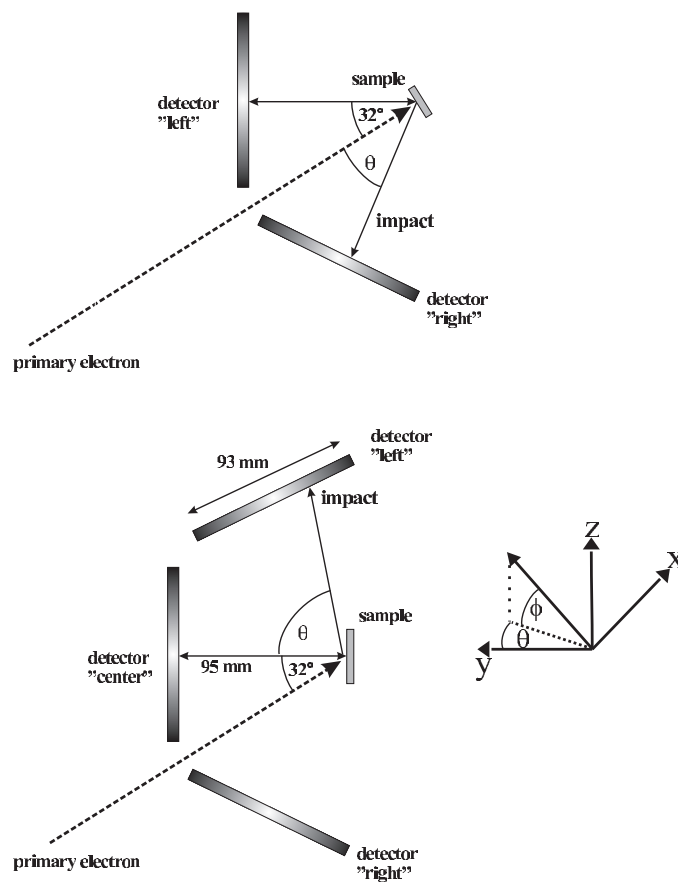


Figure 1. Sketch of the employed geometries and definition of the angles Θ and Φ .

demonstrated by the widely used technique of low electron energy diffraction (LEED). The primary electron is reflected back elastically, though energy losses via excitations of plasmons, phonons, exciton etc are possible and have been observed in electron energy loss spectroscopy (EELS). However, the contribution of the losses compared to the elastic peak is orders of magnitude smaller. The key result is that one can regard the reflection experiment we perform as a kind of transmission experiment through the topmost layers, where the reflected primary beam has a well-defined energy and momentum. Clearly, such an experiment will have a small cross-section: electrons in a solid try to avoid scattering from each other, up to ‘disguising’ themselves as neutral quasi-particles. This means that our experiments observe only that small fraction of scattering events where two quasi particles come sufficiently close (i.e. less than

the screening length) to ‘feel’ each other. In figure 1, we provide a schematic view of our time-of-flight (TOF) experimental set-up and the two geometries employed. The electron gun uses a BaO cathode and with that the overall energy spread is 0.4 eV. The pulsing is achieved via electro-static deflection of the electron beam across a small aperture within the gun. Pulse widths of 0.5 ns can be achieved at a repetition rate of 2 MHz. The primary current on to the sample is about 10^{-14} A. By performing LEED with our set-up the width of the diffraction spots are defined by the angular divergence of the gun. This is usually expressed in terms of the transfer width, we calculate a value of 140 \AA^{-1} . A coincidence circuit ensures that only electron pairs emitted from the surface are being registered thereby suppressing the large contribution of single electron emission. The TOF of the electrons depends on the energy and the emission direction, since the latter defines the actual length of the flight path. When the two electrons forming the pair leave the sample, they will have in general different energies and different flight paths. Consequently the electrons will reach the detectors at different times. For example, an electron of 30.7 eV (elastically scattered primary) has a TOF of about 30 ns, an electron with 2 eV (our low kinetic energy cut-off) travels for about 110 ns. This means that the TOF difference of electrons forming a pair has to be lower than 80 ns. The first electron to hit the detector will define electronically a time window in which the second electron has to hit the detector. Only in this case, we consider it to be a valid coincidence event. This concept only works if we ensure that only one pair exists after the excitation. This can be realized experimentally by operating with a low primary beam. We use for normal incidence of the primary electron beam two of the detectors, which we label ‘left’ and ‘right’, respectively. The reason for this comes from the fact that the sample surface partly blocks electrons from reaching the third detector. The ‘left’ and ‘right’ detectors are arranged symmetrically with respect to the primary beam and the angular acceptance is ± 0.96 rad in the drawing plane and ± 0.4 rad perpendicular to it. For a non-normal incidence, we employ three detectors, which increases the angular acceptance to ± 1.57 rad in the drawing plane, while maintaining a value of ± 0.4 rad perpendicular to it. We will label the detectors ‘left’, ‘center’ and ‘right’ in the following. Delay line anodes allow the determination of the impact position of the electrons. Further, the detectors allow also to recover the impact positions of coincident pairs even if they hit the same detector. These events we may term as ‘double hits’, whereas we refer to ‘single hits’, if the electrons are registered on different detectors. We determine the electron energies via the TOF, where the time reference comes from the pulsed electron gun. The whole set-up is realized in an ultra-high vacuum chamber equipped with standard surface science tools. We define a coordinate system, which has the origin at the sample surface. The y-axis is always parallel to the surface normal, where the x- and z-axes are in-plane. We have chosen the z-axis to be perpendicular to the drawing plane of the geometries. Each coincident event is then characterized by six coordinates, namely the individual energies and pairs of angles Θ and Φ . The total time resolution is approximately 1.8 ns. This will lead to an energy-dependent energy resolution, which is 0.7 eV for a 10 eV electron. We studied a LiF(100) surface, which was kept at a temperature of $\sim 150^\circ\text{C}$ during the measurements to maintain sufficient conductivity. Further, this temperature ensures a clean surface for the duration of the experiment and the annealing of localized electronic defects. The low coincidence count rate required a total acquisition time of ~ 500 h. An electron from the top of the valence band of LiF needs an energy of ~ 13 eV to reach the vacuum level. Therefore, the choice of a primary energy of 30.7 eV ensures that due to energy conservation only one valence band electron and the scattered primary electron can leave the sample. The low kinetic energy cut-off is 2 eV.

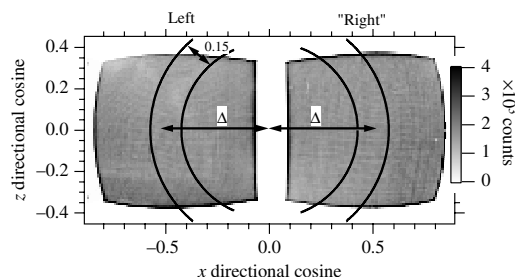


Figure 2. The hit pattern of electron pairs is displayed, where the axes are the directional cosines within the surface. The primary electron hits the surface parallel to the surface normal with an energy of 30.7 eV. The pair of lines on the ‘left’ and ‘right’ detector mark the boundary of narrow regimes. The center has a distance of Δ to the surface normal.

3. Normal incidence excitation

First, we studied the two-dimensional (2D)-energy distributions in the symmetric geometry, where the incident electron beam hits the sample along the surface normal, see figure 1 top. Referring to the detector labeling, we named the electron energies E_{left} and E_{right} , respectively. Implicitly means that we have focussed on ‘single’ hits only. In other words, for each ‘left’ electron there is a ‘right’ counterpart. We know for each coincident event in which direction the individual electrons have left the surface. This emission direction can be characterized by two coordinates and we choose the directional cosines within the surface, which we label as x and z , respectively. In figure 2, we display the hit pattern of the individual electrons of coincident pairs as a function of the directional cosine x and z irrespective of the electron energies. The incident electron beam has an energy of 30.7 eV. In this presentation the coincidence intensity is almost uniformly distributed. It is now interesting to impose a geometrical constraint. More specifically we allow only those emission directions of the ‘left’ and ‘right’ electron such that the included angle between the electron trajectories is essentially fixed and ask for the impact on the energy sharing. A major advantage of the current set-up is that the energy distribution curves can be determined in a post-experiment analysis rather than placing a mask in front of the detectors and performing experiments sequentially. As sketched in figure 2, we define the limited emission directions as follows. On each detector, we define narrow regions by a pair of arcs. They are symmetrically arranged and the mean radius is given by the value of Δ , see figure 2. The difference in radius between the smaller and the larger arc is fixed to 0.15. We allow for a finite width in order to accept enough coincidence events for reasonable statistics. We will consider only those coincidence events where the individual electrons fall within these narrow regimes. We have selected two examples, namely the smallest included angle, this means $\Delta = 0.2$. The largest included angle is obtained for $\Delta = 0.7$. We have plotted the resulting 2D-energy distributions in figure 3. The bars on the right define the color codes for the intensity given in counts. Further we added equidistant contours to the plots². In the case of $\Delta = 0.2$,

² In order to smooth the contour lines we employed a Gaussian filter.

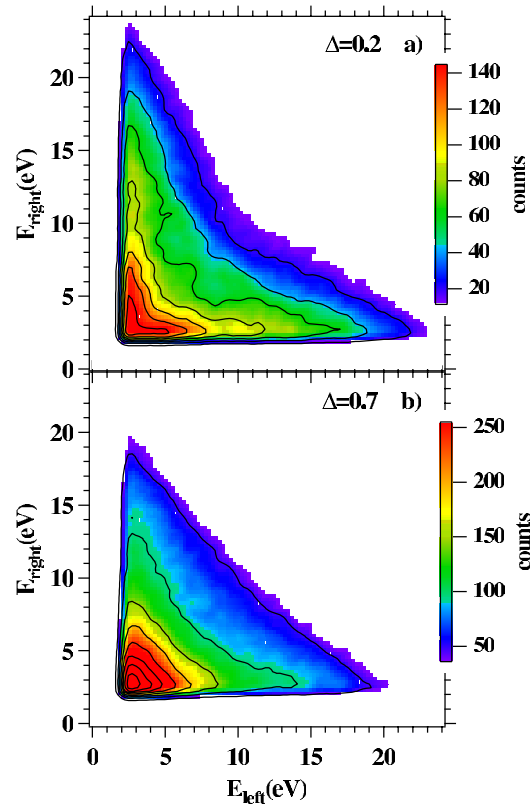


Figure 3. We show the 2D-energy distribution obtained from a LiF(100) surface excited with 30.7 eV primary electrons. In panel (a), we plot the distribution for $\Delta = 0.2$, whereas in panel (b) the result for $\Delta = 0.7$ is displayed.

we note immediately a very unequal energy sharing. Most of the coincidence intensity can be found in two narrow bands parallel to the E_{left} and E_{right} axis resembling the shape of a boomerang. Clearly one electron is essentially confined to energies below ~ 6 eV, whereas the other electron energy can be as high as ~ 18 eV. This means if the included angle between the electrons is small ($\Delta = 0.2$) one electron is ‘fast’ while the other is ‘slow’. If we allow the value of Δ to increase this unequal energy sharing gradually disappears. For $\Delta = 0.7$ the 2D-energy distribution is plotted in figure 3(b). Now the coincidence intensity is essentially constant for constant sum energies $E_{\text{sum}} = E_{\text{left}} + E_{\text{right}}$. The coincidence intensity increases if the sum energy E_{sum} decreases. We learn from figure 3 that electrons which are ‘close’ to each other have very unequal energy sharing, whereas electrons separated by large angles display equal sharing. To emphasize this point we show in figure 4 so-called sharing contributions. These are obtained by choosing a value for E_{sum} and plotting the coincidence intensity as a function of $E_{\text{right}} - E_{\text{left}}$. We

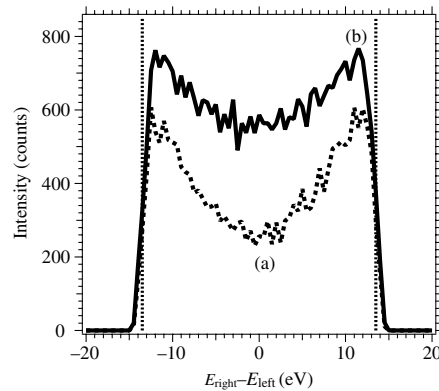


Figure 4. Energy sharing distributions for $E_{\text{sum}} = 17.5 \pm 1$ eV. The curve obtained for $\Delta = 0.2$ is labeled with (a), whereas (b) refers to $\Delta = 0.7$. The vertical dashed lines indicate the positions of the maxima and minima of the energy sharing. These are defined by the low kinetic energy cut-off.

selected $E_{\text{sum}} = 17.5 \pm 1$ eV, which is the highest possible value of E_{sum} for pair emission with a primary beam of 30.7 eV. The curve labeled (a) in figure 4 is obtained from the data shown in figure 3(a), which implies $\Delta = 0.2$. Likewise curve (b) refers to $\Delta = 0.7$. The maximum of curve (a) displays two pronounced maxima at $E_{\text{right}} - E_{\text{left}} \approx \pm 12$ eV. The minimum of curve (a) is at $E_{\text{right}} - E_{\text{left}} \approx 0$ eV and has about half of the intensity of the maxima. It is important to emphasize that the maxima of the sharing function are a result of our low kinetic energy cut-off. We stated above that this value is 2 eV, with this in mind and the chosen maximum sum energy of 17.5 eV, the cut-off occurs at $E_{\text{right}} - E_{\text{left}} = \pm 13.5$ eV. These energy values have been indicated by the vertical dashed lines in figure 4. With a smaller cut-off the sharing distribution would increase further and only if the kinetic energy of one of the electrons approaches zero would the intensity drop. Curve (b) on the other hand shows that the intensity is more uniform though a minimum at $E_{\text{right}} - E_{\text{left}} \approx 0$ eV can be still observed.

4. Non-normal incidence excitation

In the case of ‘double’ hits a meaningful label is to term one electron ‘fast’ and the other ‘slow’ with the energies E_{fast} and E_{slow} , respectively. This implies that $E_{\text{fast}} > E_{\text{slow}}$, consequently we have to label ‘single’ hits in the same fashion. We display the resulting 2D-energy distribution (‘single’ and ‘double’ hits) in figure 5. The bar on the panel defines the color code for the intensity, which is given in counts. Further we added equidistant contours to the plot³. It is apparent that the coincidence intensity is highest in a wedge-shaped region with $E_{\text{slow}} < 4$ eV and $E_{\text{fast}} < 10$ eV. This can be rephrased by saying that there is a preference for one electron being ‘fast’ while the other is ‘slow’. Individual 2D-energy plots including only either ‘single’ or ‘double’ hits reveal that this is due to the contribution of ‘double’ hits. Since those hits occur

³ In order to smooth the contour lines we employed a Gaussian filter.

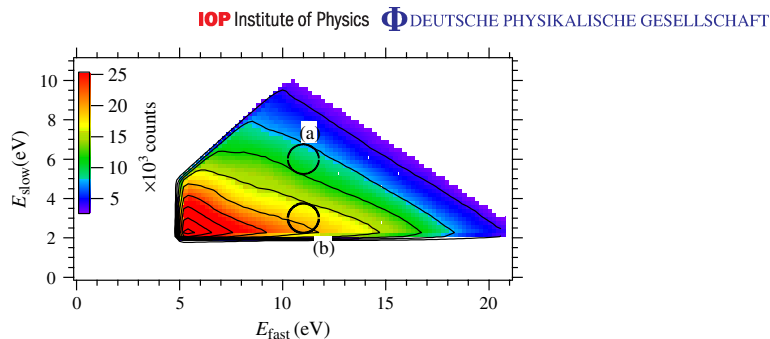


Figure 5. 2D-energy distribution obtained from a LiF(100) surface excited with 30.7 eV primary electrons. One electron of the pair is ‘fast’, whereas the other is ‘slow’ with energies $E_{\text{fast}} > E_{\text{slow}}$. The two circles with radius 0.75 eV indicate energy regions centered at $E_{\text{fast}} = 11$ eV ($E_{\text{slow}} = 6$ eV) and $E_{\text{fast}} = 11$ eV ($E_{\text{slow}} = 3$ eV). Coincident events within these windows are used for 2D-angular plots.

on the same detector we know that the trajectories of these electrons must include smaller angles compared to ‘single’ hits. This aspect will become important later on.

We continue with a 2D-angular presentation of our data. This representation requires the execution of several steps. First, we select values for E_{fast} and E_{slow} , respectively. In order to select enough coincidence events we allow an uncertainty in the energy of ± 0.75 eV. This has been indicated by the circles drawn in figure 5. After the energy selection, we can derive the angular distributions of the ‘fast’ and ‘slow’ electrons. These are not independent of each other, since electron pairs are detected. We would like to emphasize that every ‘fast’ electron has a ‘slow’ counterpart. As an example we show in figure 6 the angular distributions for ‘fast’ and ‘slow’ electrons centered at $E_{\text{fast}} = 11$ eV and $E_{\text{slow}} = 6$ eV (region (a) of figure 2). The intensity is given in counts and the color code is on the right-hand side of the plot. Both distributions display the highest intensity if the electrons leave the sample along the surface normal. The intensity drops for increasing values of $|\Theta|$. We add that the single electron distribution is essentially identical⁴. In the next step, we impose a geometrical constraint. We select only those ‘fast’ electrons, which leave the sample within a narrow angular direction. As an example, we have drawn a black circle in figure 6(b), which is centered at $\Theta = \Phi = 0$ rad. The emission direction is a cone with an angle of 0.18 rad, which is the radius of the circle in figure 6(b). In other words, we fix the direction of the ‘fast’ electron and ask for the intensity of the ‘slow’ electron around this direction. We obtain the intensity map of the ‘slow’ electron displayed in figure 6(c) after normalization to the intensity of the ‘slow’ electron in figure 6(a). This procedure is necessary in order to take into account varying detection efficiencies. It is very clear that the intensity on the center detector is lower than on the left and right detectors. To emphasize this point and to improve the statistics we integrated the data along the Φ direction and show the resulting 1D angular distribution along the Θ direction in figure 6(d). The vertical dashed lines mark the boundary of the allowed Θ values of the ‘fast’ electron. As already evident

⁴ We can determine the single electron distribution by integrating overall E_{slow} values for a given value of E_{fast} .

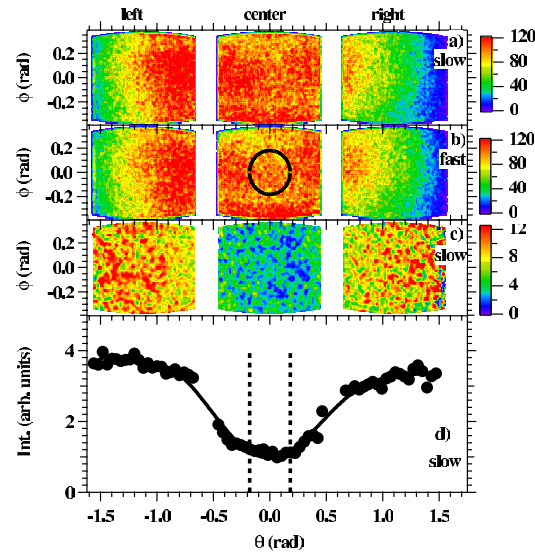


Figure 6. Angular distributions with $E_{\text{fast}} = 11 \text{ eV}$ and $E_{\text{slow}} = 6 \text{ eV}$ are displayed. Panel (a) shows the 2D-angular intensity for the ‘slow’ electron, whereas in panel (b) the same for the ‘fast’ electron is plotted. In panel (c), we plot the intensity for the ‘slow’ electron if the ‘fast’ electron is constrained to be within the area defined by the black circle of the center detector 2 in (b). From panel (c) a line scan can be computed, which is plotted in panel (d). The solid line is a guide to the eye, whereas the dashed vertical lines mark the boundary of the fixed direction.

in figure 6(c), we observe that the ‘fast’ electron is surrounded by a reduced ‘slow’ electron intensity. This is the experimental manifestation of the xc-hole [17, 18]. The key observation is that we are able to show the full extension and shape of the xc-hole. The solid line through the data serves as guide for the eye, the y-axis is in arbitrary units as a result of our normalization procedure. This procedure is the same for all 1D angular distributions to be shown, which facilitates direct comparison. We find that the intensity reaches a constant value at a radius $\Theta \sim 1.2 \text{ rad}$, which is well inside the angular range of our experiment. The position of the maxima may serve as a measure of the xc-hole. It is of course possible to fix the emission direction of the ‘slow’ electron and to determine the intensity map of the ‘fast’ electron. The result of such a presentation is qualitatively and quantitatively identical as far as the size of the depletion zone is concerned. The depletion zone could be observed for different values of E_{fast} and E_{slow} , where the size was independent of the selected energies. We would like to add that we performed some additional experiments utilizing a fourth detector, which was positioned below the ‘center’ detector, see figure 1. These experiments confirmed that the reduced intensity around the fixed emission direction of one electron is also present in the direction perpendicular to the drawing plane of figure 1. We will discuss below under which circumstances, we observe

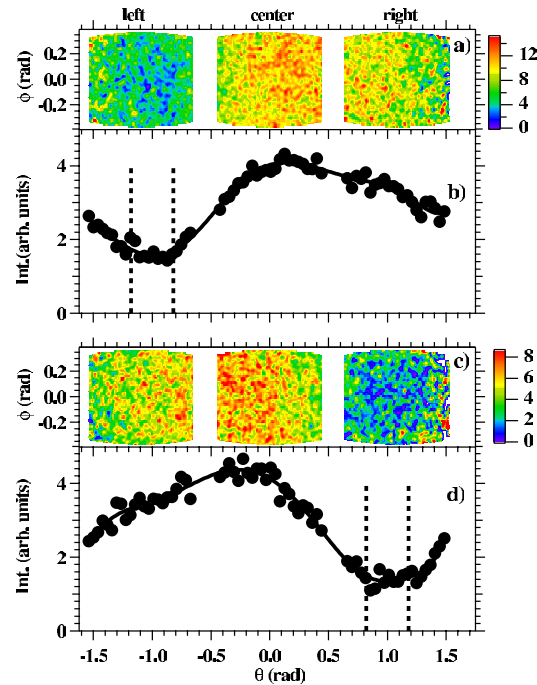


Figure 7. 2D-angular distributions and resulting line scans are shown for electron pairs with $E_{\text{fast}} = 11$ eV and $E_{\text{slow}} = 6$ eV. The direction of the fixed ‘fast’ electron is centered either at $\Theta = -1$ rad for panels (a) and (b) or $\Theta = 1$ rad for panels (c) and (d). The line scans of the intensity maps in (a) and (c) are plotted in panels (b) and (d). The solid lines are a guide to the eye, whereas the dashed vertical lines mark the boundaries of the fixed emission directions.

no xc-hole. The significant advantage of our detection scheme is the ability to select the emission direction of one electron (either ‘slow’ or ‘fast’) anywhere within the angular acceptance. We selected two other emission directions for the ‘fast’ electron. These directions are defined by a circle in the 2D-angular distribution equivalent to figure 6(b), which again has a radius of 0.18 rad. The center is either at $\Theta = -1.0$ rad for figures 4(a) and (b), the case $\Theta = 1.0$ rad is depicted in figures 7(c) and (d). The vertical dashed lines in figures 7(b) and (d) mark the range of the allowed Θ values. We lose the information on the intensity for Θ values on one side of the selected emission direction. However, we gain a larger angular range on the other side. In other words, the maximum angle between the trajectories of the fixed ‘fast’ and ‘slow’ electron is larger in this direction. With the help of the same procedure as employed before we can finally derive the 2D-angular distribution of the ‘slow’ electron around the fixed direction of the ‘fast’ electron. These are plotted in figures 7(a) and (c). In the case of panel (a) we observe a low intensity on the left detector, if we move to the center detector the intensity has increased and

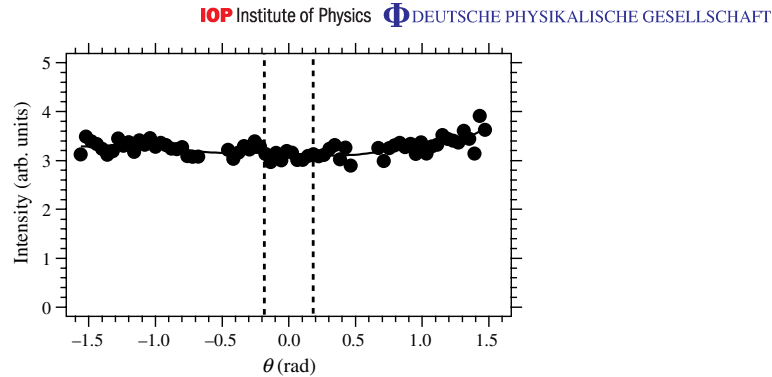


Figure 8. Coincidence intensity for the ‘slow’ electron if the direction of the ‘fast’ electron is fixed at $\Theta = 0$ rad. We selected $E_{\text{fast}} = 11$ eV and $E_{\text{slow}} = 3$ eV. The dashed vertical lines mark the boundary of the fixed direction.

finally the intensity on the right detector is smaller than on the center detector. Again improving the statistics via an integration along the Φ -direction is appropriate and gives a more detailed view, the 1D angular distribution can be seen in figure 7(b). Two important observations can be made. First, we see that the intensity peaks at $\Theta \sim 0.2$ rad, while the ‘fixed’ electron is centered at $\Theta \sim -1.0$ rad. This means that the extension of the depletion zone is ~ 1.2 rad in line with the result shown in figure 6(d). More importantly, we see that the coincidence intensity drops off again if the angle between the two electrons is beyond ~ 1.2 rad. An equivalent situation is observed in figure 7(d) despite the breaking of symmetry. We have to emphasize that the primary beam hits the sample with an angle of 32° , see figure 1. Therefore, we cannot *a priori* expect to observe a symmetric behavior as we do. A closer inspection of the line scans in figures 6 and 7 reveal a hint of symmetry breaking. In figure 6(d) the maximum for negative Θ values is slightly larger than for positive Θ values (3.8 versus 3.4 arbitrary units). Comparing figures 7(b) and (d) shows that the maximum for negative Θ values is larger than the maximum for positive Θ values (4.1 versus 4.5 arbitrary units). We can clearly see that the reduced intensity regime follows the fixed emission direction. As an example of a vanished xc-hole we display in figure 8, the intensity of the ‘slow’ electron as a function of Θ . The fixed emission direction of the ‘fast’ electron is located at the center detector like the case depicted in figure 6(b). The energies are centered at $E_{\text{fast}} = 11$ eV and $E_{\text{slow}} = 3$ eV, respectively. These are the events which are located within region (b) in the 2D-energy plot of figure 5. This choice ensures that we are in the regime where there is a preference of one electron being ‘fast’ while the other is ‘slow’. We have explained this to be due to the 2D-energy distribution of the ‘double’ hits. In this case the trajectories of the electrons include small angles, hence they are ‘close’ to each other. This is consistent with the effect of a geometrical constraint on the 2D-energy distribution as discussed in section 3. It was observed that if the electrons are forced to be close to each other ($\Delta = 0.2$) one electron carried most of the available kinetic energy. If we consider now the emission direction of either ‘fast’ or ‘slow’ fixed, the counterpart shows additional intensity for trajectories close to the fixed emission direction. The net effect is that the xc-hole will be ‘filled’ and an essentially constant intensity as a function of Θ is observed. This filling of the xc-hole

occurs gradually if we vary E_{slow} from 6 to 3 eV. More specifically the size of the xc-hole stays essentially constant, but the minimum is filled up. This observation is directly linked to the 2D-energy distribution of coincidence events. Additionally, we point out that 3 eV electrons are part of the secondary electron tail. These electrons have encountered more than one collision event. The net result is then that the coherence with the ‘fast’ electron is lost. Consequently, we should not expect to observe a depletion zone. From the above made comments it becomes obvious that the vanishing depletion zone is not related to the difference in sum energy of the data shown in figures 6 and 8, respectively. As a matter of fact choosing $E_{\text{fast}} = 14$ eV and $E_{\text{slow}} = 3$ eV, where the sum energy is identical to the data plotted in figure 6, still yields no depletion zone.

5. Discussion

From the experimental data obtained in the symmetric geometry, we learn that the angle between the trajectories has a strong influence on how the available energy is shared among the electrons. We found that if this angle is small the electrons tend to avoid having the same kinetic energy and most of the coincidence intensity is found for one electron having most of the energy of the pair, see figures 3 and 4. On the other hand, for large angles between the trajectories we observe a more equal energy sharing. A simple picture of the electron–electron scattering, where the interaction between the electrons is mediated by a screened Coulomb interaction, shows that if the trajectories are forced to be close to each other one electron is ‘fast’ while the other is ‘slow’. The introduction of a screened Coulomb potential follows (within the concept of the xc-hole) from the missing electronic charge surrounding each electron (due to the Pauli principle and Coulomb interaction). This is a valid approach following the experimental evidence employing the non-normal incidence geometry. The angular distribution of the coincidence intensity around the fixed emission direction of one electron clearly shows a depletion zone, see figures 6 and 7. Our angular acceptance of the instrument is large enough to fully map this region. This fact constitutes the major advance of our work. Due to the size of the depletion zone, which is about 1.2 rad, it is also justified to allow the fixed direction to be rather large (0.18 rad). We have found no significant variation of the angular size of the depletion zone for other values of E_{fast} and E_{slow} . This is also true for data sets obtained with different excitation energies. Of course this means that in momentum space the depletion zone size will scale with the square root of the energy. The size of the depletion zone is a measure of the electron–electron interaction inside the solid. It would be desirable to compare our experimental depletion zone size with theory. This is, however, beyond the capability of current solid state theory. Experimentally, we plan to systematically study the depletion zone for different materials. For example, how does the present result of an insulator compare with a typical metal, e.g. Cu? In general two electrons tend to avoid each other leading to the concept of the xc-hole. Our experiments confirm this picture as long as the individual energies E_{fast} and E_{slow} are not too unequal as just shown.

6. Summary

The concept of the xc-hole was introduced more than 70 years ago and is an essential part of modern solid state theory. Our results clearly demonstrate that it is an experimental reality beyond being an important theoretical concept and shows up as a depletion zone in the angular distribution of the coincidence intensity. Specifically, we have proven that we can fully map

the depletion zone in angular space. We find for the size obtained from electrons originating from a LiF(100) surface a value of ≈ 1.2 rad independent of the energy of the electrons. We also discovered a correlation in energy space proven by the disappearance of the xc-hole if the electron energies are very unequal. It would be now a challenge for theory to use our angular distributions results and solve the so-called inverse problem of scattering. In other words, to derive the scattering potential, which essentially is the key function $\mathbf{n}_{xc}(\mathbf{r}, \mathbf{r}')$. This may serve as a basis for an improvement of the DFT beyond the LDA.

Acknowledgments

We acknowledge the expert assistance in the construction and operation of the experiment by H Engelhard and D Hartung.

References

- [1] Drude P 1900 *Ann. Phys. Lpz.* **306** 566–613
- [2] Lorentz H A 1909 *The Theory of Electrons* (Leipzig: BG Teubner)
- [3] Sommerfeld A 1927 *Naturwissenschaften* **15** 63
- [4] Wigner E and Seitz F 1933 *Phys. Rev.* **43** 804
- [5] Slater J C 1934 *Rev. Mod. Phys.* **6** 209
- [6] Hohenberg P and Kohn W 1964 *Phys. Rev.* **136** B864
- [7] Kohn W and Sham L J 1965 *Phys. Rev.* **140** A1133
- [8] Kohn W 1998 *Rev. Mod. Phys.* **71** 1253
- [9] Fulde P 1993 *Electron Correlations in Molecules and Solids (Springer Series in Solid State Sciences vol 100)* (Berlin: Springer)
- [10] Alonso J A and Girifalco L A 1978 *Phys. Rev. B* **17** 3735
- [11] Krüger P, Wolfgarten G and Pollmann J 1985 *Solid State Commun.* **53** 885–9
- [12] Puzder A, Chou M Y and Hood R Q 2001 *Phys. Rev. A* **64** 022501
- [13] Rushton P P, Tozer D J and Clark S J 2002 *Phys. Rev. B* **65** 235203
- [14] Constantin L A, Perdew J P and Tao J 2006 *Phys. Rev. B* **73** 205104
- [15] Nekovee M, Foulkes W M C and Needs R J 2003 *Phys. Rev. B* **68** 235108
- [16] Rutherford E 1911 *Phil. Mag.* **21** 669
- [17] Schumann F O, Kirschner J and Berakdar J 2005 *Phys. Rev. Lett.* **95** 117601
- [18] Schumann F O, Winkler C, Kerherve G and Kirschner J 2006 *Phys. Rev. B* **73** 041404(R)
- [19] McCarthy I E and Weigold E 1991 *Rep. Prog. Phys.* **54** 789
- [20] Vos M and McCarthy I E 1995 *Rev. Mod. Phys.* **67** 713
- [21] Iacobucci S, Marassi L, Camilloni R, Nannarone S and Stefani G 1995 *Phys. Rev. B* **51** R10252
- [22] Iinokuti M 1971 *Rev. Mod. Phys.* **43** 297
- [23] Kirschner J, Artamonov O M and Samarin S N 1995 *Phys. Rev. Lett.* **75** 2424
- [24] Feder R, Gollisch H, Meinert D, Scheunemann T, Artamonov O M, Samarin S N and Kirschner J 1998 *Phys. Rev. B* **58** 16418
- [25] Samarin S, Berakdar J, Artamonov O M and Kirschner J 2000 *Phys. Rev. Lett.* **85** 1746
- [26] Berakdar J, Gollisch H and Feder R 1999 *Solid State Commun.* **112** 587
- [27] Gollisch H and Feder R 2004 *J. Phys.: Condens. Matter* **16** 2207
- [28] Rucker U, Gollisch H and Feder R 2005 *Phys. Rev. B* **72** 214424
- [29] Gollisch H, Schwartzberg N V and Feder R 2006 *Phys. Rev. B* **74** 075407



Electron pair emission from a Cu(111) surface upon photon absorption

F. O. Schumann, N. Fominykh, C. Winkler, and J. Kirschner
Max-Planck Institut für Mikrostrukturphysik, Weinberg 2, 06120 Halle, Germany

J. Berakdar
*Institut für Physik, Martin-Luther-Universität Halle-Wittenberg, Nanotechnikum-Weinberg, Heinrich-Damerow-St. 4,
 06120 Halle, Germany*

(Received 6 February 2008; revised manuscript received 7 April 2008; published 24 June 2008)

We studied the electron pair emission from a Cu(111) surface upon photon absorption. We found that the energy sharing depends on the angle between the trajectories of the two emitted electrons. The angular distribution of the coincidence intensity displays a zone of reduced intensity, if the emission direction of one electron is fixed. We are able to observe the full extension and shape of this depletion zone. It has an angular extension of ≈ 1.2 rad, which is independent of the electron energy. This depletion zone is a manifestation of the exchange-correlation hole. The experimental results are discussed in connection with a detailed theoretical description.

DOI: 10.1103/PhysRevB.77.235434

PACS number(s): 79.60.-i, 73.20.At

I. INTRODUCTION

Electrons will not move independently through a solid but will experience a mutual influence in their motion, which is mediated by the Coulomb interaction and the Pauli principle. This leads to an important concept of solid theory, namely, the exchange-correlation (xc) hole,¹⁻³ which states that electrons tend to stay away from each other. This creates a zone of reduced electronic charge around each electron. The mutual influence among electrons is ultimately responsible for many-body effects in samples, which display magnetism, superconductivity, heavy fermions, etc. These “highly correlated” systems are the focus of intense research activities. The electronic properties of solids can be accessed via photoemission. In particular, angle-resolved energy distributions allow comparison with band structure calculations. Usually, one discusses peaks in the intensity distributions within an effective single-electron picture. Recent advances in the angle and energy resolution have made it possible that photoemission allows us to observe the effects due to many-body interactions. These so-called kinks in the $E(k)$ curve are the result of the electron-electron (ee) interaction or the coupling to other degrees of freedom.⁴ An alternative way to investigate the electron-electron interaction in solids is offered by the technique of double photoemission (DPE) or $(\gamma, 2e)$, which is the absorption of a single photon followed by the simultaneous emission of an electron pair. Within the dipole approximation a noninteracting electron system has a vanishing DPE intensity, therefore a finite DPE intensity requires a finite electron-electron interaction.⁵ The possibility to probe the xc hole via DPE exists, as a theoretical treatment for a Cu(100) surface showed.⁶ This is beyond the capabilities of single photoemission. The experimental possibility to detect a finite DPE intensity from solids has been demonstrated previously.⁷⁻¹¹

In this work we present our experimental results on the double photoemission from a Cu(111) surface. We will show that the angle between the trajectories of the two emitted electrons determines how the photon energy is shared. Fur-

thermore we will demonstrate that the complete mapping of the xc hole is possible.

II. EXPERIMENT

In Fig. 1 we provide a schematic view of our time-of-flight experimental setup and the two geometries employed. Our experiment consists basically of three channel-plate detectors. If the incident photon beam is parallel to the surface normal, we use two of these [see Fig. 1(a)]. For this symmetric arrangement the angular acceptance is $\pm 55^\circ$ in the drawing plane and $\pm 20^\circ$ perpendicular to it. The second geometry, for an angle of 32° of the photon beam with respect to the surface normal, has an increased angular acceptance of $\pm 90^\circ$ in the drawing plane [Fig. 1(b)]. Delay line anodes allow the determination of the impact positions of the electrons. It is possible to recover the impact positions of coincident pairs even if they hit the same detector. These events we may term “double hits,” whereas we refer to “single hits,” if the electrons are registered on different detectors. Further details of the experimental setup can be found elsewhere.¹² As a pulsed photon source serves the BESSY storage ring operating in the single bunch mode at beamline TGM 4. The data to be presented have been obtained during the maximum available single bunch time of a year, which amounts to about 20 days. Therefore only one photon energy could be selected, which was set to $\hbar\omega = 50 \pm 0.2$ eV. The polarization plane of the linear polarized light is in the drawing plane (see Fig. 1). The electron energies are determined via the flight times, where the BESSY bunch marker is taken as the time reference. The total time resolution is approximately 1.4 ns. This will lead to an energy dependent energy resolution, which is 1.5 eV for 20 eV electrons. A low kinetic-energy cutoff is provided by a retarding mesh right in front of each channel plates. A grounded mesh placed immediately in front of this retarding mesh ensures a field-free region along the flight path. A coincidence circuit ensures that only electron pairs are detected. The spectrometer is part of an ultrahigh

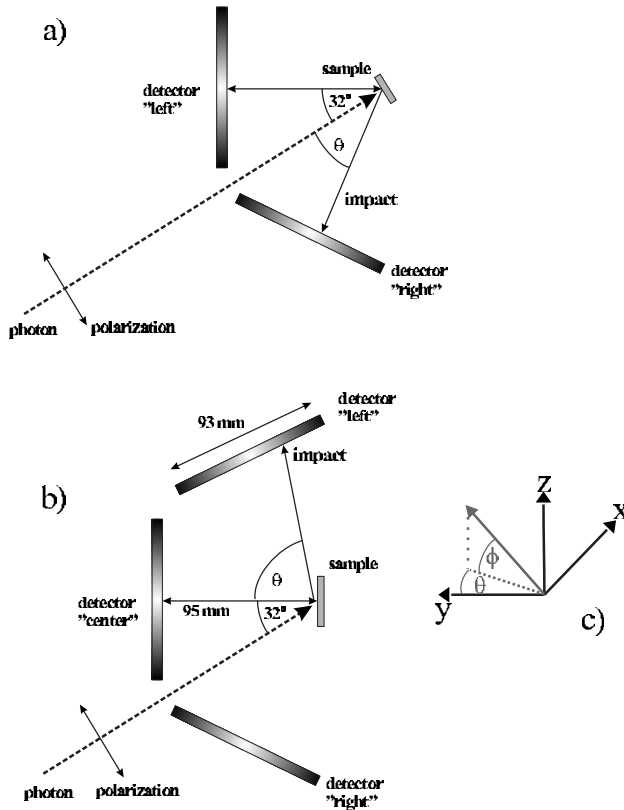


FIG. 1. Schematic view of the experiment and the two different geometries used. The polarization plane of the linear polarized light is in the drawing plane. The photon energy was set to 50 ± 0.2 eV.

vacuum system equipped with standard surface science tools. We define a coordinate system, which has the origin at the sample surface [see Fig. 1(c)]. The y axis is always parallel to the surface normal, whereas the x and z directions are in the surface plane and are orthogonal to each other. Specifically the crystallographic $[\bar{2}11]$ direction is in the drawing plane of Fig. 1, which we define to be the x axis. In order to specify the emission direction of the electrons, we compute the two in-plane components of the momentum. In order to compare the emission directions of electrons with different kinetic energies, we finally calculate the normalized components of the in-plane momentum. These are nothing but the directional cosines, which we label by X and Z, respectively. Each coincident event is then characterized by six coordinates, namely, the individual energies and the individual values of X and Z. We studied a clean and well-ordered Cu(111) surface, which was prepared via Ar sputtering and annealing up to 800 K. The experiments were performed at room temperature. Prior to the discussion of the data, a few technical aspects have to be clarified. As defined above, single hits constitute events where for example one electron is registered on the “left” detector, whereas the other hits the “center” or “right” detector. In this case there is a well-defined way to label the electrons, namely, according to the detector

they hit. It is obvious that this cannot be extended to double hits, since both electrons would get the same label. This leaves certain arbitrariness for plotting the data. This can be avoided if we use a label of either “fast” or “slow” where the distinction comes from the difference in the kinetic energy, namely, $E_{\text{fast}} > E_{\text{slow}}$. Since we want to combine double hits and single hits, we employ the same labeling for the latter, too. Another important aspect is the fact that the detection of double hits with the same kinetic energy is not possible.

III. DOUBLE PHOTOEMISSION IN NORMAL INCIDENCE

In our presentation we start with the experimental results obtained with normal incidence of the photons. As described in the experimental part, we use two detectors in this case, which we may label left and right, respectively. We further consider only single hits, this means only coincidence events where the two electrons hit different detectors are registered. In Fig. 2 we plot the coincidence intensity as a function of the sum energy $E_{\text{sum}} = E_{\text{left}} + E_{\text{right}}$. The vertical dashed line marks the energy position of the maximum sum energy $E_{\text{max}} = 40$ eV imposed by energy conservation, since the work function of the Cu(111) surface (≈ 5 eV) has to be

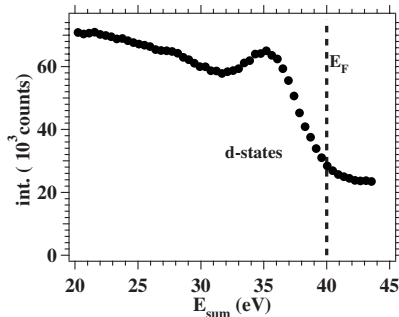


FIG. 2. Plot of the E_{sum} distribution of the $(\gamma, 2e)$ experiment. The vertical dashed line is the energy position of the highest possible sum energy, which follows from energy conservation. A pronounced emission at 35 eV can be noticed.

subtracted twice from the photon energy of 50 eV. It is apparent that the pair emission is governed by a contribution located at $E_{\text{sum}} \approx 35$ eV. We recall that the center of gravity of the Cu 3d band is roughly 2.5 eV below the Fermi level E_F , hence we identify the peak at 35 eV with the pair emission from the Cu 3d bands. It is well known that the Cu(111) surface possesses also a Shockley surface state at the $\bar{\Gamma}$ point.¹³ This state is energetically located in the interval E_F and $E_F - 0.4$ eV. From Fig. 2 we conclude that with the present apparatus and its current limited resolution it is not possible to identify the emission from the surface state. The data shown in Fig. 2 is derived from an integration over the whole accessible angular range, even though the shape of the spectrum has a weakly angular dependence. The background of the intensity distribution of Fig. 2 and its extension above $E_{\text{sum}} = 40$ eV is related to so-called random coincidences. The emission of a single photoelectron is significantly more likely (by a factor of $\approx 10^3$) than the emission of an electron pair upon absorption of a single photon. If a pulse containing two photons hits the sample, the emission of two single photoelectrons is possible. The coincidence logic cannot discriminate between these events and genuine pair emission. The only option one has is to lower the primary intensity, which in turn (due to the Poisson statistics) will increase the probability of finding one photon in a pulse compared to more than one. Two single photoelectrons are not correlated since they originate from two independent excitation processes. For single photoelectrons, energy conservation has to hold, too. This means that the maximum kinetic energy with respect to the vacuum level is the photon energy minus the work function. In our case this amounts to a maximum value of 45 eV. The maximum sum energy of an uncorrelated pair amounts to twice the value. This means if a E_{sum} spectrum is plotted, the intensity can extend up to 90 eV. Of course a genuine electron pair for our experimental conditions cannot have an energy beyond 40 eV.

In Fig. 3 we display the hit pattern of the individual electrons of coincident pairs as a function of the normalized in-plane momentum (or directional cosine). One interesting aspect is how the available energy is shared between the

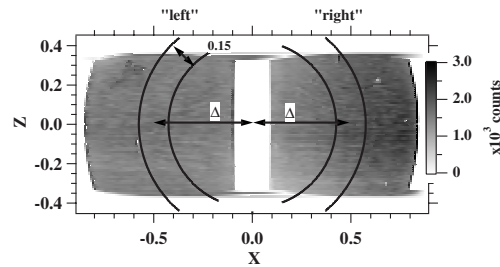


FIG. 3. The hit pattern of electron pairs is displayed. As axes, we use the components of the normalized in-plane momentum of the individual electrons. The excitation was via 50 eV photons, which hits the sample along the surface normal. The pair of arcs on the left and right detector. The gray scale on the right displays the intensity in counts.

electrons, in particular, if we impose geometric constraints. In order to address this point we select regions on the detectors left and right whose boundaries are given by the pair of arcs. The width of these regions is 0.15, and the centers have a distance to the origin given by the value of $|\Delta|$. We ask now how the energy of the two ejected electrons is distributed. This is best done by using a two-dimensional (2D) representation, where the axes are the individual kinetic energies. This we call in the following a 2D energy distribution. The result is shown in Fig. 4 for $\Delta = 0.2$ and $\Delta = 0.7$, respectively. Converted into angles, we constrain the mean angle between the trajectories to be either 23° or 89° , respectively. The dashed diagonal lines in both plots indicate the position of those events, which has a sum energy of 35 eV. We recall from Fig. 2 that at this energy a prominent pair emission occurs. In panel (a) we observe for $\Delta = 0.2$ a boomeranglike distribution. The onset of pair emission at $E_{\text{sum}} = 40$ eV occurs for very unequal energies, which means one of the electrons carries most of the energy. This preference of one electron being fast while the other is slow also occurs for decreasing sum energy. In general the coincidence intensity increases if E_{sum} decreases. The situation for $\Delta = 0.7$ is different as inspection of Fig. 4(b) shows. The onset of pair emission at around $E_{\text{sum}} = 40$ eV is not confined to those electrons that have very unequal energies but occurs for all energy combinations with very similar probability. If we reduce E_{sum} to 35 eV, we note that the intensity remains constant for as long as the energies are outside the regions $20 < E_{\text{left/right}} < 30$ eV and $E_{\text{right/left}} < 10$ eV. From these observations we learn that the prominent emission at $E_{\text{sum}} = 35$ eV occurs for unequal energy sharing and preferably for large values of Δ . In other words the trajectories of the electrons have a large angle. We can emphasize the point if we compute the so-called sharing functions. For a given value of E_{sum} one computes the coincidence intensity as a function of $E_{\text{left}} - E_{\text{right}}$, which is done for $\Delta = 0.2$ and $\Delta = 0.7$ while keeping the sum energy fixed at 35 eV, which defines the pair emission from the 3d states. We allowed an uncertainty of 3 eV, which reflects the width of the peak at $E_{\text{sum}} = 35$ eV. The resulting graph is shown in Fig. 5. These sharing curves will be discussed further in the theoretical section.

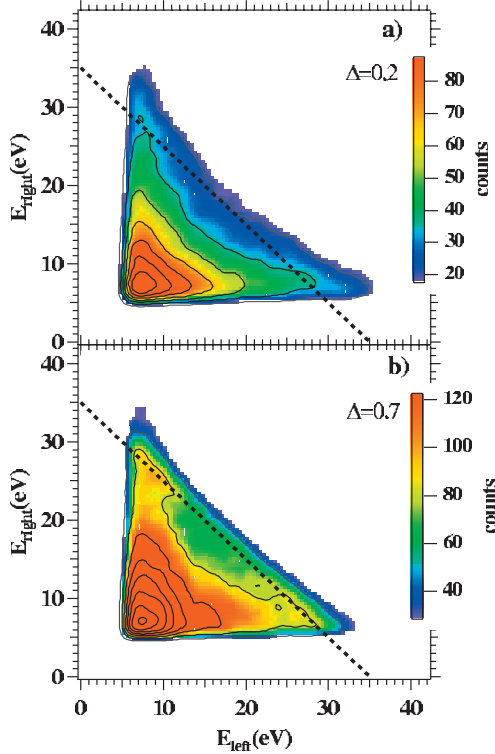


FIG. 4. (Color) 2D energy distributions for $\Delta=0.2$ in (a) and $\Delta=0.7$ in (b). The intensity is given in counts. We added equidistant contours and employed a Gaussian filter. The dashed diagonal line in both plots indicates the emission at $E_{\text{sum}}=35$ eV.

IV. 2D MOMENTUM CONTRIBUTIONS

In this section we want to discuss momentum distributions of the coincidence intensity. More specifically, we want to know what impact a fixed emission direction of one electron has on the momentum distribution of the other electron. For this we used the geometry where the incident photon has an angle of 32° with respect to the normal [see Fig. 1(b)]. This mode also includes the detection of double hits, which are events where both electrons are registered on the same detector. A first hint of the angular distribution can be obtained by an inspection of the 2D energy distributions, which we discuss separately for single and double hits. For the latter the angle between the trajectories of the electron are confined to values between 0° and $\approx 52^\circ$. For single hits the angle can be up to 180° . With this in mind we display the 2D energy distributions in Fig. 6 as a function of E_{fast} and E_{slow} . As a guide to the eye, we added contour lines to both plots representing equidistant levels. In the case of double hits these contour lines surround areas that are elongated along the x axis. Most of the intensity is confined in an area, for which E_{slow} is below 7 eV. Contrary to this the fast electron

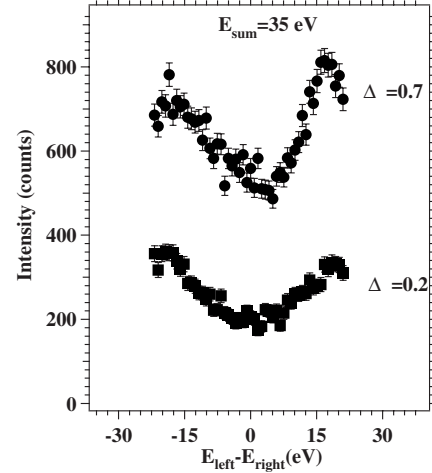


FIG. 5. Sharing curves for $E_{\text{sum}}=35 \pm 1.5$ eV and $\Delta=0.7$. Due to the low kinetic-energy cutoff of 5 eV, the sharing $E_{\text{left}}-E_{\text{right}}$ is in the interval ± 23.5 eV.

can have any value consistent with energy conservation. This unequal energy sharing was also observed in Fig. 4(a) although it was not as pronounced. We recall that the geometrical constraint imposed onto the trajectories ($\Delta=0.2$) amounts to an average angle of about 46° . Clearly for double hits, the trajectories are closer on average. From this we learn that the smaller the angle between trajectories the more pronounced the unequal energy sharing becomes.

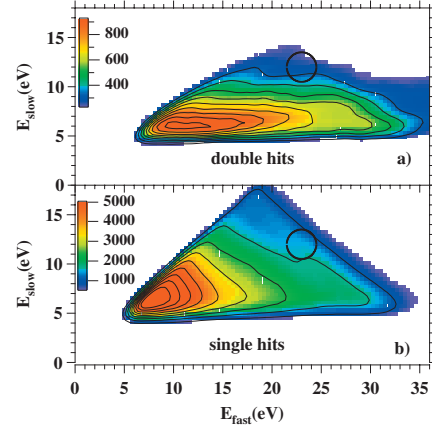


FIG. 6. (Color) 2D energy distribution of coincidence events from a Cu(111) surface excited with 50 eV photons. Panel (a) includes only double hits, in panel (b) we show single hits. Events, which have electron energies that fall into the circle located at $E_{\text{fast}}=23$ eV and $E_{\text{slow}}=12$ eV, will be used for angular distributions. We added equidistant contours and employed a Gaussian filter. The color coding for the intensity is given in counts.

If we look at the 2D energy distribution for single hits, a different picture emerges. The intensity level is about a factor of five higher compared to the double hits. This in retrospect justifies that the omission of double hits in the normal incidence geometry was warranted. Since we know that the trajectories for single hits can be up to 180° , we learn that electrons prefer to avoid each other. This statement will be confirmed and discussed more in details below. Apart from the intensity levels, we also note a different distribution of the coincidence intensity for single hits. Unlike the double hits a very unequal energy sharing is not present. Here the contour lines surround more triangular areas. Similar to the situation depicted in Fig. 4(b), we note a drop in intensity if the electron energies are becoming more equal. After the discussion of the energy distributions, we move on to the momentum distribution of the coincidence intensity. In order to facilitate comparison of electrons with different energies, we will use the normalized in-plane components (or directional cosine). These we will label with X and Z , respectively. We obtain the momentum distributions if we execute the following steps. First we select energies of the fast and slow electron, sufficient statistics require that the selected energies include also those events, where the energies are within 1.5 eV of the chosen values. After this step is completed, we obtain the 2D momentum distributions of the fast and slow electron. These are not independent of each other, we emphasize that every fast electron has a slow counterpart. In Fig. 7(a) and 7(b) the distributions for fast and slow electrons centered at $E_{\text{fast}}=23$ eV and $E_{\text{slow}}=12$ eV are plotted. The intensity is given in counts and the color code is on the right-hand side of the plot. Both distributions display intensity in the forward direction, which increases if the momentum increases. It is now interesting to look only at those events where the fast electron is detected in a narrow region. Such a constraint is indicated by the circle displayed in Fig. 7(a), which has a radius of 0.15 around the origin. One can rephrase this by saying that we fix the emission direction of the fast electron and ask for the intensity of the slow electron around this direction. The result is displayed in Fig. 7(c) after normalization to the intensity of the slow electron in Fig. 7(a). Varying detection efficiencies demand such a procedure. It is very clear that the intensity on the center detector is lower than on the left and right detectors. The coincidence intensity has a minimum, which is centered around $X=0$. The minimum is rather broad and only for $|X|>0.4$ the coincidence intensity starts to increase. At around $|X|>0.8$ the intensity starts to saturate. We can state that the slow electron tends to avoid the fast electron, which is the experimental proof of the existence of the xc hole. This is in line with our previous observations where we performed DPE measurements on a NaCl(100) surface.¹¹ The instrument used at the time had an angular acceptance of 34° . If we convert this into directional cosine, the value is 0.55. With this instrument we were able to observe the central part of the xc hole but could not see a saturation of the coincidence intensity for large momentum values. In other words, we were not able to determine the full size of the xc hole. However, our new instrument has a larger acceptance angle and that makes it possible to determine the full extent. It is of course possible to fix the direction of the slow electron and determine the

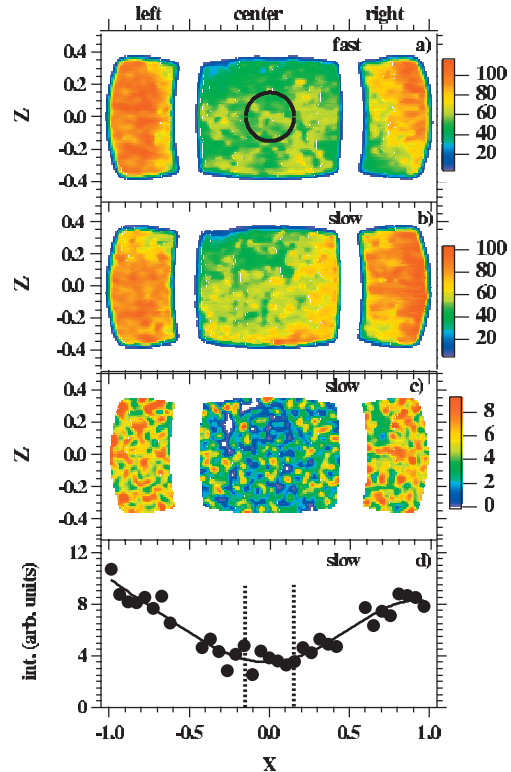


FIG. 7. (Color) The panels display the following distributions, where the electrons have the energies $E_{\text{slow}}=12 \pm 1.5$ eV and $E_{\text{fast}}=23 \pm 1.5$ eV, respectively: Panels (a)–(c) shows 2D distributions of the coincidence intensity where the axes are the components of the normalized in-plane momentum. In panel (a) we plot the for the fast electron, whereas in panel (b) the same for the slow electron is plotted. In panel (c) we plot the intensity for the slow electron if the fast electron is constrained to be within the area defined by the black circle of drawn in panel (a). The color coding indicates the intensity measured in counts. Panel (d) is the intensity profile obtained from (c) upon integrating the intensity for all Z values for a given value of X .

intensity map of the fast electron. The result of such a presentation is qualitatively and quantitatively identical as far as the size and shape of the xc hole is concerned.

V. THEORETIC DESCRIPTION

In this section we analyze our data from a theoretical point of view. For the calculation of the $(\gamma, 2e)$ spectra of the Cu(111) surface, we employ the correlated two-particle layer Korringa-Kohn-Rostoker method that we described in details elsewhere.^{6,14–17} In brief description, two *ab initio* computed single-particle electronic states are coupled via the exchange and the screened Coulomb interaction. The latter is approxi-

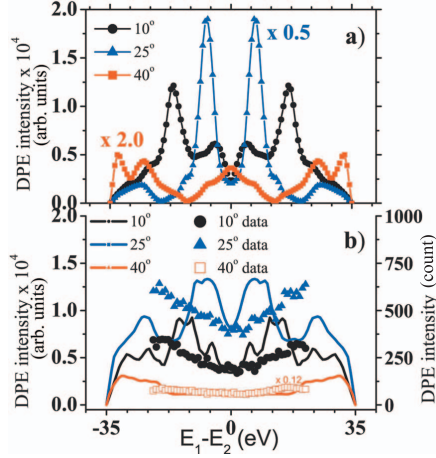


FIG. 8. (Color) The $(\gamma, 2e)$ energy sharing probability: (a) cuts through the 2D intensity map at $\theta=10^\circ$, 25° , and 40° ; (b) sharing distributions same as in (a) additionally averaged over the azimuthal angle ($\Delta\phi=20^\circ$), polar angle ($\Delta\theta=5^\circ$), and kinetic energy ($\Delta E_{1,2}=2$ eV) according to the typical experimental uncertainty values. Included are also the experimental results.

mated by its form in the long-wavelength limit and results in a generic dependence of the computed spectra on the energies and the emission directions of the photoelectrons. This model is supposed to describe only elastic two electron ionization so that energy-loss processes are not included and their contribution to the DPE signal can be a source of difference between theory and experiment. Here, we present calculations for the photon energy 50 eV. The sum energy is $E_1 + E_2 = 35$ eV. These values correspond to the peak position in experimental spectrum shown in Fig. 2. The involved initial electronic states are in the energy window E_F to $E_{\min} = E_F - 5$ eV, which covers most of the Cu(111) d band. To contrast photoemission from the d band with that from surface states, a better experimental resolution is needed. Theoretically, this has been done in Ref. 17. As the photoelectron energies are measured with respect to the Fermi level, we have $E_F = -5$ eV, and the energy conservation implies $E_{\text{sum}} - \omega = E_F + E_{\min}$. The sum energy of the pair is then between $E_{\text{sum}} = 30$ and 40 eV (constant sum energies are indicated by the dashed diagonal line in Fig. 4).

In Fig. 8(a) we present theoretical energy sharing distributions at three different angles: $\theta_{1,2} = 10^\circ, 25^\circ, 40^\circ$. Here the symmetric coplanar geometries $\theta_1 = -\theta_2 = \theta$ and $\phi_1 = \phi_2 = 0$ (Fig. 1, upper scheme) are used. To account for experimental uncertainty in angles and energies, we performed additional calculations and then average them within the domain $\Delta\theta = 5^\circ$, $\Delta\phi = 20^\circ$, and $\Delta E = 2$ eV [Fig. 8(b)]. Inspection of averaged distributions demonstrates that first the intensity grows upon increase in interelectron angle (cf. 10° and 25° curves) because very small angles are suppressed by the Coulomb repulsion. Further increase in angle (cf. 25° and 40°) leads to the intensity falloff. In our model this effect is explainable in terms of strong directional depen-

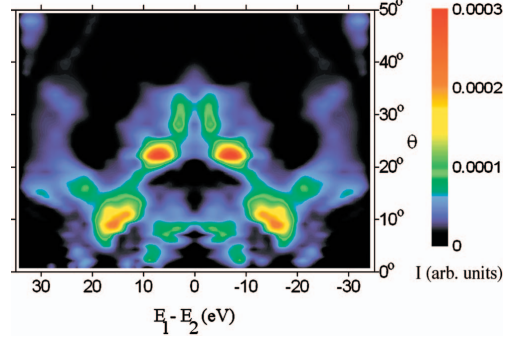


FIG. 9. (Color) The $(\gamma, 2e)$ energy-angular correlation map: the intensity (color line) as a function of the energy sharing ($E_1 - E_2$) and the angle between ejected electrons. The Cartesian coordinates are specified according to Fig. 1 so that y axis is normal to the surface and yz plane is a mirror plane. The photon energy is 50 eV, normal incidence, and is linearly polarized along x . The detection geometry is coplanar symmetric: electrons are emitted in xy plane, their polar angles are kept equal, $\theta_1 = -\theta_2 = \theta$, and serve as a vertical coordinate of the plot.

dence of ee interaction: at large angles electrons become nearly independent and hence the DPE probability rapidly decreases.

Another observation is that strong repulsion at small angles prevents equal energy sharing between electrons. This is reflected, for example, in the shift of the position of the main intensity peaks in Fig. 8(a) and 8(b) for $\theta = 10^\circ$ and $\theta = 25^\circ$; while at 25° electrons have almost the same kinetic energies, at 10° their energies tend to relate approximately as 1 is to 2.5. However, this is only a simple hand-waving argument, whereas the detailed structure of the distributions depends on the peaked structure of the k -resolved density of initial electronic states, as well as on the scattering on the lattice. As for the detailed comparison with the measured values, we concluded that a definitive statement should await further progress in refining the experimental resolution.

To present a more extensive analysis of the electronic correlation in DPE process, we calculate the full set of energy sharing distributions at constant total energy $E_1 + E_2 = 35$ eV for all possible interelectron angles. Again, we chose the symmetric coplanar geometries $\theta_1 = -\theta_2 = \theta$ and $\phi_1 = \phi_2 = 0$ (Fig. 1, upper scheme). Data are arranged in a form of the 2D map where the horizontal coordinate is again the energy difference ($E_1 - E_2$) in electron volt and the vertical coordinate is angle θ . The pattern in Fig. 9 shows that in the present model the appreciable DPE intensity can be expected up to the values of $\theta \approx 40^\circ$ (80° between electrons). In general, we also observe a weak intensity for less correlated geometries, i.e., very large mutual angles of very asymmetric energy sharing. On the other hand the pair correlation carves a hole (the exchange and correlation hole) in the DPE intensity when the two electrons are emitted in close vicinity in momentum space. What we observe in Fig. 9 is, however, a structured hole. This is a result of two further factors: When varying θ or $E_1 - E_2$ one scans through the (two particle)

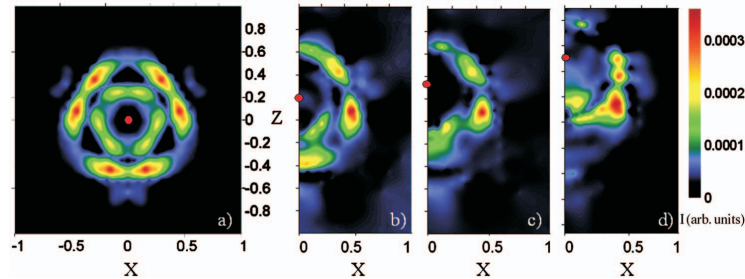


FIG. 10. (Color) The $(\gamma, 2e)$ angular distributions for the pair of slow (12 eV) and fast (23 eV) electrons projected on the normalized surface-parallel momentum plane xz . The photon energy is $\hbar\omega=50$ eV, normal incidence, p polarized. Fast electron is fixed in the position of the red spot. In panel (a) we show the full 2D momentum distribution if the fixed electron is at $X=Z=0$. Panels (b)–(d) show the resulting distribution if the fixed electron moves along Z direction: $Z=0.2, 0.3$, and 0.5 while keeping $X=0$.

initial momentum spectral density of the surface whose peaked structures are then reflected in the DPE intensity. In addition, the emitted electrons experience strong diffraction from the lattice, depending on their wave vectors and the crystal orientation. Energy-angular correlation map in Fig. 9 yields an estimate for the extent of correlation angle (the interelectron angle most favorable for the DPE events, also identified with the radius of the so-called Coulomb correlation hole). Choosing, for example, a pair of electrons with $E_1=10$ eV and $E_2=25$ eV, we find that maximal intensity for $\Delta E=15$ eV corresponds to the relative angle $\theta_1+\theta_2=20^\circ$. Combination of closer kinetic energies $E_1=20$ eV and $E_2=15$ eV results in larger correlation angle $\theta_1+\theta_2=45^\circ$.

To compare with the angular distributions shown in Fig. 7, we plot (Fig. 10) the DPE intensity as a function of the emission direction of one electron. Both kinetic energies and the emission direction of the second electron are fixed. The DPE intensity depends on angular coordinates according to two opposite trends. Interelectron angle has to be small enough to provide sufficiently strong interaction. On the other hand, this angle cannot be very small because of the Coulomb repulsion. Competition between these trends explains the depletion region and then the cloud of high coincidence signal around the position of the fixed electron (depicted by the full red circle Fig. 10). The threefold surface symmetry becomes apparent in the DPE intensity for high symmetric scattering geometry (left panel in Fig. 10). Going away from such symmetric situation (moving the fixed electron along z axis), the intensity circle becomes nonsymmetric and its shape is determined in a nontrivial manner by diffraction, correlation, and initial-state spectral density effects. These trends are also confirmed by another theoretical approach.¹⁸

VI. SUMMARY AND FINAL REMARKS

We have studied the process of electron pair emission from a Cu(111) surface. We excited the specimen with 50 eV

photons. We found that the pair emission shows a prominent contribution from the Cu $3d$ states. Most of this intensity is found for unequal energies of the electrons and a large angle between the trajectories. Participation of surface states could not be identified. Experiments with different photon energies may enhance the contribution of the surface state compared to the bulk states. Theoretical calculations support the first trend about unequal energy sharing but give a lower estimate for the angle at which the emission intensity is maximal.¹⁹ We illustrate this by the energy-angular correlation map, which allows us to trace spatial and energy aspects of $(\gamma, 2e)$ process simultaneously on the same plot. The momentum distribution of the coincidence intensity revealed that the depletion zone around the fixed emission direction of one electron can be fully mapped. The origin of this is due to the xc hole. In this context it is worthwhile to mention the relation to the two-particle intensity interferometry experiments based on the Hanbury Brown–Twiss effect,^{20–23} which leads to enhanced or decreased (also called bunching or antibunching) detection probability of respectively two close bosons or fermions. This phenomena relies purely on the symmetry and shows up for noninteracting quantum particles, e.g., photons or neutral atoms. In our experiment (and theory) this effect is present and shows up as a part of the exchange hole. On the other hand, as we demonstrated above, our spectra are dominated in addition by the interparticle interaction. A separation between the spin-induced and the Coulomb-induced features in the spectra entails the use of spin-resolved detectors. Developments in this direction are currently under way.

ACKNOWLEDGMENTS

We thank the staff of the BESSY II storage ring for the excellent support. Furthermore we wish to thank H. Engelhard and D. Hartung for their skillful work in constructing the apparatus. This work was supported by the DFG through SFB 762.

- ¹E. Wigner and F. Seitz, *Phys. Rev.* **43**, 804 (1933).
- ²J. C. Slater, *Rev. Mod. Phys.* **6**, 209 (1934).
- ³P. Fulde, *Electron Correlations in Molecules and Solids*, Springer Series in Solid State Sciences Vol. 100 (Springer, Berlin, 1993).
- ⁴K. Byczuk, M. Kollar, K. Held, Y.-F. Yang, I. A. Nekrasov, T. Pruschke, and D. Vollhardt, *Nat. Phys.* **3**, 168 (2007), and references therein.
- ⁵J. Berakdar, *Phys. Rev. B* **58**, 9808 (1998).
- ⁶N. Fominykh, J. Berakdar, J. Henk, and P. Bruno, *Phys. Rev. Lett.* **89**, 086402 (2002).
- ⁷H. W. Biester, M. J. Besnard, G. Dujardin, L. Hellner, and E. E. Koch, *Phys. Rev. Lett.* **59**, 1277 (1987).
- ⁸R. Herrmann, S. Samarin, H. Schwabe, and J. Kirschner, *Phys. Rev. Lett.* **81**, 2148 (1998).
- ⁹J. Berakdar, S. N. Samarine, R. Herrmann, and J. Kirschner, *Phys. Rev. Lett.* **81**, 3535 (1998); *J. Berakdar, Phys. Rev. A* **56**, 370 (1997).
- ¹⁰F. U. Hillebrecht, A. Morozov, and J. Kirschner, *Phys. Rev. B* **71**, 125406 (2005).
- ¹¹F.O. Schumann, C. Winkler, G. Kerhervé and J. Kirschner, *Phys. Rev. B* **73**, 041404(R) (2006).
- ¹²F. O. Schumann, C. Winkler, and J. Kirschner, *New J. Phys.* **9**, 372 (2007).
- ¹³S. G. Louie, P. Thiry, R. Pinchaux, Y. Petroff, D. Chandessris, and J. Lecante, *Phys. Rev. Lett.* **44**, 549 (1980); J. A. Knapp, F. J. Himpsel, and D. E. Eastman, *Phys. Rev. B* **19**, 4952 (1979); S. D. Kevan, *Phys. Rev. Lett.* **50**, 526 (1983).
- ¹⁴J. Berakdar, H. Gollisch, and R. Feder, *Solid State Commun.* **112**, 587 (1999).
- ¹⁵N. Fominykh, J. Henk, J. Berakdar, P. Bruno, H. Gollisch, and R. Feder, *Solid State Commun.* **113**, 665 (2000).
- ¹⁶N. Fominykh, J. Henk, J. Berakdar, and P. Bruno, in *Correlations, Polarization, and Ionization in Atomic Systems*, edited by D. H. Madison and M. Schulz (AIP, Melville, NY, 2002), pp. 210–216.
- ¹⁷N. Fominykh and J. Berakdar, *J. Electron Spectrosc. Relat. Phenom.* **161**, 125 (2007).
- ¹⁸H. Gollisch, N. v. Schwartzberg, and R. Feder, *Phys. Rev. B* **74**, 075407 (2006).
- ¹⁹F. O. Schumann, J. Kirschner, and J. Berakdar, *Phys. Rev. Lett.* **95**, 117601 (2005).
- ²⁰R. Hanbury-Brown and R. Q. Twiss, *Nature (London)* **178**, 1046 (1956).
- ²¹D. H. Boal, C. K. Gelbke, and B. K. Jennings, *Rev. Mod. Phys.* **62**, 553 (1990).
- ²²H. Kiesel, A. Renz, and F. Hasselbach, *Nature (London)* **418**, 392 (2002).
- ²³T. Jelts, J. M. McNamara, W. Hogervorst, W. Vassen, V. Krachmalnicoff, M. Schellekens, A. Perrin, H. Chang, D. Boiron, A. Aspect, and C. I. Westbrook, *Nature (London)* **445**, 402 (2007).

FAST TRACK COMMUNICATION

Correlated positron–electron emission from surfaces

G A van Riessen, F O Schumann, M Birke, C Winkler and J Kirschner

Max Planck Institute of Microstructure Physics, Weinberg 2, 06120 Halle, Germany

E-mail: riessen@mpi-halle.mpg.de and schumann@mpi-halle.mpg.de

Received 27 August 2008, in final form 1 September 2008

Published 12 September 2008

Online at stacks.iop.org/JPhysCM/20/442001

Abstract

We studied positron–electron pair emission from a LiF(100) surface following excitation by a positron beam with a kinetic energy of 85 eV. We show for the first time that emission of time-correlated positron–electron pairs occurs.

1. Introduction

Intense experimental and theoretical effort has been invested over recent decades to understand the mutual interaction of electrons in a solid that underlie phenomena such as magnetism and superconductivity. In recent years it has been demonstrated that information about the correlation between a pair of electrons in the solid can be recovered from the observed momenta of the pair of electrons emitted from the surface upon photon or electron impact [1–10]. Experimental advances have only recently overcome the inherent challenge in such correlation spectroscopy that lies in the small probability of detecting two particles produced by a single event.

Interactions between electrons in a solid are due to Coulomb and exchange interactions, the role of which was discussed in seminal papers by Wigner and Seitz [11] and Slater [12]. Notably, we have been able to directly observe the so-called exchange–correlation hole [8–10], a direct manifestation of Coulomb and exchange interactions that leads to a region of reduced electron density surrounding each electron. As Slater pointed out, the two contributions to the exchange–correlation hole may be different. Disentangling their effects is possible when one of the interacting electrons is replaced with its antiparticle, the positron. As positrons and electrons are distinguishable particles the Pauli principle does not apply and their interaction is solely Coulombic. This can be realized experimentally by measuring the momenta of an electron and positron emitted from a surface upon positron impact.

The differences and common features of electron emission from metallic surfaces upon the impact of low energy

positrons or electrons has been discussed by Berakdar [13]. Berakdar also first considered theoretically positron–electron pair emission upon the impact of low energy positrons and diffraction of the positron–electron pair, illustrating how distinguishability of the electron and positron leads to differences between the angular distribution of electron–positron pair emission upon positron impact and electron–electron pair emission upon electron impact.

In order to establish the feasibility of studying angular distributions one has to establish that correlated positron–electron pair emission from a surface does occur. Further, it must be determined whether the pair emission occurs with significant probability. In this brief report we will demonstrate that this is indeed the case.

2. Experiment

The experiment was performed at the positron beamline NEPOMUC (NEutron induced POSitron source MUniCh) located at the research reactor FRM-II in Garching [14, 20]. A beam of moderated positrons with kinetic energy of 85 eV (with respect to the vacuum level) was magnetically guided to the end of the beamline. There the beam was extracted from the magnetic field through an aperture in a magnetic shield and focused by electrostatic optics onto a LiF(100) crystal. The crystal and optics were mounted in an UHV chamber. The positron beam at the sample was aligned and characterized using a multichannel plate detector with a phosphor screen that was positioned in the plane imaged by the transfer lenses of two hemispherical analyzers (Scienta R4000). The FWHM of the beam at the sample position was approximately 1 mm. The

primary positron flux was estimated to be $5 \times 10^4 \text{ s}^{-1}$ from the rate of positron annihilation at the sample measured using a pair of gamma detectors to detect in coincidence collinear gamma rays. This was the highest positron intensity achievable at the time. The energy width (FWHM) of the positron beam was estimated from the width of the elastic peak to be approximately 4 eV.

LiF(100) was chosen as a target for this experiment because, in contrast to metals, its wide band gap prohibits an electron emitted from the valence band from losing a continuous range of energy below the band gap energy by electronic excitations. Experience with electron pair emission upon electron impact has shown that this leads to a region of low inelastic contributions in the spectrum that improves the ability to distinguish pair emission from the valence band [8, 9, 15]. The interaction of positrons with LiF has also been studied [16, 17]. Furthermore, previous experience has shown that a clean LiF(100) is easily prepared and when held at 150 °C contamination accumulating on the surface in vacuum is minimal and electrostatic charging of the surface is effectively mitigated.

As illustrated in figure 1, the primary positron beam was directed along the LiF(100) surface normal. The electron–optical axes of the analyzer input lenses were symmetrically arranged in the scattering plane with a separation of 90° such that the angle with respect to the surface normal was 45° for each one. One analyzer was configured to detect electrons while the other was configured to detect positrons by reversing the polarity of the voltages applied to the lens elements and analyzer components. We optimized the voltages applied to the analyzer transfer lens elements to provide high transmission of low kinetic energy electrons or positrons with large pass energies. Although it is possible, for the present first experiment the lenses were operated in a mode that does not preserve the angular information of the detected particles. An energy range of approximately $\pm 5\%$ of the pass energy is measured simultaneously by using a spatially resolving detection scheme. With the analyzers set to a mean energy of 30 eV and a pass energy of 300 eV it was possible to detect electron–positron pairs for which the kinetic energy of the positron E_{e^+} and of the electron E_{e^-} were in the range 15–45 eV and the sum energy of the pair $E_{\text{sum}} = E_{e^+} + E_{e^-}$ was in the range 30–90 eV.

The detectors consisted of a pair of multichannel plates (MCP) in a chevron configuration together with a resistive anode. The same detection scheme was employed for electrons and positrons, except that for the detection of positrons the front MCP was negatively biased with respect to a mesh placed in front of it. There is little information available regarding the efficiency of positron detection by MCP, although there are various reports of using channeltron detectors for positrons (e.g. Goodyear and Coleman [18]). It is reasonable to assume that it is comparable to the electron detection efficiency because the detected signal in both cases results from an electron avalanche initiated with significant probability by secondary electrons when the electron or positron impacts the MCP surface.

A conventional coincidence circuit was used to ensure that only positron–electron pairs were detected and to distinguish

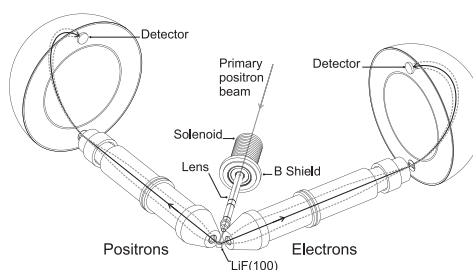


Figure 1. Simplified diagram of the experiment employing two hemispherical analyzers. A primary positron beam is focused onto a LiF(100) surface at normal incidence. The optical axis of each of the transfer lenses are symmetrically positioned in the same plane as the positron beam such that positrons or electrons were detected with a mean angle of 45° with respect to the surface normal.

those that were emitted during a single process on the basis of the time interval between detection of a particle at each of the two detectors. The time interval between the detection of a particle on one detector and the arrival of a second particle on the other detector is measured from signals originating from the multichannel plates that are digitized after amplification and constant fraction discrimination.

Correlated pairs, or *true coincidences*, are emitted during a single process that occurs on a timescale much shorter than the experimental time resolution. The process of most interest that produces correlated pairs is a single scattering event. Multiple scattering events may also occur on a timescale much smaller than the instrumental time resolution. These can generally be distinguished on the basis of the energy of the pair. The measured time interval between the detection of particles comprising a correlated pair shows a finite distribution over a time range that is characteristic of the instrument time resolution. Uncorrelated pairs, or *accidental coincidences* are also detected. These involve two particles which originate from different ionization events, predominantly from electrons emitted following interaction with two different primary positrons. The significance of such events is minimized by using a low primary positron intensity because their rate shows a quadratic dependence on the primary flux, whereas the rate of true coincidences shows a linear dependence. However, the rate of accidental coincidences can also be simply distinguished without varying the primary flux as they are detected with a randomly distributed time interval. Therefore we recorded events for which a pair was detected within a time interval of 150 ns to allow the accidental rate to be estimated and the true coincident rate to be clearly distinguished. We have verified this approach and the correct performance of the instrument by studying the electron pair emission via electron impact both in the laboratory and after installation of the spectrometer at the NEPOMUC beamline. A more detailed account of the instrument will be given elsewhere [19]. The total data acquisition time for the positron experiment was 62 h.

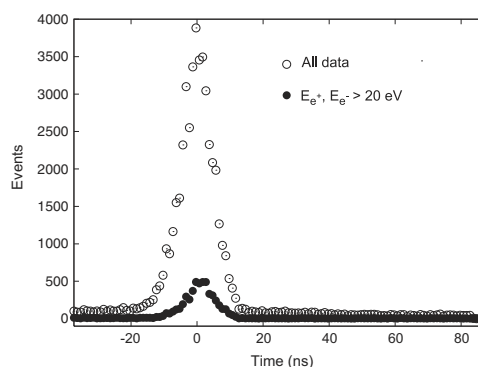


Figure 2. Intensity versus arrival time differences for all detected electron–positron pairs (open circles) and for a subset of the same data that includes only pairs for which the positron and electron were detected with kinetic energy greater than 20 eV (solid circles). The peak in the data is indicative of time-correlated pair emission of positron–electron pairs upon impact with 85 eV positrons.

3. Results

In figure 2 we show the time interval distribution for all detected positron–electron pairs (open circles). A clear peak is present on an essentially constant background. We emphasize that the presence of this peak is evidence of correlated emission of positron–electron pairs from the LiF(100) surface. The area of the peak is a factor of about 20 larger than the area of the background upon which it is superimposed. This very high ratio clearly suggests that an acceptable ratio of true to random coincidences would be maintained with much higher primary positron intensity. The FWHM of the peak, approximately 10 ns, is determined by the time resolution of the instrument, which includes a kinetic energy dependence due to variations in the flight time from the sample to the detector. No attempt has been made to correct the data for this effect as it is accompanied by a flight-time dependency on the angle at which a particle is emitted, and more significantly, on the angle at which the particle enters the hemispherical analyzer. The width is in good agreement with that observed for electron pair emission upon electron impact from the same surface under similar conditions. Our electron–optical simulations also confirm this interpretation qualitatively and quantitatively. To facilitate the discussion that follows we have also shown in figure 2 the time interval distribution for a subset of data that includes only data for which both the electron and positron were detected with a kinetic energy greater than 20 eV. The peak in this data is slightly narrowed and shifted with respect to the peak for the complete data in accordance with energy dependence of the coincidence timing.

We now turn our attention to the energy distribution of the time-correlated electron–positron pairs. The detected intensity of positron–electron pairs increases rapidly from sum energy $E_{\text{sum}} = E_{e^+} + E_{e^-}$ of approximately 60 eV toward lower sum energy. However, our interest lies in the positron–electron

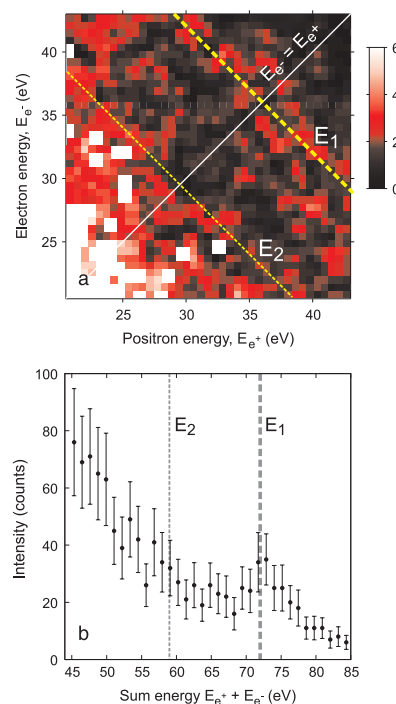


Figure 3. (a) Energy distribution of positron–electron pairs emitted from LiF(100) upon 85 eV positron impact. The intensity indicates the number of correlated pairs detected for each electron and positron energy combination. Only part of the total energy range measured is shown. (b) The positron–electron pair sum energy (E_{sum}) distribution which is the integrated intensity along a 10.3 eV wide strip centred along the line $E_{e^+} = E_{e^-}$ shown in (a). E_1 and E_2 label respectively the maximum sum energy for correlated pair emission and the maximum sum energy available to pair if a participating particle loses energy by an electronic excitation that transfers a valence electron into the conduction band.

energy distribution at higher sum values that are associated with elastic processes involving electrons in the LiF valence band. For analysis of the energy distribution in this region we consider only events for which the time difference is within ± 10 ns of the peak centroid in the subset of the data for which E_{e^+} and E_{e^-} are both greater than 20 eV, i.e. the data within the peak shown with solid circles in figure 2. This selection contains very few accidental coincidences. A two-dimensional energy spectrum, E_{e^+} versus E_{e^-} , constructed from the selected events is shown in figure 3(a). A weak ridge can be seen that along $E_{\text{sum}} \approx 72$ eV. This feature, labelled E_1 in figure 3(a), is the central result of this work. It is revealed more clearly in figure 3(b) which shows the integrated intensity along a 10.3 eV wide strip centred along the line $E_{e^+} = E_{e^-}$, indicated by the solid white line in figure 3(a), against the sum energy $E_{\text{sum}} = E_{e^+} + E_{e^-}$.

The significance of the feature at 72 eV in the sum energy distribution can be understood from a simple consideration of energy conservation that requires that the maximum sum energy for correlated positron–electron pairs to be given by the primary positron energy minus the energy required to emit an electron from the top of the valence band. Because the conduction band is close to the vacuum level in LiF, the latter quantity is essentially the band gap, which is 13.0 ± 0.4 eV [7]. Therefore the upper limit for E_{sum} in the present experiment is 72 eV, which is in close agreement with the position of the peak in the sum energy distribution. The peak can therefore be attributed to scattering events that involve an 85 eV primary positron with an electron from the top of the valence band. A corresponding feature is observed in the sum energy distribution of electron pairs under electron impact with the same apparatus and with previous experiments [15]. We emphasize that this feature is not observed in single particle spectroscopy because the energy of the single electrons detected is not constrained by the energy conservation condition described above. The feature at 72 eV sum energy in the present experiment is therefore the definitive evidence that correlated positron–electron pairs are emitted from a surface under positron impact.

The continuously increasing intensity below about 60 eV, excluded from figure 3, can be attributed to inelastic processes. If an electronic excitation transfers a valence electron into the conduction band, the maximum sum energy available will be reduced by the band gap energy of 13–59 eV. This position is labelled E_2 in figure 3. The inelastic processes that slow a positron implanted in wide band gap materials like LiF have been broadly discussed in the context of positron remission and positronium emission [17, 21, 22]. It is generally accepted that positron energy loss is dominated by production of collective electronic excitations and by electron–hole pair and exciton formation until the positron energy falls below the band gap and these processes are no longer energetically possible [17]. As with electrons, a low kinetic energy positron beam also undergoes diffraction at a crystal surface [16, 21, 23, 24]. The intensity of a Bragg peak observed for a positron energy close to that of our primary beam has been reported to be only about 0.1% of the primary intensity [16]. This is consistent with our own observations and partly explains the relatively low intensity of the peak at $E_{\text{sum}} = 72$ eV in the energy spectrum shown in figure 3.

The charged particle optics and detection scheme employed in the experiment allow the emission angle of the detected particles to be measured simultaneously with the kinetic energy, albeit with significant reduction in detection efficiency. Such a mode of operation, which is of course necessary for a momentum resolved pair emission experiment, was not used because beamtime was limited and count rates were low. Our experience with electron–electron pair emission shows that counting statistics will generally impose a practical limit on the effective energy and angular resolution. This is because the energy and angular distribution recorded by one detector must be partitioned in such a way that each partition includes sufficient data to allow statistically meaningful analysis of the corresponding (coincident) distribution seen

by the second detector. To achieve an acceptable effective energy and angular resolution we require an increase in count rate and acquisition time. The data indicate that we would have measured an acceptable ratio of true coincidences to accidental coincidences with a primary positron intensity a factor of twenty greater. We are currently in the process of improving our experimental apparatus to make this possible while minimizing the positron beam area (which affects energy and angular resolution). It has been demonstrated that NEPOMUC beamline can deliver substantially more intensity than we require [25]. We conclude that a momentum resolved experiment is therefore viable.

4. Summary

We have shown that the correlated emission of positron–electron pairs from solid surfaces occurs. Upon impact with 85 eV positrons, positron–electron pairs were detected from a LiF(100) surface with a weak peak in the pair energy distribution at approximately 72 eV that is attributed to the primary positron scattering with an electron from the top of the valence band. These observations demonstrate the viability of performing momentum resolved measurements of the positron–electron pair distribution upon positron impact.

Acknowledgments

We acknowledge the dedicated effort by the NEPOMUC team, lead by Dr C Hugenschmidt, to make the beamline available.

References

- [1] Berakdar J 1998 *Phys. Rev. B* **58** 9808
- [2] Berakdar J, Gollisch H and Feder R 1999 *Solid State Commun.* **112** 587
- [3] Feder R, Gollisch H, Meinert D, Scheunemann T, Artamonov O M, Samarin S N and Kirschner J 1998 *Phys. Rev. B* **58** 16418
- [4] Fominykh N, Henk J, Berakdar J, Bruno J, Gollisch J and Feder R 2000 *Solid State Commun.* **113** 665
- [5] Gollisch H, Schwartzberg N v and Feder R 2006 *Phys. Rev. B* **74** 075407
- [6] Kirschner J, Artamonov O M and Samarin S N 1995 *Phys. Rev. Lett.* **75** 2424
- [7] Samarin S, Artamonov O M, Suvorova A A, Sergeant A D and Williams J F 2004 *Solid State Commun.* **129** 389
- [8] Schumann F O, Kirschner J and Berakdar J 2005 *Phys. Rev. Lett.* **95** 117601
- [9] Schumann F O, Winkler C and Kirschner J 2007 *New J. Phys.* **9** 372
- [10] Schumann F O, Winkler C and Kirschner J 2007 *Phys. Rev. Lett.* **98** 257604
- [11] Wigner E and Seitz F 1933 *Phys. Rev.* **43** 804
- [12] Slater J C 1951 *Phys. Rev.* **81** 385
- [13] Berakdar J 2000 *Nucl. Instrum. Methods Phys. Res. B* **171** 204
- [14] Hugenschmidt C, Schreckenbach K, Stadlbauer M and Straßer B 2005 *Nucl. Instrum. Methods Phys. Res. A* **554** 384
- [15] Samarin S, Berakdar J, Suvorova A, Artamonov O M, Waterhouse D K, Kirschner J and Williams J F 2004 *Surf. Sci.* **548** 187
- [16] Mills A P and Crane W S 1985 *Phys. Rev. B* **31** 3988
- [17] Tuomisaari M, Howell R H and McMullen T 1989 *Phys. Rev. B* **40** 2060

- [18] Goodyear A and Coleman P G 1995 *Meas. Sci. Technol.* **6** 415
- [19] van Riessen G, Birke M, Winkler C, Schumann F O and Kirschner J 2008 in preparation
- [20] Hugenschmidt C, Brunner T, Legl S, Mayer J, Piochacz C, Stadlbauer M and Schreckenbach K 2007 *Phys. Status Solidi c* **4** 3947
- [21] Schultz P J and Lynn K G 1988 *Rev. Mod. Phys.* **60** 701
- [22] Mills A P and Crane W S 1984 *Phys. Rev. Lett.* **53** 2165
- [23] Rosenberg I J, Weiss A H and Canter K F 1980 *Phys. Rev. Lett.* **44** 1139
- [24] Weiss A H, Rosenberg I J, Canter K F, Duke C B and Paton A 1983 *Phys. Rev. B* **27** 867
- [25] Hugenschmidt C, Löwe B, Mayer J and Piochacz C 2008 *Nucl. Instrum. Methods Phys. Res. A* **593** 616–8

Sensing the electron-electron correlation in solids via double photoemission

F.O. Schumann^{*}, C Winkler, and J. Kirschner

Max-Planck Institute of Microstructure Physics, Weinberg 2, 06120 Halle, Germany

Received XXXX, revised XXXX, accepted XXXX
Published online XXXX

PACS 79.60.-i, 73.20.At, 79.60Bm, 73.20.-r

^{*} Corresponding author: e-mail schumann@mpi-halle.de, Phone +49-345-5582616, Fax +49-345-5511223

We discuss the electron pair emission from surfaces upon the absorption of a single photon, also called double photoemission (DPE). This experiment is particularly sensitive to the electron-electron interaction, because for independent electrons the DPE intensity is zero. We outline the experimental development of this technique over the past decade. Going beyond the mere detection of pairs we advanced the instrumentation, we are able to measure the kinetic energies and emission angles of a wide angular acceptance.

We will show how the available energy is distributed among the electrons and how the angular distributions look like. The latter enabled us to make contact to an important concept of modern solid state theory, namely the exchange-correlation hole. We demonstrate that the exchange-correlation hole manifests itself in a depletion zone of the coincidence intensity around the fixed emission direction of one electron. The experiments were performed at the synchrotron facilities BESSY I and BESSY II.

Copyright line will be provided by the publisher

1 Introduction In electronic systems which contain more than one electron the interaction between electrons plays an important role. The origin of the mutual influence is due to the Pauli principle and the Coulomb interaction. The additional term in the Schrödinger equation describing the electron-electron interaction makes an analytical solution impossible. Therefore one has to resort to approximations and appealing ones are those, which employ an effective single particle picture. As an example one may consider the He atom, the simplest two-electron system besides the H₂ molecule. If one completely neglects the electron-electron interaction in the description one obtains for the energy required to double ionize a He atom a value of 108.8 eV. For this determination we make use of the known exact solution of the H atom. This value is different by a large margin from the experimental observation. Using photons for excitation to ionize the He atom and to liberate the two electrons an energy in excess of 79 eV is required. An improved description can be formulated if one makes use of the intuitively clear assumption that each electron is located near the nucleus.

This in turn means that each electron does not experience the full Coulomb potential of the nucleus. We expect that effectively each electron will screen to some extent this bare Coulomb potential. Consequently one replaces the nuclear charge $Z=2$ by $Z=2-S$, where the parameter S describes the amount of screening. By doing so we have included the electron-electron interaction in an approximation, while maintaining in a formal sense an independent electron picture. For this model an analytic solution is possible, again we make essentially use of the known result for the H-atom. Adopting a value of $S=0.656$ one obtains good agreement with experiment as far as the energy required to ionize and double ionize the He atom is concerned.

The treatment of an electronic system with a large number of electrons becomes rapidly more complex than the atomic case. There exist a variety of so-called many body effects, which are the manifestation of the electron-electron interaction. Ferromagnetism and superconductivity may suffice as examples. In a ferromagnet the spins at different lattice sites align parallel to each other, which is due to

Copyright line will be provided by the publisher

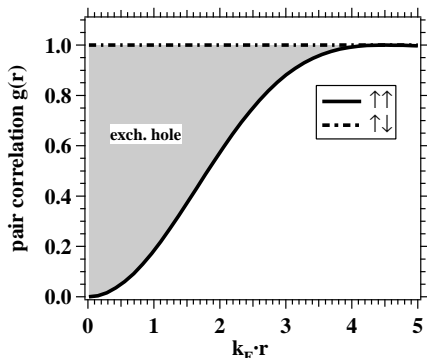


Figure 1 Pair correlation function $g(x)$ for the free (non-interacting) electron gas, where x equals $k_F r$. The solid line shows the dependence for parallel spins, while the dashed line is for antiparallel aligned spins. The shaded area is a measure of the charge missing around the vicinity of an electron. This amount equals exactly one elementary charge and is called the exchange-hole.

the exchange interaction between the electrons, which is essentially the Coulomb interaction modified by the Pauli principle. Likewise electrons forming a Cooper pair interact (within the BCS theory) via electron-phonon coupling.

Nevertheless we start to discuss the simplest model for describing a metallic solid, namely the free electron gas. There one neglects the Coulomb interaction and hence the electrons move independently from each other. Despite the fact that this picture has to be a crude approximation, it contains very important features. For the development of the solid state theory it was a great success of this model that it was able to predict the temperature dependence of the electronic specific heat correctly. In context of our work another feature of the free electron model is of relevance. Although the global charge distribution is uniform within this model it turns out that the charge distribution around each electron is not uniform. In order to elaborate on this it is now instructive to pose the question what is the probability to find one electron at location \mathbf{r}_1 , while the other is at \mathbf{r}_2 and how does it vary with the difference vector $\mathbf{r}_1 - \mathbf{r}_2$ between them. The free electron gas is isotropic, hence only the length of the distance vector $r = |\mathbf{r}_1 - \mathbf{r}_2|$ is of relevance. We have to distinguish parallel ($\uparrow\uparrow$) and antiparallel ($\uparrow\downarrow$) alignment of spins. The entity we are looking for is the so-called pair correlation function $g_{\uparrow\uparrow}(r)$ and $g_{\uparrow\downarrow}(r)$, respectively. For parallel spins we know immediately from the Pauli principle that the two electrons with the same spin cannot be at the same location. For very large distances we expect to find with certainty another electron, after all there are electrons in this model, which are described by plane waves. Consequently what is left to do

is to determine the length scale over which the probability rises from 0 to 1. The calculation of $g_{\uparrow\uparrow}(r)$ is straightforward and was first reported by Wigner and Seitz [1], it can be found in solid state physics textbooks, e.g. [2]. It turns out that the natural variable is the term $k_F r$ in which k_F is the Fermi momentum, the result for $g_{\uparrow\uparrow}$ is:

$$g_{\uparrow\uparrow}(x) = 1 - 9 \cdot \frac{(\sin(x) - x \cdot \cos(x))^2}{x^6} \quad (1)$$

with $x = k_F r$. We have plotted this result in fig.1 as the solid line. We notice that $g_{\uparrow\uparrow}$ rapidly increases and at about $x = 4$ has essentially approached one. We recall that for metals typical values for k_F are of the order $1-2 \text{ \AA}^{-1}$. This means that over a length scale of a few nearest neighbors $g_{\uparrow\uparrow}(r)$ has the value 1. For antiparallel spins the result for $g_{\uparrow\downarrow}(r)$ is particularly simple since it has a constant value of 1, which is drawn as dashed line in fig.1. The Pauli principle does not prohibit two electrons to be at the same location if the spins of the electrons are different. From this evaluation of the pair correlation function it becomes apparent that each electron is surrounded by a reduced electron density compared to the global average

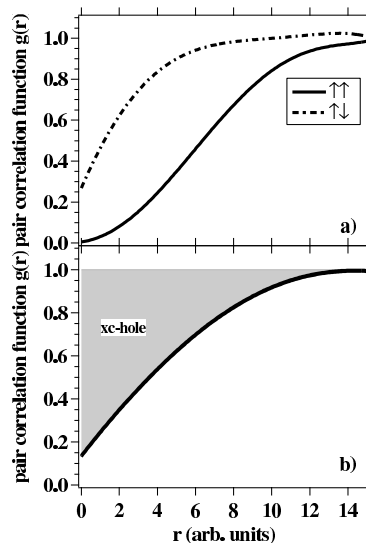


Figure 2 Schematic behavior of the pair correlation function $g(r)$ for an interacting electronic system following the idea of Slater [3]. In panel a) we plot $g(r)$ for parallel (solid curve) and antiparallel (dashed curve) spin alignment. In panel b) we show the average of the two functions. The shaded area is a measure of the charge missing around the vicinity of an electron. This amount equals exactly one elementary charge and is called the exchange-correlation hole.

of the free electron gas. The area of the shaded region of fig.1 is a measure of this and it turns out that exactly one electron charge is missing, which is also known as the exchange hole. From this we learn an important fact, namely that each electron is effectively screened for distances more than a few lattice constants away. If we consider an electronic system including the Coulomb interaction we expect that also electrons with antiparallel spins to avoid each other. The schematic behavior of the pair correlation as a function of the distance between the electrons is depicted in fig.2, where made use of the ideas suggested by Slater [3]. As for the case of non-interacting electrons $g_{\uparrow\uparrow}(\mathbf{r})$ vanishes if $r=0$, while $g_{\uparrow\downarrow}(\mathbf{r})$ is strongly reduced from the value 1. It is intuitively clear that it is energetically not favorable for electrons to be close to each other, although it is not forbidden as for the case of electrons with parallel spins. The average of the $g_{\uparrow\uparrow}(\mathbf{r})$ and $g_{\uparrow\downarrow}(\mathbf{r})$ distributions is shown in panel b) of fig.2. This curve describes the probability to find an electron of any spin around a fixed electron and the net result is that each electron is surrounded by a reduced electronic charge. The shaded area is a measure of the missing charge and one finds that exactly one electronic charge is missing. In this context we talk about the exchange-correlation (xc) hole. From this discussion we learn that a more appropriate description of the electron-electron interaction is to use a screened Coulomb potential of the form $V \sim \frac{1}{r} e^{-\frac{r}{\lambda}}$ rather than the bare Coulomb interaction. In this context the screening length λ is a measure of the lateral dimension of the xc-hole. This concept of the exchange-correlation hole was introduced in seminal papers by Wigner & Seitz and Slater more than 70 years ago [1, 3, 4]. It is important to point out that this concept is an integral part of modern solid state theory. Within the framework of the density functional theory one employs often the so-called local density approximation (LDA). Essentially all many-body effects of the interacting electron system are cast into the so-called exchange-correlation energy functional. For this one usually uses the expression for an interacting electron gas, which incorporates the exchange-correlation hole. There are strong theoretical efforts underway, which aim to derive a more accurate description beyond the LDA. Central to these activities is the pair correlation function.

The properties of matter are ultimately determined by the electronic properties. A spectroscopic means to study the electronic properties is photoemission. In particular, angle-resolved energy distributions allow comparison with band structure calculations. Usually, one discusses peaks in the intensity distributions within an effective single-electron picture. Recent advances in the angle and energy resolution have made it possible that photoemission allows to observe effects due to many-body interactions. These so-called kinks in the $E(k)$ curve or dispersion are the result of the electron-electron interaction or the coupling to other degrees of freedom [5]. Electrons will not move independently through a solid, but will experience a mutual

influence in their motion. Clearly the route, which goes beyond single electron spectroscopy will reveal aspects of the electron-electron correlation not accessible by photoemission. An experimental access to study the electron-electron interaction is to use the technique of double photoemission (DPE), which is absorption of a single photon and the simultaneous emission of an electron pair. The power of the tool can be understood by considering some basic facts. In the absence of an electron-electron interaction the electronic system consists of independent electrons, consequently the description with single electron wave functions is allowed, for example via a Slater determinant. If an electron of such a system absorbs a photon and is ejected other electrons will not "feel" this and the emission of a second electron (or more electrons) will not occur, although it is energetically possible if the photon energy is higher than twice the work function. This intuitive picture can be cast into a theoretical framework, which shows that within the dipole approximation a finite electron-electron interaction leads to a finite DPE intensity [6]. With this in mind it becomes clear that DPE is particularly sensitive to the electron-electron interaction. Moreover, a theoretical study on the DPE emission from a Cu(100) surface clearly showed that the exchange-correlation hole manifests itself in the angular distribution of the coincidence intensity [7–9]. The power of DPE has also been recognized in studies of atomic or molecular targets [10–12]. As it turns out the first DPE experiment on solids was performed on alkali samples in the year 1970 by Gazier and Prescott [13]. The next experimental result, obtained from noble gas films, appeared in 1987 [14, 15]. In both of these early experiments it was demonstrated that the process of electron pair emission upon photon absorption does exist, though no discrimination with respect to energy was performed at the time. In order to make DPE from surfaces a viable tool major developments are necessary to obtain energy and angular distributions. Our recent achievements are the subject of this review. In particular, we will show that we are able to observe the manifestation of the exchange-correlation hole.

2 General aspects of the experiment The recent success has been only possible because of significant technical improvements of the instrumentation. The results we are going to present in this review have been obtained with different generations of machines. In common to all is the use of the time-of-flight (TOF) technique together with a fast coincidence circuit, which ensures the detection of electron pairs only. A TOF set-up needs a pulsed excitation source for which we employed the single-bunch mode of the BESSY I and BESSY II storage rings at the beamlines TGM 4 and CP-NIM. The storage ring bunch marker was used as a time reference in order to determine the kinetic energy of the electrons from the TOF spectra. We quote the kinetic energy with respect to the vacuum level. As we go along, we will briefly describe the set-up used, a more detailed account can be found in the original publications.

A few general remarks of electron pair detection are in order. The process we are interested in is the emission of a pair upon absorption of a single photon. It is important to realize that it is not possible that each light pulse hitting the sample contains exactly one photon. The distribution of the number of photons in a light pulse is of statistical nature and is described by the Poisson statistics. The only adjustment possible is to fix the average number of photons in the light pulses. Suppose that we adjusted the primary intensity such that the average number of photons per light pulse is 1. For this example we find for the percentage of pulses containing 0,1 or 2 photons the values 36%, 37% and 19%, respectively. Of course the light pulse can contain also more than 2 photons, but we can ignore these in the following. The important fact is that besides the genuine pair emission (absorption of a single photon), which we term "true" coincidences, also two independent single photoemission processes are possible, whereby the uncorrelated electron pair also will trigger the coincidence circuit. In this context we talk about "random" coincidences. We know that the single photoemission process is much more likely to occur in contrast to the DPE process. An usual experimental observation is that the single photoemission count rate is about a factor of 1000 higher than the coincidence rate as observed in the pioneering experiment by Gazier and Prescott [13]. Therefore one has to pay attention to reduce the number of "random" coincidences. The obvious way is to reduce the primary intensity. As an example, we assume now that on average each light pulse contains 0.01 photons. Via Poisson-statistics we have for the percentage of pulses contain 0,1 and 2 photons values of 99%, 0.99% and 0.0049%. We immediately notice that the number of pulses containing a single photon is by a factor of 200 higher than the number of pulses containing 2 photons. The drawback is that 99% of the pulses are empty hence one has to operate at a low primary flux, which in turn means that the "true" coincidence rate is low, too. We achieve with an apparatus with large angular acceptance values up to 50 coincidence counts per sec. We point out that the low count rates are not due to a deficiency of the experimental set-up, but due to the fact that the xc-hole effectively screens the electrons. This is the reason why our coincidence experiments require data accumulation times of the order of weeks to obtain sufficient statistics.

3 Results

3.1 Energy distributions of electron pairs If electron pairs are emitted it is of great interest to know how the available energy is shared among the electrons. For example, is there a tendency for both electrons to have similar energies or are they rather different? The first experimental account on solids was given by Hermann et al. [16], who investigated Cu(100) and Ni(100) surfaces, respectively. A sketch of the apparatus used is depicted in fig.3. In brief, linearly polarized light hits the sample along the surface normal. The light polarization is in the drawing plane as in-

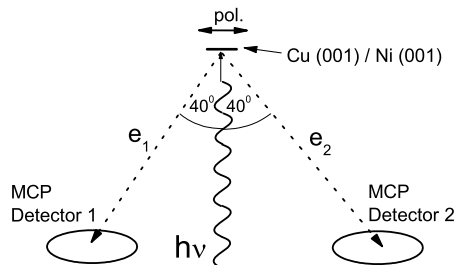


Figure 3 Sketch of the experimental apparatus used by Herrmann et al. [16]. Linear polarized light impinges normal to the surface. The polarization direction is in the drawing plane

dicated by the arrow. Emitted electrons are registered via a pair of detectors arranged symmetrically with respect to the surface normal, such that electrons with an emission angle of 40° can be detected. In fig.4 we display the 2D-Energy distribution from a Cu(100) surface, where the photon energy was fixed to 45 eV. For the process of DPE energy conservation has to hold. We write for the sum energy of a pair $E_{sum}=E_1+E_2$, where the E_1 and E_2 are the kinetic energies of the electrons constituting the pair. Both electrons have to overcome the vacuum barrier given by the work function W_A of the surface. From this it follows that the maximum sum energy E_{sum}^{max} is determined by:

$$E_{sum}^{max} = h\nu - 2 \cdot W_A \quad (2)$$

In the present example the photon energy $h\nu$ was set to 45 eV and for a Cu(100) surface W_A equals 4.5 eV, hence we obtain $E_{sum}^{max}=36$ eV. In a 2D-Energy distribution lines of constant sum energy are represented by the equation $E_2=\text{const.}-E_1$, which are diagonal lines intercepting the x- and y- axis at an energy value given by the constant. In fig.4 a) we have added the diagonal line defining E_{sum}^{max} as a solid black line dividing the 2D-Energy window into two parts. We note that in the upper right hand part virtually no intensity is recorded, while in the lower left hand part essentially all intensity is found. This is the consequence of the above discussed energy conservation. This fact demonstrates that we have detected essentially "true" coincidences rather than "random" coincidences. For the latter the maximum sum energy is higher, because we have put the energy of at least two photons into the equation. This result showed that we have successfully moved beyond the mere detection of correlated electron pairs from solid surfaces. We know about the electronic structure of Cu that the 3d-states are energetically about 2-4 eV below the Fermi level, the center of gravity is about 2.5 eV below E_F . The dashed diagonal line marks the energetic position of pairs, if both electrons come from this average energy level. Since the d-band is completely filled with 10 electrons, whereas the free-electron type sp-band is occu-

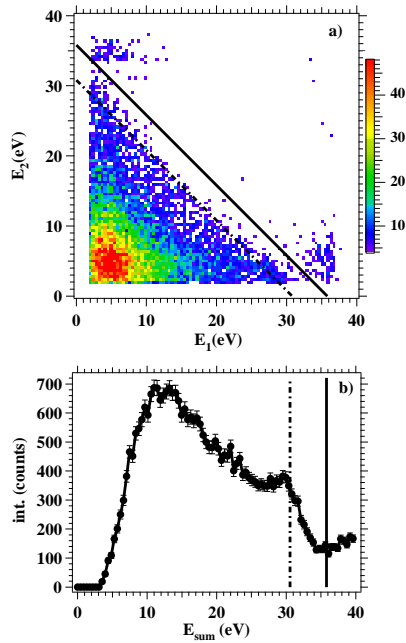


Figure 4 In panel a) we plot the 2D-Energy distribution of the coincidence intensity in counts obtained from a Cu(100) surface excited with 45 eV photons. The color coding represents the intensity, which is given in counts. The axis are the energies of the individual electron energies. The solid diagonal line indicated the position of the maximum sum energy the pair can have. The dashed diagonal line marks the energetic position of pairs, if both electrons come from the 3d-levels. In panel b) we display the coincidence intensity as a function of the sum energy.

ped by approximately 1 electron. We expect the emission from the d-bands to dominate the spectrum. This expectation can be checked, if we use the data shown in fig.4 a) and compute the coincidence intensity as a function of E_{sum} . The result can be seen in fig.4 b), where the vertical solid lines marks the maximum sum energy as determined by eq.(2). We see at this point that the coincidence intensity is very low. The finite value is due to the contribution of "random" coincidences. As before, the vertical dashed line labels the position if the valence band electrons come from the 3d-states with an average binding energy of 2.5 eV. Near this energy position we observe a peak in the spectrum, which tells us that two valence electrons from the d-levels have been emitted. For smaller values of E_{sum} the intensity starts to rise, which is followed by a sudden fall-off for E_{sum} at 15 eV. First, we have to recognize that there is a low kinetic energy cut-off of about 2 eV. There-

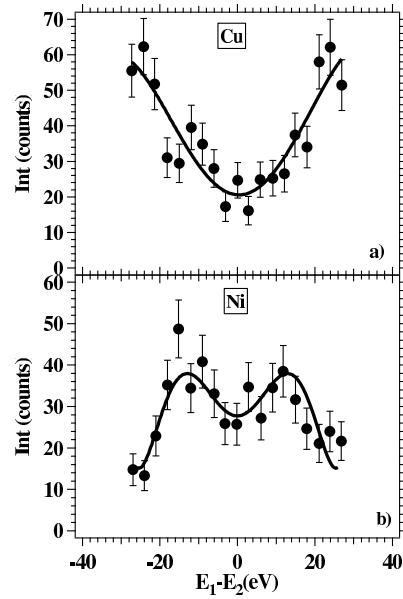


Figure 5 We show the sharing curves for a sum energy $E_{sum} = 35 \pm 1$ eV. In panel a) we plot the result obtained from a Cu(100) surface, while the data measured from a Ni(100) surface are shown in panel b). In both cases the photon energy was set to 50 eV. The solid lines serve as guide for the eye.

fore electron pairs with sum energies below 4 eV are not detected. Second, a simple geometric fact tells us that the line of constant sum energy in the 2D-Energy plot becomes shorter if the value of E_{sum} becomes smaller. Within the data shown in fig.4 a) lies the answer how the energy is shared among the electrons. To make this more apparent it is useful to plot so-called sharing functions. For a given sum energy E_{sum} the coincidence intensity as a function of E_1-E_2 is computed. As an example we show in fig.5 the result for $E_{sum} = 35 \pm 1$ eV at a photon energy of 50 eV. With this energy selection we focus on those events, where both electrons come from the vicinity of E_F . We can clearly observe that for equal energies the intensity is lower than for unequal energies. If we compare the result for both samples, we note that in both cases the sharing function displays a minimum for equal energies of the electron. The minimum can be understood in terms of a selection rule for DPE, which predicts a vanishing DPE intensity if the sum momentum k_1+k_2 is perpendicular to the polarization vector of the light. For the geometry shown in fig.3 the polarization is parallel to the surface plane. If the electrons forming a pair have the same kinetic energy and opposite emission angles the sum momentum is along the surface nor-

mal and perpendicular to the polarization vector. The difference in the sharing curve can be related to a competing process, which also leads to the emission of electron pairs.

In general two possible pathways for pair emission exist [16, 17]. On one hand, a single photon can be absorbed, which is accompanied by the emission of an electron pair. This is regarded to be a direct double photoemission process (DPE). This process is only possible if the two electrons are correlated [6]. A simple picture illustrating the plausibility of this point is to consider two valence electrons, which initially move independently of each other. Once they collide their motion through the crystal is correlated. Within the dipole approximation the photon is absorbed by one electron, but by virtue of the electron correlation the second electron is affected as well, which can lead to the emission of a pair. Without correlation between the electrons only single photoemission is possible. This leads us immediately to the other pathway. It is conceivable that the photon is absorbed by a single electron resulting in the creation of a photoelectron. After a series of collisions, in which it loses its initial phase, it may collide with another electron, which creates an electron pair. The process may be called an internal (e,2e) event. The time scale over which these processes take place is of the order of 10 fs. This is beyond the current experimental time resolution of ≈ 1 ns. This issue has been addressed recently by comparing coincidence experiments, where the excitation was via photons or electrons, which will be discussed in detail elsewhere [18]. As far as the data shown in fig.5 indicate that in Ni the internal (e,2e) process is more dominant compared to the observation for Cu(100). A theoretical explanation connects these difference to the higher density of states at E_F for Ni compared to Cu [17].

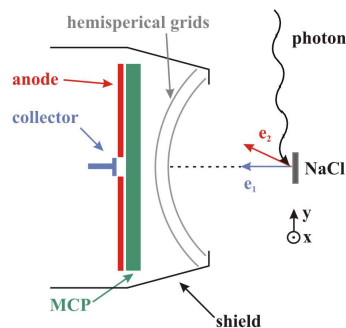


Figure 6 Photons hit the surface under a grazing angle of 12° . The emitted electrons hit a channelplate, if their trajectories are within the angular acceptance. The electrons are detected either on a resistive anode or small central collector. Two electrons with momenta \mathbf{k}_1 , \mathbf{k}_2 and energies E_1 and E_2 are detected in coincidence.

3.2 Angular distributions of the double photoemission intensity

In the introduction we discussed the concept of the exchange-correlation hole, which is defined in real space. This entity is not accessible via our experiments, because we cannot determine the initial positions of the electrons, which are emitted. What we are able to measure are emission angles and from those it should be in principle possible to deduce the situation in real space. It may be useful at this point to recall the famous Rutherford experiment, where the scattering of α -particles from a thin gold foil was studied. At the time the surprising result was that the α -particles experienced also large angular deflections. These could be explained only if the positive nuclear charge was confined into a small region of space. This is an example where angular distributions in scattering experiments reveal the nature of the interaction in real space. Thinking along these lines one should try to access the xc-hole via the observation of angular distributions of electron pairs. More precisely one should ask the question, how does the angular distribution look like, if the emission direction of one of the electrons of the pair is fixed. The experimental realization is depicted in fig.6. A NaCl(100) surface is excited by a photon beam, which hits the sample under a grazing angle of 12° . The emitted electron pairs travel towards a channelplate detector. The actual detector consists of two parts, namely a central collector and a resistive anode. The central collector accepts electrons only within a narrow solid angle of ~ 0.02 sr, the detected electron we may term as "fixed electron" in the following. For electrons, which hit the resistive anode the impact position can be determined. Electrons within a solid angle of ~ 1 sr can be detected, which we may term as "free electron". With this instrument we are able to determine the kinetic energies and emission angles of the electrons constituting the pair. Alternatively, we can characterize the coincidence intensity via the momentum of the electrons. More experimental details can be found elsewhere [19].

From our previous discussion it is clear that a reasonable starting point to describe the electron-electron interaction is to use a screened Coulomb potential $V \propto \frac{1}{r} e^{-\frac{r}{\lambda}}$ acting between the two electrons. The distance between the electrons is given by r , while the screening length is labelled with λ . For crystalline solids the Bloch theorem holds and is therefore adequate to describe the electronic properties in momentum space. In this case the screened Coulomb interaction takes the form $V \propto \frac{1}{k^2 + \lambda^{-2}}$, where $k = |\mathbf{k}_1 - \mathbf{k}_2|$ is determined by the momenta of the individual electrons labelled \mathbf{k}_1 and \mathbf{k}_2 , respectively. From this formula one can derive the following picture. If electrons are well-separated in momentum space, e.g. $|\mathbf{k}_1| = 0$ and \mathbf{k}_2 large compared to the inverse of the screening length, the interaction is weak and one may consider electrons to be independent. This has the immediate implication that the DPE intensity has to vanish as discussed previously. The other extreme is, if both momenta have the same value the interaction is very strong. The probability

to find two electrons in such a state however is strongly reduced as a consequence of the xc-hole, which can of course also be introduced in momentum space [20]. As a matter of fact from eq.(1) can see immediately that the expression of the pair correlation function xc-hole already connects real space and momentum space, because the pair correlation function depends on the product $\mathbf{r} \cdot \mathbf{k}_F$. The consequence is that the DPE intensity should be very small. In between these two extremes the DPE intensity should have a maximum, since it is more likely to find electrons with slightly different momenta, while the electron-electron interaction is still strong. In summary we derive the following simple picture of the DPE intensity as a function of the difference momentum \mathbf{k} . A minimum of the intensity at $\mathbf{k} = 0$ is followed by a maximum for intermediate values of \mathbf{k} , finally at large \mathbf{k} values the DPE intensity vanishes. This simple picture is on firm ground, because a dedicated theoretical study of the DPE intensity from a Cu(100) surface reveals exactly this picture. Fominykh et al. [7] find that the emission direction of the fixed electron is surrounded by a reduced intensity of the other electron. This depletion zone is the manifestation of the xc-hole. Since the theoretical study used the components of the in-plane momentum rather than emission angles, we display our experimental study accordingly. The energy of the "fixed electron" is labelled with E_1 whereas the "free electron" has the energy E_2 . We observe the onset of DPE when the sum energy E_1+E_2 equals ~ 14.6 eV if the photon energy is set to 34 eV. This can be easily understood when considering the known binding energies of NaCl determined by photoemission. Wertheim et al. found that the highest occupied level (Cl 3p band) has a binding energy $E_B=9.66$ eV with respect to the vacuum level. Since for DPE two electrons leave the solid this energy needs to be accounted for twice and subtracting this value from the photon energy yields the maximum kinetic sum energy, see eq.(2). The numerical result is 14.7 eV in agreement with our observation. In the following we want to focus on the momentum distribution rather than the energy distributions. For this we take advantage of the lateral resolution of the set-up. In a first step we select only those coincidences for which the energies E_1 and E_2 are fixed. In order to obtain sufficient statistics we actually select an energy window of ± 0.8 eV around the respective energies. We can now proceed and plot the coincidence intensity as a function of the in-plane momentum k_{\parallel} of the "free electron", see fig.7. We would like to point out that all momentum plots display a zero intensity at a position where the central collector is positioned. The position and size of this "blind spot" depends on the momentum of the "free electron". For the plots shown in fig.7 this "blind spot" is centered at $k_{\parallel}=0$ and has a radius of $\sim 0.1 \text{ \AA}^{-1}$. In fig.7 a) the energies are $E_1=5.5$ eV and $E_2=9.5$ eV. This means we are at the onset of DPE emission. We clearly observe that the region $k_{\parallel}=0$ (outside the "blind spot") is surrounded by a region of diminished intensity. The intensity

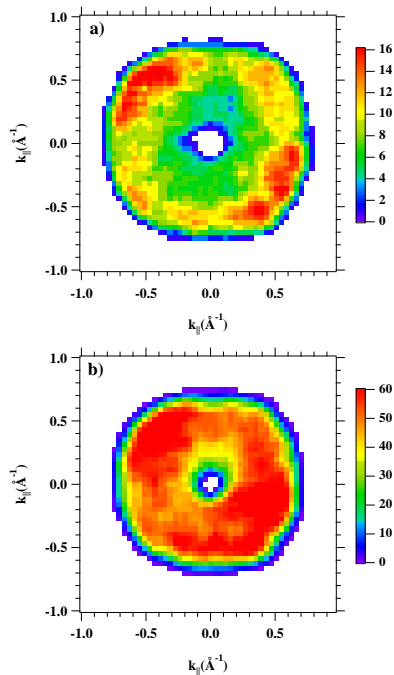


Figure 7 The 2D in-plane momentum distribution for two different energy pairs from a NaCl(100). In panel a) we have selected $E_1=5.5$ eV and $E_2=9.5$ eV. Whereas in panel b) we have chosen $E_1=5.5$ eV and $E_2=7.5$ eV, respectively. The color coding represents the intensity, which is given in counts.

increases for larger k_{\parallel} values and reaches a maximum for $k_{\parallel} \approx 0.55 \text{ \AA}^{-1}$ and then falls off rapidly at the edge of the channelplate. The reduced intensity around the emission direction of the "fixed" electron will be called the depletion zone in the following. While the theoretical work by Fominykh et al. [7] predicted such a behavior for a Cu(100) surface, we show that this feature also exists for an insulator like NaCl. Because the depletion zone is a manifestation of the xc-hole it is fair to state that the concept of the xc-hole is an experimental reality not just a theoretical concept.

A dramatically different situation is depicted in fig. 7b) where we select $E_1=5.5$ eV and $E_2=7.5$ eV. Now the depletion zone is essentially gone. Energetically the sum energy E_1+E_2 has been reduced from 15 eV to 13 eV. Clearly the emergence of the depletion zone is tied to the selection of the energies E_1 and E_2 . We may summarize our observations as follows: (i) if we select the energies E_1 and E_2 such that the sum energy E_1+E_2 has the largest possible value

for pair emission the 2D momentum plots display a region of reduced intensity which is centered around the "fixed" electron. (ii) if the sum energy is below the maximum value a more or less uniform momentum distribution is the result.

The experiments using the set-up displayed in fig.6 suggested that the angular acceptance is not sufficient to observe the full extension of the depletion zone. Therefore we designed a completely new instrument, which incorporates a large angular acceptance. This results obtained with this set-up will be discussed in the next section.

4 Large angular acceptance set-up The main feature of our new experiment is that it consists of 3 channelplate detectors, which ensure a large angular acceptance, which is in the drawing plane ± 1.57 rad, perpendicular to it ± 0.4 rad is available, see fig.8. Delay line anodes allow the determination of the impact positions of electrons even if two electrons hit the same detector. These events we may term as "double hits", whereas we refer to "single hits", if the electrons are registered on different detectors. We operated this instrument in two geometries labelled a) and b) in fig.8. For normal incidence of the light the sample masks a large area of one of the detectors. Therefore we operate with only two detectors. In the other geometry the light impinges under an angle of 32 degrees with respect to the normal. We studied a well-ordered Cu(111) surface, which was obtained via Ar sputtering and annealing up to 800 K. The crystallographic $[\bar{2}11]$ direction is in the drawing plane of fig.8. The experiments were performed at room temperature. More details of the instrument can be founded elsewhere [21]. The photon energy was set to 50 ± 0.2 eV. The polarization plane is in the drawing plane, see fig.8. We define a coordinate system, which has the origin at the sample surface, see fig.8 c). The y-axis is always parallel to the surface normal, whereas the x- and z-direction are in the surface plane and orthogonal to each other. The impact positions are characterized by two angles measured with respect to the surface normal. The angle Θ is in the drawing plane of fig.8, while Φ is perpendicular to the drawing plane. Each coincident event is then characterized by 6 coordinates, namely the individual energies and pair of angles Θ and Φ . The total time resolution is approximately 1.4 ns. This will lead to an energy dependent energy resolution, which is 1.5 eV for 20 eV electrons. It is clear that a six-dimensional presentation of the data is not possible. Therefore one has to reduce the data set such that two-dimensional presentations can be generated. Two possible examples, which demonstrate the capability of the new instrument are: (i) the 2D-energy distribution under a geometrical constraint and (ii) the angular intensity distribution if the emission direction of one electron is fixed.

4.1 Double photoemission at normal photon incidence In our presentation we start with the experimental results obtained with normal incidence of the photons. As described in the experimental part, we use two detectors in this case we may label them "left" and "right", respec-

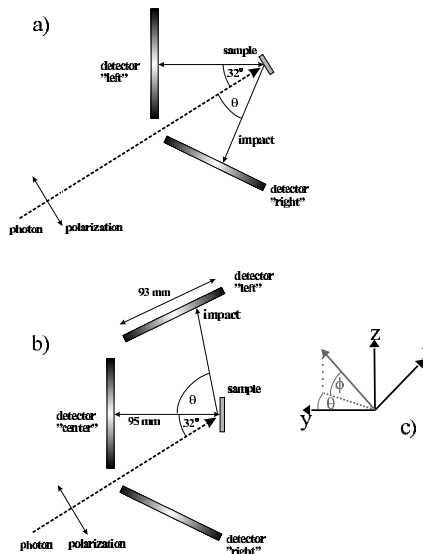


Figure 8 Sketch of the experimental apparatus and the two geometries used. The linear polarization of the light was in the drawing plane. The z-axis of our coordinate system is perpendicular of the drawing plane of the geometries a) and b). The orientation is of the y-axis is along the surface normal of the sample. The emission direction are specified by the angles ϕ and θ , respectively.

tively. We further consider only "single" hits, this means only coincidence events where the two electrons hit different detectors are registered. In fig.9 we plot the coincidence intensity as a function of the sum energy $E_{sum} = E_{left} + E_{right}$. The vertical dashed line marks the energy position of the maximum sum energy $E_{max} = 40$ eV imposed by energy conservation, since the work function of the Cu(111) surface (≈ 5 eV) has to be subtracted twice from the photon energy of 50 eV (see eq.(2)). It is apparent that the pair emission is governed by a contribution located at $E_{sum} \approx 35$ eV. We recall that the center of gravity of the Cu 3d band is roughly 2.5 eV below the Fermi level E_F , hence we identify the peak at 35 eV with the pair emission from the Cu 3d bands. It is well-known that the Cu(111) surface possesses also a Shockley surface state at the $\bar{\Gamma}$ point [?]. This state is energetically located in the interval E_F and $E_F - 0.4$ eV. From fig.9 we conclude that with the present apparatus and its current resolution it is not possible to identify the emission from the surface state. The data shown in fig.9 is derived from an integration over the whole accessible angular range, even though the shape of the spectrum has a weak angular dependence. The back-

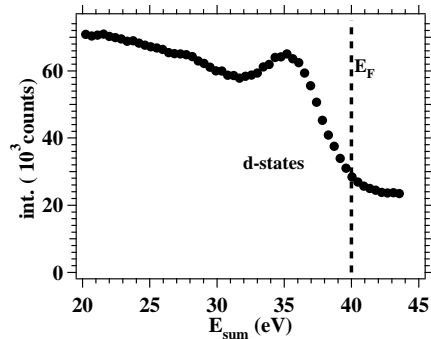


Figure 9 Plot of the E_{sum} distribution of the DPE intensity obtained from a Cu(111) sample. The photon energy is set to 50 eV, the light propagation direction is along the surface normal. The vertical dashed line is the energy position of the highest possible sum energy, which follows from energy conservation. A pronounced emission at 35 eV can be noticed.

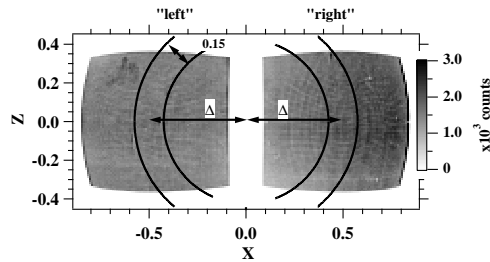


Figure 10 The hit pattern of electron pairs is displayed. As axes we use the components of the normalized in-plane momentum of the individual electrons labelled X and Z, respectively. The excitation was via 50 eV photons, which hit the sample along the surface normal. The gray scale on the right displays the intensity in counts. The pair of arcs on the "left" and "right" detector define narrow regions. We will select those events where the "left" and "right" electron come from these regions and compute the energy distributions.

ground of the intensity distribution of fig.9 and its extension above $E_{sum} = 40$ eV is related to so-called "random" coincidences. The determination of 2D-Energy distributions requires the execution of several steps, therefore we display in fig.10 the hit pattern of the individual electrons of coincident pairs as a function of the components of the normalized in-plane momentum (or directional cosine). The directional cosine is labelled X and Z and can be computed from the known emission angles and kinetic energy. One interesting aspect is how the available energy is shared between the electrons, in particular, if we im-

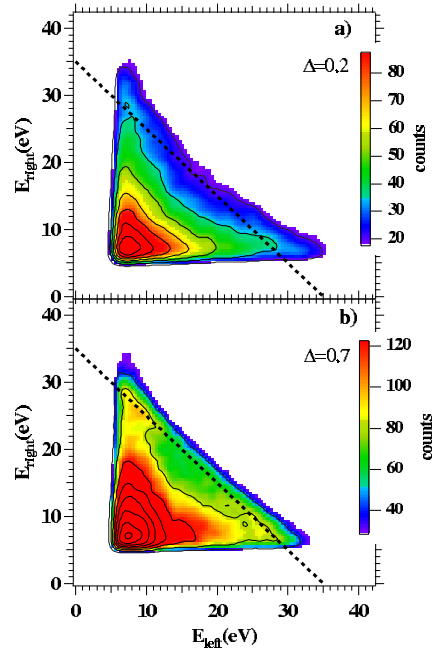


Figure 11 (color) 2D-energy distributions for $\Delta=0.2$ in a) and $\Delta=0.7$ in b). The intensity is given in counts. We added equidistant contours and employed a Gaussian filter. The dashed diagonal line in both plots indicates the emission at $E_{sum}=35$ eV.

pose geometric constraints. In order to address this point we select regions on the detectors "left" and "right" whose boundaries are given by the pair of arcs in fig.10. The width of these regions are 0.15, and the centers have a distance to the origin given by the value of $|\Delta|$. The value chosen for the width is solely determined by statistics. We can now compare the energy distributions for different values of $|\Delta|$. The result is shown in fig.11 for a choice of $\Delta=0.2$ and $\Delta=0.7$, respectively. Converted into angles, we constrain the mean angle between the trajectories to be either 23° or 89° , respectively. These are the extreme values for the present geometry. The dashed diagonal lines in both plots indicate the position of those events, which have a sum energy of 35 eV. We recall from fig.9 that at this energy a prominent pair emission occurs. In fig.11 panel a) we observe for $\Delta=0.2$ a boomerang like distribution. The onset of pair emission at $E_{sum}=40$ eV occurs for very unequal energies, which means one of the electrons carries most of the energy. This preference of one electron being "fast" while the other is "slow" also occurs for decreasing sum energy. In general the coincidence intensity increases

if E_{sum} decreases. The situation for $\Delta=0.7$ is different as inspection of fig.11 b) shows. The onset of pair emission at around $E_{sum}=40$ eV is not confined to those electrons which have very unequal energies, but occurs for all energy combinations with very similar probability. If we reduce E_{sum} to 35 eV we note that the intensity remains constant as long as the energies are outside the regions $20 \text{ eV} < E_{left/right} < 30 \text{ eV}$ and $E_{right/left} < 10 \text{ eV}$. From these observations we learn that the prominent emission at $E_{sum}=35$ eV occurs for unequal energy sharing and preferably for large values of Δ . In other words the trajectories of the electrons have a large angle between each other.

4.2 Depletion zone in the angular distribution

We discuss now our results we obtained for the geometry labelled b) in fig.8, in this case the light impinges under an angle of 32° with respect to the surface normal. For this we made use of all three detectors, which means we utilized the full angular acceptance of the instrument. Additionally we also considered "double" hits in this experiment. In this case a remark regarding the bookkeeping is necessary. If the two electrons constituting a pair hit different detectors ("single" hits) it is quite natural to label these electrons according to the name given to the detector. If the two electrons hit the same detector ("double" hits) a certain ambiguity arises, since both electrons will have the same label. It is more appropriate to choose a label like "fast" and "slow" with the energies E_{fast} and E_{slow} , respectively. This implies that $E_{fast} > E_{slow}$, and in order to compare "single" and "double" hits, we need to use the same labelling for "single" hits, too. After this comment it is warranted to start with the E_{sum} distribution of the coincidence intensity, which we display in fig.12. A comparison with fig.9, obtained with normal incidence but the same photon energy of 50 eV, shows that the essential features are identical. In both cases we observe the onset of pair emission at about 40 eV, which is dictated by energy conservation, see eq.(2). A prominent peak at 35 eV can be associated to the emission of 3d valence electrons, as discussed above. The next aspect we want to discuss concerns the 2D-energy distribution, which we show separately for "single" and "double" hits in fig.13. The bar on the panel defines the color code for the intensity, which is given in counts. Further, we added equidistant contours to the plot.

In panel a) we plot the distribution for "double hits" and we clearly observe that E_{slow} is confined to values below 10 eV, while it is centered around 5 eV. In contrast to this E_{fast} adopts all values allowed by energy conservation. However, the intensity is not uniform, but we note a steady increase if E_{fast} is below about 20 eV. A comparison of fig.13a) and fig.9a) reveals a strong similarity. This is not surprising if we recall that the definition of "double hits" requires both electrons to hit the same detector. By geometry this inevitably means that the trajectories of the electrons are close to each other. In fig.9 a) we imposed

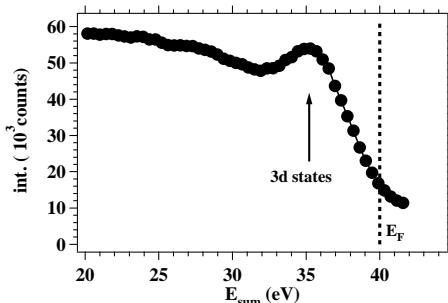


Figure 12 Plot of the E_{sum} distribution of the DPE experiment for light incidence of 32° with respect to the normal. The sample is a Cu(111) surface and the photon energy is set to 50 eV. The vertical dashed line is the energy position of the highest possible sum energy, which follows from energy conservation. A pronounced emission at 35 eV can be noticed. This distribution is very similar to the data shown in fig.9.

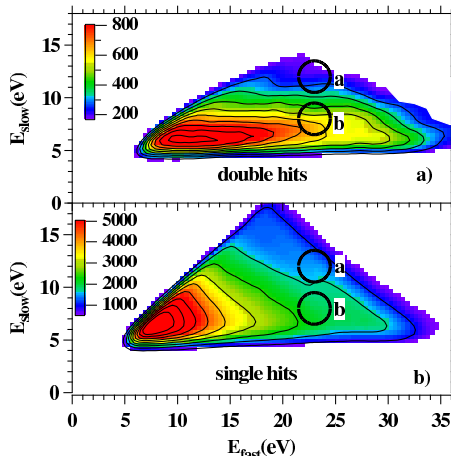


Figure 13 2D-Energy distribution of the DPE intensity from a Cu(111) surface, the photon energy is 50 eV. One electron is termed "fast", whereas the other is called "slow" with energies $E_{fast} > E_{slow}$. In panel a) we show the data for "double" hits, whereas panel b) refers to "single" hits. In both panels we have drawn two circles with radius 1.5 eV. This indicate energy regions centered at $E_{fast}=23$ eV ($E_{slow}=12$ eV) and $E_{fast}=23$ eV ($E_{slow}=6$ eV). Coincident events within these windows are used for angular distributions of the coincidence intensity, see below.

a similar constraint by selecting a value of $\Delta=0.2$. Again we state that there is a preference of one electron being

"fast" while the other is "slow". In fig.13 b) we display the 2D-Energy distribution for "single" hits. The first aspect, which we would like to emphasize, is the fact that the intensity is higher compared to "double" hits. This can be read easily from the color bars of the two plots, which shows that the maximum of the 2D-Energy distribution for "single" hits is by a factor of 6 higher than "double" hits. This ratio is also maintained if we compute the total number of these two types of events. From geometry we know that for "single" hits the trajectories of the electrons include a larger angle than those for "double" hits. In other words the emitted electrons of a pair tend to avoid each other. This aspect will become important later on.

A 2D-angular presentation of our data requires the execution of several steps. First we select values for E_{fast} and E_{slow} , respectively. In order to select enough coincidence events we allow an uncertainty in the energy of ± 1.5 eV. This has been indicated by the circles drawn in fig.13. Now we can derive the angular distributions of the "fast" and "slow" electron. These are not independent of each other, since electron pairs are detected. We emphasize that every "fast" electron has a "slow" counterpart. As an example we show in fig.14 the angular distributions for "fast" and "slow" electrons centered at $E_{fast}=23$ eV and $E_{slow}=12$ eV (region a) of fig.13. Both distributions display the highest intensity if the electrons leave the sample along the surface normal. The intensity drops for increasing values of $|\Theta|$. The above energy selection for E_{fast} and E_{slow} focusses on the emission from the 3d-states. Contributions from the Shockley surface state were too weak to be identified in our experiments. In the next step we impose a geometrical constraint. We select only those "fast" electrons, which leave the sample within a narrow angular direction. As an example we have drawn a black circle in fig.14 b), which is centered at $\Theta=\Phi=0$ rad. The emission direction is a cone with an angle of 0.18 rad, which is the radius of the circle in fig.14 b). In other words, we fix the direction of the "fast" electron and ask for the intensity of the "slow" electron around this direction. This is displayed in fig.14 c) after normalization to the intensity of the "slow" electron in fig.14 a). This procedure is necessary in order to take into account varying detection efficiencies across the active areas of the detectors. It is obvious that the intensity on the center detector is lower than on the left and right detectors. To emphasize the point and to improve the statistics we integrated the data along the Φ direction and show the resulting profile along the Θ direction in fig.14 d). The vertical dashed lines mark the boundary of the allowed Θ values of the "fast" electron. The solid line through the data serves as guide for the eye, whereas the dashed vertical lines mark the boundary of the fixed direction. The intensity is given in counts and the color code is on the right hand side of the plot.

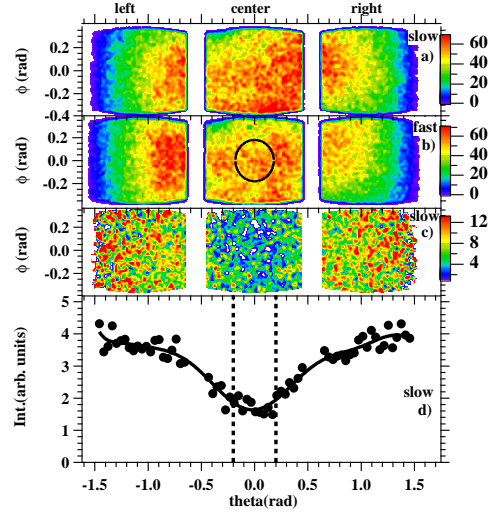


Figure 14 Angular distributions with $E_{fast}=23$ eV and $E_{slow}=12$ eV are displayed. Panel a) shows the 2D angular intensity for the "slow" electron, whereas in panel b) the same for the "fast" electron is plotted. In panel c) we plot the intensity for the "slow" electron if the "fast" electron is constrained to be within the area defined by the black circle of the center detector 2 in b). From panel c) a profile can be computed, which is plotted in panel d). The solid line is guide to eye, whereas the dashed vertical lines mark the boundary of the fixed direction. The intensity is given in counts and the color code is on the right hand side of the plot.

dium $\Theta \sim 1.2$ rad, which is well inside the angular range of our experiment. The key observation is that we are able to show the full extension and shape of the depletion zone. It is of course possible to fix the emission direction of the "slow" electron and determine the intensity map of the "fast" electron. The result of such a presentation is qualitatively and quantitatively identical as far as the size of the depletion zone is concerned. The depletion zone could be observed for different values of E_{fast} and E_{slow} , where the size was independent of the selected energies. We will discuss below under which circumstances, we observe an almost vanishing depletion zone.

If we choose the fixed direction to be centered at $\Theta=0$ rad the maximum angle of the counterpart cannot exceed 1.57 rad if they are to leave the sample surface. This means the maximum angle between the trajectories is 1.57 rad. However, it is possible to detect electron pairs, whose trajectories include larger angles and to study the angular distribution. This is possible if we explore a significant advantage of our detection scheme. We can select the emission direction of one electron (either "slow" or "fast") anywhere within

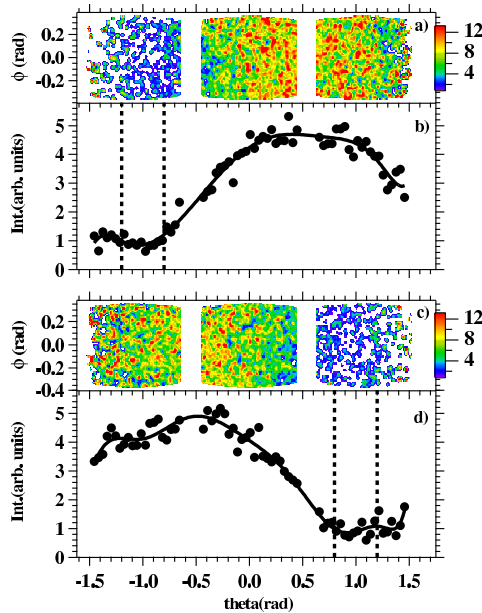


Figure 15 2D-angular distributions and resulting profiles are shown for electron pairs with $E_{fast}=23$ eV and $E_{slow}=12$ eV. The direction of the fixed "fast" electron is centered either at $\Theta = -1$ rad for panels a) and b) or $\Theta = 1$ rad for panels c) and d). The line profiles of the intensity maps in a) and c) are plotted in panels b) and d). The solid lines are guide to eye, whereas the dashed vertical lines mark the boundaries of the fixed emission directions. The color coding in panels a) and c) represents the intensity, which is given in counts.

the angular acceptance. We demonstrate this in fig.15. The fixed emission directions are defined by a circle in the 2D angular distribution equivalent to fig.14 b), which again has a radius of 0.18 rad. The center is either at $\Theta = -1.0$ rad for plots in fig.15a) and b), the case $\Theta = 1.0$ rad is depicted in fig.15 c) and d). The vertical dashed lines in fig.15 c) and d) mark the range of the allowed Θ values for the fixed electron. With this choice of the emission directions we lose information of the intensity for Θ values on one side of the selected emission direction, but we gain a larger angular range on the other side. In other words: the maximum angle between the trajectories of the fixed "fast" and "slow" electron is larger in this direction. Using the same procedure as before we finally derive the 2D angular distribution of the "slow" electron around the fixed direction of the "fast" electron. These are plotted in fig.15 a) and c). In the case of panel a) we observe a low intensity on the left detector. If we move to the center detector the intensity

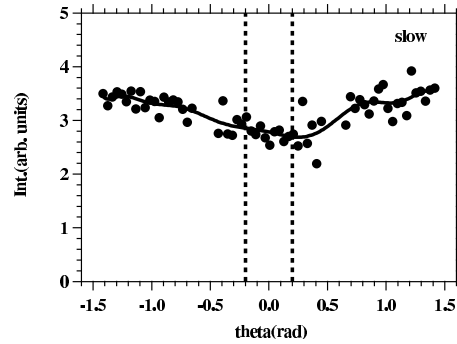


Figure 16 Coincidence intensity for the "slow" electron if the direction of the "fast" electron is fixed at $\Theta = 0$ rad. We selected $E_{fast}=23$ eV and $E_{slow}=6$ eV. The solid line is guide to eye, whereas the dashed vertical lines mark the boundary of the fixed direction.

has increased and finally the intensity on the right detector is smaller than on the center detector. Again improving the statistics via an integration along the Φ direction is appropriate and gives a more detailed view, the resulting profile can be seen in fig.15 b). Two important observations can be made. First we see that the intensity peaks at $\Theta \approx 0.2$ rad, while the "fixed" electron is centered at $\Theta \approx -1.0$ rad. This means that the angular size of the depletion zone is ≈ 1.2 rad, in line with the result shown in fig.14 d). More importantly, we see that the coincidence intensity drops off again if the angle between the two electrons is beyond ≈ 1.2 rad. An equivalent situation is observed in fig.15 d) despite the breaking of symmetry. We have to emphasize that the photon beam hits the sample with an angle of 32° , see fig.8. Therefore we cannot a priori expect to observe a symmetric behavior as we do. We can clearly see that the reduced intensity regime follows the fixed emission direction. The fall-off of the coincidence intensity for large angles between the "fast" and "slow" electron is expected, because ultimately two electrons are not correlated if they are well separated (in angular or momentum space).

Due to the size of the depletion zone, it is also justified to allow the fixed direction to be rather large. We have found no significant variation of the angular size of the depletion zone for other values of E_{fast} and E_{slow} . This means that in momentum space the depletion zone size will scale with the square root of the energy.

We would like to come back to the 2D-Energy distribution shown in fig.13. We have pointed out before that most of the coincidence intensity occurs for $E_{slow} < 10$ eV. This preference was mainly due to "double" hits. Detection on the same detector implicitly means that the trajectories of the electrons include small angles, hence they are "close" to each other. If we select the energies centered at

$E_{fast}=23$ eV and $E_{slow}=6$ eV (region b) of fig.13, we are focussing on such events and ask how the angular distributions are affected. The result for the "slow" electron around the fixed direction of the "fast" electron is plotted in fig.16. We observe that the depletion zone has been "filled" and an almost constant intensity as a function of Θ is observed. This filling of the depletion zone occurs gradually if we vary E_{slow} from 12 to 6 eV. More specifically the size of the depletion zone stays essentially constant, but the minimum is filled up. A simple picture of the electron-electron scattering, where the interaction between the electrons is mediated by the Coulomb interaction, shows that if the trajectories are forced to be close to each other one electron is "fast" while the other is "slow". In general two electrons tend to avoid each other (due to the Pauli principle and Coulomb interaction) leading to the concept of the depletion zone. Our experiments confirm this picture as long as the individual energies E_{fast} and E_{slow} are not too unequal as just shown.

We conclude that we are able to fully map the depletion zone. This statement constitutes the major achievement of this work. We find for the depletion zone from electrons originating from a Cu(111) surface a size of ~ 1.2 rad independent of the energy of the electrons. We also discovered a correlation in energy space proven by an almost disappearing depletion zone if the electron energies are very unequal. It would be desirable to compare our experimental depletion zone size with theory. This is, however, beyond the capability of current solid state theory. Eventually, the comparison of theory and experiment of the depletion zone may lead to an improved description of the exchange-correlation hole in solids.

5 Summary We have outlined the development of double photoemission from solid surfaces over recent years. The relevance of this technique rests on the fact that for independent electrons the DPE intensity vanishes. Therefore DPE experiments are particularly suited to study the electron-electron interaction. This in turn holds the promise that these experiments help to develop a theory beyond the effective independent electron description. We established that energy and angular distributions can be obtained, the latter over a large angular acceptance. The sum energy distributions reveal that the onset of the coincidence intensity occurs at an energy, which is determined by the photon energy and the work function of the sample. We learn further that the available energy is in general unequally shared.

The angular distributions of the DPE intensity prove that the exchange-correlation hole is an experimental reality. It manifests itself in a depletion zone of the coincidence intensity around the fixed emission direction of one electron. It is a challenge for theory to determine from our angular distributions the exchange-correlation hole in real space.

Acknowledgements The presented studies were only possible due to the dedicated support by the staff of the BESSY I and BESSY II light sources over more than a decade. In this respect we are obliged to thank Dr. Walter Braun for his support and his

continuing effort to ensure a user friendly operation. We appreciate the very important contribution of Mr. Engelhard and Mr. Hartung in the construction of the various apparatuses.

References

- [1] E. Wigner and F. Seitz, Phys. Rev. **43**, 804 (1933).
- [2] H. Ibach and H. Lüth, Solid-State Physics (Springer-Verlag, Berlin, 1991).
- [3] J.C. Slater, Rev. Mod. Phys. **6**, 209 (1934).
- [4] N.F. Mott and H. Jones, The Theory of the properties of metals and alloys (Oxford University Press, Oxford, 1936).
- [5] K. Byczuk, M. Kollar, K. Held, Y.-F. Yang, I.A. Nekrasov, T. Pruschke, and D. Vollhardt, Nat Phys **3**, 168 (2007) and references therein.
- [6] J. Berakdar, Phys. Rev. B **58**, 9808 (1998).
- [7] N. Fominykh, J. Berakdar, J. Henk, and P. Bruno, Phys. Rev. Lett. **89**, 086402 (2002).
- [8] N. Fominykh, J. Henk, J. Berakdar, P. Bruno, H. Gollisch, and R. Feder, Solid State Commun. **113**, 665 (2000).
- [9] H. Gollisch, N.v. Schwartzberg, and R. Feder, Phys. Rev. B **74**, 075407 (2006).
- [10] P. Lablanquie, J.H.D. Eland, I. Nenner, P. Morin, J. Delwiche, and M.-J. Hubin-Franskin, Phys. Rev. Lett. **58**, 992 (1987).
- [11] J. Mazeau, P. Selles, D. Waymel, and A. Huetz, Phys. Rev. Lett. **67**, 820 (1991).
- [12] O. Schwarzkopf, B. Krässig, J. Elmiger, and V. Schmidt, Phys. Rev. Lett. **70**, 3008 (1993).
- [13] C. Gazier and J.R. Prescott, Phys. Lett. A **32**, 425 (1970).
- [14] H.W. Biester, M.J. Besnard, G. Dujardin, L. Hellner, and E.E. Koch, Phys. Rev. Lett. **59**, 1277 (1987).
- [15] H.W. Biester, M.J. Besnard, G. Dujardin, L. Hellner, and E.E. Koch, Phys. Rev. Lett. **60**, 1589 (1988).
- [16] R. Herrmann, S. Samarin, H. Schwabe, and J. Kirschner, Phys. Rev. Lett. **81**, 2148 (1998).
- [17] N. Fominykh, J. Berakdar, J. Henk, S. Samarin, A. Morozov, F.U. Hillebrecht, J. Kirschner, and P. Bruno, in: Solid-State Photoemission and Related Methods: Theory and Experiment, edited by W. Schatke and M.A. van Hove (Wiley-VCH Verlag, Weinheim, 2003) chap. 10.
- [18] M. Munoz-Navia, C. Winkler, R. Patel, M. Birke, F.O. Schumann, and J. Kirschner (to be published).
- [19] F.O. Schumann, C. Winkler, G. Kerhervé, and J. Kirschner, Phys. Rev. B **73**, 041404(R) (2006).
- [20] P. Fulde, Electron Correlations in Molecules and Solids, Springer Series in Solid-State Sciences Vol.100 (Springer, Berlin, 1991).
- [21] F.O. Schumann, C. Winkler, and J. Kirschner, New J. Phys. **9**, 372 (2007).
- [22] S.G. Louie, P. Thyry, R. Pinchaux, Y. Petroff, D. Chandesris, and J. Lecante, Phys. Rev. Lett. **44**, 549 (1980).

FAST TRACK COMMUNICATION

Direct and core-resonant double photoemission from Cu(001)

Grant van Riessen, Zheng Wei, Rajendra S Dhaka,
Carsten Winkler, Frank O Schumann and Jürgen Kirschner

Max-Planck-Institut für Mikrostrukturphysik, Weinberg 2, D-06120 Halle, Germany

Received 27 January 2010, in final form 29 January 2010

Published 15 February 2010

Online at stacks.iop.org/JPhysCM/22/092201

Abstract

We have measured the correlated electron pair emission from a Cu(001) surface by both direct and core-resonant channels upon excitation with linearly polarized photons of energy far above the 3p threshold. As expected for a single-step process mediated by electron correlation in the initial and final states, the two electrons emitted by the direct channel continuously share the sum of the energy available to them. The core-resonant channel is often considered in terms of successive and independent steps of photoexcitation and Auger decay. However, electron pairs emitted by the core-resonant channel also share their energy continuously to jointly conserve the energy of the complete process. By detecting the electron pairs in parallel over a wide range of energy, evidence of the core-resonant double photoemission proceeding by a coherent single-step process is most strikingly manifested by a continuum of correlated electron pairs with a sum energy characteristic of the process but for which the individual electrons have arbitrary energies and cannot meaningfully be distinguished as a photoelectron or Auger electron.

1. Introduction

The emission of two electrons from a solid surface upon the absorption of a single photon has become of much current interest due to the decisive role played by electron–electron correlation in such processes. Because of the single-particle nature of the dipole interaction, the electric field of the photon directly interacts with only a single electron. However, if the photon energy exceeds the double photoemission (DPE) threshold, two interacting electrons may be directly emitted from the valence band, sharing the photon energy in excess of that needed to eject both of them [1]. Detecting the emitted pair in coincidence with energy and momentum discrimination yields observables relevant to the electron–electron interaction in the solid [1–7]. When the energy of the incident photon exceeds the binding energy of a core-level electron, the electron is excited to the continuum above the vacuum level. A second electron may be excited to the continuum by an Auger (autoionization) transition in which the core–hole is annihilated, leaving two holes in the valence band. Auger photoelectron coincidence spectroscopy (APECS) has been

developed to study this process, motivated also by the ability to yield information not directly accessible by single-electron spectroscopy [8–16].

The emission of two electrons by core-resonant DPE proceeds through the formation of an intermediate core–hole state and is therefore often considered within a two-step model, whereby the Auger transition is treated independently from the photoemission process. Such an approximation is valid if no additional excitations occur upon creation of the core–hole intermediate state and its lifetime is sufficiently long to prevent any final-state interactions in the continuum [14, 15]. Then the photoelectron energy alone depends on the photon energy, the core–hole state can be described as a well-defined real state and the Auger electron should have energy given independently by the difference in total energy between the core–hole state and the final two-hole state. Due to the finite lifetime of the core–hole, the photoelectron energy is uncertain within its lifetime broadened width. However, when the photoelectron is detected in coincidence with the Auger electron, the uncertainty in the sum of the kinetic energy of the two electrons is due only to the lifetime broadening of the final two-hole valence state. As the

lifetime of this two-hole state is smaller than that of the core-hole state, the photoemission spectrum may be measured with energy resolution not limited by the natural linewidth [8]. This was demonstrated by measurement of the $M_{2,3}$ photoemission lines in coincidence with the $M_{2,3}$ -VV Auger line from Cu(001) with an energy resolution smaller than the lifetime broadening of the $M_{2,3}$ core-hole state [10, 12]. The coincident photoelectron lines were narrowed compared to those of the total (noncoincidence) photoelectron spectrum and the energy position of their maximum showed, within the lifetime-broadened photoelectron linewidth, linear dispersion with the energy of the detected Auger electron [10]. This behaviour shows that the Auger process is not independent of photoemission and was interpreted as evidence of the inadequacy of the two-step description of photoexcitation and decay [10, 12, 17].

Earlier observations of dynamical screening effects had already led to the understanding that adequate interpretation of APECS must go beyond the independent-particle approximation and describe photoemission and Auger decay as a coherent single-step process [14, 15]. In such descriptions the core-hole may be described by virtual intermediate states spanning all excited single-electron states including the continuum. The Coulomb operator responsible for the Auger transition acts on the complete system involving both final electrons. The complete process can thus be considered a resonance in the double-photoionization continuum [17], which is particularly suitable in the present context where we also consider direct DPE processes. A complete description of both processes must account for the initial-state electron correlation and interaction of the final-state correlated wavefunction of the emitted electron pair with the crystal lattice. [1, 17, 18].

The angular correlation between correlated electron pairs emitted by core-resonant double photoemission has recently been explored in detail [12, 18]. To extend an understanding of energy sharing between the electrons of correlated pairs by direct and core-resonant DPE, electrons pairs must be detected within a large energy window without selectively constraining the energy of either electron. Core-level photoemission and Auger emission can be observed in parallel by an appropriate choice of photon energy. By applying time coincidence techniques, we can simultaneously identify within this range correlated electron pairs emitted by direct or core-resonant double photoemission. We report here the first observation of direct and core-resonant double photoemission measured simultaneously in an energy area of almost $30 \text{ eV} \times 30 \text{ eV}$. In the present paper we focus on the experimental observation that electron pairs emitted by double photoemission resonant with core excitation share the total sum of their energy continuously without their individual energies being conserved during successive steps of photoexcitation and decay or constrained to the energy with which they are observed in single-electron spectroscopy.

2. Experimental details

A new two-electron coincidence spectrometer for surfaces was implemented by combining two hemispherical energy analysers (Scienta R4000, Sweden) with wide-angle transfer

lenses. The analysers were modified by the installation of two-dimensional detectors (microchannel plates (MCP) and resistive anodes) and the lenses are operated in customized modes optimized for the requirements of high transmission with large pass energy, low mean kinetic energy and small temporal dispersion. Angular dispersion characteristics are compromised to achieve these requirements and only energy information was recorded. Constant energy resolution can be preserved independently of the electron kinetic energy, which allows DPE experiments to be extended to photon energies previously inaccessible with time-of-flight spectrometers which presently cannot achieve comparable energy resolution beyond energies $\geq 50 \text{ eV}$ [2, 6].

The spectrometer was installed at the UE56/2-PGM-2 beamline at the BESSY II storage ring [19]. Figure 1 schematically illustrates the geometry of the experiment. Linearly polarized radiation of energy 125 eV was incident upon a Cu(001) surface at a grazing angle of 10° . Electrons emitted within the solid angle of collection of the lenses are transported to hemispherical analysers that energetically disperse the electrons onto the detectors. The optical axes of the lenses define the scattering plane and are separated by 90° with one axis in the plane of the storage ring and the other perpendicular to it. The sample was oriented such that the mean take-off angles for the horizontal and vertical analyser with respect to the surface normal were 15° and 75° , respectively.

Each analyser was operated in a mode that allowed the collection of electrons within an angular range of $\approx 30^\circ$ within the xy plane (figure 1) and, simultaneously, within a 30 eV energy range centred at 50 eV . The energy range recorded in parallel by each analyser is partitioned respectively into discrete values E_1 and E_2 for the vertical and horizontal analysers in order to represent two-dimensional (2D) electron pair energy distributions. The total energy resolution for each analyser was $\approx 0.8 \text{ eV}$. Consequently the total energy resolution for electron pairs was $\approx 1.1 \text{ eV}$. All kinetic energies were measured with respect to the vacuum level of the Cu(001) surface.

The Cu(001) single crystal was chosen as a target due to its well-known electronic structure. It was cleaned by the standard procedures of Ar^+ sputtering and annealing at 750 K before initial measurements and every 12 h thereafter. The base pressure of the chamber was $5 \times 10^{-11} \text{ mbar}$. The sample was at room temperature during the measurements.

A timing coincidence logic unit was used to determine when an electron was detected at each of the two detectors within a relatively large time range of 150 ns and to provide a timing signal relative to which the arrival time of each electron t_1 and t_2 was measured. For each such event, the energy of the two electrons and their arrival times were recorded in list mode (E_1, E_2, t_1, t_2). The distribution of the differences between the arrival times of the two electrons, $\Delta t = t_1 - t_2$, was then analysed to distinguish *true* coincidences of two correlated electrons instantaneously emitted after the absorption of a single photon from *random* coincidences of two unrelated electrons arriving at each of the detectors due, typically, to the absorption of two photons within the 150 ns time window. True

coincidences are characterized by having a Δt value within a narrow range t_c determined by the temporal resolution of the apparatus which is dominated by the energy and emission-angle-dependent temporal dispersion of the electron optics. The Δt value for fortuitously time-coincident but uncorrelated electrons is randomly distributed across the 150 ns time window. By well-established methods [20, 21] the energy-dependent background of random coincidences can therefore be subtracted from the energy distribution of true correlated pairs. The ratio of the rates of true and random coincidences was maintained above one for all spectral features of interest by reducing the photon flux at the sample by a series of apertures.

3. Experimental results and discussion

Figure 2(a) shows a histogram of arrival time differences Δt for all detected pairs from a Cu(001) surface upon excitation with linearly polarized photons of energy 125 eV. The area of the prominent peak (shaded) at $\Delta t = 0$ ns that lies above the flat background is a measure of the total number of true coincidences. Its width t_c is consistent with an estimation of the temporal resolution by simulating the dominant contribution of time dispersion through the electron optics. The number of correlated events (true coincidences) N_t is found from the total number of counts within a region of width t_c centred on the peak minus the number of random coincidence events in the same area which is estimated from the average intensity away from the peak.

The 2D energy distribution of correlated electron pairs (true coincidences) detected from the Cu(001) surface upon excitation with 125 eV photons is presented in figure 2(b). This data is obtained by determining the number of true coincidences at each locus (E_1, E_2) by the method described above. Several distinctive spectral features appear that have not previously been observed together in a single spectrum from a solid surface. The highest energy structure is related to the onset of direct DPE. Below that there are three regions of interest labelled as A, B and C which are situated around $(E_1, E_2) = (56 \text{ eV}, 46 \text{ eV}), (46 \text{ eV}, 56 \text{ eV})$ and $(46 \text{ eV}, 58 \text{ eV})$, respectively. These regions correspond to the nominal energy of 3p photoelectrons and $M_{2,3}-M_{45}M_{45}$ Auger electron pairs, i.e. the process studied by APECS. Their structure in and between these regions is considered in more detail below. The difference in the sum energy of the detected pairs emitted by these processes will be discussed elsewhere.

We first turn our attention to the onset of the DPE process. In the DPE process, a photon of energy $h\nu = 125 \text{ eV}$ excites the system and two unbound electrons may be detected with kinetic energy E_1 and E_2 after they have overcome the vacuum barrier given by the work function ϕ of the sample. By energy conservation, the electron pair sum energy is given by

$$E_{\text{sum}} = E_1 + E_2 = h\nu - (E_{b_1} + E_{b_2}) - 2\phi \quad (1)$$

where E_{b_1} and E_{b_2} are the electrons' bound-state energies as measured from the Fermi level E_F . The work function ϕ for the Cu(001) surface is 4.63 eV [22]. If both detected electrons were ejected from the Fermi level ($E_{b_1} + E_{b_2} = E_F$) their

sum energy would be 115.7 eV. However, it is known that the density of states at E_F , due to sp states, is small compared to the density of 3d states approximately 2 eV below E_F . In the 2D pair energy distribution (figure 2(b)) the onset of direct DPE can be easily recognized as a continuous line at a pair sum energy $E_A = E_{\text{sum}} \approx 112 \text{ eV}$ below which the coincident electron pair intensity increases. The continuous distribution of pair intensity at the onset is characteristic of the pair conserving the sum of their energy but sharing it continuously. The pair sum energy at the DPE onset corresponds to $E_{b_1} = E_{b_2} = 1.9 \text{ eV}$, which is consistent with the initial bound state of the emitted electrons being located at the top of the d-band. Thus the onset of the DPE process is dominated by the bulk d-band electrons of the Cu(001) surface.

For a photon energy $h\nu = 125 \text{ eV}$, 3p photoelectrons and $M_{23}-M_{45}M_{45}$ Auger electrons can be distinguished on the basis of the difference in their nominal energy. Accordingly, the intensity at region A would be attributed to 3p photoelectrons detected by the vertical (E_1) analyser and Auger electrons by the horizontal (E_2) analyser; similarly, intensity at B would be due to 3p photoelectrons detected by the horizontal analyser and Auger electrons by the vertical analyser. By applying the constraints to the data that E_1 (E_2) lies in the range of either $2p_{1/2}$ or $2p_{3/2}$ photoemission, a line profile along E_2 (E_1) reveals the coincident spectrum containing only the $M_2-M_{45}M_{45}$ or $M_3-M_{45}M_{45}$ ($M_3-M_{45}M_{45}$ or $M_2-M_{45}M_{45}$) Auger component, respectively. The results of this process (not shown) are equivalent to scanning over the Auger spectrum with one analyser while keeping the other fixed at a particular kinetic energy and are in general agreement with the recent work of Gotter *et al* [12]. Structure in the regions labelled A, B and C can be attributed to the spin-orbit splitting ($\approx 2.5 \text{ eV}$) of the M_{23} level, which also manifests in the corresponding $M_2-M_{45}M_{45}$ and $M_3-M_{45}M_{45}$ Auger energy and the multiplet structure of the Auger final state. The Coster-Kronig preceded $M_3M_{45}-M_3M_{45}M_{45}$ Auger process can be expected to make only a small contribution overlapping that of the $M_3-M_{45}M_{45}$ process [10]. Most clearly seen, the 1G and 3F multiplet components associated with the configuration of the two-hole final state that dominates the Auger spectrum are separated by $\approx 3 \text{ eV}$ [12]. The intensity at regions A and C in figure 2(b) can be attributed, respectively, to transitions resulting in 1G and 3F two-hole final states. We briefly note here that asymmetry about the line $E_1 - E_2$, including the absence of an intense feature corresponding to C at $(E_1, E_2) = (46 \text{ eV}, 58 \text{ eV})$, is related to the asymmetric scattering geometry which influences the relative contribution of the final multiplet components by constraining the emission direction of both electrons as reported by Gotter *et al* [12].

The structures in the regions labelled A, B and C have a diagonally oriented structure which is characteristic of a pair of electrons sharing the sum of their energy. Energy sharing between Auger and photoelectrons has previously been inferred from the shifts in the Cu 3p photoelectron line in coincidence with Auger electrons from several discrete energy ranges within the Auger envelope [10, 12]. The linear relationship between the energy of the correlated electrons is clearly evident in the 2D representation of the pair energy

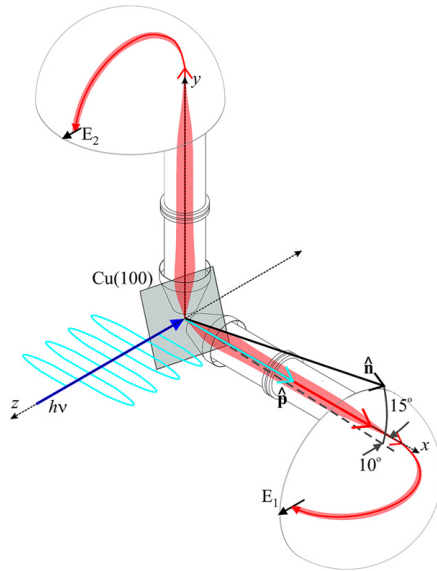


Figure 1. The schematic view of experimental set-up showing in outline the two analysers and their orientation. The light was incident on the Cu(001) crystal surface at a grazing incidence of 9.6° . The axis of the analyser transfer lenses lies in a plane perpendicular to the incident light and at an angle of 90° to each other. The energy dispersing directions are marked E_1 and E_2 , respectively. \hat{n} is the surface normal while \hat{p} gives the direction of light polarization.

distribution. A striking aspect revealed by the present work is the continuous diagonal structure of constant sum energy that connects regions A and B, extending even to where $E_1 = E_2$, where the former distinction made between Auger electron and photoelectron becomes completely meaningless.

In previous APECS experiments the energy of one fixed analyser scanned [8–13], which imposes a constraint on the uncertainty of one electron and consequently on the other electron of the correlated pair. By detecting correlated pairs over a wide energy range without imposing any restriction on the energy of either electron we reveal that the energy of both electrons is not strictly limited to the lifetime-broadened lines that are observed when each electron is detected individually by single-electron (noncoincidence) spectroscopy. This provides dramatic evidence for the inadequacy of a two-step description of the process in terms of photoexcitation and Auger decay and highlights the significance of correlation between the emitted electron pair.

We have confirmed that the continuous line between regions A and B is not an artefact by decreasing the photon energy by 5 eV to 120 eV. For this case the energy differences between the photoelectrons and Auger electrons increase and result in a larger separation between the maxima in the sharing curve. A continuous line of pair intensity still extends through $E_1 = E_2$. It is worth noting also that $h\nu = 120$ eV is below the 3s level threshold.

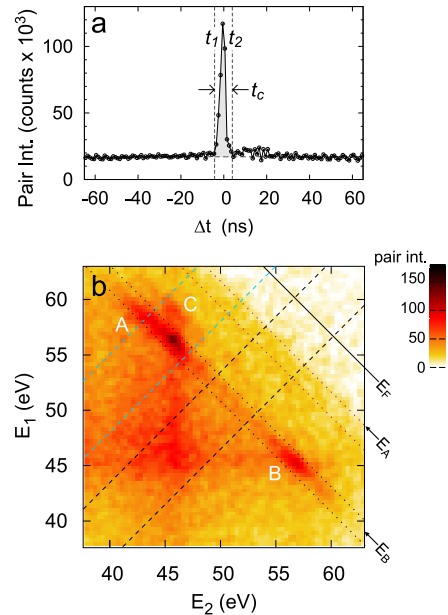


Figure 2. Experimental data from a Cu(001) surface excited by linearly polarized 125 eV photons. In panel (a) the coincident pair intensity is displayed as a function of Δt for all detected pairs. The shaded region represents the total number of true coincidences (correlated pairs) which fall within an interval $t_1 \leq \Delta t \leq t_2$. The contribution of random coincidences in this interval is estimated from the height of the constant background outside the interval. The energy distribution of the correlated pairs displayed in panel (b) was obtained by subtracting the distribution of random coincidences from the distribution of all events in intervals $t_1 \leq \Delta t \leq t_2$. E_F , E_A and E_B which label, respectively the Fermi level, the onset of direct DPE from the d states and the most intense part of the core-resonant DPE. Structures within the core-resonant DPE envelope are labelled A, B and C. Dashed and dotted lines indicate the boundary of areas from which the sum energy ($E_1 + E_2$) and energy sharing ($E_1 - E_2$) profiles in figure 3 are obtained. See the text for further details.

It is evident in the finite width of the line between A and B that the sum energy of the electron pair is conserved and constrained by the lifetime-broadened width of the final two-hole state. This can be examined more closely by constructing a sum energy spectrum under the constraint $E_1 - E_2 \approx 0$, i.e. the integrated pair intensity along a 5 eV wide region centred on $E_1 - E_2 = 0$ eV and bound between the dashed black lines in figure 2(b). The result is shown in figure 3(a). The sum energy spectrum across the region containing the features labelled A and B in figure 2(b) (the integrated pair intensity along $E_1 - E_2 = 11.5$ eV) is included for comparison. In both profiles the onset of d-band DPE at around 112 eV can be recognized. The peak at lower sum energy may be attributed predominantly to electron pairs emitted by the core-resonant DPE process, which result in a $^1G M_{45} M_{45}$ Auger final state. A smaller component attributable to 3F final states appears as an

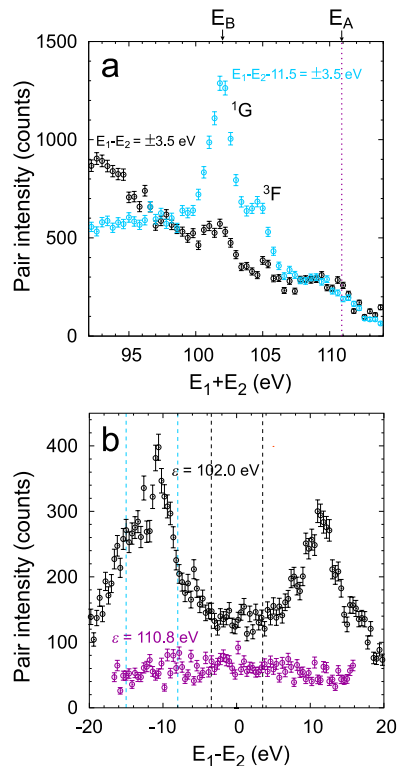


Figure 3. (a) The pair sum energy spectra of electron pairs with energy difference $E_1 - E_2 + 11.5 \text{ eV} = \pm 3.5 \text{ eV}$ (blue circles) and nearly equal energy $E_1 - E_2 = \pm 3.5 \text{ eV}$ obtained by integrating the pair intensity along the region bound by the pairs of dashed lines in figure 2(b). In both spectra both the onset of direct DPE from the d-band and DPE resonant with 3p excitation can be recognized. Lines corresponding to those in figure 2(b) are included for reference. (b) The energy sharing curves of electron pairs with sum energies of $E_1 + E_2 = \varepsilon \pm 0.9 \text{ eV}$ for $\varepsilon = 102 \text{ eV}$ (black circles) and $\varepsilon = 110.8 \text{ eV}$ (magenta circles) obtained by integrating the pair intensity along the regions bound by the pairs of dotted lines in figure 2(b). The former corresponds to electron pairs emitted by the core-resonant DPE process, resulting in a $^1G M_{45}M_{45}$ final state configuration. The latter corresponds to pairs emitted by direct DPE of electron pairs from the top of the d-band.

energy shoulder on the high energy side of the 1G component. The width of these components, taking into account the experimental resolution, can be estimated from the present data to be 1.6 eV. This is consistent with the pair sum energy being uncertain within the lifetime-broadened width of the two-hole final state.

The energy sharing distribution of correlated electron pairs can be extracted from the 2D electron pair energy distribution as the integrated intensity along a 1.3 eV wide region centred on the line $E_1 + E_2 - \varepsilon = 0$, where ε is the sum energy available to a pair for a particular process. In figure 3(b) we present a

sharing curve for $\varepsilon = 102 \text{ eV}$ that corresponds energetically to $3p_{1/2}$ and $3p_{3/2}$ photoemission and Auger transitions to $^1G M_{45}M_{45}$ final states (small overlapping contribution from other final states can be neglected). The region is shown bound by dotted black lines in figure 2(b). The sharing curve for $\varepsilon = 111 \text{ eV}$ that corresponds to direct DPE final states, included in figure 3(b), is comparatively flat. The broad peaks in the energy sharing distribution (figure 3(b)) for pairs emitted by core-resonant DPE may suggest that the energy sharing between electrons is not completely arbitrary and may be sensitive to the particular initial, intermediate and final states involved in each of the allowed transitions. Detailed analysis of the shape of the peaks in the sharing curves requires consideration of the angle-dependent contribution from each transition due to dipole and Coulomb selection rules, together with diffraction of the electron pairs within the crystal and the discrimination between the transitions imposed by the arrangement of the detectors [12]. It should be added that the origin of the intensity extending in broad bands from region A in the $-E_1$ direction and from region B in the $-E_2$ direction and overlapping around $(E_1, E_2) = (45, 45)$ is not yet completely understood. The direction of these bands, parallel to the energy axes, is characteristic of nonconservation of the sum energy of the pair due to inelastic scattering processes. The contribution of an incoherent process and its influence in the sharing curve for the electrons emitted by core-resonant DPE will be investigated in future experiments.

To explain the continuous energy sharing we consider that the system is collectively excited upon absorption of the photon into an intermediate many-body state that cannot be decomposed into products of single-particle states. The system decays to a two-hole final state by the emission of a pair of electrons in an interacting two-particle state. The emitted electrons should therefore be regarded as a single entity. There is, in principle, no constraint on the energy of each electron but they may arbitrarily share the total energy available which is determined by energy conservation of the complete process. In this regard the processes of direct and core-resonant DPE are similar. We emphasize that without Coulomb interaction neither process can occur. If the coherence of the two-particle state is broken by, for example, inelastic scattering, it will decay into single-particle states and each electron will be observed with an average energy equal to the nominal photoelectron or Auger electron energy. Similarly, the two-particle nature of the emitted electrons can only be observed when both electrons are detected and correlated in time. The spectra observed by single (noncoincidence) photoelectron or Auger electron spectroscopy may be considered to be equivalent to the pair spectrum integrated over all possible emission directions and energy of the undetected electron.

4. Conclusions

We have presented the two-particle emission spectra from a Cu(001) surface upon excitation with linearly polarized photons with sufficiently high energy to excite the 3p core level. We observe both direct DPE and core-resonant DPE in the same spectrum. The final state of both processes

contain two holes in the d-band but is distinguished on the basis of the total energy available to the pair. In the energy sharing distribution of electron pairs, the direct DPE manifests as a continuum without discrete structure. Pairs emitted by core-resonant double photoemission are also clearly shown to share their total energy continuously while jointly conserving the energy of the complete process. The energy of both electrons is not constrained to the energy they are observed to have when detected independently. These results confirm that core-resonant double photoemission must be described by a coherent single-step process in which the emitted electrons represent a correlated two-particle state. Detailed comparison of the dynamics of direct double photoemission and core-resonant double photoemission is currently being investigated for different scattering geometries and photon energies and is expected to yield further insight into the role of correlation in these processes.

Acknowledgments

We thank the BESSY II staff, particularly W Mahler and B Zada, for excellent experimental conditions at the beamline.

References

- [1] Berakdar J 1998 *Phys. Rev. B* **58** 9808
- [2] Schumann F O, Winkler C and Kirschner J 2007 *Phys. Rev. Lett.* **98** 257604
- [3] Fominykh N, Henk J, Berakdar J and Bruno P 2002 *Surf. Sci.* **507–510** 229
- [4] Fominykh N, Henk J, Berakdar J, Bruno P, Gollisch H and Feder R 2000 *Solid State Commun.* **113** 665
- [5] Fominykh N, Berakdar J, Henk J and Bruno P 2002 *Phys. Rev. Lett.* **89** 086402
- [6] Herrmann R, Samarin S, Schwabe H and Kirschner J 1998 *Phys. Rev. Lett.* **81** 2148
- [7] Gollisch H, v Schwartzberg N and Feder R 2006 *Phys. Rev. B* **74** 075407
- [8] Sawatzky G A 1988 *Treatise on Materials Science and Technology* ed C L Briant and R P Messmer (New York: Academic) pp 167–243
- [9] Haak H W, Sawatzky G A and Thomas T D 1978 *Phys. Rev. Lett.* **41** 1825
- [10] Jensen E, Bartynski R A, Hulbert S L, Johnson E D and Garrett R 1989 *Phys. Rev. Lett.* **62** 71
- [11] Stefani G, Gotter R, Ruocco A, Offi F, Pieve F D, Iacobucci S, Morgante A, Verdini A L A, Yao H and Bartynski R A 2004 *J. Electron. Relat. Phenom.* **141** 149
- [12] Gotter R, Da Pieve F, Offi F, Ruocco A, Verdini A, Yao H, Bartynski R and Stefani G 2009 *Phys. Rev. B* **79** 075108
- [13] van Riessen G A and Thurgate S M 2006 *Surf. Int. Anal.* **38** 691
- [14] Gunnarsson O and Schönhammer K 1980 *Phys. Rev. B* **22** 3710
- [15] Ohno M and Wendin G 1979 *J. Phys. B: At. Mol. Phys.* **12** 1305
- [16] Ohno M 1999 *J. Electron Spectrosc. Relat. Phenom.* **109** 109
- [17] Stefani G, Iacobucci S, Ruocco A and Gotter R 2002 *J. Electron. Relat. Phenom.* **127** 1
- [18] Da Pieve F, Sebilliau D, Di Matteo S, Gunnella R, Gotter R, Ruocco A, Stefani G and Natoli C R 2008 *Phys. Rev. B* **78** 035122
- [19] Sawhney K, Senf F, Scheer M, Schafers F, Bahrtdt J, Gaupp A and Gudat W 1997 *Nucl. Instrum. Methods* **390** 395
- [20] Jensen E, Bartynski R A, Hulbert S L and Johnson E D 1992 *Rev. Sci. Instrum.* **63** 3013
- [21] Hayes P, Bennett M A, Flexman J and Williams J F 1988 *Rev. Sci. Instrum.* **59** 2445
- [22] Weinelt M 2002 *J. Phys.: Condens. Matter* **14** R1099

Spin-Resolved Mapping of Spin Contribution to Exchange-Correlation Holes

F. O. Schumann, C. Winkler, and J. Kirschner

Max-Planck Institut für Mikrostrukturphysik, Weinberg 2, 06120 Halle, Germany

F. Giebels, H. Gollisch, and R. Feder

Theoretische Festkörperphysik, Universität Duisburg-Essen, 47048 Duisburg, Germany

(Received 10 November 2009; published 26 February 2010)

By means of spin-polarized electron coincidence spectroscopy we explore the fundamental issue of spin-resolved contributions to the exchange-correlation hole in many-electron systems. We present a joint experimental and theoretical study of correlated electron pair emission from a ferromagnetic Fe(001) surface induced by spin-polarized low-energy electrons. We demonstrate that the contribution to the exchange-correlation hole due to exchange is more extended than the contribution due to the screened Coulomb interaction.

DOI: [10.1103/PhysRevLett.104.087602](https://doi.org/10.1103/PhysRevLett.104.087602)

PACS numbers: 79.60.-i, 73.20.At

In seminal papers Wigner & Seitz [1] and Slater [2] introduced the concept of the exchange-correlation (xc) hole in many-electron systems. This is defined in real space and is closely related to the pair correlation function. The essential point is that around each electron the electronic charge density is reduced such that the charge deficit amounts to exactly one elementary charge. This result is a combination of two effects, namely, the Pauli principle and the repulsive Coulomb interaction. The Pauli principle demands that two electrons with parallel spins can not be at the same location, while the Coulomb correlation will force electrons to stay apart independent of the spin orientation. The extension of the exchange part and correlation part of the xc hole do not have to be necessarily the same. Slater discussed these differences in the pair correlation function [2]. For parallel spins both exchange and Coulomb interaction play a role, while antiparallel spin electrons experience only the Coulomb interaction. The region of reduced charge density is larger for parallel spins than for antiparallel spins. The concept of the xc hole is of pivotal importance in modern solid state theory, because it determines the exchange-correlation energy term which is a central part within density functional theory. There are currently intense efforts underway to improve the accuracy of the exchange-correlation term. The importance of this term becomes clear if we recall that it contains essential many-body effects, e.g., magnetism.

It would be interesting to perform experiments aimed to separate the relative size and magnitude of the exchange and correlation contribution to the xc hole. An experimental approach, which is sensitive to the electron-electron interaction, is the electron pair emission from surfaces excited by a sufficiently energetic primary electron. It has been demonstrated that the concept of the xc hole can be studied by the electron pair emission from surfaces. The xc hole manifests itself through a reduction of the pair emission intensity around the fixed emission direction of one electron, which we may call the depletion zone [3–8].

We learn from this that the minimum of the momentum distribution correlates with the minimum of the pair correlation function. One may speculate whether a spin dependence can be observed in the momentum distribution. For this one needs to be able to adjust the relative spin orientation of the incoming electron and the target electron. In this way it is possible to “switch off” the contribution due to exchange. The generation of a spin-polarized primary beam is an established technique [9–11]. Spin-polarized target electrons are available in ferromagnets, where the overall population of one spin direction (called majority) is larger than for the opposite spin direction (called minority). The orientation of the majority direction can be controlled via an external magnetic field. To maximize the spin dependence of the observable momentum distribution, one needs energy and momentum conditions, for which target electrons with one spin orientation strongly predominate. We find such conditions by means of an *ab initio* electronic structure calculation. By experiment and corresponding pair emission theory we provide the first demonstration that it is possible to disentangle exchange and correlation. We observe that the depletion zone for exchange is larger than for correlation.

We built a time-of-flight (TOF) coincidence apparatus using a spin-polarized primary beam and a ferromagnetic sample; see Fig. 1. A spin-polarized electron beam is created via photoemission with circular polarized light from a GaAs surface [9–11]. Switching the light helicity reverses the polarization direction. This spin-polarized primary beam hits the sample along the surface normal. In our coordinate system the x and y axis are in the surface plane. Two channelplate detectors (labeled “left” and “right”) with delay line anodes allow the determination of the impact positions of the electrons. A coincidence circuit ensures that only one electron pair per incident electron pulse is detected. From the flight time and the impact position we determine the kinetic energy and the in-plane components of the momentum for each electron. The

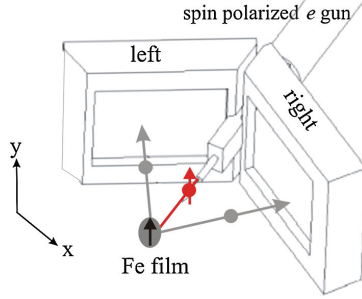


FIG. 1 (color). A transversely spin-polarized electron hits a ferromagnetic sample. The relative orientation of the majority and polarization direction can be independently reversed. Momentum distributions are obtained via position sensitive detectors and time-of-flight analysis.

kinetic energy is defined with respect to the vacuum level. We grow an approximately 20 ML thick Fe film on a W(001) surface. It is magnetized in-plane with the easy axis along the [010] direction which is parallel to the y axis; see Fig. 1. We can apply a pulsed magnetic field along the y axis for reversing the magnetization. The spin polarization of the incoming beam is also along the y axis. The primary spin polarization and majority spin direction can be individually controlled. Therefore, the observed spectra can be grouped into two subsets: (i) for subset I^+ primary spin and majority spin directions are parallel (ii) events with antiparallel alignment of primary electron and majority spin are contained in subset I^- . The reversal of the relative spin orientation occurred every few minutes. The data acquisition times for both spin alignments are equal allowing direct comparison of the intensity levels. The total acquisition time was a few months due to the requirement to operate at low primary flux. This is mandatory in order to reduce the detection from two electrons in coincidence which come from different primary electrons. Our target is a single crystalline surface therefore the in-plane component of the momentum must be conserved (modulo a reciprocal surface lattice vector). This can be written as

$$\mathbf{k}_{\parallel}^{\nu} + \mathbf{k}_{\parallel}^{\rho} = \mathbf{k}_{\parallel}^{\ell} + \mathbf{k}_{\parallel}^{\tau} = \mathbf{k}_{\parallel}^{\text{sum}}. \quad (1)$$

On the left side of the equation we have the contribution of the valence electron $\mathbf{k}_{\parallel}^{\nu}$ and the primary electron $\mathbf{k}_{\parallel}^{\rho}$, while on the right side the contribution of the detected electrons $\mathbf{k}_{\parallel}^{\ell}$ (“left”) and $\mathbf{k}_{\parallel}^{\tau}$ (“right”) can be found. The sum of these two terms is called sum momentum $\mathbf{k}_{\parallel}^{\text{sum}}$. Since we operate with a normal incidence primary beam we have $\mathbf{k}_{\parallel}^{\rho} = 0$. We note that $\mathbf{k}_{\parallel}^{\text{sum}}$ determines the value of the valence electron $\mathbf{k}_{\parallel}^{\nu}$. Since energy conservation has to hold the energy of the emitted electrons specify the binding energy of the valence electron. Therefore the position of the valence electron within the band structure is uniquely defined.

In order to disentangle exchange and correlation contributions, it is important, as will be described later in detail, to find a position with a high density of valence electron states of mainly one spin type. To this end we have calculated the electronic structure of the ground state of a thick Fe(001) film by means of an *ab initio* full-potential linear augmented-plane-wave (FLAPW) method [12]. The resulting spin- and layer-resolved densities of states reveal a strong predominance of majority spin for $\mathbf{k}_{\parallel}^{\nu} = 0$ and $E = -0.8$ eV.

Further, we calculated (e , $2e$) spectra with the aims of a quantitative comparison with our experimental spectra and of resolving them with respect to the valence electron spins. For these calculations we used a formalism, which has previously been presented in detail [7,8]. We therefore briefly recall only the concepts and expressions which are most essential for the present purpose. The central ingredients are matrix elements of the form

$$f^{\sigma\tau} = \langle l^{\sigma} r^{\tau} | U | p^{\sigma} \rangle | v^{\tau} \rangle, \quad (2)$$

where $|p^{\sigma}\rangle$ and $|v^{\tau}\rangle$ are the (spin-dependent) spatial parts of the primary and the valence electron states with spin orientations $\sigma = \pm$ and $\tau = \pm$ relative to the majority spin axis of the target. U denotes the screened Coulomb interaction. The two detected electrons are described by an antisymmetric two-electron state, the direct spatial part of which is

$$|l^{\sigma} r^{\tau}\rangle = |l^{\sigma}\rangle |r^{\tau}\rangle F_{\text{corr}}(\mathbf{k}, \mathbf{r}), \quad (3)$$

where $|l^{\sigma}\rangle$ and $|r^{\tau}\rangle$ are the spatial parts of time-reversed LEED states. These are coupled by the Coulomb correlation factor $F_{\text{corr}}(\mathbf{k}, \mathbf{r})$, which is a function of the relative momentum \mathbf{k} and the relative coordinate \mathbf{r} obtained as the numerical solution of a relative-particle Schrödinger equation involving U [8]. Because of the antisymmetry of the two-electron states we have, in addition to the direct matrix element $f^{\sigma\tau}$ [cf. Eq. (2)], an exchange matrix element $g^{\sigma\tau}$ which is analogous to $f^{\sigma\tau}$, with l^{σ} and r^{τ} interchanged.

For the cases spin σ of the primary electron parallel and antiparallel to the spin τ of the valence electron, i.e., $\tau = \sigma$ and $\tau = -\sigma = \bar{\sigma}$, we then have the fully spin-resolved (e , $2e$) reaction cross sections

$$I^{\sigma\sigma} \propto |f^{\sigma\sigma} - g^{\sigma\sigma}|^2 \delta \quad \text{and} \quad I^{\sigma\bar{\sigma}} \propto (|f^{\sigma\bar{\sigma}}|^2 + |g^{\sigma\bar{\sigma}}|^2) \delta, \quad (4)$$

where δ symbolizes the conservation of energy and surface-parallel momentum. From these partial intensities, summation over the valence electron spins yields the experimentally observable intensities

$$I^+ = I^{++} + I^{+-} \text{ for primary electron spin-up,} \quad (5a)$$

$$I^- = I^{-+} + I^{--} \text{ for primary electron spin-down.} \quad (5b)$$

For the application of the above (e , $2e$) formalism to Fe(001) we constructed from our ground state spin densities spin-dependent effective quasiparticle potentials.

These contain, in particular, spin-dependent imaginary self-energy parts V_{im}^σ , with $\sigma = +$ for spin-up and $\sigma = -$ for spin-down electrons. For the valence electron, V_{im}^σ was taken from a many-body calculation [13]. For the primary electron and the two detected electrons, which are represented by LEED states, we used the form $V_{\text{im}}^\sigma = a^\sigma(E + b^\sigma)c^\sigma$, where $a^+ = -0.22$, $b^+ = 2.67$, $c^+ = 0.69$, $a^- = -0.33$, $b^- = 4.67$, $c^- = 0.62$, and E is the kinetic energy. This choice is in quantitative accordance with experimental mean-free path data, which show that spin-down electrons are more strongly damped than spin-up electrons [14–16]. Using the above V_{im}^σ in a spin-dependent LEED calculation from Fe(001), we obtained the best agreement with experimental data [17]. In our present ($e, 2e$) calculations, this V_{im}^σ yields significantly better agreement with our experimental data than a spin-independent V_{im} .

For the electron-electron interaction U in Eq. (2) we used a screened Coulomb potential in the Thomas-Fermi approximation $U \propto \exp(-r/\lambda)/r$ with the screening length as a parameter determined as $\lambda = 2.65 \text{ \AA}$ by comparing, for several primary energies, calculated ($e, 2e$) spectra with their experimental counterparts.

Our aim is to disentangle exchange and correlation which requires a valence state of high spin polarization. From theory we know that the choice of $\mathbf{k}_{\parallel}^{\text{sum}} = 0$ and a binding energy 0.8 eV below the Fermi level E_F fulfills this. Experimentally, we allow $|\mathbf{k}_{\parallel}^{\text{sum}}| \leq 0.16 \text{ \AA}^{-1}$ in order to have sufficient statistics. Further, the symmetry of the experiment suggests to select those coincidence events, where the kinetic energy of both emitted electrons is equal. A primary energy of 25 eV demands both emitted electrons have a mean energy of 9.7 eV in order to access the selected valence state. For statistics reasons the energy sum of these two electrons has a window of 1 eV. For 2D momentum distributions of the data we note that for each coincident event the in-plane components of electron left and right are known. According to our coordinate system k_x^l is always negative while k_x^r is positive. Therefore, a coincidence event has an entry on the left and right half of the plot. In contrast to theory which covers the full momentum space the experiment has a limited range. Only momenta which fall inside the area, which has the solid lines as boundary, can be recorded; see Figs. 2(a) and 2(b). Let us discuss the experimental intensities I^+ and I^- shown in panels (a) and (b). Starting at $|k_x^{l,r}| = 0$ we note that the coincidence intensity is zero which is purely instrumental since there is a gap between the detectors. Outside this “blind” region, starting at about $|k_x^{l,r}| = 0.2 \text{ \AA}^{-1}$, we observe an increase of the coincidence intensity for increasing k values. A maximum is reached at $|k_x^{l,r}| 0.7 \text{ \AA}^{-1}$. This reduced intensity for small $|k_x^{l,r}|$ values is a manifestation of the xc hole as shown previously in experiment and theory [4–6,8]. Apart from this similarity important differences between I^+ and I^- can be noticed. First, the integrated intensity for I^+ is higher than for I^- . Second, the

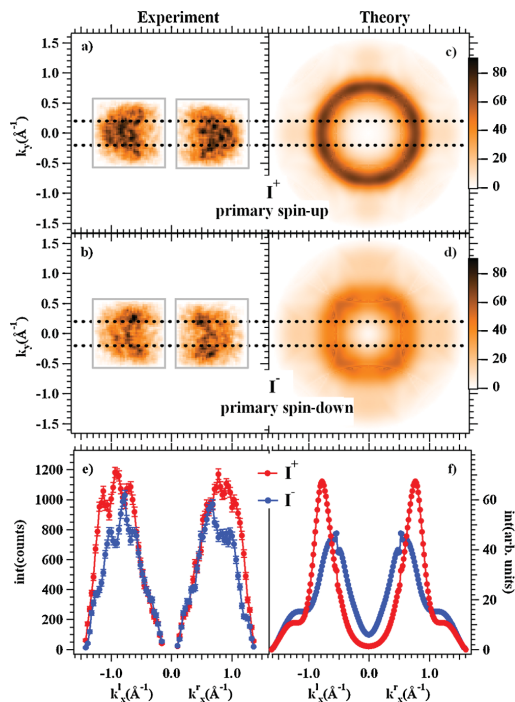


FIG. 2 (color). Results for excitation with a primary energy of 25 eV and emission of 9.7 eV electrons. In panels (a) and (c) the spin polarization of the primary beam and spin direction of the majority electrons are parallel (I^+), while they are antiparallel (I^-) in panels (b) and (d). Only momenta which fall inside the area which has the solid lines as boundary can be measured. Panels (e) and (f) are line scans through the distributions I^+ and I^- with an integration width determined by the dashed lines in the upper panels.

intensity distribution for I^+ is very different from I^- . Intensities of I^- close to the maximum value are confined to $|k_x^{l,r}|$ values near 0.7 \AA^{-1} . For I^+ the intensity levels are close to the maximum value up to $|k_x^{l,r}|$ of 1.1 \AA^{-1} , before a drop can be observed. This is a consequence of the finite angular acceptance of the instrument.

Experimental and theoretical data are best compared via line scans through the 2D-momentum distributions for I^+ and I^- , respectively, Figs. 2(e) and 2(f). The integration range along $|k_x^{l,r}|$ is indicated by the dashed horizontal lines in Fig. 2. Both experiment and theory clearly show that the maximum intensity for I^+ is larger than the corresponding maximum for I^- . Further agreement consists in the larger extension of the depletion zone for I^+ . The pair distributions in Fig. 2 contain, for each primary electron spin direction, collision events with both a majority- and a minority-spin valence electron according to Eq. (5). Further insight is obtained by considering these two events separately. To this end we show in Fig. 3 the calculated four

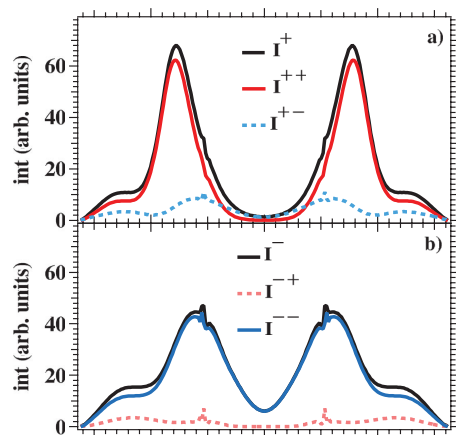


FIG. 3 (color). Spin-dependent intensities as calculated for the surface-parallel momentum along the [100] direction [Fig. 2(f)] cf. Eq. (5). (a) The solid red line shows the intensity of I^{++} (primary spin-up and valence electron spin-up). The dotted blue line relates to the intensity I^{+-} (primary spin-up and valence electron spin-down). The solid black line represents the sum of $I^{++} + I^{+-} = I^+$. (b) The solid blue line shows the intensity of I^{-+} (primary spin-down and valence electron spin-up). The dotted red line relates to the intensity I^{--} (primary spin-down and valence electron spin-down). The solid black line represents the sum of $I^{-+} + I^{--} = I^-$.

fully spin-resolved intensities $I^{\sigma\sigma}$ and $I^{\sigma\bar{\sigma}}$ [cf. Eq. (4)]. In Fig. 3(a) we show the decomposition of I^+ according to Eq. (5). We note that the main intensity to I^+ comes from the term I^{++} (primary spin-up and valence electron spin-up), whereas the term I^{+-} (primary spin-up and valence electron spin-down) is almost negligible. In other words: the intensity I^+ contains essentially only those collision events, where the spins of the primary and collision partner are parallel. Therefore exchange and correlation play a role. In a similar way the intensity I^- is mainly given by the contribution I^{-+} (primary spin-down and valence electron spin-up); see Fig. 3(b). Again, one can rephrase this by saying that the spin of the collision partner is antiparallel to the spin of the primary and only correlation is important. The origin of this spin selection is that the chosen valence state is essentially of majority type. This intrinsic spin resolution has an important consequence, namely, the possibility to separate exchange and correlation effects between the two outgoing electrons. For the parallel spin case $I^{++} \approx I^+$ both exchange and Coulomb correlation deter-

mine the size of the depletion zone, whereas for the antiparallel spin case $I^{-+} \approx I^-$ only the correlation plays a role. The size of the depletion zone for I^+ is larger than for I^- . Therefore, one can say that the size of the exchange depletion zone has to exceed the size of the correlation depletion zone.

In summary, we have demonstrated by experimental and theoretical analysis that it is possible to identify the different contributions of exchange and Coulomb interaction to the size of the depletion zone observed in spin-dependent electron pair emission. Since this zone is closely related to the spin-dependent pair correlation function, our results also apply to the latter and thereby to the spin-dependent parts of the exchange-correlation hole.

We acknowledge the expert assistance of H. Engelhard and D. Hartung in designing and building the experimental apparatus.

- [1] E. Wigner and F. Seitz, Phys. Rev. **43**, 804 (1933).
- [2] J. C. Slater, Rev. Mod. Phys. **6**, 209 (1934).
- [3] J. Berakdar, H. Gollisch, and R. Feder, Solid State Commun. **112**, 587 (1999).
- [4] N. Fominykh, J. Berakdar, J. Henk, and P. Bruno, Phys. Rev. Lett. **89**, 086402 (2002).
- [5] F. O. Schumann, J. Kirschner, and J. Berakdar, Phys. Rev. Lett. **95**, 117601 (2005).
- [6] F. O. Schumann, C. Winkler, and J. Kirschner, Phys. Rev. Lett. **98**, 257604 (2007).
- [7] H. Gollisch and R. Feder, J. Phys. Condens. Matter **16**, 2207 (2004).
- [8] H. Gollisch, N. v. Schwartzberg, and R. Feder, Phys. Rev. B **74**, 075407 (2006).
- [9] D. T. Pierce and F. Meier, Phys. Rev. B **13**, 5484 (1976).
- [10] S. Samarin, J. Berakdar, O. M. Artamonov, and J. Kirschner, Phys. Rev. Lett. **85**, 1746 (2000).
- [11] A. Morozov, J. Berakdar, S. N. Samarin, F. U. Hillebrecht, and J. Kirschner, Phys. Rev. B **65**, 104425 (2002).
- [12] See www.flapw.de.
- [13] L. Chioncel, L. Vitos, I. A. Abrikosov, J. Kollár, M. I. Katsnelson, and A. I. Lichtenstein, Phys. Rev. B **67**, 235106 (2003).
- [14] M. Getzlaff, J. Bansmann, and G. Schönense, Solid State Commun. **87**, 467 (1993).
- [15] D. P. Pappas, K. P. Kämper, B. P. Miller, H. Hopster, D. E. Fowler, C. R. Brundle, A. C. Luntz, and Z. X. Shen, Phys. Rev. Lett. **66**, 504 (1991).
- [16] F. Passek, M. Donath, and K. Ertl, J. Magn. Magn. Mater. **159**, 103 (1996).
- [17] R. Bertacco and F. Ciccacci, Phys. Rev. B **59**, 4207 (1999).

9. Acknowledgement

This work would not have been possible without the contribution of many people.

First and foremost, I have to thank Prof. J. Kirschner. It is a privilege to acknowledge the strong support I received from him. He introduced me to the field of electron coincidence spectroscopy and shared with me his vast knowledge and experience. Prof. J. Kirschner took a keen interest in the progress of this work. I also benefited from numerous late night discussions in which facts were critically reviewed.

Over the years a number of people joined the (e,2e) team who made important contributions to this work. I have to thank Dr. M. Birke, Dr. R. Dhaka, K. Hünlich, Dr. M. Muñoz-Navia, Dr. G. van Riessen, Dr. Z. Wei and Dr. C. Winkler. In particular, I am indebted to Dr. C. Winkler with whom I spent the longest spell. To most of the work he made important contributions and he introduced me to the programming in Labview. Dr. M. Birke and Dr. G. van Riessen made the electro-static set-up operational.

The experiments at the BESSY II storage ring were only possible due to the excellent support of the beamline personnel. It is my pleasure to thank Dr. K. Godehusen, Dr. W. Mahler, M. Mertins, Dr. F. Schäfers and B. Zada for their contribution. I am also obliged to Dr. W. Braun for his continuous effort to ensure a user friendly operation at BESSY II.

The positron experiment at the NEPOMUC facility at the FRM II was only successful due to the dedicated effort by Dr. C. Hugenschmidt and his team. They went so far and sacrificed some of their beamtime to allow us to complete our study.

The understanding of the experimental data requires a dedicated theoretical description. I am very grateful to have collaborated with my theoretical colleagues Prof. J. Berakdar, Prof. R. Feder, Dr. N. Fominykh, F. Giebels, Dr. H. Gollisch, Dr. O. Kidun and Dr. Y. Pavlyuk. Furthermore, the stimulating discussions and their patience to explain their theory to me contributed to the success of this work.

During a conference I was introduced to Dr. S. Samarin who made important contributions to the (e,2e) technique. I benefited from many discussions during conferences and his visits at our institute. Very valuable were also aspects which never made it into publications.

The studies on the Auger emission via DPE made it natural to seek a collaboration with Prof. G. Stefani who is an expert in this field. We stand at the beginning but joint experiments at BESSY have been conducted. I thank G. di Filippo, Dr. S. Iacobucci, Dr. F. Offi and Prof. G. Stefani for their participation. I appreciate also the invitation to come to Rome and the hospitality experienced during the stay.

I also benefited from discussions (about physics and other things) with my colleagues at the institute. I mention in particular Dr. P. Ignatiev, Dr. J. Prokop, Prof. M. Przybylski, Dr. D. Sander, Dr. V. Stepanyuk and Dr. A. Winkelmann. The latter I thank for the proof reading of this thesis.

The expert assistance of H. Engelhard, D. Hartung and F. Helbig in the construction, assembly and operation of the various apparatus was vital to achieve the scientific results. Likewise, I have to acknowledge the support of the mechanical and electronics workshop led by J. Wille and the late W. Eberhardt. High quality crystals were provided by H. Menge.

This work was partly supported by third party funding via the DFG within the SFB 762 which is acknowledged.

Last but not least, I have to praise my family for their patience and understanding during this journey. Words can not express what I owe to them.

Lebenslauf

Persönliche Daten:

Name: Frank Oliver Schumann
Geburtsdatum: 07.05.1964
Geburtsort: Dortmund
Staatsangehörigkeit: Deutsch
Familienstand: verheiratet, zwei Kinder

Schulbildung:

1970-1974: Gemeinschaftsgrundschule Steinenbrück
1974-1978: Gymnasium Herkenrath
1978-1983: Gymnasium Adolfinum, Moers
Juni 1983: Abitur am Gymnasium Adolfinum, Moers

Grundwehrdienst:

1983-1984

Wissenschaftlicher Werdegang:

Oktober 1984-April 1990: Studium der Physik an der RWTH Aachen, Diplom am 18.4.1990, Titel der Diplomarbeit: „Langreichweitiger Ordnungsparameter zweidimensionaler magnetischer Systeme“

Oktober 1990-Mai 1994: Promotion an der University of Cambridge (UK), Prüfung August 1994, Titel der Dissertation: „2D magnetism of ultrathin Co/Cu(001) films“

September 1994-Februar 1998: Post-doc an der Pennsylvania State University (USA)

März 1998-Oktober 1999: Post-doc am Lawrence Livermore National Lab (USA)

November 1999-Oktober 2004: Leiter einer Nachwuchswissenschaftlergruppe an der FU Berlin

Seit November 2004: Wissenschaftlicher Mitarbeiter am Max-Planck-Institut für Mikrostrukturphysik, Halle(Saale)

Erklärung an Eides statt

Ich erkläre hiermit, die vorliegende Habilitationsschrift

Studying the electron-electron correlation by pair emission from surfaces

selbständig und ohne fremde Hilfe verfasst und keine anderen als die von mir angegebenen Quellen und Hilfsmittel benutzt zu haben. Die den benutzten Werken wörtlich oder inhaltlich entnommenen Stellen sind als solche kenntlich gemacht.

Halle, 26. April 2011